INFORMATION TO USERS

This manuscript has been reproduced from the microfilm master. UMI films the text directly from the original or copy submitted. Thus, some thesis and dissertation copies are in typewriter face, while others may be from any type of computer printer.

The quality of this reproduction is dependent upon the quality of the copy submitted. Broken or indistinct print, colored or poor quality illustrations and photographs, print bleedthrough, substandard margins, and improper alignment can adversely affect reproduction.

In the unlikely event that the author did not send UMI a complete manuscript and there are missing pages, these will be noted. Also, if unauthorized copyright material had to be removed, a note will indicate the deletion.

Oversize materials (e.g., maps, drawings, charts) are reproduced by sectioning the original, beginning at the upper left-hand corner and continuing from left to right in equal sections with small overlaps. Each original is also photographed in one exposure and is included in reduced form at the back of the book.

Photographs included in the original manuscript have been reproduced xerographically in this copy. Higher quality 6" x 9" black and white photographic prints are available for any photographs or illustrations appearing in this copy for an additional charge. Contact UMI directly to order.

UMI

A Bell & Howell Information Company
300 North Zeeb Road, Ann Arbor, MI 48106-1346 USA
313/761-4700 800/521-0600

Order Number 9521318

Carrier and exciton dynamics in strained semiconductor bulk and quantum wells

Takiguchi, Yoshihiro, Ph.D.

City University of New York, 1995

U·M·I
300 N. Zeeb Rd.
Ann Arbor, MI 48106

A

CARRIER AND EXCITON DYNAMICS IN STRAINED SEMICONDUCTOR BULK AND QUANTUM WELLS

by

YOSHIHIRO TAKIGUCHI

A dissertation submitted to the Graduate Faculty in Engineering in partial fulfillment of the requirements for the degree of Doctor of Philosophy, The City University of New York

1995

This manuscript has been read and accepted for the Graduate Faculty in Engineering in satisfaction of the dissertation requirement for the degree of Doctor of Philosophy.

9/27/94

Date

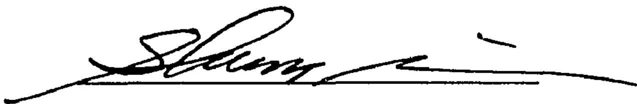

Chair of Examining Committee
Prof.Kai Shum (Thesis Advisor)

9/27/94

Date

Prof. R.R.Alfano(Co-Thesis Advisor)

9/27/94

Date

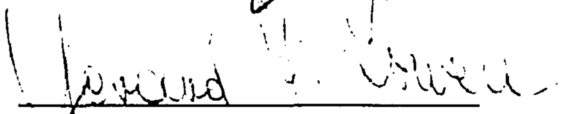

Executive Office

Prof. P. P. Ho (CCNY)

Prof. F. Pollak (BCNY)

Prof. G. Subak-Sharp (CCNY)

Dr. Mittra Dutta (U.S.Army Electronic Technology and Device Laboratory)

Prof. R. Dorsinvile (CCNY)

Dean G. Lowen (CUNY)

The City University of New York

ABSTRACT

CARRIER AND EXCITON DYNAMICS IN STRAINED SEMICONDUCTOR BULK AND QUANTUM WELLS

by

YOSHIHIRO TAKIGUCHI

Thesis Advisor : Professor Kai Shum

Co-Thesis Advisor : Professor Robert R. Alfano

In this thesis, I have investigated carrier and exciton dynamics in strained semiconductor bulk and quantum well samples. In these samples, the band structures were altered by a combination of the built-in and/or externally applied stresses and the quantum confinement. External uniaxial compressive stress on the bulk and QWs at 4 °K tuned the band structures continuously and showed effects on transient carrier and exciton dynamics. I have examined the photoluminescence kinetics in time and energy domains using picosecond time-resolved photoluminescence spectroscopy at 4 to 300 °K sample temperatures. Intra-subband carrier and exciton thermalization, and inter-subband scattering, cooling, exciton formation, exciton localization to interface islands, and recombination processes were investigated by taking into account carrier-carrier scattering, carrier- and exciton-phonon interactions, and spontaneous emission processes.

I investigated the hole thermalization and cooling processes at low lattice temperatures in 2 μm and 4 μm thick n-type GaAs epilayers grown on Si substrates(GaAs/Si), whose valence bands split to heavy and light hole subbands due to built-in biaxial tension perpendicular to the growth direction. In both samples, I found the hole temperature decreased exponentially with the cooling time of 28 ps. The cooling rate of 0.115 meV/ps was about six times smaller than the theoretically expected rate for the LO phonon emission process. The slow energy relaxation was attributed to the non-equilibrium LO phonon accumulation in the system.

I investigated the electron thermalization and cooling processes in Beryllium modulation-doped multiple quantum wells (MQWs) with 40 Å and 188Å well widths fabricated on Si substrates. Because of the combined effects of stress and quantum confinement, a light mass hole (lmh) subband located at lowest energy in the 188Å MQW while a heavy mass hole (hmh) subband located at the lowest energy in the 40Å MQWs. I determined the electron cooling times and rates to be 46±4 ps and 0.2 meV/ps in the 188Å MQW/Si and 30 ps and 0.2 meV/ps in the 40Å MQW/Si, respectively. The external uniaxial compressive stress applied onto the 188Å MQW/Si (maximum pressure was 14 kbar) altered the electron cooling time due to the change in the electron-LO phonon interaction through the hole mass.

I also investigated the exciton dynamics in a 188Å single QW/Si (SQW/Si) under external uniaxial compressive stress (maximum pressure ~13 kbar) and a built-in tensioned GaAsP QWs. The intrinsic 188Å SQW/Si under uniaxial compression showed a fast and a slow energy relaxation processes.

The fast process arises from the exciton-LO phonon interaction and the slow process was attributed to inter-subband scattering. In the GaAsP QW, the photogenerated carriers were found to form hot excitons within 30 ps and the excitons relax down to the lowest exciton levels through intra- and inter-subband scattering within 30 ps to 100 ps depending on the well width, the exciton mass, and the lattice temperature. The exciton localization process into the interface islands was found to consist of a fast energy relaxation which was attributed to acoustic deformation potential interaction and a slow energy relaxation process which was attributed to the exciton trapping process to the widest island which is considered to be quasi-zero dimensional square wells.

ACKNOWLEDGEMENT

I would like to thank Professor Robert R. Alfano, Distinguished Professor of Science and Engineering at CUNY, for introducing me to ultrafast semiconductor material science, suggesting this area of research, and help with thesis reaserch. I thank Professor Kai Shum, an associate professor of Electrical Engineering at CCNY, for his knowledgeable suggestions, assistance, advice, and mentorship directing this research projects. I am grateful to Professor K. M. Yoo, now a lecturer of Physics Department at the Hong Kong University of Science and Technology, for his effort in maintaining our research lab. to operate well and for his friendship and to other members of Photonic Application Laboratory for their collaboration. I greatly appreciate the collaboration with Distinguished Professor Fred H. Pollak of the Brooklyn College of CUNY and my friend Hao Qiang who worked together on a complicate and old stress dewar with me. I sincerely thank Dr. M. Dutta of U.S. Army Electronics Technology and Devices Laboratory, Prof. H. Morkoc of Univ. of Illinois at Urbana-Champain, and Dr. Emil S. Koteles of GTE for kindly giving me the opportunity to investigate their important samples for my research. I thank Dr. N. Ockman for reading and correcting parts of this thesis. I am greatly thankful to President T. Hiruma, Dr. Y. Suzuki and Dr. Y. Tsuchiya of Hamamatsu Photonics K.K. for giving me the opportunity to visit City College and encouraging me to work towards a Ph. D. Finally, I sincerely thank my wife Yoshimi for daily help with love and to my children, Yu, Ai, and Kei for encouraging me every day from their heart.

TABLE OF CONTENT

Abstract iii

Acknowledgement vi

Table of Contents vii

List of Tables xiv

List of illustrations xv

1. Introduction 1

    1.1 . Reference 11

2. Band structure with and without stress 14

    2. 1. Band structure without stress 14

        2.1.1 Band structure of a semiconductor 20

        2.1.2. One dimensional finite quantum well model 21

        2.1.3. Superlattice (Knonig-Penny model) 26

        2.1.4. k•p approximation 30

    2. 2. Strain and stress in semiconductor 33

        2.2.1. Lattice mismatch 34

        2.2.2. Thermal expansion 41

    2. 3. Band structure under stress 43

        2.3.1. Bulk material under stress 44

        2.3.2. QW band structure under stress 50

    2.4 Dislocation 55

    2.5. Reference 57

3. Carrier energy relaxation 59

    3.1 Introduction 59

3.2 Carrier-carrier scattering 64
3.3 Energy relaxation through phonon interactions 65
3.3.1. Acoustic deformation potential (ADP) interaction 69
3.3.2. Piezoelectric scattering 70
3.3.3. Optical phonon 71
3.3.4. Non-polar optical phonon 72
3.3.5. Momentum and energy relaxation through phonon interaction 72
3.3.6. Hole energy relaxation 75
3.4. Carrier energy distribution change through phonon interaction ..75
3.5. Average carrier and average carrier kinetic energies 78
3.6. Carrier recombination through spontaneous emission 79
3.6.1 Spontaneous emission from bulk GaAs 84
3.6.2. Spontaneous emission from QWs 88
3.6.3. Real spectrum 92
3.4. Reference 95
4. Experimental Methods 97
4. 1. Steady state PL spectroscopy 97
4.1.1. CW Laser 100
4.1.2. Lock-'in amplifier detection 101
4.1.3. Optical dewar 103
4.1.4. Temperature controller 104
4.1.5. Glue 105
4. 2. Picosecond time-resolved PL spectroscopy 105
4.2.1. Ultrashort laser system 108
4.2.2. Pulse duration measurement using an optical

autocorrelator 111
4.2.3 Streak camera system 116
4.2.3.1. Spectral sensitivity 119
4.2.3.2. Time resolution 120
4.2.3.3. Dynamic range 121
4.2.3.4. Time spread in the streak camera 123
4.2.3.5. Streak trace overlap 126
4.2.3.6. Streak camera time axis calibration 130
4.2.3.7. Photocathode sensitivity uniformity 134
4.2.4.Spectrometer and spectrograph 136
4.2.4.1 Operational principle 136
4.2.4.2. Time spread of reflection grating 137
4.2.4.3. Spectral resolution of the system 140
4.2.4.4. Spectral calibration 141
4. 3. External pressure apparatus 147
4.3.1 Cryostats with stress apparatus 147
4.3.2. Stress apparatus 149
4.4. Reference 152
5. Hole dynamics in GaAs/Si under biaxial stress 154
5.1. Introduction 154
5.2. 2μm thick n-type GaAs/Si 155
5.2.1. Sample and experimental setup 156
5.2.2. Experimental results 158
5.2.2.1 Steady state PL spectrum 158
5.2.2.2 Time-resolved PL spectrum 160
5.2.3. Discussion 164

5.2.3.1 Hot carrier dynamics model 164

5.2.3.2 Initial hot carrier thermalization model 167

5.2.3.3 Hole temperature cooling 173

5.2.4. Summary 184

5.3. 4μm thick n-type GaAs/Si 186

5.3.1. Introduction 186

5.3.2. Sample and experimental setup 187

5.3.3. Experimental results 187

5.3.4. Discussion 192

5.3.4.1 Initial hole relaxation and slow recombination tail 192

5.3.4.2 Average energy relaxation 194

5.3.5. Summary 197

5.4. Conclusion 198

5.5. Reference 200

6. 2D Electron dynamics in Be modulation-doped GaAs MQW/Si under stress 201

6. 1. Biaxially tensioned Be-modulation doped MWQ/Si 201

6.1.1. Introduction 201

6.1.2. Samples 202

6.1.3. Experimental method 204

6.1.4. Experimental results 205

6.1.5. Discussion 205

6.1.6. Conclusion 219

6. 2. External uniaxial stress on Be-modulation doped 188Å MQW/Si 220

6.2.1. Introduction 220

6.2.2. Sample and experimental setup 221

6.2.3. Experimental results 223

6.2.4. Discussion 228

6.2.5. Conclusion 241

6.3. Reference 243

7. 2D Exciton dynamics in intrinsic GaAs SQW/Si 244

7.1. Introduction 244

7.2. Sample and experiments 245

7.3. Experimental results 246

7.4. Discussion 248

7.4.1. Initial exciton dynamics 248

7.4.2. Exciton average energy relaxation 250

7.5. Conclusion 256

7.6. Reference 257

8. 2D Exciton dynamics in biaxial strained GaAsP QWs 259

8.1 Introduction 259

8.2. Sample 261

8.3. Experimental setup 262

8.4. Experimental results 263

8.4.1. Steady state PL and PLE spectra 263

8.4.2. Time-resolved PL spectra 266

8.4.3. Dynamic Stokes shift 269

8.5. Discussion 271

8.5.1. Exciton binding energy 271

8.5.2. Exciton dynamics model 274

8.5.3. Average exciton kinetic energy relaxation 284
8.6. Conclusion 291
8.7. Reference 294
9. Conclusion 296
10. Future direction 301
11. List of publications 303
12. Physical constants and material parameters 305
12.1. Physical Constant 305
12.2. Material parameters 307

Glossary 312

Appendix 318
A. 1. Time spread in optics 318
A.1.1. Introduction 318
A.1.2. Index of refraction 318
A.1.3 Group velocity and group velocity dispersion 319
A.1.4. Pulse propagation in dispersive medium 321
A.1.5. Gaussian pulse propagation 322
A.1.6. GV and GVD effects in different structure optical elements ... 328
A.1.6.1. Plates 328
A.1.6.2. Prisms 328
A.1.6.3. Lenses 331
A.1.7. Reference 334
A. 2. Computer Programs 335
A.2. 1. Communication programs 336

A. 2. 2. Data analysis programs 345

A. 2. 3. Theoretical calculation programs 366

Bibliography 375

LIST OF TABLES

Chapter 2

Table 2.3.1 Band edge shifts due to 2 kbar of various types 49

Chapter 4

Table 4.2.1 Time spread due to the gsquare rating with 139

Chapter 5

Table 5.4.1 Experimentally evaluated time constants from 199

Table 5.4.2. Estimated hole intra-subband relaxation times 199

Chapter 8

Table 8.5.1. The exciton dynamics parameters obtained 282

Chapter 12

Table 12.1 Physical constants 305

Table 12.2 Pressure units 306

Table 12.3 Band gap energy as function of lattice temperature ... 307

Table 12.4 Material parameters 1 308

Table 12.5 Material parameters 2 309

Table 12.6 Material parameters 3 310

Table 12.7 Material parameters 4 311

Appendix

Table A.1.1. A and λ_0 values for various kinds of optical 319

Table A.1.2. B values for various materials 324

LIST OF ILLUSTRATIONS

Chapter 1

Fig.1.1. The progress in ultrafast laser pulse generation 2

Chapter 2

Fig. 2.1.1. Band structure of GaAs material without stress 15

Fig. 2.1.2. Constant energy surfaces for the $m_j=\pm1/2$ and 17

Fig. 2.1.3. AlAs band structure 19

Fig. 2.1.4. Finite barrier height single quantum well model 21

Fig. 2.1.5. n=1 and n=2 quantized wave function in a one 22

Fig. 2.1.6. Energy eigen states and wave functions in a 24

Fig. 2.1.7. Periodic finite potential barriers in Kronig- 26

Fig. 2.1.8. L(ε/V0) vs. ε/V_0 diagram obtained from the 28

Fig. 2.1.9. Band structure calculated from the Kronig-Penney 28

Fig. 2.2.1. Tension generated by the lattice mismatch at 34

Fig. 2.2.2. (a) Measured and (b) calculated tensile stresses 38

Fig. 2.2.3. Tension generated in GaAsP well layers 39

Fig. 2.2.4. The biaxial tension as function of lattice 42

Fig. 2.3.1. Kronig-Penney multiple QW model under 44

Fig. 2.3.2. Uniaxial compression and tension on a GaAs 46

Fig. 2.3.3. Built-in biaxial tension in a GaAs/Si sample. 47

Fig. 2.3.4. Band structures of GaAs without stress and 49

Fig. 2.3.5. Schematic band structures of bulk GaAs and 52

Fig. 2.4.1. (a) Cross-section of TEM image of GaAs/Si 56

Chapter 3

Fig. 3.1.1. Energy relaxation processes of carriers in GaAs 61

Fig. 3.3.1. Relative momentum relaxation time through 73

Fig. 3.3.2. Electron-hole plasma energy relaxation rates 74

Fig. 3.4.1. Calculated carrier density change by energy 76

Fig. 3.4.2. Calculated carrier density change by energy 77

Fig. 3.6.1. Band structure and radiative transitions between 80

Fig. 3.6.2. Spontaneous emission PL spectrum for a 85

Fig. 3.6.3. Radiative transitions in a GaAs/AlGaAs QW 89

Fig. 3.6.4. (a) potential structure along z-axis and its quantized 90

Fig. 3.6.5. PL emission spectrum with homogeneous and 93

Chapter 4

Fig. 4.1.1. Steady State PL Measurement setup 98

Fig. 4.1.2. Photon absorption depth in a GaAs material. 99

Fig. 4.1.3. Frequency distribution of incident electronic 102

Fig. 4.1.4. Schematic diagram of optical cryostat, diffusion ... 103

Fig. 4.2.1. Time-resolved photoluminescence spectroscopy 106

Fig. 4.2.2. Colliding pulse mode-locked ring dye laser 108

Fig. 4.2.3. Four prism configuration to create negative 110

Fig. 4.2.4. Optical dispersion free autocorrelator 112

Fig. 4.2.5. Autocorrelation trace of femtosecond pulse 115

Fig. 4.2.6. Streak camera system block diagram. 117

Fig. 4.2.7. Streak tube structure. 117

Fig. 4.2.8. Typical spectral sensitivity of S-20 and S-1 type 119

Fig. 4.2.9. Dynamic range of a streak camera defined as 121

Fig. 4.2.10. Time resolved pulse images within (pulse image 122

Fig. 4.2.11. Optical pulse delay at different incident 125
Fig. 4.2.12. Group delay effect at 530 nm and 350 nm laser 125
Fig. 4.2.13. Synchroscan deflection signal and its linear 127
Fig. 4.2.14. Circular scan operation which enables to avoid 128
Fig. 4.2.15. Overlap effect of back trace of synchroscan 129
Fig. 4.2.16. Time axis calibration using a Michelson 130
Fig. 4.2.17. Train pulse generation through etalon mirror. 131
Fig. 4.2.18. Streak image and its intensity profile obtained 132
Fig. 4.2.19. Time calibration curve obtained for a synchroscan 133
Fig. 4.2.20. An experimental setup to evaluate uniformity 135
Fig. 4.2.21. Spectral sensitively of a synchroscan streak casmera .. 135
Fig. 4.2.22. Reflection grating structure and light diffraction 138
Fig. 4.2.23. Ultimate spectral resolution determined by the 140
Fig. 4.2.24. Spectra of Ne lamp observed at (a) 143,144
Fig. 4.2.25. Spectral calibration curves for Ne lamp 145,146
Fig. 4.3.1. Stress dewar structure. 148
Fig. 4.3.2. Schematic diagram of compressive stress 150
Fig. 4.3.3. Stress apparatus diagram. The stress can be 151

Chapter 5

Fig. 5.2.1. (a) Band structure of biaxially tensile strained 157
Fig. 5.2.2. A steady state PL spectrum from the 2μm 159
Fig. 5.2.3. Three dimensional display of the time-resolved 161
Fig. 5.2.4. The time integrated PL spectrum between 161
Fig. 5.2.5. Initial PL kinetics from the 2μm GaAs/Si 162
Fig. 5.2.6. Temporal profile of the donor to hmh transition 164

Fig. 5.2.7. Diagram of photogenerated electron and hole 165

Fig. 5.2.8. Five energy level model including initial hole 167

Fig. 5.2.9. Measured PL spectra (a) at 19~21 ps (c) 51 ~54 ps 179

Fig. 5.2.10. Hole cooling process analyzed with Fröhlich 180

Fig. 5.2.11. Average hole kinetic energy relaxation for the 184

Fig. 5.3.1. Time-resolved PL spectrum in three dimensional 188

Fig. 5.3.2. Time integrated PL spectrum from t=0 to 500 ps 189

Fig. 5.3.3. Initial PL spectral change for the 4μm GaAs/Si 190

Fig. 5.3.4. Temporal profiles for the donor-hmh, the donor 191

Fig. 5.3.5. A hole temperature dependent intra-subband 193

Fig. 5.3.6. Average hole energy and PL intensity profiles 196

Fig. 5.3.7. Average hole kinetic energy relaxation within 196

Chapter 6

Fig. 6.1.1. Band structures of the (a) 188Å and (b) 40Å 203

Fig. 6.1.2. Three dimensional display of the time-resolved 206

Fig. 6.1.3. Band structures of the (a) 188Å MQW/Si and 208

Fig. 6.1.4. Experimental PL spectra for (a) the 188Å QW 214

Fig. 6.1.5. Electron thermalization in the modulation Be- 216

Fig. 6.1.6. Average electron energy relaxation in the 188Å 218

Fig. 6.2.1. (a) Sample and (b) band structures 221

Fig. 6.2.2. Band edge energy shifts due to the externally 224

Fig. 6.2.3. Calculated transition energies between 226

Fig. 6.2.4. Calculated valence subband structure under 226

Fig. 6.2.5. 3D time-resolved PL spectra under (a) 0 kbar, ... 227,228

Fig. 6.2.6. Spontaneous emission spectral spectral fit at 229

Fig. 6.2.7. Electron temerpature cooling under 0 and 9.6 kbar 230

Fig. 6.2.8 Average carrier energy (a) under and (b) above 231

Fig. 6.2.9. Average carrier kinetic energy after subtracting 233

Fig. 6.2.10. Average carrier energy relaxation time and the 234

Fig. 6.2.11. Average kinetic energy relaxation rates under 235

Fig. 6.2.12. Five level energy relaxation model 237

Fig. 6.2.13. Calculated average energy using the five level 240

Chapter 7

Fig. 7.2.1. (a) Sample and (b) band structure of the 188Å 245

Fig. 7.3.1. PL spectra for the SQW/Si under uniaxial stress 247

Fig. 7.3.2. PL intensity profiles for the SQW/Si under 247

Fig. 7.4.1. Band structures of the 188Å SQW/Si (a) under 0 k 249

Fig. 7.4.2. <E(t)> for the SQW/Si without stress and under ... 251

Fig. 7.4.3. The fast and slow relaxation rates under various 252

Fig. 7.4.4. The exciton relaxation energy for fast (dots) and 253

Fig. 7.4.5. Average exciton energy relaxation rates for the 254

Fig. 7.4.6. Exciton energy relaxation rate as function of hole 255

Fig. 7.4.7. Effective hole mass in a 220 Å QW under [100] 256

Chapter 8

Fig. 8.2.1. (a) Sample and (b) band structures of the GaAsP 262

Fig. 8.4.1. The steady state PL and PLE spectra for 121Å 264

Fig. 8.4.2. Energy separation between the lowest hmh and 265

Fig. 8.4.3. Temperature dependence on the PL spectra of 266

Fig. 8.4.4. Three dimensional time-resolved spectra of (a) ... 267, 268

Fig. 8.4.5. Dynamic Stokes shifts of the PL peak energy 269
Fig. 8.4.6. Monolayer fluctuation of interface in GaAsP 270
Fig. 8.5.1. Exciton PL peak intensities as function of inverse 272
Fig. 8.5.2. Energy diagram of the six level model transition 275
Fig. 8.5.3. Measured PL time profiles (thick solid 281,282
Fig. 8.5.4. Average exciton energy relaxation and integrated 284
Fig. 8.5.5. The exciton average kinetic energy relaxation of 284
Fig. 8.5.6. L_z dependence on the exciton energy relaxation 288
Fig. 8.5.7. The exciton relaxation energy for the 79Å (open 290
Fig. 8.5.8. Energy relaxation rate determined from the 291

Appendix

Fig.A.1.1. Phase and group refractive index of BK7 glass 321
Fig.A.1.2. Pulse broadening due to GVD in BK7 glass 327
Fig.A. 1.3. Pulse broadening due to GVD in air 327
Fig.A.1.4. Retardation time of pulse front due to the GV in 329
Fig. A.1.5. Complex loop of pulse front after a convex lens 330

CHAPTER 1

INTRODUCTION

Over the past twenty years, electronics and optics have merged into a new field called "photonics". Electronics use various characteristics of the interactions between carriers (electrons and holes) and electric field while optics uses the wave nature or energy quanta "photons" of light. Electro-optical materials for high speed devices such as III-V semiconductor materials, especially GaAs and its alloys, are being widely used for ultrafast electronic and optical devices because of their large value of mobilities and excellent linear and non-linear optical properties.[1-7] The major goal of photonics will be the development of devices operating at higher speed for faster communications, computers, and information processing .

The progress in electronics started in 1948 when a semiconductor transistor was invented by Shockley. A major advance occurred in electronics in 1969 when Esaki and Tsu[8] at IBM introduced the concepts of quantum confinement and tunneling. When a device size becomes comparable to the de-Broglie wavelength of the electron, quantum mechanical effects determine the electron energy states and the electron behavior in the device. The quantum confinement is the result of the wave nature of the electrons which produces discrete energy levels. Quantum devices were realized due to progress

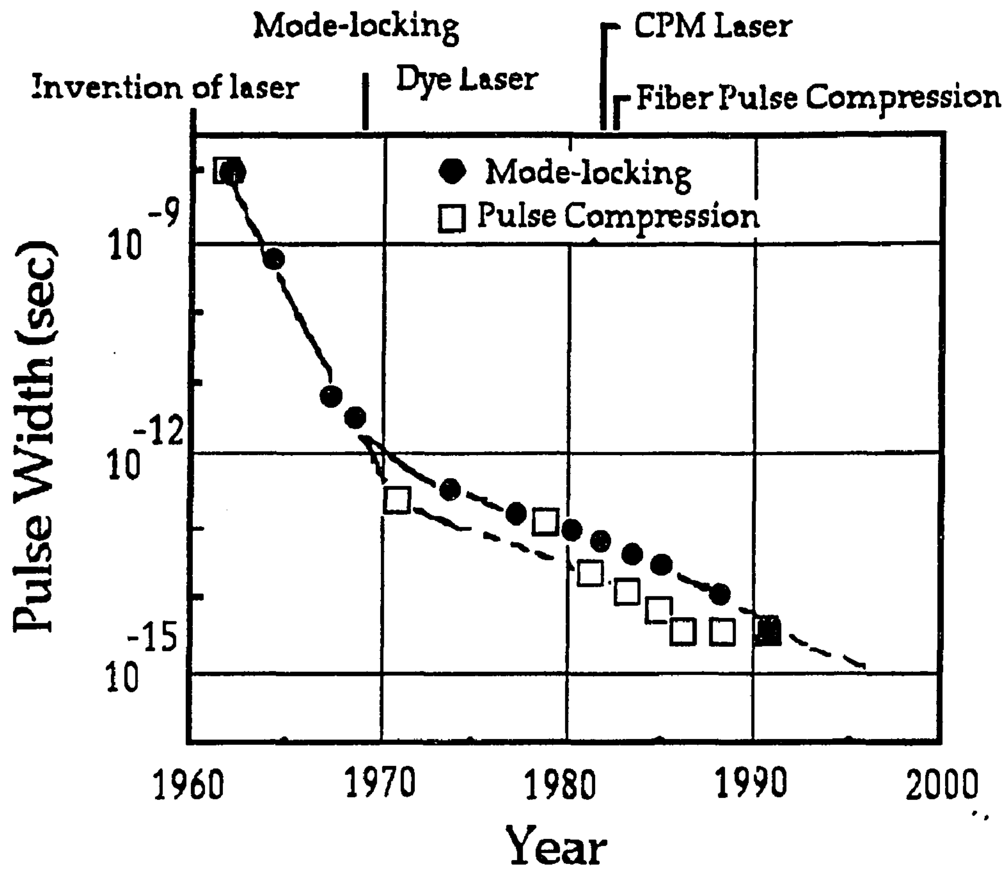

Fig.1.1 The progress in ultrafast laser pulse generation from mode-locking and pulse compression techniques.

in thin atomic layer growth techniques such as Molecular Beam Epitaxy (MBE) and Metal Organic Chemical Vapor Deposition (MOCVD). A few tens Å thick heterostructures, quantum wells (QWs), superlattices, and III-V material epitaxy layers can be grown with desired doping, high purity, and monolayer accuracy.

In optics, since the invention of the laser by Maimann in 1960, ultrafast laser technology (based on mode-locking and pulse compression techniques) was advanced into the femtosecond time region as shown in Fig. 1.1. Laser pulses were reduced from ns (nanosecond: 10^{-9} s) to fs (femtosecond:10^{-15} s) from 1960 to 1990. Today, a 6 fs laser pulse duration can

be obtained in visible to infrared region.[9] A new candidate for a solid state femtosecond laser is semiconductor lasers consisting of III-V materials. GaAs is a direct band gap material and population inversion can be created between the conduction and valence bands. A GaAs laser was developed in 1975 by introducing the double-heterostructure fabrication technique.[10] The double-heterostructure consists of a semiconductor active layer sandwiched by different semiconductor materials. Since the double-heterostructure confines both carriers and photons in the same layer, electronic excitation creates population inversion of excited carriers, enhances stimulated emission, and thus produces efficient lasing. In a QW structure, since the carrier density of states is larger in both the conduction and valence bands and the transition oscillator strength is larger than in a GaAs bulk material, QW lasers can have higher gain, low threshold, and emits visible light. QW lasers were introduced in 1981[11] and opened up lower threshold and high energy photon semiconductor laser applications.[12] Original GaAs heterostructure lasers required high current density because of a high lasing threshold while recent QW lasers generate a few mW of laser light powered with a regular battery. Recently, 200 fs pulse duration has been obtained by using pulse compression technique.

GaAs QW based electronics and optics have been combined to create new photonic devices such as GHz modulated lasers, receivers, and analog to digital converters on a single integrated circuit. The ultrafast photonic devices based on GaAs and InGaAs compounds are utilized especially in optical communications with the help of the dramatic progress in optical fiber technology. In optical communications, 1 GHz transmission bandwidth has been commercialized and a soliton communication experiment which enables a

THz bandwidth has been carried out successfully with few hundred km of dispersion free single mode optical fiber. Using not only the linear property of the GaAs QWs but also their non-linear optical property, QW devices direct the current and future developments of novel non-linear photonic devices.

GaAs quantum structures enable the creation of excellent electro-optic devices. However, this GaAs based technology has some problems to overcome. GaAs is a very rare material, the cost of the mass-production of photonic devices becomes large. Since it is difficult to grow a larger diameter crystal, a commercially available GaAs wafer size is about 3 inch in diameter. Therefore, the size of a photonic device is limited. A GaAs wafer is mechanically fragile and has low thermal conductivity which shortens the device lifetime and raises the quarities of reliability. On the other hand, Si substrates and epilayers are currently used for commercial integrated electronic circuits because of their low cost, good thermal conductivity, mechanical hardness, and large wafer availability as well as the fact that SiO_2 is an excellent electronic insulating compound. Due to these good electronic properties, Si based electronic technology was widely used and introduced this computer era. Si based photodiode has excellent characteristics for photon detection with a few tens ps time response when a p-i-n junction is fabricated. As a reversed bias voltage is applied to the very thin intrinsic Si layer sandwiched by the n- and p-type doped silicon layers (diode structure), the carriers photogenerated in the depletion layer is collected rapidly by the electrodes deposited on both the n- and p-type layers. The thinner the depletion layer, the faster the response time of the photodiode. Since Si is an indirect band gap semiconductor material, it is difficultto make a light emitter such as a laser and a modulator using Si based

material at this time. To obtain an optical transition in Si between its conduction and valence bands, electron-phonon interaction is necessary and the light emission probability is small. This Si band structure impedes the development of a laser diode using Si material. A combined hybrid semiconductor system is needed using GaAs and Si technology to combine the superior properties of each material.

When the excellent characteristics of GaAs and Si such as ultrahigh mobility and photoemissivity of GaAs and high thermal conductivity, strong device hardness, low cost, and large wafer sizes of the Si substrate are combined to make hybrid devices on a chip, it would be a major breakthrough for electronics and photonics.

GaAs epilayers grown on Si substrates have been attempted. However, it was difficult to grow the GaAs epilayer on a Si substrate without dislocations or misfits which arise from the lattice mismatch and the difference of thermal expansion coefficients between Si substrate and GaAs layers. Recent progress in microstructure fabrication techniques enabled the growth of most material on different lattice mismatched substrate when a surface of the substrate is covered by many layers of a strained superlattice. There were several attempts to obtain hybrid devices of Si logic electronics with GaAs laser diodes[13-17], photodetectors[18] and microwave circuits.

The first laser oscillation of a GaAs QW fabricated on a Si substrate has been demonstrated in 1985 by Windhorn et al.[19] followed by Fisher et al.[20] and Sakai et al. [21] in 1986. The QW lasers have shown excellent lasing characteristics such as a low-threshold and high power output. [14-18] These lattice mismatches or thermally mismatched devices contain residual strain in

the material layers when the device was cooled after the high temperature fabrication process. Especially, GaAs and Si materials have quite different thermal expansion coefficients. The difference causes a large biaxial stress perpendicular to the growth direction in GaAs epilayers. When the stress is above a critical value, the dislocation of the layers takes place. The built-in stress alters the band structures and removes the valence subband degeneracy and improves the laser performance. Not only GaAs/Si devices but also GaAs/InGaAs[15] and GaInP/AlGaInP[16] heterostructures also contain built-in biaxial stresses in well materials and are key structures for diode lasers suitable for optical communication and for a pumping source of an optical fiber amplifier. The underlying physics in such GaAs/Si systems needs to be studied to understand high power laser action and carrier dynamics under the stress altered band structure.

During the early 1920's, the band structures of most semiconductor materials were calculated theoretically using quantum mechanics. Kronig and Penney used a one-dimensional atomic model to explain the band structure of a simple one dimensional crystal in 1930.[22] Solving a Schrödinger equation in a periodic potential barrier structure to obtain the electron wave functions, the origin of the energy band gaps and the periodic band structure has been explained as will be discussed in the following chapter. The Kronig-Penney model was further investigated with a (k•p) approximation as a perturbation theory. The k•p approximation simplified the difficult procedure to obtain analytic solutions of the wave equation of the many atom system.

It has been well known that stress alters the band structure and changes carrier and/or exciton dynamics which determines the ultimate speed and the

electronic and optical operational efficiency of a device. Since the stress changes the separation between the atoms, the potential field generated by the atoms and the surrounding electrons is altered. The closer the distance between the atoms, the higher the potential field which alters the band structure. The band structures altered by the various types of stress applied on different crystal orientations has been determined experimentally and theoretically.

A theoretical analysis of the effect of uniaxial shear stress on the band structure of semiconductor materials has been performed by F. Pollak et al.[23) The valence subbands are split to heavy and light hole bands by the stress and the energy band gap between the conduction and valence bands changes according to the magnitude of the compressive or tensile stress. The amount of shifts are different for each subband. Analyzing the experimental data on the energy shifts, deformation potentials have been determined.[23)]

Over the past ten years, carrier and exciton interactions with phonons in non-strained bulk and QWs have been theoretically investigated. Conwell analyzed the carrier-phonon interaction in bulk semiconductor in detail.[24)] The energy and momentum relaxation rates of hot carriers by various phonon interactions have been discussed and listed by B. R. Nag.[25)] In general, the carriers loose their momentum through acoustic deformation potential interactions, piezoelectric interactions, non-polar or polar optical phonon interactions, impurity scattering, and alloy scattering within a few tens of fs to ps depending on the lattice temperature. The excess carrier kinetic energy above the lattice thermal energy is released to the lattice through these phonon interactions within a few hundred fs to a few hundred ps which is much longer than the momentum relaxation time. Several scientists have investigated the

hot carrier temperature thermalization in bulk GaAs materials [26] including, for example, J. Shah.[27] Due to the dramatic progress in femtosecond laser technology, carrier and exciton dynamics have been studied with few tens fs time resolution. Carrier thermalization processes as well as many-body effects such as screening and band renormalization which occur within one hundred fs have been investigated with optical methods.

Quasi-two dimensional exciton dynamics in QWs has also been extensively studied because QWs are important for high speed non-linear switching and for laser devices. The 2D exciton formation time of 15 to 20 ps (by T. C. Damen et al. [28] and by R. Strobel et al. [29], inter-subband exciton relaxation time of 90 ps, and exciton localization time of 130 ps, (by J. Kusano et al.[30] have been determined. Localized exciton energy relaxation process due to acoustic deformation potential (ADP) and LO phonon interactions have been studied. (by Masumoto[31], Takagahara[32], Basu et al.[33] Bacher et al.[34]) 2D exciton recombination process are discussed by Feldmann et at.[35], both experimentally and theoretically.

Carriers and excitons generated in the strained quantum devices propagate in a deformed energy band structure[36,37]. The dynamics of carriers and excitons, including energy thermalization, cooling, relaxation, trapping to interface islands or impurities, and recombination processes through phonon interactions should be different from those in unstrained quantum devices. Especially, when GaAs QWs are fabricated on a Si substrate, carrier and exciton dynamics in the QW structure is more complex because of the complex valence subband structure which is altered by a combination of the spatial quantum

confinement and the stress effects. The carrier and exciton dynamics in these strained materials has not been fully studied in any detail. As the strained devices become applied in photonic devices, the fundamentals of understanding the underlying carrier and exciton dynamics needs to be understood in such strained material. The research in this thesis is devoted to give a better understanding of stress effects.

In this thesis, I have investigated photogenerated carrier and exciton thermalization, cooling, inter-subband relaxation, trapping to interface islands or impurities, and recombination processes with phonon interaction in bulk GaAs and GaAs QW and GaAsP QW under various internal and external stress conditions.

The following is the organization of my thesis:

In chapter 2, I discuss the fundamental concepts and models of GaAs semiconductor band structure and quantum confinement. I discuss stress effects on the fundamental characteristics of the semiconductor band structure. In chapter 3, I discuss the carrier and exciton energy relaxation processes. In chapter 4, I discuss my experimental setup and equipment characteristics which determines the experimental accuracy and its reliability. In chapters 5 through 8, I describe the research carried out in this thesis on carrier and exciton dynamics in various samples under different experimental conditions to understand carrier-carrier and carrier phonon interaction under the stress altered band structure. In chapter 9, I summarize my accomplishments and what I contributed to the knowledge in the field. In chapter 10, I discuss future

directions of this research. In chapter 11, my publications are listed. In chapter 12, I have tabulated physical constants and material parameters used in this thesis. To help understanding technical terms used in this thesis, I have attached the glossary in Chapter 13. The appendix presents information on the temporal broadening effect in optical elements and the computer programs used in the analysis of the data I used in this research program. Finally, I present the bibliography.

1.1. References in Chapter 1

1). W. Schokley and W. T. Read, Jr., Phys. Rev. **87**, 835 (1952)

2). J. M. Luttinger and W. Kohn, Phys. Rev. **97**, 869 (1955)

3). J. M. Luttinger, Phys. Rev. **102**, 1030 (1956)

4). P. Lawaetz, Phys. Rev. B, **4**, 3460 (1971)

5). J. Shah and R C.C. Leite, Phy. Rev. Lett. **22**, 1304 (1969)

6). K. Kash and J. Shah, Appl. Phys. Lett. **45**, 401 (1984)

7). J. Shah and R.F. Leheny, in 'Semiconductor Probed by Ultrafast Laser Spectroscopy" edited by R.R.Alfano, Academic Press, New York (1984)

8). L. Esaki and R. Tsu, IBM Research Note, RC-2418 (1969) and IBM J. Res. Develop.61, Jan. (1970)

9). Harris, et al. "Ultrafast Phenomena VII", Springer Verlag, New York, (1990)

10). J. P. van der Ziel, R. Dingle, R. C. Miller, W. Wieg, and W. A. Nordland, Appl. Phys. Lett. **26**, 463 (1975)

11). W. T. Tang, Appl. Phys. Lett. **39**, 786 (1981)

12). R.N. Hall, G.E. Fenner, J.D. Kingsley, T.J. Soltys, and R. O. Carlson, Phys. Rev. Lett. **9**, 366 (1962)

13). G. Bernier, J. Beerens, J. De Boeck, K. Deneffe, C. van Hoof, and G. Borghs, Solid State Comm. **69**, 727 (1989)

14). M. Joma, et al., Appl. Phys. Lett. **58**, 2220 (1990)

15). L. F. Lester, et al., IEEE Photonics Tech. Lett. **3**, 403 (1991)

16). H. B. Serreze and Y. C. Chen, IEEE Photonics Tech. Lett. **3**, 397 (1991)

17). H. Asono, at al., IEEE Photonics Tech. Lett. **3**, 415 (1991)

18). L. Yang, at al., IEEE Photonics Tech. Lett. **3**, 430 (1991)

19). T. H. Windhorn and G.M. Metze, Appl. Phys. Lett. **47**, 1031 (1985)

20). R. Fischer, W. Kopp, H. Morkoc, M. Pion, et al. , Appl. Phys. Lett. 48, 1360 (1986)

21). S. Sakai, T. Soga, M. Takeyasu, X. W. Hu, et al., Proc. IEEE Int. Semiconductor Laser Conf. D-3 (1986)

22). R. de Kronig and W. J. Penney, Proc. Royal Sco. London, A130, 499 (1930)

23). F. H. Pollack and M. Cardona ,Phys. Rev. 172, 816 (1968)

24). E. M. Conwell "High Field transport in semiconductor", Academic Press, New York (1967)

25). Nag. in "Semiconductor Probed by Ultrafast Laser Spectroscopy", R.R. Alfano edited. Academic Press,New York(1984)

26). R. M. Hochstrasser, W. Kaiser, and C. V. Shank, "Picosecond Phenomena II", Springer-Verlag, Berlin and New York (1980)

27). J.Shah, Phys. Rev. B, 10, 3697 (1978)

28). T. C. Damen, J. Shah, D. Y. Oberli, D. S. Chemla, J. E. Cunningham, and J. M. Kuo, Phys. Rev. B 42, 7434 (1990)

29). R. Strobel, R. Eccleston, J. Kuhl, and K. Kohler, Phys. Rev. B, 43, 12564, (1991)

30). J. Kusano, Y. Segawa, Y. Aoyagi, S. Namba, and H. Okamoto, Phys. Rev. B, 40, 1685 (1989)

31). Y. Masumoto, S, Shionoya, and H. Kawaguchi, Phys. Rev. B, 29, 2324 (1984)

32). T. Takagahara, Phys. Rev. B 31, 6552 (1985)

33). P. K. Basu and Partha Ray, Phys. Rev. B, 45, 1907 (1992)

34). G. Bacher, J. Kovac, K. Streubel, H. Schweizer, and F. Scholz, Phys. Rev. B, 45, 9136(1992)

35). J. Feldmann, G. Peter, E. O. Gobel, P. Dawson, K. Moore, C. Foxon, and R. J. Elliott, Phys. Rev. Lett. 59, 2337 (1987)

36). K. Shum, Y.Takiguchi, J.M. Mohaidat, F. Liu, R.R.Alfano and H. Morkoc, Appl. Phys. Lett. 56, 2328 (1990)

37). E. S.Koteles, D.A.Owens, D. C. Bertolet, J-K. Hsu, and K.M.Lau, Surface Science, 228, 314 (1990)

CHAPTER 2

BAND STRUCTURE WITH AND WITHOUT STRESS

In this chapter, the GaAs band structure, quantum confinement, and the origin of the band structure using Kronig-Penney model with and without stress will be described.

2.1. Band structure without stress

In this section, I will review the band structures of GaAs and AlGaAs. The band structures of materials are the allowed energy levels for electrons in form of dispersion curves of E vs. k. The curves determine the electron energy states and dynamics. The electron position (point) on a band curve gives the electron's energy and momentum(ε, k). The band structure of a material can be altered by mixing different materials, changing the lattice temperature, fabricating quantum confinement structure, and generating deformation by stress-induced strain. A new band structure produces new electronic and optical characteristics which in turn causes the change of the carrier and exciton dynamics.

The band structure of GaAs at room temperature given by John S. Blakemore[1)] is shown in Fig.2.1.1. The valence band consists of three subbands, heavy mass hole(hmh), light mass hole(lmh), and split-off (s.o) which shows maxima at the center of first Brillouin zone where the wave vector k=0. The split-off band is separated from the heavy and light mass hole subbands due to

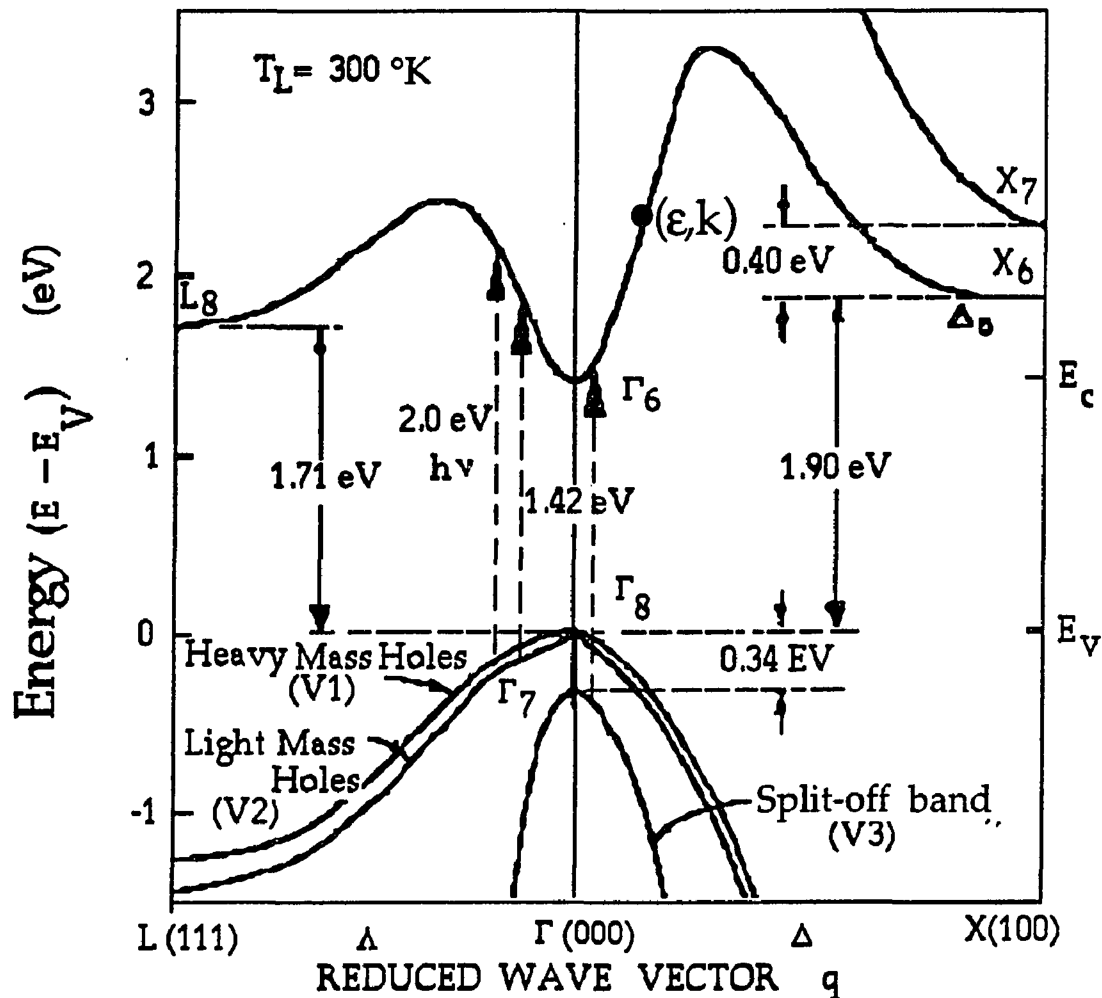

Fig. 2.1.1 Band structure of GaAs without stress.[1]

electron spin-orbital interaction. The heavy and light mass hole subbands degenerate at k=0 with the potential energy of E_V. The split-off band locates 0.34 eV below the heavy and light mass hole subbands. It is clearly shown that the band structures are anisotropic along different crystal orientations.

It is important to note that the in-plane mass notations are used for heavy mass hole subband ($m_j=\pm 1/2$) and light mass hole subband ($m_j=\pm 3/2$), because the photoexcitation is in-plane direction of the epilayers (xy-plane) in this thesis. This notation is opposite from those used for the growth direction(z-axis).

The conduction band has three minima along different crystal orientations. At the center of Brillouin zone, the minima locates 1.42 eV above the valence band maxima at room temperature and is called Γ-valley. X-valley locates 0.48 eV above the Γ-valley minima along (100) direction and L-valley locates 0.29 eV above the Γ-minima along (111) direction. Since GaAs is a zincblende structure, there exists six X-valleys and eight L-valley in a GaAs crystal. The band gap is between the Γ-minima and the valence band maxima and is direct transition scheme at energy of. 1.42 eV.

The band structure of GaAs near k=0 is described by following equations.[2] For the conduction band, its parabolic band structure is described as,

$$E_c(\vec{k}_c) = \hbar^2 \vec{k}_c^2 / 2\, m^*_c \qquad (2.1.1)$$

where E_c is the energy measured from the conduction band edge, $\vec{k}_c$ is the wave vector of the conduction electron and m^*_c is the effective mass of electron in the Γ-valley and is $0.067m_0$ (where m_0 is the free electron mass). The band curvature in Fig.2.1.1. indicate effective carrier mass because the carrier effective mass is defined as $m^*=\hbar^2/[d^2E/dk^2]$.

For the valence band, the non-parabolic heavy and light mass hole bands are given by,

$$E_v(\vec{k}_v) = \hbar^2 [a_1(k_x^2+k_y^2)+b_1 k_z^2]/2m^*_0 \qquad (2.1.2a)$$

with

$$a_1=\gamma_1 - \gamma_2\,, \qquad (2.1.2b)$$

$$b_1=\gamma_1 + 2\gamma_2\,, \qquad (2.1.2c)$$

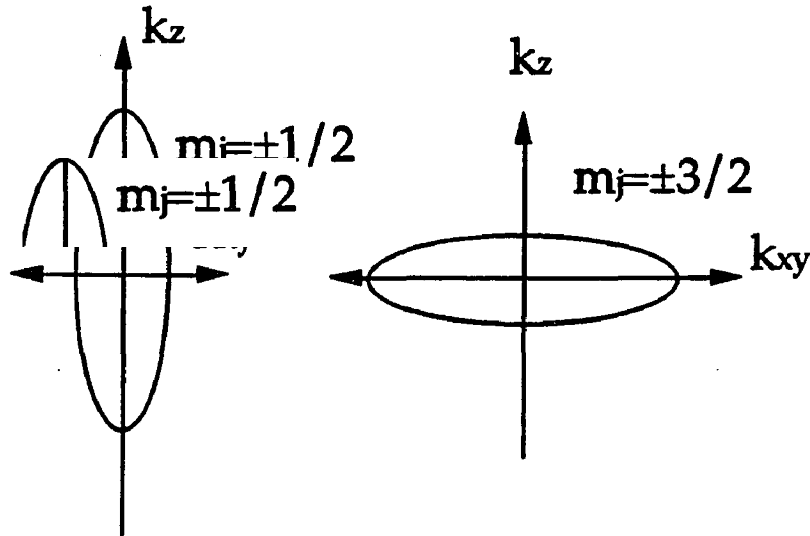

Fig. 2.1.2. Constant energy surfaces for the m_j=±1/2 and m_j=±3/2 valence subbands under compressive stress which lifts the degeneracy.

for the heavy hole (m_j=±1/2) and

$$a_1=\gamma_1+\gamma_2\ , \tag{2.1.2d}$$

$$b_1=\gamma_1-2\gamma_2\ , \tag{2.1.2e}$$

for the light mass hole (m_j=±3/2) where E_v is the hole energy measured from the valence band maxima, respectively. For GaAs, γ_1=6.85 and γ_2=2.1. Fig. 2.1.2 depicts the constant energy surfaces of the heavy and light mass hole subbands under compressive stress which removes the valence band degeneracy. The constant surfaces shows the masses along z-axis and xy-plane are different. For example, the m_j=±1/2 subband effective mass is heavy in k_{xy} plane and light along k_z direction.

In the conduction band, the effective mass of electron in X-valley is $0.23m_0$ which is about four times heavier than those in Γ- ($0.067m_0$) and L-

valleys($0.073m_0$). When the majority carrier effective mass is heavy, a temporal response of the electronic device is slow.

When a 2.0 eV photon is absorbed by the GaAs bulk material, the 2.0 eV photoexcitation creates electron in the conduction Γ-valley and holes in the heavy, light mass and split-off valence bands. The transitions are indicated by upward arrows in Fig.2 1.1. The photoexcitation process conserves energy and momentum between photon and photogenerated carriers. Since the momentum of photon is negligibly small compare with those of carriers, the energy conservation is described by,

$$h\nu = E_c(\vec{k}_c) + E_v(\vec{k}_v) + E_g \qquad (2.1.3a)$$

where Eg is the band gap energy. The momentum conservation is given by,

$$\vec{k}_c = \vec{k}_v \quad . \qquad (2.1.3b)$$

On the other hand, when an electron in the conduction band recombines with a hole in the valence band, photoluminescence with emission photon energy of hν' arising from the transitions between the Γ-valley minima and the valence band maxima in a GaAs bulk material is generated in the near infrared region(hν'=1.42 eV=873 nm). When there exist impurity or doped ions, the radiative transition occurs between the impurity states to one of the band edges. The energy and momentum of the transition are also conserved as,

$$h\nu = E_g - \Delta E_{d,a} \qquad (2.1.4)$$

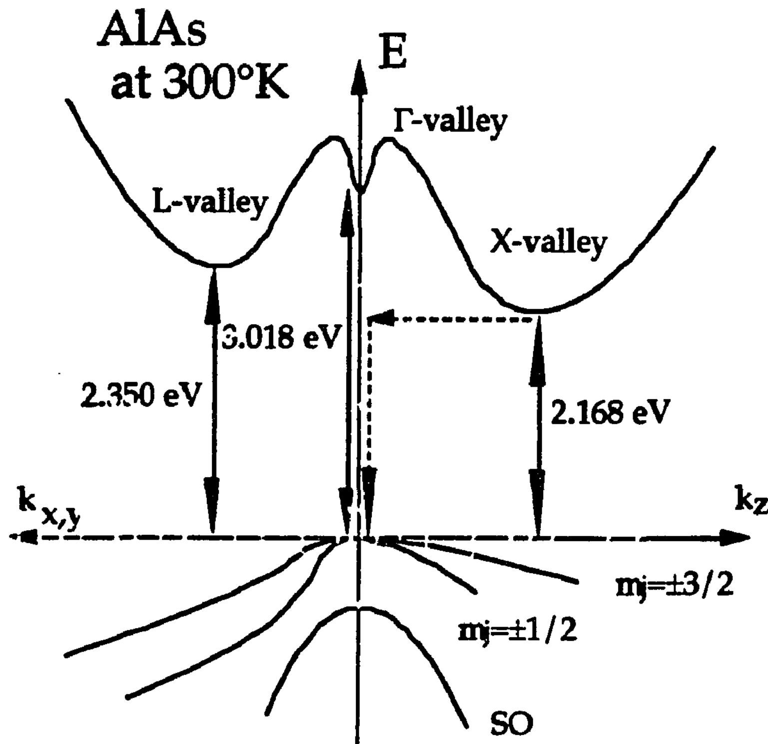

Fig.2.1.3. AlAs band structure

where $\Delta E_{d,a}$ are the donor and/or acceptor ionization energies.

When a phonon assists the transition, the transition energy is determined by,

$$E_i - E_f = h\nu' \pm E_{phonon} \tag{2.1.5}$$

where E_i and E_f are the initial and final state of the transition and E_{phonon} is the phonon energy. The plus sign corresponds to a phonon emission while the minus sign corresponds to a phonon absorption. The momentum of carriers and phonon is conserved during the transition.

The transition probability is determined by the density of states of the electron and the holes and the carrier temperature as will be described in Chapter 3 in detail.

Fig.2.1.3. schematically depicts a band structure of AlAs. Since the AlAs is indirect material, the X-valley is the lowest conduction band minima. The Γ-valley and L-valley are located 0.182 and 0.85 eV above the X-valley minima, respectively. 2.0 eV photon can not excite valence electron to Γ-valley. The carrier may be photogenerated only when a high energy phonon is absorbed to allow transition between the valence band to the X-valley as described by Eq.(2.1.5). The probability is very small at a low lattice temperature because the available phonon density is not high. The radiative transition also needs an assistance of phonon as depicted by the dashed arrows in Fig.2.1.3. The horizontal dashed arrow corresponds to the phonon emission of the X-valley electron and the vertical dashed arrow corresponds to the radiative transition. Since this transition probability is small, the photogenerated electron in the X-valley takes long time to decay to the valence band.

2.1.1. Band structure of a semiconductor

The wavefunction ψ of an electron (which describes the electron behavior) can be obtained by solving a Schrödinger equation using a Hamiltonian H as,

$$H\psi = \varepsilon\psi \tag{2.1.6}$$

where the Hamiltonian is the energy operator and ε is the eigen energy for the Hamiltonian with the eigen wavefunction ψ. To solve the Schrödinger equation for real semiconductor materials, it requires an approximation method because it is difficult to obtain analytical solution for the complicate potential structure of the material ions.

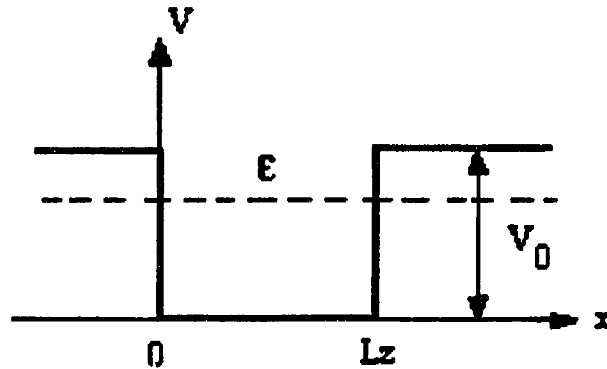

Fig. 2.1.4 Finite barrier height single quantum well model in one dimension.

Since the potential field of ions of the material can be modeled as three dimensional potential wells, it may be easy to start from one dimensional finite barrier QW to understand the origin of band structure. A simple QW model is extended to periodic potential well structure to approximate the periodic atomic ion field as follows.

2.1.2. One dimensional finite quantum well model

The discrete energy eigen states of atoms can be simulated assuming a square well potential structure in one dimension with a finite well depth V_0 and a well width L_z as shown in Fig. 2.1.4.

The Hamiltonian of such quantum well is given as,

$$H = p^2 / 2m^* + V(x) \qquad (2.1.7)$$

where p is a momentum operator of free electron with mass m^* (in this case the m^* is free electron mass) and V(x) is the atomic potential distribution. V(x) is zero within the well ($0<x<L_z$) and V_0 outside the well. Using the momentum

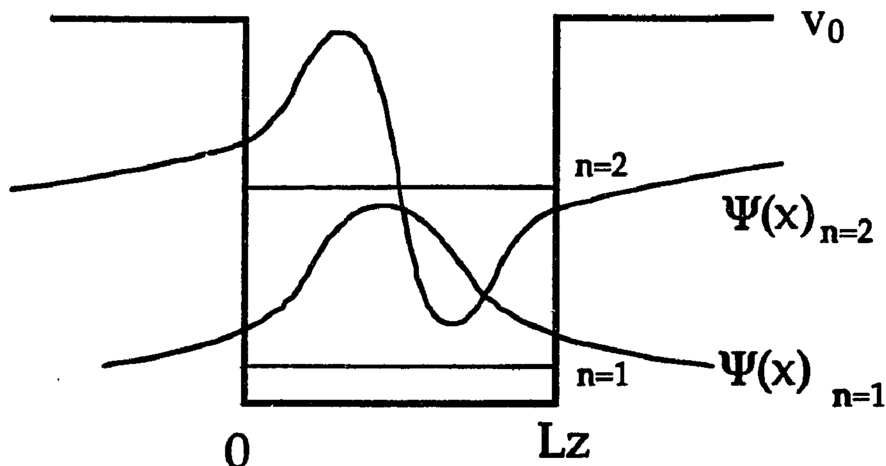

Fig. 2.1.5. n=1 and n=2 quantized wave function in a one dimensional finite potential well model.

operator $p=-i\hbar\nabla$, the time independent Schrödinger equation (2.1.6) is solved to determine the wavefunction $\psi(x)$ of electron inside and outside the well and are given by

$$d^2\psi/dx^2+\alpha^2\psi=0 \qquad \text{for } 0 \le x \le L_z \qquad (2.1.8a)$$

and

$$d^2\psi/dx^2-\beta^2\psi=0 \qquad \text{for } x<0 \text{ and } L_z<x \qquad (2.1.8b)$$

with following notations:

$$\alpha^2 = 2\, m^*\varepsilon/\hbar^2, \qquad (2.1.9a)$$

and

$$\beta^2 = 2\, m^*(V_0-\varepsilon)/\hbar^2\ . \qquad (2.1.9b)$$

where ε is the energy of the electron in the QW and $\hbar$ is the Planck constant divided by 2π.

The wavefunction was assumed to have the formula as,

$$\psi(x) = A \bullet \sin(\alpha x + \delta) \qquad \text{for } 0 \le x \le L_z, \qquad (2.1.10a)$$

$$\psi(x) = B \bullet \exp(\beta x) \qquad \text{for } x < 0, \qquad (2.1.10b)$$

and

$$\psi(x) = B \bullet \exp\{-\beta(x - L_z)\} \qquad \text{for } L_z < x, \qquad (2.1.10c)$$

where A, C, and δ are constants which satisfy the continuity of $\psi(x)$ and $1/m^* \bullet d\psi(x)/dx$ at x=0 and x=L_z and $|\psi(\pm\infty)|^2=0$. By solving the wavefunctions with the boundary conditions, the eigen state energies satisfy a relationship given by,

$$\tan \alpha L_z = \beta / \alpha. \qquad (2.1.11)$$

The eigen states in the well can be determined by calculating the relation (2.1.11) numerically. The eigen state energies are discrete and are determined by the electron mass m^*, well width L_z, and the quantum number which represents the energy states. Fig. 2.1.5. schematically shows the quantized wave functions of n=1 and n=2 in the finite potential height QW. The wavefunctions are cosine and sine function shapes in the well and exponentially decaying function in the barriers. To understand the physcal meanings of eigen states and the wave function, infinite potential well model is adequate. The eigen states E_n are given by,

$$E_n = (\hbar n \pi)^2 / 2m^* L_z^2. \qquad (n=1,2,3 \text{-----}) \qquad (2.1.12a)$$

and the wave functions are expressed as,

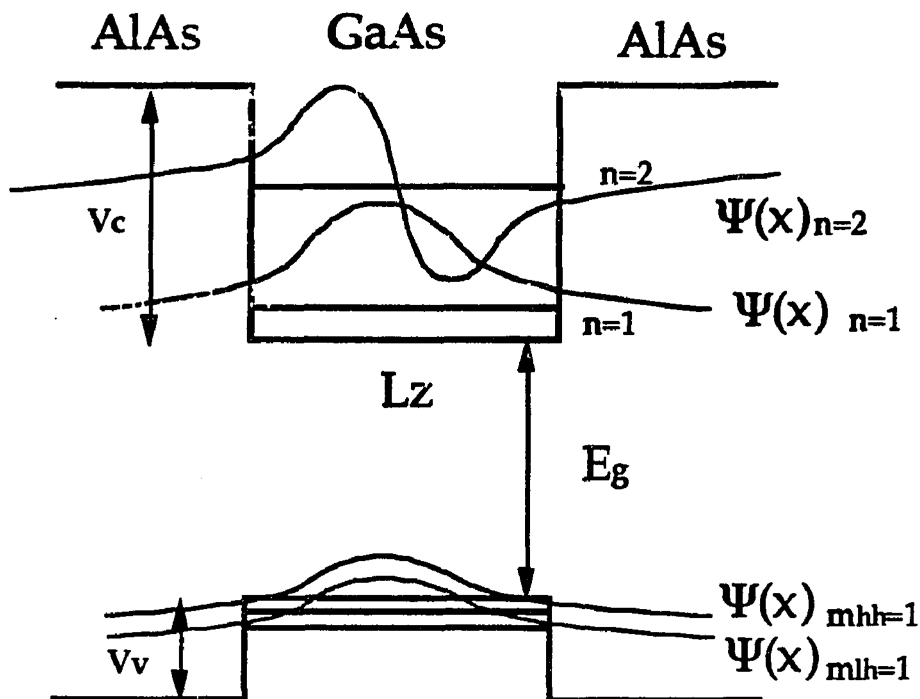

Fig.2.1.6. Energy eigen states and wave functions in a GaAs/AlAs QW structure.

$$\psi_n = \sin(n\pi x/L_z) \quad . \quad (n=1,2,3 \text{---}) \qquad (2.1.12b)$$

Therefore, the quantized eigen states are located higher energy as the m^* becomes lighter and the well width L_z becomes narrower.

One can extend this one dimensional QW model to a QW structured devices.

When the size of semiconductor structure becomes a few hundred Å and when its size further approaches the size of lattice and Bohr radius of lattice atoms, quantum mechanical description of electrons becomes important Quantum wells and superlattice structures are fabricated by growing different thin epilayers on a semiconductor substrate. One material has smaller band gap than that of the another material. By alternating few tens of monolayers of material, a potential well structure is realized. The potential structure confines

the motion of electron along the growth direction resulting discrete electron energy levels. The confined energy level can be tuned by selecting the materials and the well width. In this approximation, the fine potential structure of atoms are included in the concept of effective mass of the electrons and holes in the materials.

A GaAs/AlAs type-I quantum structure consists of a finite potential well in the conduction band and a finite well in the valence band as shown in Fig. 2.1.6. Since the GaAs has low energy band gap than AlAs, the heterostructure of AlAs-GaAs-AlAs layers constructs the QW structure. The potential height of the conduction and valence bands are determined to be about 2 to 1 ratio of the band gap difference between the GaAs and AlAs,that is, $V_c=2/3(E_{gAlAs}-E_{gGaAs})$ and $V_v=1/3(E_{gAlAs}-E_{gGaAs})$. Fig. 2.1.6 shows some of the quantized states in the conduction and valence bands with the wave functions at the states. The valence band degeneracy is removed because of the mass dependence of the quantized eigen state energy as given by the Eq. 2.1.12. The dashed curve corresponds to the wave function of a light hole (lh) and the solid curve corresponds to that for a heavy hole (hh) in the valence band.

As an example, the energy eigen states of L_z=100Å GaAs QW is estimated using Eq. 2.1.12 for the infinite barrier model. For the conduction electron($m_e^*=0.067m_0$),

$$E_{cn1}=56\text{ meV},\ E_{cn2}=225\text{ meV}. \qquad (2.1.13a)$$

For the heavy hole ($m_j=\pm3/2$, $m_{hh}^*=0.45m_0$) along z-axis,

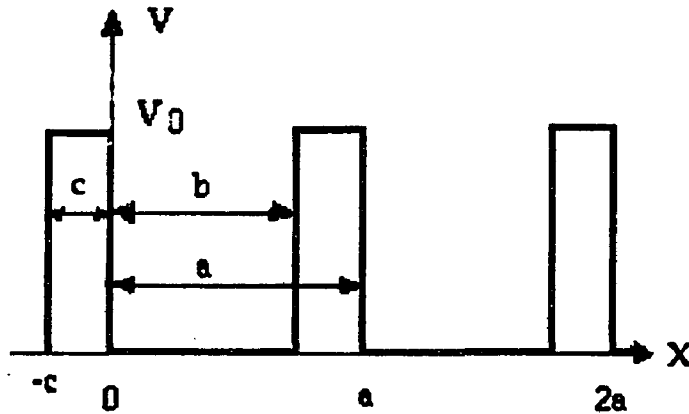

Fig.2.1.7. Periodic finite potential barriers in Kronig-Penney model.

$$E_{mhh1} = 9 \text{ meV}, \ E_{mhh2} = 36 \text{ meV}, \tag{2.1.13b}$$

and for the light hole ($m_j = \pm 1/2$, $m_{lh}^* = 0.082\ m_0$),

$$E_{mlh=1} = 42 \text{ meV}, \ E_{mlh=2} = 168 \text{ meV}. \tag{2.1.13c}$$

2.1.3. Superlattice (Kronig-Penney model)

When a QW structure is repeated more than ten times, the structure is usually called a superlattice structure which may be used as a more realistic model to understand the atomic band structure. In a superlattice with narrow enough potential barriers, the eigen states in the wells form mini-band structures because the electron wave functions in the wells leak to neighboring wells through electron tunneling. The electrons in the superlattice structure can move along the growth direction while the electron in a multiple quantum well(MQW) structure with thick barriers can not tunnel easily between the neighbored wells. Kronig and Penney calculated the miniband structure using one dimensional superlattice model.[3)]

Suppose there are infinite number of finite potential square wells with a separation (lattice constant) of a=b+c as shown in Fig. 2.1.7. Since the potential is periodic as $V(x)=V(x+na)$ where n=0,1,2,3,----, the electron wavefunctions $\psi(x)$ satisfy the periodicity as $\psi(x)=\psi(x+a)=\psi(x+2a)=$ ----. In this case, the wave function is expressed using a Bloch function u(x) which is periodic function of the lattice constant, ie. $u(x)=u(x+a)=u(x+2a)=$ ----- as,

$$\psi(x) = u(x) \exp(ikx) \qquad (2.1.14)$$

where k is the wave vector of electron wave function. Using the Bloch function, the time independent Schrödinger equation with a Hamiltonian can be expressed as,

$$H\, u \bullet \exp(ikx) = \varepsilon\, u \bullet \exp(ikx) \qquad (2.1.15)$$

Describing the Schrödinger equation with the α and β as in same manner as the single QW case, the wave function for this Kronig-Penney model is give as,

$$d^2\psi/dx^2+\alpha^2\psi=0 \qquad \text{for } 0<x<b,\ a<x<a+b, \text{----} \qquad (2.1.16a)$$

and

$$d^2\psi/dx^2 - \beta^2\psi=0 \qquad \text{for } -c<x<0,\ b<x<a, \text{----} \qquad (2.1.16b)$$

Using the Bloch function for the repetitive wave function plug into Eq.s 2.1.16 a and b, the Schrödinger equation is simplified with the Bloch function as,

$$d^2u/dx^2+2ikdu/dx+(\alpha^2-k^2)u=0 \qquad \text{for } 0<x<b,\ a<x<a+b, \text{---} \qquad (2.1.17a)$$

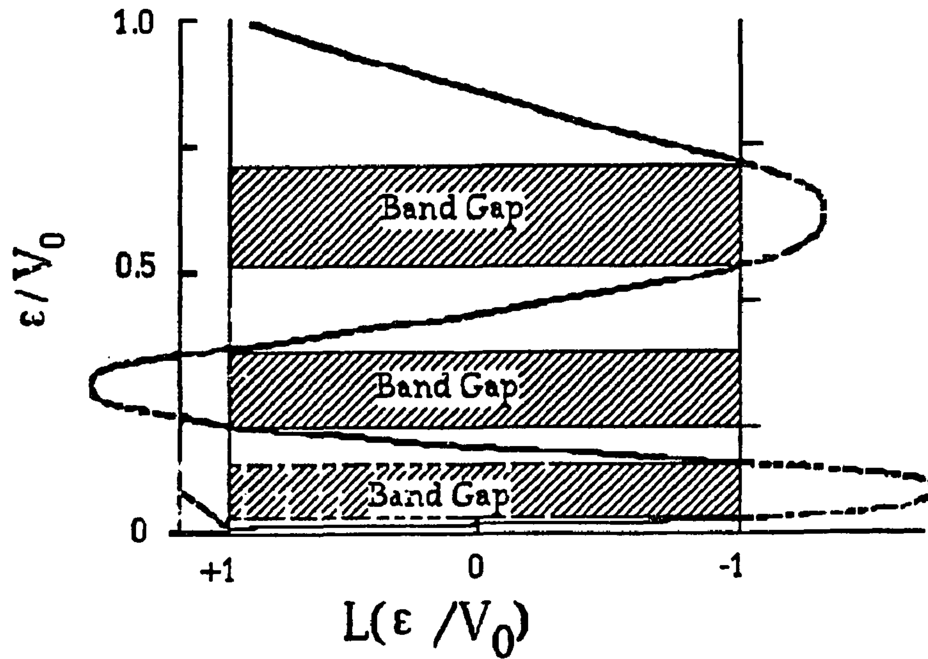

Fig. 2.1.8. $L(\varepsilon/V_0)$ vs. ε/V_0 diagram obtained from the Kronig-Penney model.

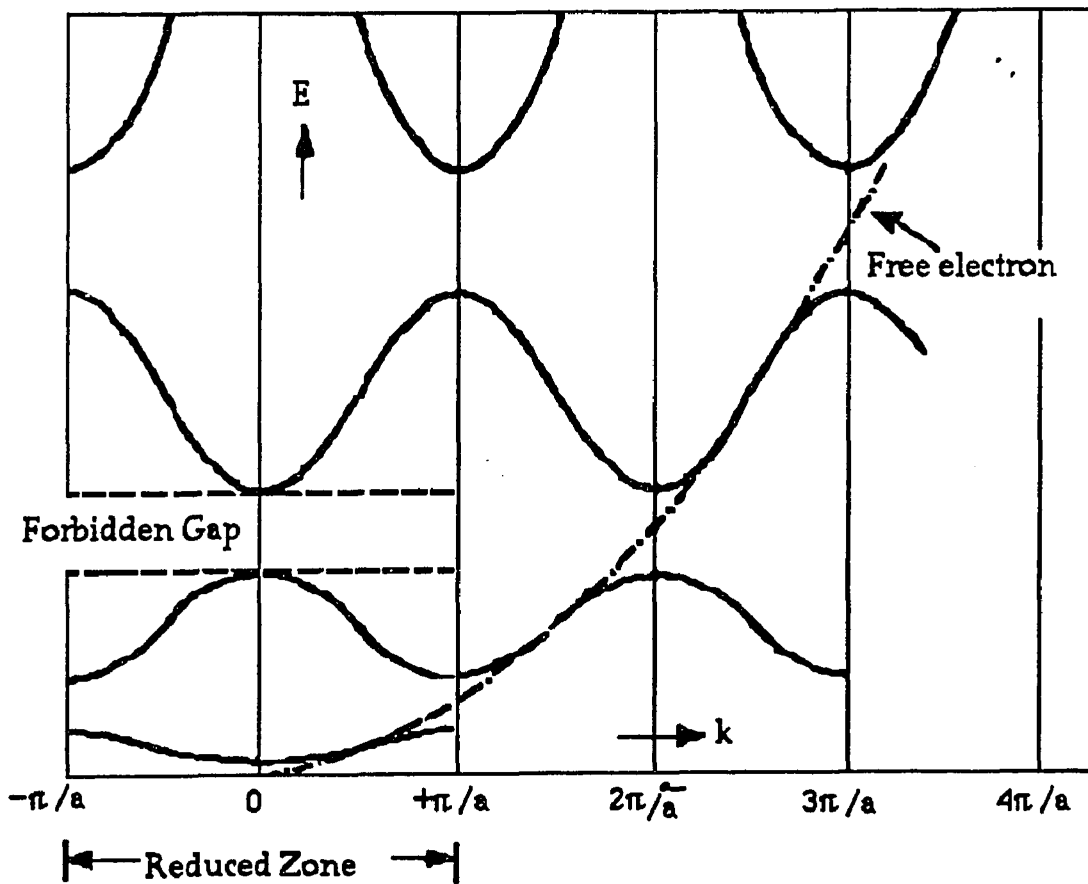

Fig. 2.1.9. Band structure calculated from the Kronig-Penney model.

and

$$d^2u/dx^2+2ikdu/dx-(\beta^2+k^2)u=0 \qquad \text{for } -c<x<0,\ b<x<a. \quad \text{---} \quad (2.1.17b)$$

To solve these differential equations, the Bloch function in the periodic structure is usually assumed as,

$$u=A\bullet\exp\{i(\alpha-k)x\}+B\bullet\exp\{-i(\alpha+k)x\} \qquad \text{for } 0<x<b,\ a<x<a+b,$$

—— (2.1.18a)

and

$$u=C\bullet\exp\{(\beta-ik)x\}+D\bullet\exp\{-(\beta+ik)x\} \qquad \text{for } -c<x<0,\ b<x<a,$$

—— (2.1.18b)

where the A,B,C, and D are determined by the boundary condition of continuity of the wave function. To satisfy the boundary conditions, a determinant of coupled equations of A,B,C, and D has to vanish. The determinant is zero when

$$k(\varepsilon)=1/a\bullet\arccos\{L(\varepsilon/V_0)\}. \qquad (2.1.19)$$

with a function $L=L(\varepsilon/V_0)$ introduced as,

$$L\left(\frac{\varepsilon}{V_0}\right)=\frac{1-2\varepsilon/V_0}{\sqrt{\varepsilon/V_0-(\varepsilon/V_0)^2}}\sinh\left[c\sqrt{\frac{2mV_0}{h^2}\left(1-\frac{\varepsilon}{V_0}\right)}\right]\bullet\sin\left(b\sqrt{\frac{2mV_0}{h^2}\frac{\varepsilon}{V_0}}\right)$$
$$+\cosh\left[c\sqrt{\frac{2mV_0}{h^2}\left(1-\frac{\varepsilon}{V_0}\right)}\right]\bullet\cos\left(b\sqrt{\frac{2mV_0}{h^2}\frac{\varepsilon}{V_0}}\right).$$

(2.1.20)

The Eq. (2.1.19) with Eq.(2.1.20) determined the band structure: i.e. E vs. k relationship. The $L(\varepsilon/V_0)$ was calculated as function of ε/V_0 with $2m/h^2 \bullet V_0/(b/2)^2=36$ and $c/b=0.1$ as shown in Fig. 2.1.8. It is clear that there are band gaps where $L(\varepsilon/V_0)$ becomes larger than 1 or smaller than -1. Calculating band structure using the results obtained from Fig 2.1.8, a periodic miniband structure is depicted in Fig 2.1.9. When the periodic structure becomes the size of lattice of the crystal, the dispersion curve descibes the conduction and valence band structure of the crystal. Fig.2.1.9. also shows a dispersion curve for a free electron in dashed line which is obtained by $E^2=\hbar^2k^2/2m^*$. The effective mass determined by an inverse of the second derivative of energy with respect to the wave vector is negative for the valence band (positive for holes) and positive for the conduction band.

If c >> b, the result of $k(\varepsilon)$ determines the eigen states in the simple QW case as discussed previously.

The calculation program to determine the eigen states is attached in Appendix 2.

2.1.4 k•p approximation

A more realistic semiconductor band structure can be obtained by solving the Schrödinger equation with the help of experimental results. There are several approximation methods such as k•p model[4] started from a Kronig-Penney model and a tight binding atomic interaction model. Some review paper should be refered to help understanding the model calculation in detail.

The k•p model modifies the Kronig-Penney periodic potential model and derives band structures as follows.

The time independent Schrödinger equation expressed with the Bloch function can be given by Eq.2.1.15 as $H u \bullet \exp(ikr) = \varepsilon u \bullet \exp(ikr)$. Using $p = -i\hbar \bullet \nabla$, the Schrödinger equation is given by,

$$\{(p+\hbar k)^2/2m_0+V\}u = \varepsilon u. \qquad (2.1.21)$$

This equation is expanded and rewritten using a perturbation formula as,

$$(H_0 + H_1 + H_2)u = \varepsilon u \qquad (2.1.22a)$$

where

$$H_0 = p^2/2m_0 + V \quad \text{(zero-order)}, \qquad (2.1.22b)$$

$$H_1 = \hbar/m_0\, k \bullet p \quad \text{(first order perturbation)}, \qquad (2.1.22c)$$

and

$$H_2 = \hbar k^2/2m_0 \quad \text{(second-order perturbation)}. \qquad (2.1.22d)$$

Kane (1957) used effective mass approximation (parabolic band structure) for the second order perturbation around k=0 and obtained the conduction and valence bands structure near k=0.[4] For the conduction band, the energy states are given by,

$$E_c = E_{g\Gamma} + \hbar^2 k^2/2m^*_c \qquad (2.1.23a)$$

with

$$m_0/m^*_c = 1 + 2p_{cv}^2/3m_0\{2/E_{g\Gamma}+1/(E_{g\Gamma}+\Delta_0)\} \ . \qquad (2.1.23b)$$

Those for the light mass hole ($m_j=\pm3/2$) are given by,

$$E_{v1} = \hbar^2k^2/2m^*_{lmh} \quad (2.1.24a)$$

with

$$m_0/m^*_{lmh} = 1, \quad (2.1.24b)$$

for heavy mass hole subband($m_j=\pm1/2$),

$$E_{v2} = \hbar^2k^2/2m^*_{hmh} \quad (2.1.25a)$$

with

$$m_0/m^*_{hmh} = 4\, p^2_{cv}/3m_0\, Eg_\Gamma - 1. \quad (2.1.25b)$$

For split-off band, the band structure is expressed as,

$$E_{so} = -\Delta_0 - \hbar^2k^2/2m^*_{so} \quad (2.1.26a)$$

with

$$m_0/m^*_{so} = 4p^2_{cv}/3m_0(Eg_\Gamma+\Delta_0) - 1, \quad (2.1.26b)$$

where Δ_0 is the energy separation between the split-off band and the degenerate top valence band. The momentum matrix element p_{cv} is between the conduction and valence bands and is given as $2p^2_{vc}/m_0=21.5$ eV for GaAs.

2.2. Strain and stress in semiconductor

Strain in semiconductor alters the band structure because the three dimensional position of atoms are shifted from the original stable positions by the stress . There are several way to generate strain in semiconductor either externally or internally. When a different material is grown on another material, the lattice mismatch between the materials causes a strain at the interface. The difference in the thermal expansion coefficients of the materials also generates strain in the material when the material is cooled from a sample growth temperature (around 700°C) to room temperature. These two mechanisms generate biaxial stress in a plane perpendicular to the material growth direction. One can apply external hydrostatic or uniaxial pressure depending on the stress machine configuration used. Within the elastic limit of the sample, the dislocations will not be generated.

Pressure X applied to a material is converted into the strain ε in the material through elastic compliance constants S by Hook's law as,

$$\varepsilon = S \bullet X$$
$$= \Delta l / l \qquad (2.2.1)$$

where Δl is the displacement for the lattice constant l.[5)]

Let's first review the effects of lattice mismatch and thermal expansion in a GaAs structure due to presence of secondary semiconductor
(AlGaAs or Si) to produce biaxial strain. I will also review the effect of uniaxial stress on a GaAs semiconductor by applying external stress.

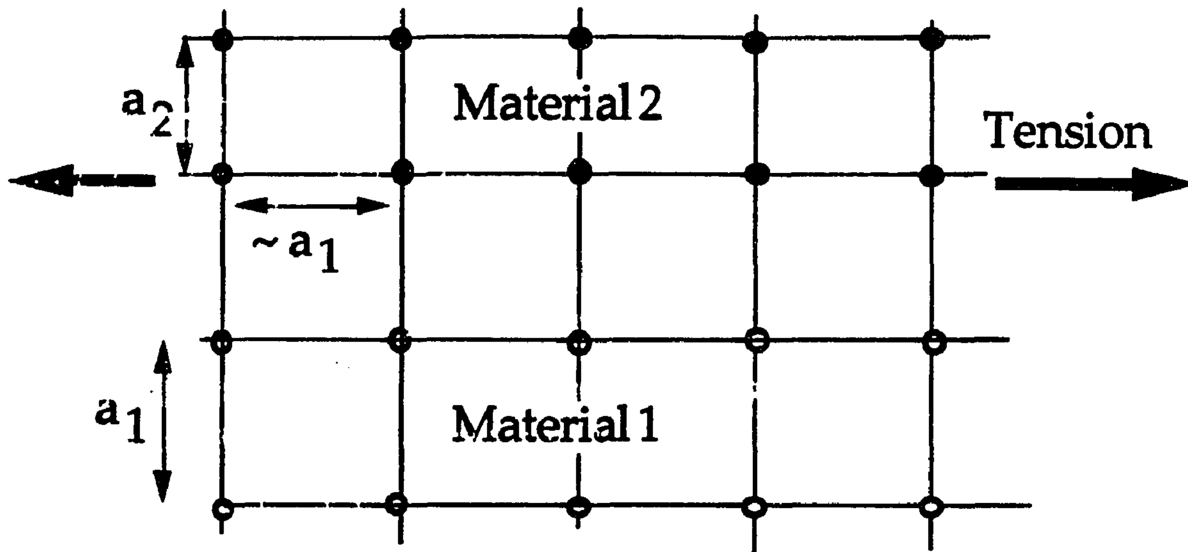

Fig. 2.2.1. Tension generated by the lattice mismatch at the interface between materials 1 and 2.

2.2.1. Lattice mismatch

At the interface of the lattice mismatched semiconductor heterostructure (material 1 and 2) as shown in Fig. 2.2.1, the material 2 with smaller lattice constant forces another material1 with larger lattice constant to shrink while the material 1 forces the material 2 to expand. The overall effect results in the strain near the interface of materials 1 and 2. The material 1 contains tension while the material 2 contains compressive stress along the interface plane between them.

The amount of stress X generated in a QW between well and barrier materials is given by,[6]

$$X = \left(\frac{2}{9K} + \frac{1}{6\mu}\right)^{-1} \bullet \left(\frac{a_\perp - a_w}{a_\perp}\right) , \qquad (2.2.2)$$

The parameters in the equation are : $a_\perp$ is an in-plane lattice parameter of the strained layers which is given by,

$$a_{\perp}=\left(\frac{a_w d_w + a_b d_b}{d_w + d_b}\right) \quad , \qquad (2.2.3)$$

and a_i and d_i (i=w and b) are lattice constants and layer thickness of two materials, respectively. $K=(C_{11}+2C_{12})/3$ and $\mu=C_{44}/2$ where C_{ij} are stiffness constants of the material layer observed. Since the carrier in the well material is usually important, the K and μ are calculated for the well material. The first term in the right hand side of Eq.2.2.2 corresponds to a compliance constant and the second term corresponds to the strain in Eq. 2.2.1. Eq.2.2.2 shows that the amount of strain is determined by the layer thicknesses and the difference in the material lattice constants. The larger the difference of the lattice constants between two layers, the larger the amount of stress. A 0.2% of lattice mismatch generates about 1 kbar of stress in the material.

Even for an AlGaAs alloy material which is thought to lattice match to a GaAs layer, there exists a biaxial tension in the GaAs layer.7) Fig. 2.2.2 (a) shows measured compressive stresses in an AlGaAs layer grown on a GaAs substrate as function of the Al concentration. As the Al concentration increases, the compressive stress in the AlGaAs layer increases linearly. At the Al concentration of 0.35, there exists about 0.8 kbar of compressive stress. The lattice constants of GaAs and AlAs are 5.6533Å and 5.6611Å, respectively. For a GaAs/AlGaAs heterostructure, the tensile strain generated in the GaAs well layer depends on the layer thickness of both materials and their material compositions.

The magnitude of tensile stress was calculated using Eq.s 2.2.2. and 2.2.3 as function of Al concentration and the thickness of AlGaAs layer as shown in

Fig.2.2.2(b). The open circles with a dotted line are the case when the AlGaAs layer thickness is same as the GaAs layer. The dots with a solid line are the case when the AlGaAs layer is one thousand times thicker than the GaAs layer. The stress linearly increases as the Al concentration increases. The stress approaches its maximum as the AlGaAs layer thickness increases. On the other hand, as thinner the AlGaAs layer, the GaAs layer shrinks the lattice of the AlGaAs layer and generate compression in the AlGaAs layer.

The parameters (lattice constant and elastic stiffness constants) for the $Al_xGa_{1-x}As$ used in these calculations were given by linear interpolations between those of GaAs and AlAs as,

$$a_{AlGaAs} = 5.6533+0.0078x \text{ (Å)}, \qquad (2.2.4)$$

$$C_{11}(x) = (11.88+0.14x)*10^{11} \quad (\text{dyn/cm}^2), \qquad (2.2.5a)$$

$$C_{12}(x) = (5.38+0.32x)*10^{11} \quad (\text{dyn/cm}^2), \qquad (2.2.5b)$$

and

$$C_{44}(x) = (5.94+-0.05x)*10^{11} \quad (\text{dyn/cm}^2). \qquad (2.2.5c)$$

Using $K = (C_{11}+2C_{12})/3$ and $\mu = C_{44}/2$, the values for K and μ are equated as,

$$K = (7.55+0.26x)*10^{11} \quad (\text{dyn/cm}^2), \qquad (2.2.5d)$$

and

$$\mu = (2.97+0.025x)*10^{11} \quad (\text{dyn/cm}^2), \qquad (2.2.5e)$$

where 10^9(dyn/cm^2)=1kbar.

Another example of the stressed structure due to the lattice mismatch is GaAsP layer grown on AlGaAs layer case. Since the lattice constant of 5.4512Å of GaP is smaller than GaAs, a GaAsP layer grown on an AlGaAs layer contains a tension. In this thesis, I have used $GaAs_{1-y}P_y$/AlGaAs quantum well structures with various phosphor concentration to investigate exciton dynamics under the tension altered band structure. The lattice constant of GaAsP alloy can be varied by the phosphor concentration. The higher the phosphor concentration, the higher the magnitude of tensile stress. Since the thickness of well layer relative to the thickness of barrier layers also determines the strain, the thicker the well width, the lower the stress.

I calculated the tension generated in GaAsP well layers, containing 5% and 8% phosphor, grown on a 400Å thick AlGaAs layer with a 35% Al concentration as function of well width using Eq. 2.2.2 and 2.2.3. and the tensions in two QWs were also estimated as shown in Fig. 2.2.3. using the following parameters for GaAsP. The parameters in Eq.s2.2.4 and 2.2.5. for the AlGaAs were also used.

The lattice constant for the $GaAs_{1-y}P_y$ alloy material is given as function of the phosphor concentration (y) by,

$$a_{GaAsP}(y) = 5.6533-0.2021y \quad . \qquad (2.2.6)$$

The elastic stiffness constants for the GaAsP are,

$$C_{11}(y) = (11.88+2.24y)*10^{11} \quad (dyn/cm^2), \qquad (2.2.7a)$$

$$C_{12}(y) = (5.38+0.873y)*10^{11} \quad (dyn/cm^2), \qquad (2.2.7b)$$

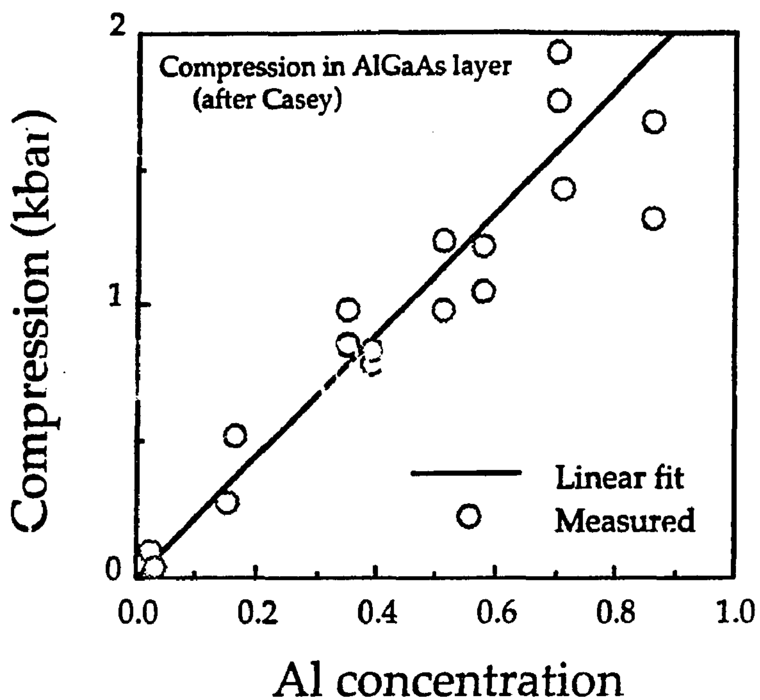

(a)

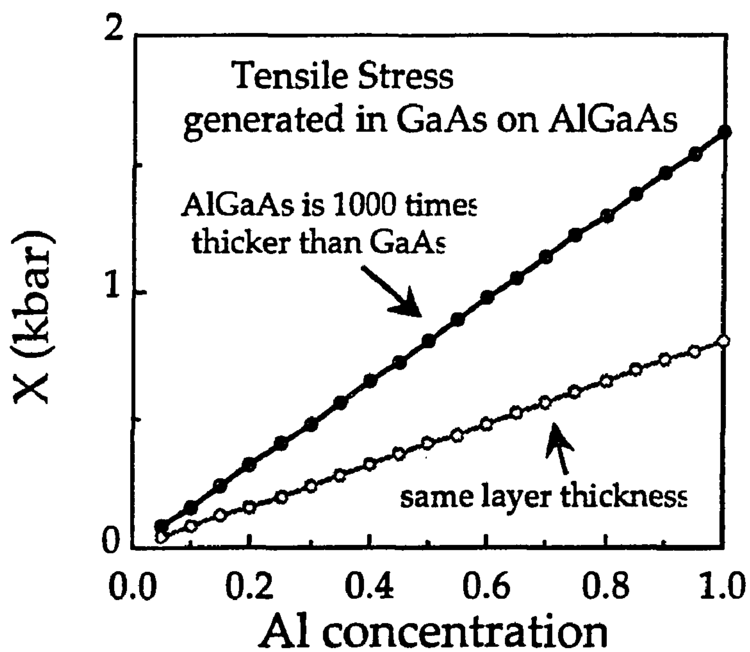

(b)

Fig.2.2.2. (a) Measured and (b)calculated tensile stresses generated in an AlGaAs and a GaAs epilayer grown on a GaAs and an AlGaAs layer respectively. (1kbar=10^9 dyn/cm^2)

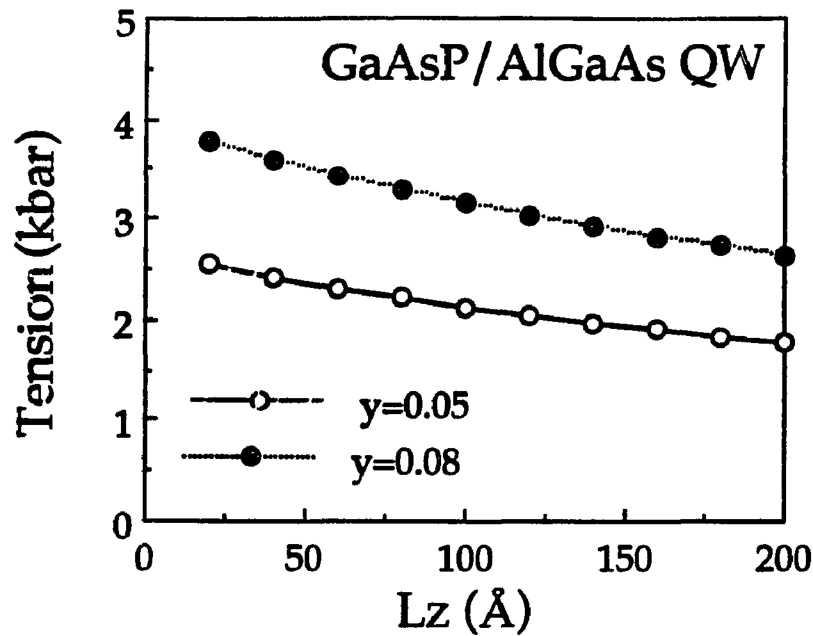

Fig.2.2.3. Tension generated in GaAsP well layers in GaAsP/AlGaAs QW structures with various well widths at two phosphor concentration of y=0.05 and 0.08. The AlGaAs barriers contain 35% of aluminum and are 400Å thick.

$$C_{44}(y) = (5.94+1.107y)*10^{11} \quad (dyn/cm^2) \qquad (2.2.7c)$$

$$K(y) = (7.547+0.657y)*10^{11} \quad (dyn/cm^2) \qquad (2.2.7d)$$

and

$$\mu(y) = (2.97+0.5535y)*10^{11} \quad (dyn/cm^2) \quad . \qquad (2.2.7e)$$

where 10^9 (dyn/cm^2) = 1 kbar.

Since the lattice constants are a_{GaAsP}=5.6432$_{(y=0.05)}$, 5.63713$_{(y=0.08)}$ and $a_{AlGaAs(x=0.35)}$=5.6560, $a_\perp$s were calculated using Eq. 2.2.3 to be,

$$a_\perp = (5.6432^*L_z + 5.6560^*400)/(L_z + 400), \quad (2.2.8a)$$

for y=0.05 QWs and

$$a_\perp = (5.63713^*L_z + 5.6560^*400)/(L_z + 400), \quad (2.2.8b)$$

for y=0.08 QWs, respectively.

The tension for a 121Å GaAsP(y=0.05) QW used in this thesis is estimated. Substituting the $a_\perp$ determined by Eq. 2.2.8a and L_z=121Å into the second term of Eq. 2.2.2, the strain ε in the 121Å well is calculated to be,

$$\varepsilon = (5.653\text{-}5.6432)/5.653 = 1.734 \times 10^{-3} \quad . \quad (2.2.9a)$$

Thus, there exists 0.17 % of strain in the well material. For the GaAsP y=0.05, K= 7.6107x10^{11}(dyn/cm^2) and μ=2.9975x10^{11} (dyn/cm^2) is obtained from the Eq.s 2.2.7d and 2.2.7e. The stress generated in the 121Å well is calculated to be,

$$\begin{aligned} X &= 1.1792 \times 10^{12} \bullet 0.001738 \\ &= 2.05 \times 10^{9} \quad (\text{dyn/cm}^2) \\ &= 2.05 \quad (\text{kbar}) \quad . \end{aligned} \quad (2.2.9b)$$

Therefore, there exists the built-in tension of 2.05 kbar in the GaAsP well layer in the 121Å GaAsP/ AlGaAs QW sample with y=0.05.

2.2.2. Thermal expansion

When the thermal expansion coefficients are different between layers or between a layer and a substrate, stresses are generated in the layers. Suppose an epilayer is grown on another material substrate which has a smaller thermal expansion coefficient than that of the epilayer, the epilayer shrinks faster than the substrate as the sample temperature goes down from a growth temperature. As the result, the atoms of the epilayer will be stretched in the plane perpendicular to the growth direction(biaxial direction). Therefore, the epilayer having larger thermal expansion coefficient contains biaxial tension while the another layer having the smaller thermal expansion coefficient contains biaxial compression. An example is GaAs epilayer grown on Si substrate. A simple model is given below.

For a GaAs epilayer grown on a Si substrate, the GaAs epilayer shrinks faster (in all direction) than the Si substrate as the sample temperature goes down from the sample growth temperature. The GaAs atoms at the interface keeps their arrangement against the Si atom as long as no misfit dislocation occurs. The GaAs atoms are stretched by Si atoms in the plane perpendicular to the growth direction(biaxial direction). The Si atoms are shrunk by the GaAs atoms. However, the Si substrate is very thick. Therefore, the Si atoms do not move much.

As the results, The difference in thermal expansion coefficients between GaAs and Si materials causes built-in tension in GaAs epilayer grown on Si substrate. The magnitude of stress in a GaAs epilayer is evaluated by Chen et al.[8] experimentally as shown in Fig.2.2.4. The tension in the GaAs/Si sample as function of substrate temperature T (°K) was evaluated to be,

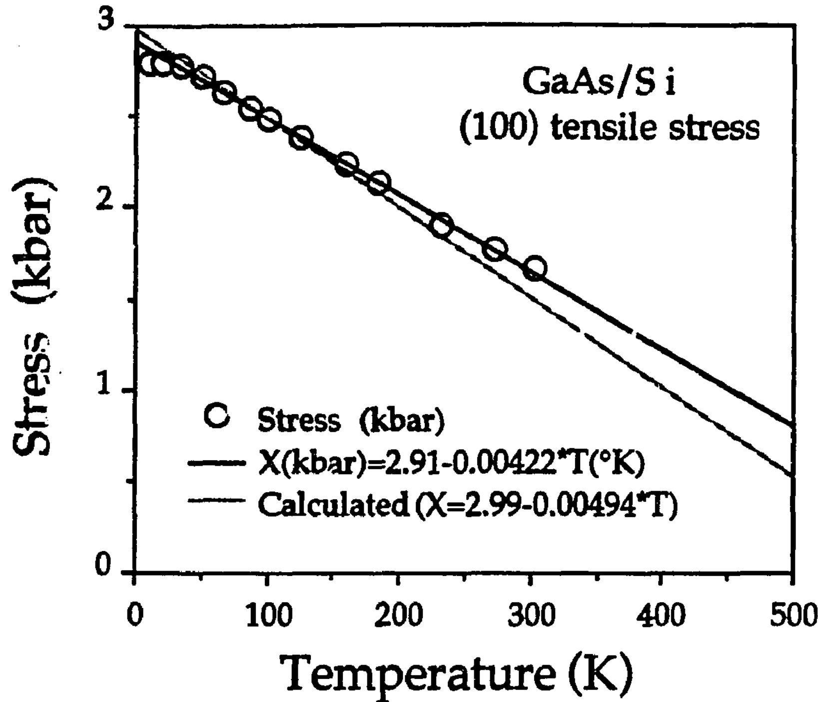

Fig.2.2.4. The biaxial tension as function of lattice temperature in a GaAs/Si sample (by Chen et al.[8]).

$$X=-4.22\times10^{-3}\bullet T+2.91 \quad \text{(kbar)}. \tag{2.2.10}$$

using a simple linear fit to the measured data. In Fig. 2.2.4, the open circles are measured data by Chen and the solid line is the curve given by Eq.2.2.10.

As the sample temperature increases, the tension decreases because the sample temperature approaches toward the sample growth temperature where a lower stress was built-in. From Fig. 2.2.4, it was found that there exists a residual tensile stress of 0.99 kbar at the growth temperature 650 °C.

To evaluate the magnitude of the stress, one uses the lattice mismatch equation. The thermal expansion coefficient α is given as a form $\alpha=(\Delta l/l)/\Delta T$.

Therefore, one can determine a strain $\Delta l/l$ using a rate $\alpha\Delta T$ of lattice expansion from the growth temperature T_{growth}.

The magnitude of the built-in stress at a lattice temperature T_L can be calculated as,

$$X = \left(\frac{2}{9K} + \frac{1}{6\mu}\right)^{-1} \bullet \left(\alpha_{GaAs} - \alpha_{Si}\right) \bullet \left(T_{growth} - T_L\right) + X_{resid} \qquad (2.2.11)$$

where α_{GaAs} and α_{Si} are the thermal expansion coefficients for GaAs and Si, respectively. X_{resid} is the residual stress remained at the sample growth temperature T_{growth}. The stress $X(T_L)$ linearly depends on the lattice temperature. At room temperature T_L=300 °K, there exists about 1.6 kbar of tension for the case of GaAs/Si in Fig. 2.2.4.

By taking a derivative of Eq. 2.2.11. with respect to T_L, a stress generation rate per unit temperature can be estimated. Using $\alpha_{GaAs}=6.63\times10^{-6}$ (°K^{-1}) and $\alpha_{Si} = 2.4\times10^{-6}$ (°K^{-1}), $K_{GaAs}=7.547\times10^{4}$ (dyn/cm^2), $\mu_{GaAs}=2.97\times10^{-11}$ (dyn/cm^2) and the sample growth temperature of 650 °C, the stress generation rate is calculated to be 4.94×10^{-3} (kbar/°K). A fitting curve using the generation rate is displayed in Fig. 2.2.4 as a dashed curve. This value is in good agreement with the measured slope of 4.25×10^{-3} (kbar/°K) shown in Fig.2.2.4.

2.3. Band structure under stress

Since the stress in a material changes the lattice constant between the atoms the energy band structure of the material is altered according to the magnitude and the type of the stress (compressive or tensile, and uniaxial, biaxial or hydrostatic) from that of the non-strained material.[9-16] To calculate the detail band structure under stress with the k•p approximation, one can refer the

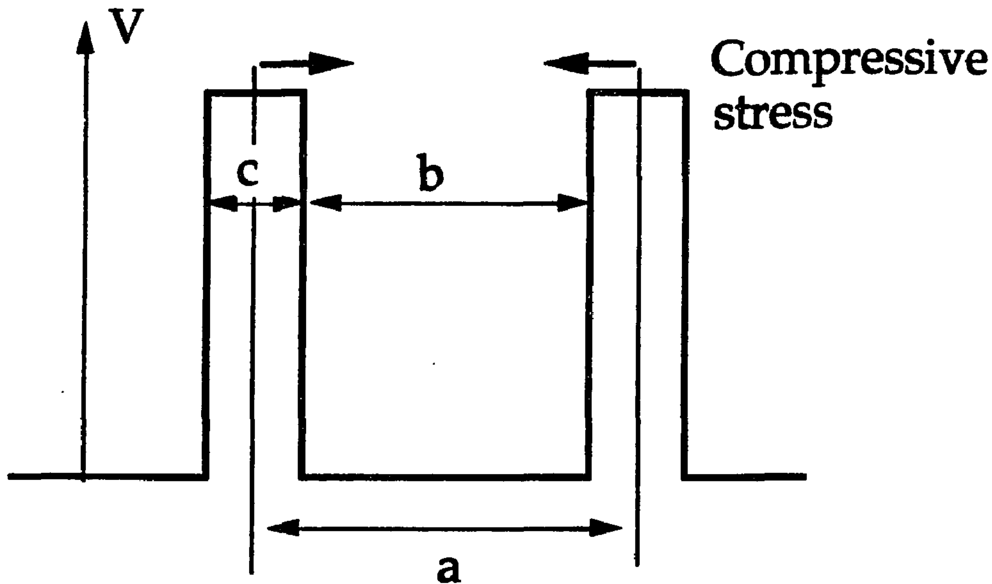

Fig.2.3.1. Kronig-Penney multiple QW model under compressive stress

Ph.D thesis by Shun Lee,[17] papers by Johnson Lee and M. O. Vassel,[18,19] and by F. H. Pollak, et al.[20] It is beyond the scope of my thesis to go into depth.

The following reviews stress effects on GaAs bulk and QW band structures.

2.3.1. Bulk material under stress

To physically understand the effect of stress on the band structure, one uses the Kronig-Penney model described in the previous section 2.1. As an uniaxial compressive stress applied to the one dimensional periodic potential structure, the potential barriers (atomic ions) move closer and thus the lattice constant **a** becomes smaller in the model as shown in Fig.2.3.1. Assuming the barrier width **c** does not change, the eigen states become higher energy because the well width **b** simply becomes narrower. On the other hand, when a tension is applied to the model, the lattice constant and the well width **b** become

wider and the levels of the energy eigen states becomes lower. This simple concept can be extended to biaxial and hydrostatic stress in three dimensional case. However, the calculation of the band structure becomes complicate and will not be described in detail in this thesis.

In this thesis, the first order effect of stress on the band edge around k=0 is described. In the following discussion, the value X is positive for tension and negative for compression.

As a first order approximation, the energy shifts at k=0 are proportional to the stress applied and are given by the following equations:

The hydrostatic stress effect on energy gap between the conduction band E_c and the valence band E_v is given by,[1]

$$\Delta(E_c - E_v)_{hydrostatic} = 3a\,(S_{11} + 2\,S_{12}) \bullet X$$
$$= -10.962 \bullet X \quad \text{(meV/kbar) for strained GaAs.} \qquad (2.3.1)$$

where a is the hydrostatic deformation potential and S_{11} and S_{12} are the compliance coefficients. As the result, the hydrostatic dilation shift the energy gap to be smaller and the opposite is true for the compression.

The uniaxial stress effects on the energy gap between the conduction band edge E_c and either heavy mass hole $E_{hmh}(m_j=\pm1/2)$ or light mass hole $E_{lmh}(m_j=\pm3/2)$ subbands are given by,

$$\Delta(E_c - E_{hmh})_{uni} = \{\, a(S_{11}+2S_{12}) - b(S_{11}-S_{12})\,\} \bullet X$$
$$= -\,0.6024 \bullet X \quad \text{(meV/kbar) for strained GaAs,} \qquad (2.3.2a)$$

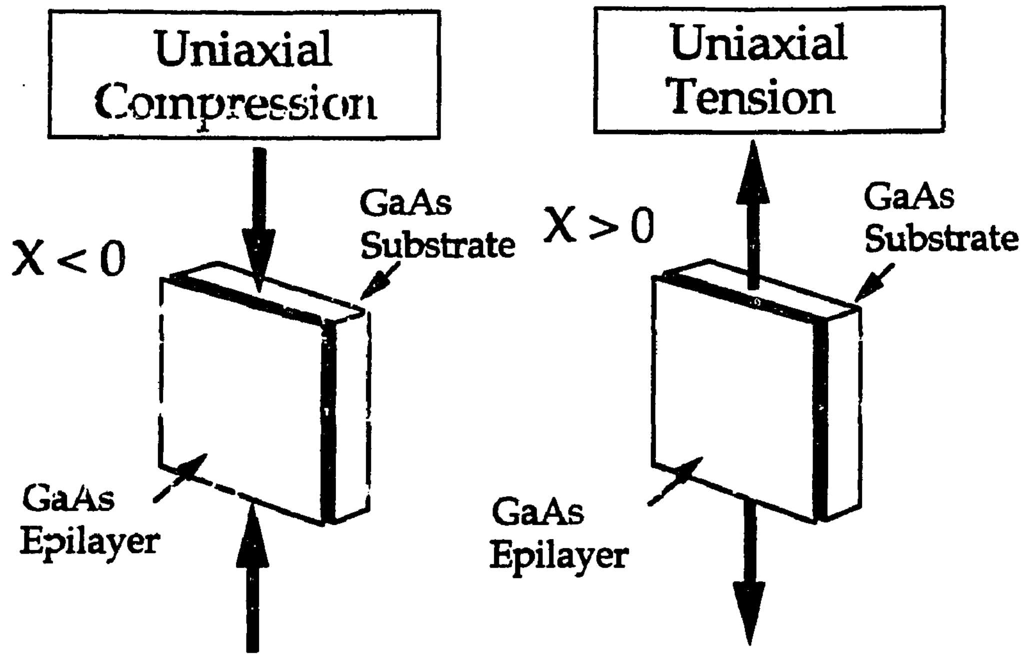

Fig. 2.3.2. Uniaxial compression and tension on a GaAs/GaAs sample.

and

$$\Delta(E_c\text{-}E_{lmh})_{uni} = \{ a(S_{11}+2S_{12}) + b(S_{11}\text{-}S_{12}) \}\bullet X$$
$$= -6.722\bullet X \text{ (meV/kbar) for strained GaAs.} \qquad (2.3.2b)$$

where b is the shear deformation potential and X is the uniaxial stress in kbar in the layers ($X<0$ for compressive while $X>0$ for tension as shown in Fig.2.3.2.). $S_{11}=11.6\times10^{-4}$/kbar, $S_{12}=-3.7\times10^{-4}$/kbar, a= -8.7 eV, and b= -2.0 eV are used to calculate the shifts in the strained GaAs[1]). From Eq.s 2.3.2a and b, the light mass hole subband is ten times more sensitive to the uniaxial stress than the heavy mass hole subband.

For 2kbar uniaxial tensile stress in a GaAs layer, the hmh and lmh subbands move by,

$$\Delta(E_c\text{-}E_{hmh})_{uni} = -1.2 \text{ meV} \qquad (2.3.3a)$$

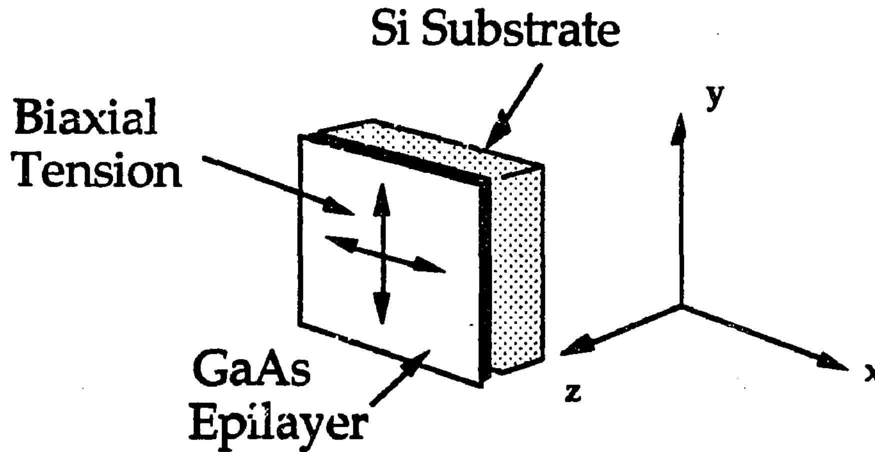

Fig. 2.3.3. Built-in biaxial tension in a GaAs/Si sample.

and

$$\Delta(E_c\text{-}E_{lmh})_{uni} = -13.4 \text{ meV}. \qquad (2.3.3b)$$

A biaxial tension (two dimensional stress along an xy plane perpendicular to the growth direction z) can be generated in an epilayer by either lattice mismatch or mismatch in the thermal expansion coefficients between heterostructure materials as discussed previously. The biaxial stress is the combination of a hydrostatic stress and an uniaxial stress. For the case of biaxial tension, X(x,y,0)=X(x,y,z)-X(0,0,z) where X(x,y,z) denotes the hydrostatic dilation and -X(0,0,z) is the uniaxial compression along the sample growth direction.

As discussed in section 2.2.2, the GaAs epilayer grown on a Si substrate is biaxially tentioned.

As the result of the combination of the hydrostatic tensile and the compressive shear strain, the energy gap shifts for the heavy E_{hmh} and light hole E_{lmh} subbands in the GaAs/Si are given by:

$$\Delta(E_c\text{-}E_{hmh})_{biax} = \Delta(E_c\text{-}E_v)_{hydrostatic} + \Delta(E_c\text{-}E_{hmh})_{uni}$$

$$= -10.962 \bullet X + \{-0.6024 \bullet (-X)\}$$

$$= -10.36 \bullet X \quad (\text{meV/kbar}), \qquad (2.3.4a)$$

and

$$\Delta(E_c - E_{lmh})_{biax} = \Delta(E_c - E_v)_{hydrostatic} + \Delta(E_c - E_{lmh})_{uni}$$

$$= -10.962 \bullet X + \{-6.722 \bullet (-X)\}$$

$$= -4.239 \bullet X \quad (\text{meV/kbar}). \qquad (2.3.4b)$$

Therefore, the heavy mass hole subband is about twice as sensitive to the biaxial tensile stress as the light mass hole subband.

The energy shifts for a 2 kbar of biaxial tension are calculated as,

$$\Delta(E_c - E_{hmh})_{biax} = -20.7 \text{ meV} \qquad (2.3.5a)$$

and

$$\Delta(E_c - E_{lmh})_{biax} = -8.5 \text{ meV} \qquad (2.3.5b)$$

The hmh subband moves closer to the conduction band than the lmh subband.

Table 2.3.1. shows amounts of the energy shifts arising from various types of 2 kbar tensions in a bulk GaAs. The energy shifts were calculated using Eq.s 2.3.1, 2.3.2, and 2.3.4. Fig.2.3.4. schematically summarizes the effect of various types of tensile stresses on the band structure of bulk GaAs along the growth direction(z-axis, k_z) and along an xy plane perpendicular to the z-axis (k_{xy}). For 2 kbar hydrostatic tension, the band gap shrinks 22 meV (used Eq.(2.3.1.) substituted by X=2kbar) and the valence hmh and lmh subbands are still degenerate at k=0. The 2 kbar of uniaxial stress removes the valence band degeneracy and moves the hmh and lmh subbands 1.2 and 13.4 meV toward the conduction band(used Eq.(2.3.3 a and b). The 2 kbar of biaxial tension moves

Table 2.3.1. Band edge shifts due to 2 kbar of various types of tensions in a bulk GaAs material (first order approximation)

	Hydrostatic	Uniaxial	Biaxial
$\Delta(E_c - E_{hh})$	-21.9 meV	-1.20 meV	-20.7 meV
$\Delta(E_c - E_{lh})$	-21.9 meV	-13.4 meV	-8.48 meV

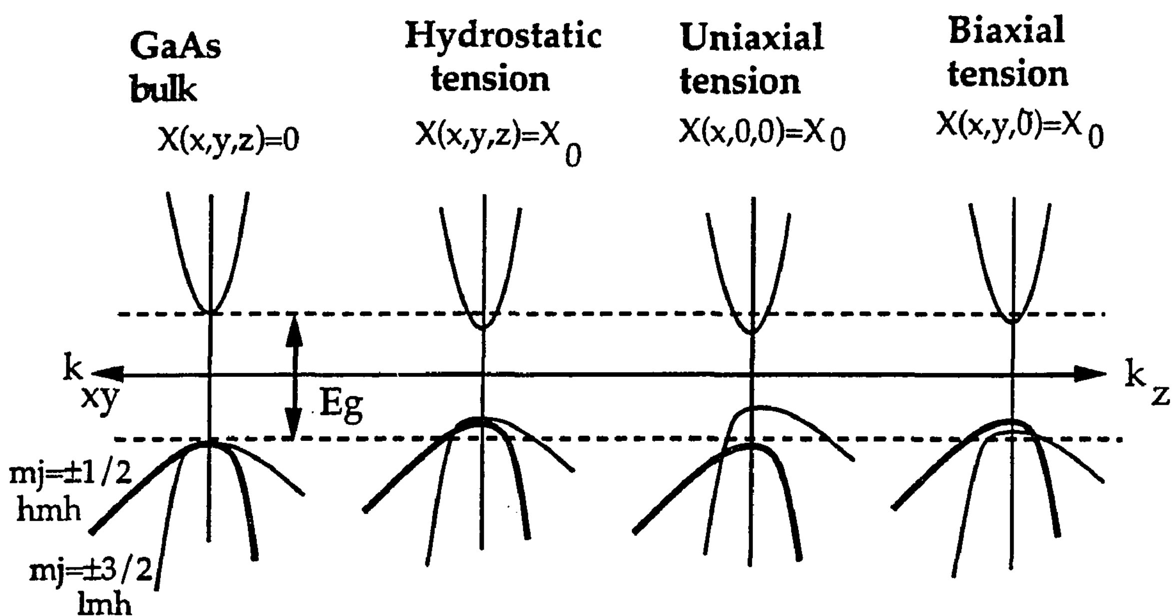

Fig.2.3.4. Band structures of GaAs without stress and with hydrostatic, uniaxial, and biaxial tension. In these cases, anti-crossing effects are neglected.

the hmh and lmh subband 20.7 and 8.5 meV toward the conduction band(used Eq.(2.3.5a)). Therefore, the lmh subband locates at a lowest energy in the valence band under the uniaxial tension while the hmh subband locates at a lowest energy in the valence band under the biaxial tension.

The GaAs/Si sample at 4 °K lattice temperature contains 2.91 kbar of stress as calculated in the section 2.2.2. Thus, the lmh and hmh subband energy difference should be about 17.8 meV using Eq.s 2.3.4 and 2.3.5 as,

$$\Delta(E_c\text{-}E_{hmh})_{biax}-\Delta(E_c\text{-}E_{lmh})_{biax}=-6.121\bullet X$$
$$=-6.121\bullet 2.91$$
$$=-17.8\ \text{meV} \quad . \qquad (2.3.6)$$

The experimental result shows a difference of 14 meV which is slightly smaller shift than the theoretically expected value of 17.8 meV. This may be explained by existence of dislocation at the interface as seen in Fig. 2.4.1(a). The dislocation might reduce the stress.

2.3.2. QW Band structure under stress

In a GaAs/AlGaAs QW structure, the energy states in the GaAs well along the growth direction (z-axis) are quantized. The energy levels generate higher quantized states represented by their quantum numbers while the dispersion in the plane perpendicular to the growth direction (xy-plane) remains same as bulk GaAs. The eigen energy of quantized states of the QW depend on the effective masses along the growth direction as discussed in section 2.1.2. When the GaAs/AlGaAs QW is grown on a Si substrate, the band structure is determined not only by the quantum confinement but also the biaxial tension in

the GaAs well layer. The tension shifts the conduction and valence bands and alters the splitting energy between the quantized hmh and lmh subbands in the valence band. The biaxial tension compensates the quantization because the energy shifts due to the stress are negative so that the lifted subbands are shifted to lower energy and the energy separation between the hmh and lmh subbands becomes smaller. At a certain amount of the tension and the quantum confinement, the valence subbands becomes degenerate as similar manner as a bulk GaAs and are quantized along z-axis. It should be emphasized that the hmh and lmh notations are defined in the xy-plane and the mass of the hmh (lmh) subband along z-direction is light(heavy).

The effect of the biaxial tension and quantum confinement effects on the band structure along the growth and xy-plane directions around k=0 are schematically shown in Fig. 2.3.5 (a) to (e). Note, that the lowest hmh subband($m_j=\pm1/2$) is shown in thick solid lines and the lowest lmh subband($m_j=\pm3/2$) is shown in thin solid lines in the valence band. The split-off band and higher quantized states are not shown in the band structures and the band mixing, interaction, which causes the anti-crossings, is not taken into account.

Fig. 2.3.5. (a) shows a band structure for a GaAs bulk without strain. The heavy and light mass hole subbands are degenerate in this system. The energy band gap is shown by Eg (1.42 eV at room temperature) and the energies of the conduction and valence band edges are indicated by dashed lines.

For the case of bulk GaAs / Si,[11-13] about 2.9 kbar of biaxial tensile stress exists in the GaAs at 4 °K lattice temperature as discussed in the section 2.2.2. From Eq. 2.2.10, the built-in tension at room temperature is estimated to be 1.6

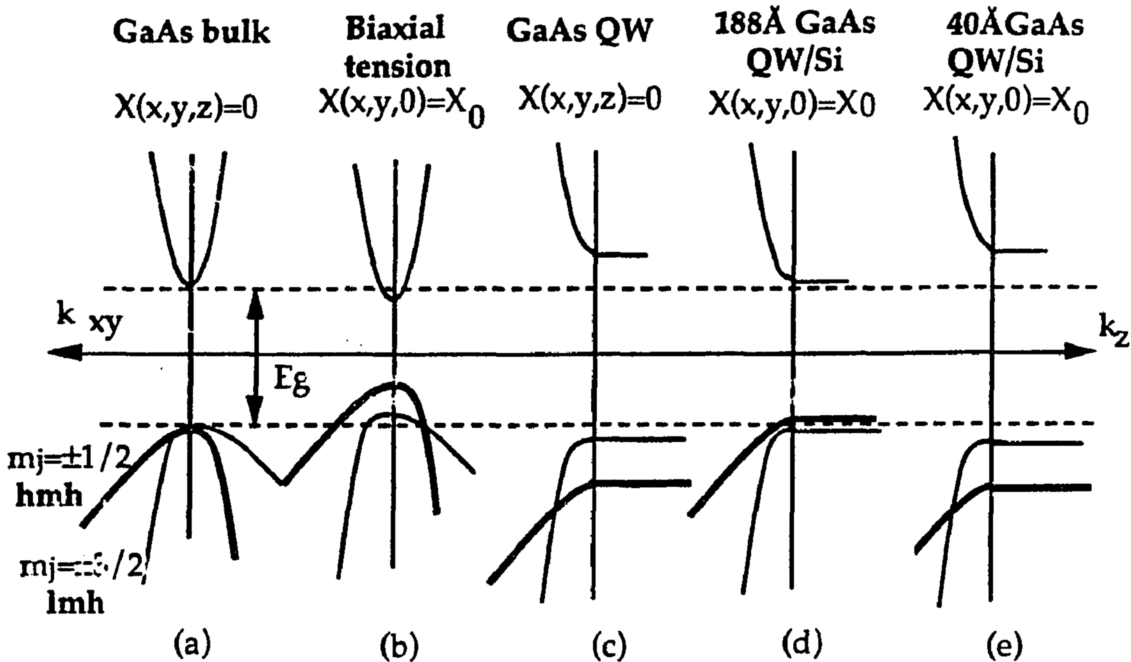

Fig.2.3.5. Schematic band structures of bulk GaAs and quantum well with and without biaxial tensile stress. In these cases, anti-crossing effects are neglected.

kbar. Fig.2.3.5 (b) shows the band structure for the bulk GaAs/Si. The tension shifts the valence and conduction bands closer and splits the J=±3/2 valence band into the hmh and lmh subbands. As the result, the band gap energy becomes smaller and is determined by the energy separation between the conduction band edge and the hmh subband edge. The band gap shifts between the conduction band edge and the hmh is 1.403 eV ($\Delta(E_c\text{-}E_{hmh})_{biax}$=-17 meV) while that for the lmh is 1.413 eV ($\Delta(E_c\text{-}E_{lmh})_{biax}$=-7 meV) at room temperature. The energy separation between the hmh and lmh subbands at k=0 is about 10 meV.

In a GaAs QW grown on a GaAs substrate(no strain in the layer), the quantum confinement lifts the subbands higher energy in both conduction and valence bands and splits the valence subbands according to the well width and the effective masses in the growth direction as shown in Fig. 2.3.5 (c). Since the

hmh (lmh) mass along the growth direction (k_z direction) is light (heavy), the quantization acting on the growth direction lifts the hmh (lmh) strongly (weakly). As the result, the lmh locates lower energy than the hmh along the xy-plane due to the asymmetric structure of $m_j=\pm 1/2$ and $m_j=\pm 3/2$ subbands.

In the cases of GaAs QW/Si as shown in Fig.2.3.5.(d) and (e), the GaAs well epilayer contains biaxial tensile stress. The tension shrinks the band gap and shifts the hmh and lmh subbands to lower energy separately as shown the figure (a). On the other hand, the quantum confinement lifts the conduction and the valence subbands higher energy as shown in the figure (b). As the same manner, the conduction band is lowed by the hydrostatic component of the stress and is lifted by the quantization. The energy level of the conduction band is determined by their joint effect. The tensile stress and the confinement act on the band structure in opposite direction. Therefore, the band structure in the tensioned QW is determined by the balance between the quantum confinement and the stress induced subband splitting. In real cases, the effect is more complicate as shown in the paper by J. Lee. [17,18] The tension in the GaAs layer is 2.9 kbar at 4 °K lattice temperature and thus the band shifts due to the stress are similar for any QW structures grown on Si substrates. The energy states, therefore, are tuned by the quantization determined by well width. In a QW/Si with 188Å well width as shown in Fig. 2.3.5. (d), both lmh and hmh subbands are quantized along the z-axis and do not shift much from the bulk band edges because the confinement is weak. When a well width is 40Å, the quantization is strong, the hmh subband shifts to higher energy than the lmh subband. The confinement give enough energy shift to the valence subbands to compensate the energy shift due to the stress as shown in Fig. 2.3.5. (e).

The stress induced band shift for the case of a 121Å GaAsP/AlGaAs QW with y=0.05 is calculated using the magnitude of stress determined in the previous section. Since the calculated stress of 2.05 kbar is biaxial tension(see Eq.(2.2.9b), the energy shifts are estimated approximately using Eq. 2.3.4 (there is negligibly small difference in the amount of shifts of hmh and lmh subband between GaAsP and GaAs because the phosphor concentration is small) as,

$$\Delta(E_c\text{-}E_{hmh})_{biax} = -10.36*2.05 = -21 \text{ meV} \qquad (2.3.7a)$$

and

$$\Delta(E_c\text{-}E_{lmh})_{biax} = -4.239*2.05 = -8.7 \text{ meV}. \qquad (2.3.7b)$$

The energy split between the hmh and lmh subband is calculated to be -(21-8.7)= -12.54 meV from the difference between Eq.s 2.3.7 (a) and (b). Since a 121Å GaAs reference QW (no built-in stress) shows 11 meV of confinement shift, the GaAsP 121Å should show -12.54-11=-1.54 meV energy difference (which is almost degenerate) in the PL excitation absorption spectra. The experimental data shows the degeneracy as expected as will be discussed in Chapter 8.

As demonstrated in Fig. 2.3.5. (a)-(e), one can tune the band structure using the combination of quantum confinement and stress effects. The tuning parameters depend on material composition, quantum well width, and the substrate material. The band structure of semiconductor material can be artificially controlled as required.

2.4. Dislocation

Another important characteristics of a strained sample is the dislocation and defects at the boundary between the layers because they may cause non-radiative recombination and defect scattering. To avoid the dislocation, a few μm thick buffer layers are usually grown between the substrate and the epilayer to compensate the built-in stress and to avoid defects.

Because of the built-in strain in GaAs/Si, there exists dislocations in the GaAs epilayer as shown in Fig.2.4.1.(a) taken by T. Soga et al.[21] with a transmission electron microscopy (TEM) for a GaAs epilayer directly grown on a Si substrate and in Fig.2.4.1(b) for a superlattice buffered GaAs epilayer on a Si substrate. As clearly shown in both figures, the dislocation can reach more than 0.5 μm from the interface. Using the strained superlattice structures as buffer layers, the density of dislocation can be decreased.

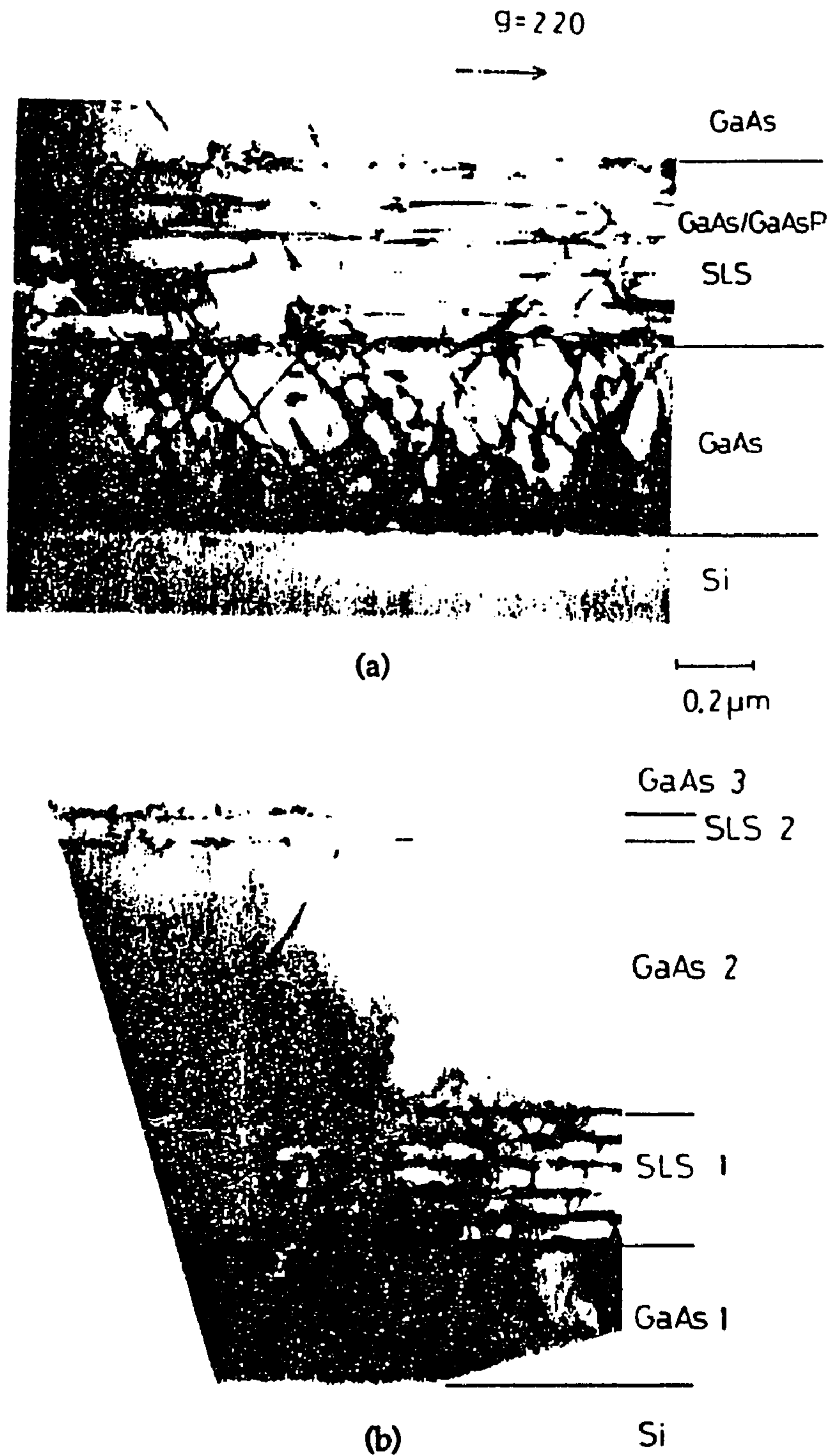

Fig.2.4.1 (a) Cross-section of TEM image of GaAs/Si sample grown by MOCVD method by T. Soga (b) cross-section of TEM image of GaAs/Si buffered by $GaAs_{0.72}P_{0.28}$/GaAs strained superlattice.

2.5. References in chapter 2

1). J. Blakemore, "Gallium Arsenide", American Institute of Physics (New York, 1987)

2). J. M. Luttinger, Phys. Rev. 102, 1030 (1956)

3). R. de Kronig and W. J. Penney, Proc. Royal Sco. London, A130, 499 (1930)

4). E. O. Kane, J. Phys. Chem. Solid, 1, 249 (1957)

5). J. F. Nye, "Physical Properties of crystal", Oxford at the Clarendon Press, (1984)

6). F. Voisin, C. Delalande, M. Voos, L.L Chang, A. Segmuller, C. A. Chang, L. Esaki, Phys.Rev. B 30, 2276,(1984)

7). Casey et.al " Heterostructure lasers" Part A and B, Academic Press, Inc. California(1978)

8).Y. Chen, A. Freundlich, H. Kamada and G. Neu, Appl. Phys. Lett. 54 (1989)

9). F. H. Pollack and M. Cardona, Phys. Rev. 172, 816 (1968)

10). Johnson Lee, M. O. Vassell, E. Koteles, C. Jagannth, K.T. Hsu, G. J. Jan, C. P. Liu, and I. F. Change, Phys. Rev. B, 40, 1703 (1989)

11). M. Chandrasekhar and F.H. Pollak, Phys. Rev. B, 15, 2127 (1977)

12). K. Shum, Y.Takiguchi, J.M. Mohaidat, F. Liu, R.R.Alfano and H. Morkoc, Appl. Phys. Lett. 56, 2328 (1990)

13). E. S.Koteles, D.A.Owens, D. C. Bertolet, J-K. Hsu, and K.M.Lau, Surface Science, 228, 314 (1990)

14). S. Zemon, S. K. Shastry, P. Norris, C. Jagannath, and G. Lambert, Solid State Comm. 58,457, (1986)

15). P. L. Gourley, M. Longerbone, S.L. Zhang, and H. Morkoc, Appl. Phys.

Lett.

16). A. Freundlich, H. Kamada, and G. Neu, Phys. Rev. B. 40, 1652 (1989)

17). Shun Lee , Ph. D thesis at the City College of CUNY (1992)

18). Johnson Lee and M. O. Vassel , Phy. Rev. B. 37, 8855 (1988)

19). Johnson Lee and M. O. Vassel , Phy. Rev. B. 37, 8861 (1988)

20). F. H. Pollak, C. W. Higginbothan, and M. Cardona, J. Phys. Soc. Jpn. Suppl. 21,20 (1966).

21). T. Soga, T. Jimbo, and M. Umeno, Appl. Phys. Lett. 56, 1433 (1990)

CHAPTER 3

CARRIER ENERGY RELAXATION

The carrier energy relaxation process through carrier-phonon and exciton-phonon interactions and carrier recombination processes through spontaneous emission will be reviewed in this chapter.

3.1. Introduction

In an intrinsic GaAs, all valence bands are occupied by electrons at absolute zero temperature. As the lattice temperature increases, the electrons in the valence band start gaining kinetic energy from the thermally excited vibration of the lattice (called "phonon"). The energy distribution of the electrons f(E) at a lattice temperature T_L is described by Fermi-Dirac distribution function as,

$$f(E) = \frac{1}{1 + e^{(E - E_f)/k_B T_I}} \qquad (3.1.1)$$

where k_B is the Boltzmann constant and E_f is the Fermi energy level of the electrons. A hole distribution function is described by 1-f(E) because the hole is a vacancy of an electron.

The lattice vibration is characterized by phonon (quantized vibrational mode) which follows Bose distribution given by,

$$N(T_q)=1/\{\exp(\hbar\,\omega_0/k_BT_q)-1\} \qquad (3.1.2)$$

where T_q is the phonon temperature and ω_0 is the phonon angular frequency.

The capacity of band to contain a number of electron is called density of states $\rho(E)$. The higher the density of states, the larger the number of electron to be accumulated in the state. The product of the electron distribution function $f(E)$ and the density of states $\rho(E)$ determines the electron population at an electron energy $n(E)$ in the band structure which is given by,

$$n(E)=\rho(E)\cdot f(E) \quad . \qquad (3.1.3)$$

The hole population can be estimated similar way as for the electrons by using the hole distribution function and the hole density of states.

The density of states for a QW is different from that of bulk materials because the band structure are quantized and split into subbands. The detail on this matter will be discussed in Chapter 3.6.2.

When an external perturbation such as an electric field or an optical field is applied to a thermally equilibrium state, the carriers and excitons at the state will be excited to higher energy at different momentum as shown in Fig.3.1.1.(a). In this thesis, I used an ultrafast optical pulse field as the perturbation from a femtosecond laser whose photon energy $h\nu$ is larger than the band gap energy E_g. The excess energy E_k above the band gap energy obtained from the optical perturbation is given by,

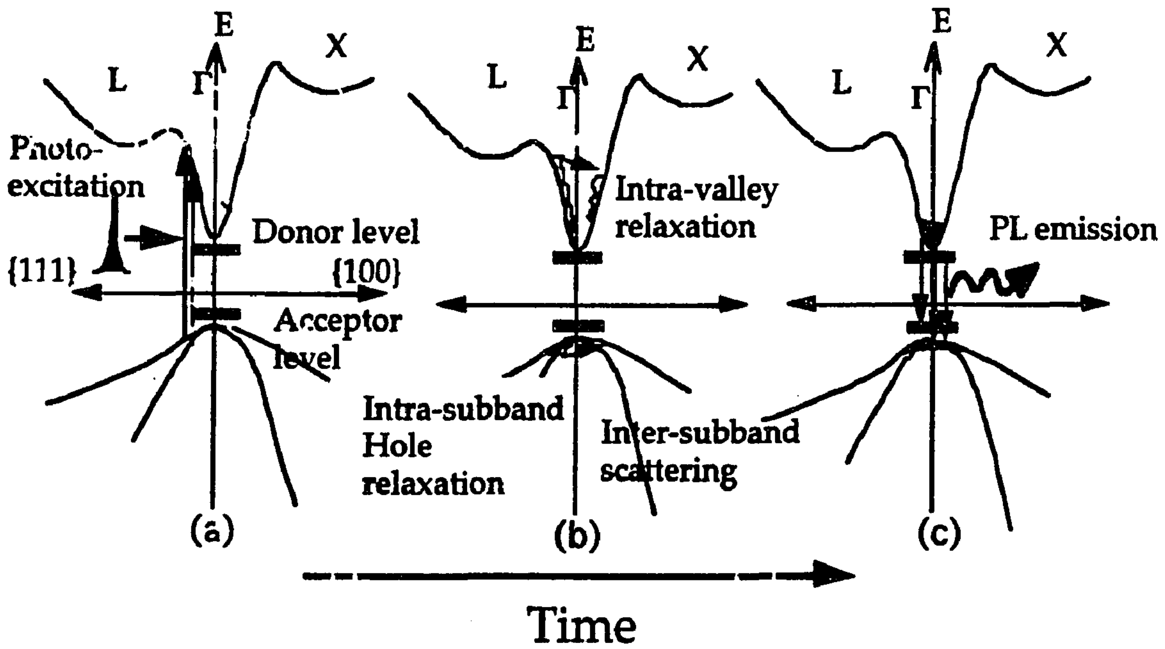

Fig. 3.1.1 Energy relaxation processes of carriers in GaAs after ultrashort pulse photoexcitation.

$$E_k=h\nu-E_g \quad . \qquad (3.1.4)$$

The excess energy becomes the kinetic energy of the electron and the hole. Assuming parabolic band structures for the conduction and valence bands, the kinetic energies for the electron (E_e) and hole (E_h) are given by,

$$E_k = E_e+E_h$$
$$= \hbar^2 k_c^2/2m_c^* + \hbar^2 k_v^2/2m_h^* \quad . \qquad (3.1.5)$$

where m_c^* and m_h^* are the effective masses of the conduction electron and the valence hole, respectively. Since the momentum of carriers and photon are conserved during the transition(k_c=k_v, the momentum of photon is negligible

compare to those of the elctrons and holes), the excess energies for the carriers are calculated as,

$$E_h = E_e \bullet m_c^* / m_h^* \quad . \tag{3.1.6}$$

Substituting Eq.3.1.6. into Eq.3 1.5 with Eq.3.1.4, the electron and hole kinetic energies are determined to be,

$$E_e = (h\nu - E_g) / (1 + m_e^* / m_h^*) \quad . \tag{3.1.7a}$$

and

$$E_h = h\nu - E_g - E_e \quad . \tag{3.1.7b}$$

For 2.0 eV pumping photon energy, E_e in a GaAs (E_g=1.5 eV) assuming parabolic band structures is calculated to be 440 meV. The kinetic energy of hole at the initial time is determined to be 60 meV because the effective masses are $0.067m_0$ for the conduction electron and $0.45m_0$ for the valence hole.

From the kinetic energy, the carrier temperature can be estimated using,

$$E_{e(h)} = 3k_B T_{e(h)} / 2 \quad . \tag{3.1.8}$$

The initial electron temperature with the 2.0 eV photon excitation is calculated to be T_e=3400 °K and the initial hole temperature is estimated to be 500 °K.

These photoexcited carriers relax to thermally equilibrium state by loosing their energy to the lattice, other carriers and impurities through carrier-

carrier scattering and phonon emission as shown in Fig.3.1.1.(b). The cooled electrons within the conduction band or donor level around k=0 recombine with holes in the valence band or acceptor level. As the result of the recombination, the transition energy E_q is re-emitted as a photon $h\nu'=E_q$ as shown in Fig.3.1.1. The transition may occur with carrier-carrier scattering or phonon assisted recombination.

As the kinetic energy transferred to other carriers or states, the cooled electrons and holes located within their Coulomb field can form a meta-stable state, which is called "exciton", and it shows hydrogen atom like optical properties. The exciton decays with its lifetime depending on its mass and binding energy. During the kinetic energy release process, the carriers and exciton interact with phonon and other carriers either elastically or inelastically. For the elastic scattering, the carriers and excitons loose their momentum while the inelastic process changes the carrier and exciton kinetic energies. These energy release and momentum exchange processes are called "Scattering" in general as similar manner as atomic collision in the nuclear physics. Since the scattering process conserves energy and momentum before and after the interactions, the hot carriers and excitons can interact only certain phonons and other particles and satisfy the conservations. (The band structure and the phonon dispersion relation determine the coupling of carrier and phonon.) The momentum loss process is called momentum relaxation process while the energy loss process is called energy relaxation process.

The photogenerated hot electrons, holes, and excitons in semiconductor samples are scattered and thermalize in femtosecond to picosecond time scale

and finally reach thermal equilibrium states as described above. Since the momentum of carrier can be immediately changed by one phonon scattering, the momentum relaxation time is usually much faster than the energy relaxation time.

In the following sections, I will discuss the carrier and exciton energy relaxation and their spontaneous emission process.

3.2. Carrier-carrier scattering

Hot carriers and excitons can exchange their energies with other carriers and excitons through collision (carrier-carrier and exciton-exciton interaction) and their interaction becomes significant above the carrier density of higher than 10^{18} cm^{-3}. When there exists a lot of cool carriers before the photoexcitation, the photogenerated hot carriers mainly loose their energy to the cool carriers through the collision. The collision process is elastic and its energy exchange rate is determined by the mass difference between the colliding carriers. This process does not transfer carrier kinetic energies to lattice directly. However, it may couple with other scattering mechanisms which transfer the earned energy to the lattice and enhance the other scattering rates.

When an electron having a high kinetic energy incidents into a cold electron gas, the incident electron looses its kinetic energy through electron-electron (e-e) elastic scattering. Since the e-e scattering exchanges their energies at a rate given by,[12)]

$$\left(\frac{dE}{dt}\right)_{e\text{-}e} = \frac{4\pi N_e e^4}{\varepsilon_0^2 (2m_e E)^{1/2}} \tag{3.2.1}$$

where N_e is cold electron density, e is the electron charge, ε_0=8.854x10^{-14}(F/cm), E is the kinetic energy of incident electron, and m_e is the electron effective mass. As clear from Eq 3.2.1, the higher the electron density, the larger the energy exchange rate. The heavier the mass and the lower the kinetic energy, the smaller the energy relaxation rate. This relation can be extended to e-hole scattering. The energy relaxation due to the e-lmh is much faster than that for e-hmh because of the mass difference.

3.3. Energy relaxation through phonon interactions

The lattice vibration causes perturbation in the periodicity of the crystal potential. The vibration effect is to scatter a free carrier from its current state to a new state. The scattering is treated using a time-dependent perturbation theory. The scattering probability S(k , k') from a state E_k with a wave vector k to $E_{k'}$ with another wave vector k' is described by,

$$S(k, k')=(2\pi/\hbar)\,|M(k,k')|^2\,\delta(E_k - E_{k'} \pm \hbar\,\omega_q \tag{3.3.1}$$

where $|M(k, k')|^2$ is a matrix element between the k and k' states, $\hbar\,\omega_q$ is the phonon energy, the plus and minus signs correspond to phonon absorption and emission, respectively. The matrix element is given by,

$$M(k, k') = \int_{V_c} X^*_{n'_{qk'}} \Delta V X_{n_{qk}} d\Omega \bullet \delta(k\text{-}k'\pm\hbar\omega q) \tag{3.3.2}$$

where V_c is the crystal volume and $X_{n'_q,k'}$ and $X_{n_q,k}$ are the wave function for the electron-phonon system after and before the scattering. The phonon occupation number changes from n_q to $n_{q'}$. ΔV is the perturbation due to the scattering and arises from the alteration of the position of the crystal atoms from the equilibrium position when the lattice vibrates. There are several scattering mechanism such as acoustic deformation potential interaction, piezoelectric scattering, alloy scattering, polar and non-polar optical phonon interaction, impurity scattering, and inter-valley scattering. These scatterings are fundamental energy transfer mechanism for the hot carriers to either cold lattice or to other cold particles. The inter- and intra-valley scatterings occur between different valleys and within the same valley, respectively. The inter-subband scattering is the scattering between different subbands and is in the same category.

To estimate the scattering probabilities, the matrix elements are the important parameters. The square of matrix element $|M|^2$ of these scattering processes were equated by Nag[1] and are given as follows.

For acoustic phonon deformation interaction, the $|M|^2_{ADP}$ is given by,

$$|M|^2_{ADP} = E_1^2 \hbar \omega_q (n_q \text{ or } n_q+1)/(2V_c\rho s^2) \tag{3.3.3a}$$

where E_1 is the deformation potential and s is the longitudinal acoustic velocity.

The acoustic phonon also induces a potential arising from piezoelectricity. The $|M|^2_{pz}$ for the piezoelectric scattering is given by,

$$|M|^2_{pz} = e^2 h^2_{pz} \hbar (n_q \text{ or } n_q + 1)/(2V_c \rho\, \varepsilon^2 \omega_q), \tag{3.3.3b}$$

where h_{pz} is the suitably averaged constant derived from the piezoelectric tensor, q is the phonon wave vector, and ε the permitivity.

The electric field created by the electron couple to the lattice atoms through an electric dipole interaction which causes out-of-phase atomic motion (LO phonon). For such optical phonons, the nonpolar optical phonon interaction matrix element $|M|^2_{nop}$ for non-polart materials is given by,

$$|M|^2_{nop} = D_0^2\, \hbar\, (n_0 \text{ or } n_0 + 1)/(2V_c\, \rho\, \omega_0)\,, \qquad (3.3.3c)$$

where D_0 is the optical deformation potential constant and n_0 is the optical phonon occupation number.

The optical phonon induces polarization potentials in polar paterials and the matrix element $|M|^2_{pop}$ for such polar optical phonon is given by,

$$|M|^2_{pop} = \hbar\, e^2\omega_0(K_\infty^{-1}\text{-}K_s^{-1})\,(n_0 \text{ or } n_0\text{+}1)/(2V_c\, \varepsilon_0\, q^2)\ . \qquad (3.3.3d)$$

where ω_0 is the optical phonon angular frequency, ρ is the mass density, and $K_{\infty,s}$ are the dielectric constants at optical frequency and steady state, respectively.

The matrix element $|M|^2_{imp}$ of the impurity scattering is given by,

$$|M|^2_{imp} = e^4/(|\mathbf{k}-\mathbf{k}'|^2\text{+}1/\lambda^2)^2/(V_c^2\, \varepsilon^2)\ , \qquad (3.3.3e)$$

where k and k′ are the electron wave vectors before and after the scattering.

The matrix element $|M|^2_{iv}$ for the inter-valley scattering is given by,

$$|M|^2_{iv} = D_i^2 \hbar (n_i \text{ or } n_i+1)/(2 V_c \rho \omega_i) \; , \qquad (3.3.3f)$$

where n_i is the inter-valley phonon occupation number, D_i is the inter-valley scattering deformation potential, and ω_i is the angular frequency of the inter-valley phonon.

Finally, the alloy scattering matrix element $|M|^2_{alloy}$ is given by,

$$|M|^2_{alloy} = 2 V_0 \alpha_1(1-\alpha_1) E_{ab}^2 / V_c \qquad (3.3.3g)$$

where V_0 is the volume per atoms in the crystal, α_1 is the concentration of atoms of one type, E_{ab} is the scattering potential.

The detailed delivations of these matrix elements are discussed in Ref. 10.

As listed above, the scattering processes depend on the mechanical, optical, and electronic properties of the semiconductors. The larger the matrix elements become, the larger the scattering probabilities for the carriers and phonons become.

Since the carrier-phonon interaction is the main process for cariers to loose and gain there energies except photon-carrier interactions, the energy relaxation of the carrier can be estimated by using these scattering matrix elements as follows and the energy relaxation through these scattering processes was reviewed by Conwell[10] and Nag.[1]

They described the energy relaxation processes starting from Fermi's Golden rule for a phonon emission and absorption process as:

$$-\frac{dE}{dt}=\left(\frac{V_c}{8\pi^3}\right)\left[\int\left[dk\,\{h\omega_q\bullet S(k,k')\}\right]_{emission}-\int\left[dk\,\{h\omega_q\bullet S(k,k')\}\right]_{absorption}\right]$$

(3.3.4)

where k and k' are the wave vectors of initial and final phonon states, $\hbar\omega_q$ is the phonon energy, and S(k,k') is the scattering probability between the initial k and final k' states given by Eq. 3.3.1. Since the phonon density is hardly measured directly from experiments, the PL kinetics are being analyzed to determined the carrier and exciton energy relaxation rates. In this thesis, I have evaluated the carrier and exciton energy relaxation rates from time resolved PL spectrum.

Following sections describe the energy relaxation through various kinds of phonon interactions.

3.3.1. Acoustic deformation potential (ADP) interaction

This mechanism dominates the energy relaxation process when energies of carriers are much less than the optical phonon energy. At a low lattice temperature below 40 °K, acoustic deformation potential (ADP) interaction determines the energy relaxation rate for these warm electrons. In a simple parabolic band, the average energy relaxation rate per electron due to the ADP averaged over a Fermi distribution at an electron temperature of T_c is estimated by[1]:

$$\left\langle\frac{dE}{dt}\right\rangle_{ADP}=-\frac{8\sqrt{2}}{\pi^{3/2}}\bullet\frac{m^{*5/2}E_1^2}{\rho h^4}\bullet(kT_c)^{3/2}\left(1-\frac{T_L}{T_c}\right)\frac{F_1(\eta)}{F_{1/2}(\eta)}, \quad (3.3.5a)$$

with Fermi integral

$$F_j(\eta) = \frac{1}{\Gamma(j+1)} \int_0^{\infty} \frac{\varepsilon^{j}\, d\varepsilon}{1+e^{(\varepsilon-\eta)}} \qquad , \qquad (3.3.5b)$$

where E_1 is the ADP for conduction band, m^* the electron effective mass, ρ the density of material, T_L the lattice temperature, $\varepsilon=(E-E_c)/k_BT_c$, $\eta=(E_F-E_c)/k_BT_c$, and $\Gamma(j+1)$ is the gamma function of (j+1)th order. For non-degenerate (when the carrier density is less than the effective density of states) semiconductor material, $\eta<<0$ thus $F_j(\eta)\sim\exp(\eta)$ and the ratio of the Fermi integral becomes 1.

From Eq.s 3.3.5, the electron energy relaxation through the ADP interaction is determined by the electron effective mass, material density, and electron and lattice temperatures. For strained material, since the change in electron effective mass and material density is small, the energy relaxation rates for strained and non-strained semiconductor materials are not so much different.

3.3.2. Piezoelectric scattering

For piezoelectric semiconductors, the piezoelectric scattering also dominates the electron energy relaxation at a low lattice temperature. The relaxation rate is given by[1],

$$\left\langle \frac{dE}{dt} \right\rangle_{PE} = -0.4 \left(\frac{2m^*}{\pi} \right)^{3/2} \left(\frac{q\, e_{14}}{h \varepsilon_0 K_s} \right)^2 \frac{(kT_c)^{1/2}}{\rho} \left(1 - \frac{T_L}{T_c} \right) \frac{F_0(\eta)}{F_{1/2}(\eta)} , \qquad (3.3.6)$$

where e_{14} is the piezoelectric coupling constant, ε_0 the free space permittivity, and K_s the static dielectric constant. As the same manner as the ADP interaction, the ratio of Fermi integrals is 1 for non-degenerate piezoelectric semiconductors. Thus, the electron energy relaxation through piezoelectric scattering is determined by electronic property of material such as K_s, e_{14}, electron effective mass, and electron and lattice temperatures. For the strained semiconductor materials, the piezoelectric scattering is not affected by stress so much. The piezoelectric constants for GaAs and AlAs are given by -0.16 and -0.225 (C/m^2), respectively. The AlAs shows stronger coupling to the piezoelectric scattering than GaAs.

3.3.3. Optical phonon

Above 100 °K of a lattice or an electron temperature in GaAs, the polar optical phonon interaction dominates the electron energy relaxation process because $\hbar\omega_{LO}$~37 meV which corresponds to a Debye temperature of 430°C. The relaxation rate for a non-degenerate semiconductor is given by,

$$\left\langle\frac{dE}{dt}\right\rangle_{OP} = -\frac{\sqrt{2m^*}\,e^2}{4\varepsilon_0 h^2}\left(\frac{h\omega_{LO}}{\pi}\right)^{3/2} \bullet \left[\frac{1}{K_\infty}-\frac{1}{K_s}\right] \bullet \left[\frac{e^{x_0-x_c}-1}{e^{x_0}-1}\right] \bullet \left[(x_c)^{1/2} e^{x_c/2} K_0(x_c/2)\right] \tag{3.3.7}$$

with $x_c = h\omega_{LO}/k_B T_c$, $x_0 = h\omega_{LO}/k_B T_L$ where $K_{\infty,s}$ are optical and static dielectric constants, $h\omega_{LO}$ is the optical phonon energy, and $K_0(x)$ is the modified Bessel function of zero order. The energy loss rate is determined by the electron effective mass, the difference between the optical and static dielectric constants, and the electron T_c and lattice T_L temperatures. Therefore, the lighter the

electron mass, the smaller the energy loss rate. A Fröhlich coupling constant which indicates the strength of LO phonon interaction is defined by,

$$\alpha_F = \frac{1}{2}\frac{e^2}{(h/2m^*\omega_{LO})^{1/2} h\omega_{LO}}\left(\frac{1}{K_\infty}-\frac{1}{K_s}\right) \quad . \tag{3.3.8}$$

The Fröhlich coupling constant in Γ-valley for GaAs and AlAs are given by 0.068 and 0.126, respectively. The LO phonon in AlAs couples with an electron in Γ-valley twice stronger than in GaAs. In X-valleys for GaAs and AlAs, the coupling constants are similar values such as 0.152 and 0.166, respectively.

3.3.4. Non-polar optical phonon

Electrons interact with optical phonon through optical deformation potential scattering. This process is called "non-polar optical (NPO) scattering". For electrons with s-symmetry around k=0, the matrix element for the NPO scattering vanishes in III-V semiconductors such as GaAs and its alloy. When electrons at a high energy have a p-symmetry component to their wave function, the electrons are scattered by NPO interaction and loose their energies. The coupling strength of NPO phonon to electrons for GaAs and AlAs are given by phenomenological optical deformation potentials which are same value of 5.9 eV for both materials.

3.3.5. Momentum and energy relaxation through phonon interaction

The relative momentum relaxation times for different phonon scattering process in non-parabolic band are depicted in Fig.3.3.1 as function of lattice temperature calculated by Nag.[1] At a low lattice temperature, the impurity

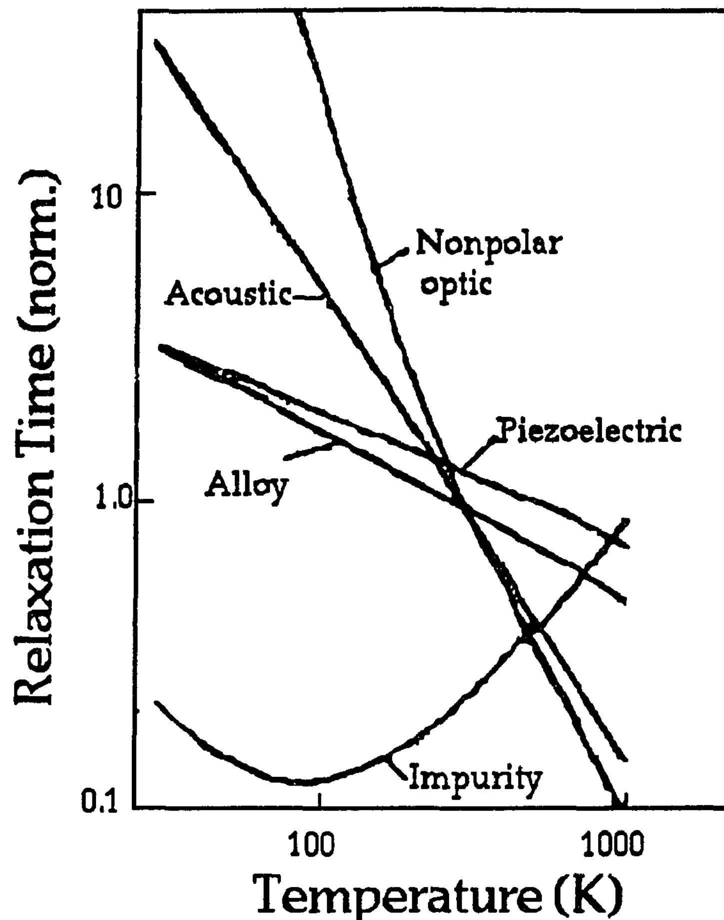

Fig.3.3.1 Relative momentum relaxation time through various scattering process for non-parabolic band. (after Nag [1])

scattering dominates the momentum relaxation. The alloy, acoustic phonon, and non-polar optic phonon scatterings are weaker scattering mechanisms. As higher temperature, the acoustic and non-polar optic phonon interactions dominate the relaxation.

The energy relaxation rates for acoustic and polar optical phonons in a GaAs are illustrated in Fig.3.3.2 as function of electron-hole plasma temperature at lattice temperature of 2 °K (calculated by Goebel and Hildebrand 1978). At non-equilibrium, the carriers or excitons can have a thermal distribution represented by a carrier or exciton temperature which is different from the

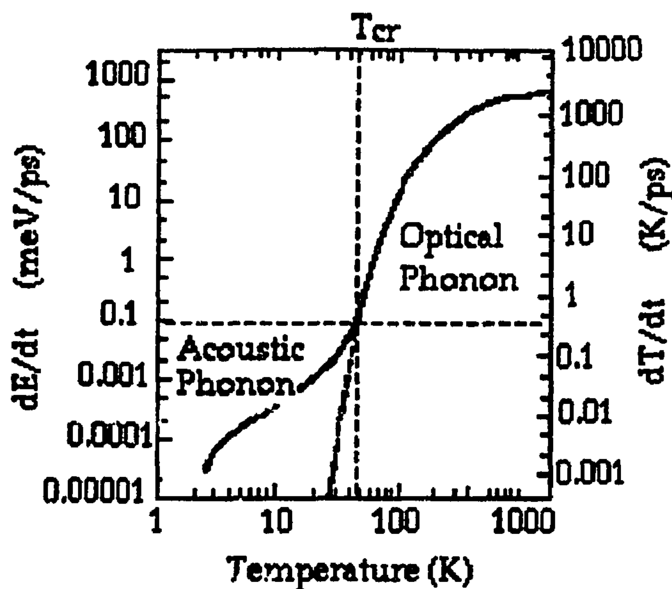

Fig. 3.3.2 Electron-hole plasma energy relaxation rates through interactions with acoustic and optical phonon at various electron-hole plasma temperature with a lattice temperature of 2 °K for a bulk GaAs.(after Goebel and Hildebrand)

lattice temperature. When the carriers do not have enough kinetic energies $E_k=k_BT_c$ below 40 °K temperature, they mainly interact with lattice through acoustic deformation potential interaction. T_{cr} (40 °K) is the critical temperature where the energy relaxation rate becomes same for the acoustic and optical phonon scatterings. The energy relaxation rate at T_{cr} (shown in Fig. 3.3.2 as dashed lines) is around 0.1 meV/ps. The energy relaxation rate for LO phonon interaction is typically larger than 0.1 meV/ps at higher carrier temperature than 40 °K.

A LO phonon interaction time is a few tens of femtoseconds. When a lot of phonons are created within a short time, the phonons distribution function described by Boltzmann distribution could be hot so that the hot phonons regulate the carrier and exciton scattering.[2-9]

3.3.6. Hole energy relaxation

Hole energy relaxation process is much more complicate and can not be simply equated as for electrons because of band degeneracy, anisotropy, warping of band structure, and symmetry problem of wave function. For simplifiedmodels[1)], Eq.s 3.3.5, 3.3.6, and 3.3.7 for the electron divided by 2 can be applied for the hole energy relaxation rates. This means the hole energy relaxation rates through various scattering are typically twice slower than the electron in the conduction band.

3.4. Carrier energy distribution change through phonon interaction

To demonstrate the carrier-phonon and carrier-carrier interaction on low density hot electron gas, P.H. Maksym and C. J. Hearn[1)] calculated the electron distribution at various delay times after a photoexcitation and showed the transient carrier distribution clearly. Fig.3.4.1 and 3.4.2. show dynamic carrier density change for hot and warm carrier cases, respectively. In the case of Fig.3.4.1, a GaAs sample at 1 °K lattice temperature is photoexcited with a 5 ps pulse and hot carriers having 40.9 meV kinetic energy with 10^{16} e/cm^3 electron density are generated. The kinetic energy of carriers are higher than LO phonon energy ($\hbar\omega_{LO}$=37 meV). Within the pulse duration, there appears a phonon replica at 37 meV below the photoexcitation energy. The fast energy relaxation at 1 °K lattice temperature is induced by LO phonon emission to the lattice followed by acoustic phonon emission as the carrier looses its kinetic energy through LO phonon emission. Then, the carriers thermalizes and re-distributes as Boltzmann distribution in a few ps. Therefore, a time-resolved PL spectroscopy with a 10 ps time resolution may hardly observe the LO phonon

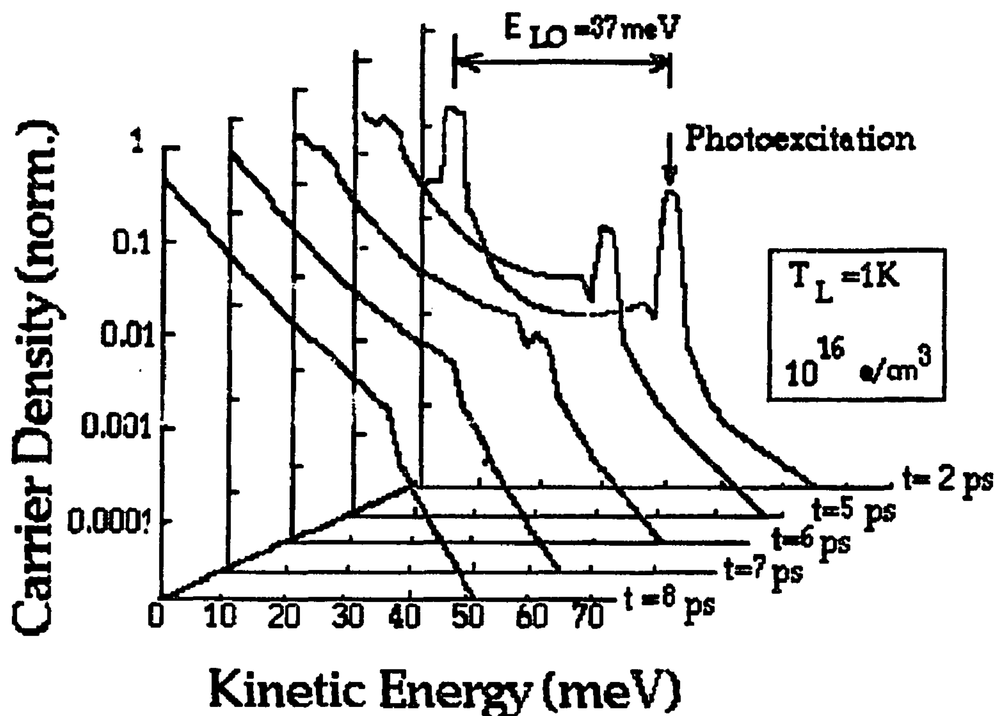

Fig.3.4.1. Calculated carrier density change by energy relaxation through LO and acoustic phonon interaction. (after Maksym and Hearn[1)])

emission process directly but the carrier-carrier and acoustic deformation potential interaction should be observed.

Suppose a near resonance excitation experiment, ie: the incident photon energy is little above the band gap energy, is carried out at 1 °K lattice temperature with low photoexcitation density. The acoustic phonon interaction takes place and shows slow energy relaxation process as shown in Fig.3.4.2. The warm electron re-distribution process though acoustic phonon emission is clearly depicted. The warm electron takes about 50 ns to reach equilibrium described by Boltzmann distribution because of the acoustic phonon energy is low compare with a LO phonon energy.

Substantial researches has been carried out to investigate hot electron or

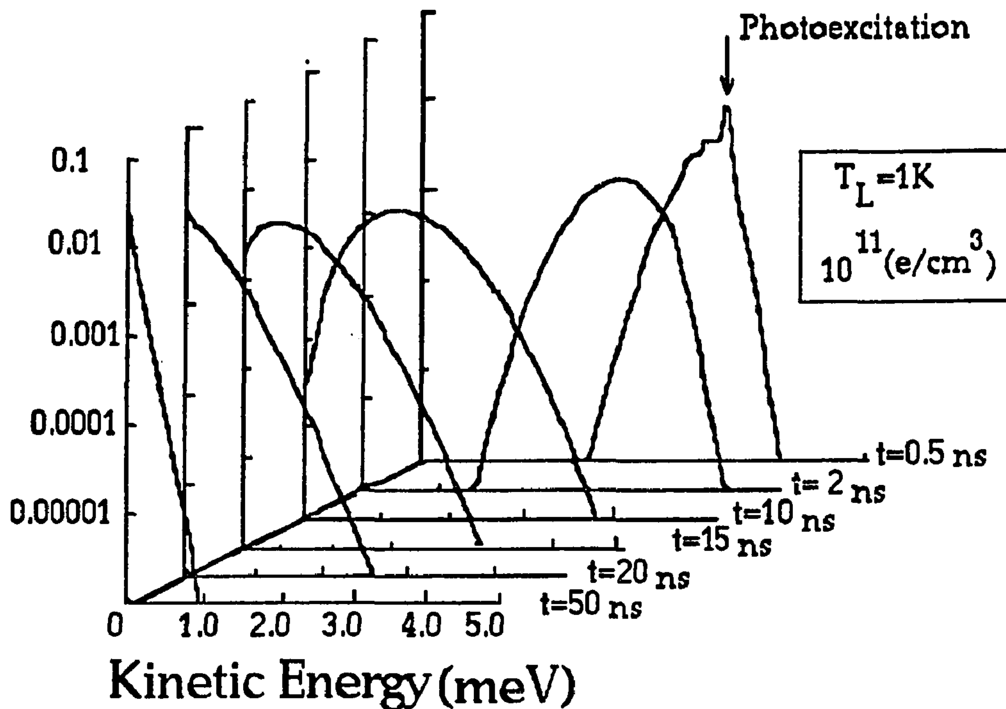

Fig.3.4.2. Calculated carrier density change by energy relaxation through acoustic phonon interaction in a GaAs at 1K lattice temperature. The photogenerated electron density is 10^{11} /cm^3. (after Maksym and Hearn[1)])

hole thermalization rates[10)], impurity scattering rate, electron-electron scattering rates, electron-hole scattering rate, hole-hole scattering rate, heavy hole-light hole scattering rate, X-Γ or X-L inter-valley scattering rates, surface recombination rate, exciton formation rate[12)], and so on by taking into account phonon interaction. If the carrier and exciton distribution function at various delay time is directly measured and compared with the theoretically calculated distribution function with certain carrier-carrier and carrier-phonon scattering, the energy and momentum relaxation mechanism can be determined in detail. However, it was difficult to distinguish individual scattering process because the band structure is complicated with existence of impurity, defect, and built-in potential or strain and many scattering processes occurs at the same time within

100 ps. Therefore, the energy relaxation process has not been well determined individually.

3.5. Average carrier and average carrier kinetic energies

A PL spectrum I(E) is determined by the carrier (or exciton) population as function of energy E and is proportional to the product of a carrier (or an exciton) density of states ρ(E) and a carrier (or an exciton) distribution function f(E) at a carrier (or exciton) temperature and a lattice temperature. The PL spectrum is given by,

$$I(E) \propto \rho(E) \bullet f(E). \qquad (3.5.1)$$

Since averaged carrier dynamics is observed in a PL measurement, the average energy of carrier at various delay times after the photoexcitation is important.

An average carrier and exciton energy <E> can be calculated using the density of states ρ(E) and the distribution function f(E) as[11],

$$\langle E \rangle = \int_0^\infty E \bullet \rho(E) \bullet f(E)\ dE \Big/ \int_0^\infty \rho(E) \bullet f(E)\ dE \qquad (3.5.2)$$

Using the relation of Eq.3.5.1, this average carrier and exciton energy is rewritten using the PL spectrum I(E, t) at a delay time t as,

$$\langle E(t) \rangle = \int_0^\infty E \bullet I(E, t)\ dE \Big/ \int_0^\infty I(E, t)\ dE \qquad (3.5.3)$$

Further, since an average carrier and exciton kinetic energy at various delay time after the photoexcitation is determined by the energy transfer rate to the lattice, the average carrier and exciton kinetic energy $<E_k(t)>$ is also calculated with respect to delay time t from the PL spectrum I(E, t) using,

$$<E_k(t)> = \int_{E_1}^{E_2} I(E,t) \cdot E \, dE / \int_{E_1}^{E_2} I(E,t) \, dt - E_0 \quad (3.5.4)$$

where E_1 and E_2 are low and high energy edges of the PL spectrum because the experiment is carried out within a certain PL energy region, and E_0 is the lowest carrier and exciton state energy determined from a steady state PL peak position at the same lattice temperature at which the time-resolved PL measurement is carried out.

Therefore, the PL kinetics measured in this thesis gives the average carrier and exciton dynamics.

3.6. Carrier recombination through spontaneous emission

Spontaneous emission and absorption are the quantum mechanical interactions between photons and carriers and arise from carrier transitions between electron-hole, donor-hole, acceptor-electron, and exciton annihilation as depicted in Fig.3.6.1. The transition rates between two discrete states (an initial and a final states) are described by Fermi's Golden rule which is given by

$$W = \frac{2\pi}{h} |H'_{if}|^2 \rho(E_f) \, \delta(E - E_i + E_f) \quad (3.6.1)$$

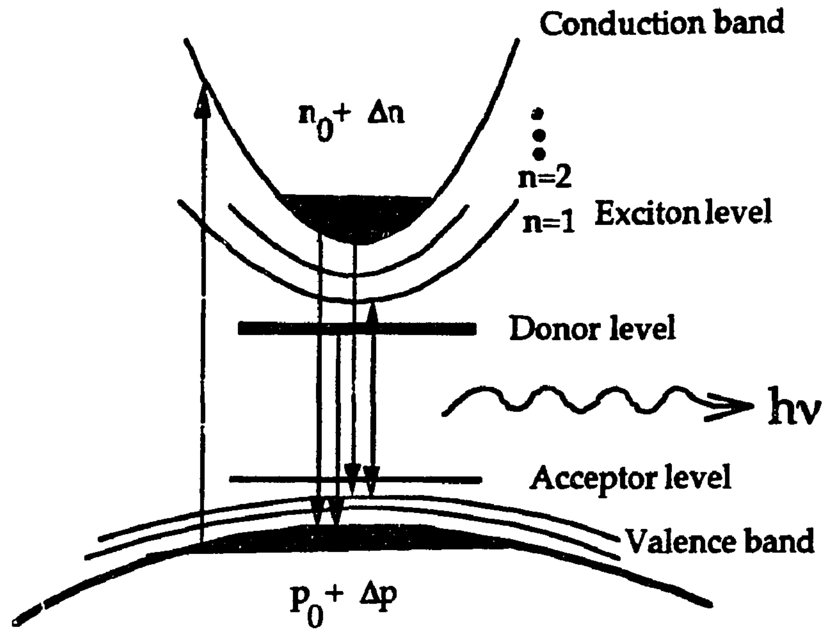

Fig.3.6.1 Band structure and radiative transitions between the conduction and valence bands.

where W is the transition rate per unit volume per unit energy, $|H'_{if}|^2$ is the time independent part of matrix element of the interaction Hamiltonian $2H'_{if}$ $\sin\omega t$ (between photon and electron), $\rho(E_f)$ is the density of the final state, and E_i and E_f are the energy levels of the initial and final states. The energy and momentum between initial and final states have to be conserved and the energy conservation is represented by the delta function. The following is simple approach to give a form of emission process.

The interaction Hamiltonian H_I for an interaction between photons and electrons as in the cases of photoemission and photoabsorption is given by a product of electron momentum operator $\vec{p}$ and vector potential $\vec{A}$ of photon as,

$$H_I = -\frac{q}{m_0}\vec{A} \bullet \vec{p} \quad , \qquad (3.6.2)$$

where q is the electron charge and m_0 is the free electron mass. The photon couples with an electron within the material. The vector potential for a photon with an energy of $\hbar\omega$ is given as,

$$\vec{A} = \hat{\varepsilon} \bullet \left(\frac{2h}{\varepsilon_0 \bar{\mu}^2 \omega} \right)^{1/2} \sin(\omega t - \vec{k} \bullet \vec{r}) \quad , \qquad (3.6.3)$$

where $\hat{\varepsilon}$ is polarization vector, ε_0 is dielectric constant in vacuum, $\bar{\mu}$ is the refractive index, $\vec{k}$ is the wave vector, and $\vec{r}$ is the position vector. The electronic properties of the material determines the coupling strength and the interaction Hamiltonian. Substituting Eq. 3.6.3 into Eq.3.6.1, the interaction Hamiltonian can be expressed as,

$$H_I = \frac{q}{m_0} \left(\frac{2h}{\varepsilon_0 \bar{\mu}^2 \omega} \right)^{2} \left(\hat{\varepsilon} \bullet \vec{p} \right) \sin(\omega t - \vec{k} \bullet \vec{r}) \quad . \qquad (3.6.4)$$

Therefore, the matrix element using the time independent part of the interaction Hamiltonian is given by,

$$|H'_{if}|^2 = \frac{q^2}{4m_0^2}\left(\frac{2h}{\varepsilon_0\mu\,\bar{\omega}^2}\right)\left|\langle i|\hat{\varepsilon}\cdot\vec{p}|f\rangle\right|^2$$

$$= \frac{q^2}{4m_0^2}\left(\frac{2h}{\varepsilon_0\mu\,\bar{\omega}^2}\right)|M_{if}|^2 \quad , \tag{3.6.5}$$

with an assumption that the $\vec{k}\cdot\vec{r} \ll 1$. The transition rate between the two energy states can be rewritten as,

$$W = \frac{\pi q^2}{m_0^2}\left(\frac{h}{\varepsilon_0\mu\,\bar{\omega}^2}\right)\rho(E)\cdot|M_{if}|^2\delta(E_i - E_f - E) \quad . \tag{3.6.6a}$$

The density of final state is given by,

$$\rho(E) = 2\,\frac{4\pi k^2}{8\pi^3}\frac{dk}{dE} \quad . \tag{3.6.6b}$$

where the factor 2 in front of the right hand term arises from the spin of electron.

Since the spontaneous transitions conserve energy and momentum of electron and hole, there exists selection rule. The matrix element $|M_{if}|^2$ contains the k-selection rule as,

$$|M_{if}|^2 = \frac{8\pi^3}{V}|M_b|^2\delta(k_c - k_v) \tag{3.6.7}$$

where V is a volume of the semiconductor, $|M_b|$ is the average matrix element for the Bloch states. ($2|M_b|^2/\hbar\omega m$ is called as "Oscillator strength" which determines the transition strength.) The delta function is non-zero when $k_c=k_v$. The momentum of electron and photon (~0) are conserved.

According to the k•p theory by Kane, the average matrix element for the Bloch state is given by,

$$|M_b|^2=\frac{m_0^2 E_g(E_g+\Delta)}{12m_c(E_g+2\Delta/3)}$$
$$= \xi\, m_0 E_g \qquad (3.6.8a)$$

where Δ is the split-off separation energy between the degenerate band and the sprit-off band. The matrix element is a function of energy band gap, the energy separation of the split-off band, and the effective mass (in this case electron in the conduction band). For a GaAs bulk, ξ is evaluated to be 1.327 at room temperature.

For impurity transition such as donor level to valence band and conduction band to acceptor level, the matrix element is described as,

$$|M_{if}|^2=64\pi a^{*3}(1+a^{*2}k_b^2)^{-4}V^{-1}\bullet|M_b|^2 \qquad (3.6.8b)$$

where a^* is the effective Bohr radius($a^*=4\pi\varepsilon\hbar^2/m^*q^2$), k_b is the band structure of either conduction or valence band as final state, and V is the volume of the system.

3.6.1 Spontaneous emission from bulk GaAs

The equilibrium carrier distribution in bulk semiconductor like GaAs is described by Fermi-Dirac distribution with a Fermi energy level which characterizes the instantaneous distribution. The total number of electrons n in a parabolic conduction band($E=\hbar^2k^2/2m_c$) is determined by an integral as,

$$n=\int \frac{\rho_c(E)}{1+\exp\{(E-E_{fc})/k_BT\}}dE \tag{3.6.9a}$$

with

$$\rho_c(E) = 4\pi\left(\frac{2m_c}{h^2}\right)^{3/2} E^{1/2} \tag{3.6.9b}$$

where $\rho_c(E)$ is the density of states using an effective mass m_c, E_{fc} is a quasi-Fermi level in the conduction band, k_B is the Boltzmann constant, and T is the electron temperature. By substituting summation of the photoinjected electron number Δn and the residual electron number n_0 into $n=n_0+\Delta n$, a quasi-Fermi level in the parabolic conduction band E_{fc} after the photoexcitation can be determined. If the electron temperature is extremely high so that electron distributes within X- or L-valley, the integration has to include the valleys.

A quasi-Fermi level in a parabolic valence band can also be determined in the same manner. Since the valence band consists from three subbands such as hh, lh, and sprit-off bands, it is required to integrate the hole distribution in the three bands. The total hole number p in the valence bands is determined using a quasi-Fermi level E_{fv} as,

$$p = \sum_{i=hh,lh,so} \int \frac{\rho_{vi}(E)}{1+\exp\{(E - E_{fvi})/k_B T\}} dE \quad , \qquad (3.6.10)$$

where ρ_{vi} is the hole density of states, E_{fvi} the Fermi energy, and T the hole temperature in the subband, respectively. The Fermi level in the valence band measured from the valence band edge is determined by substituting $p=p_0+\Delta p$ where p_0 is the residual hole concentration and Δp is the photoinjected hole.

From Eq.s 3.6.9 and 3.6.10, the electron and hole distribution functions are uniquely determined using the Fermi energies at the carrier temperature.

For the case of the direct parabolic conduction to heavy mass hole parabolic subband transition around k=0, the spontaneous emission rate r(E) per unit volume is given by,[13]

$$r(E) = \frac{2\bar{\mu}q^2 E |M_b|^2}{\pi m_0^2 \varepsilon_0 h^2 c^3} \left(\frac{2m_r}{h^2}\right)^{3/2} (E - E_g)^{1/2} f_c(E_c)\, f_v(E_v) \qquad (3.6.11a)$$

with

$$E_c = \frac{m_r}{m_c}(E - E_g) \quad , \quad E_v = \frac{m_r}{m_v}(E - E_g) \quad , \qquad (3.6.11b)$$

and

$$m_r = \frac{m_c m_v}{m_c + m_v} \quad , \qquad (3.6.11c)$$

where m_v is the effective hole mass. Eq.s 3.6.11b and c are obtained for the parabolic band structure from the momentum conservation ($k_c = k_v$,because

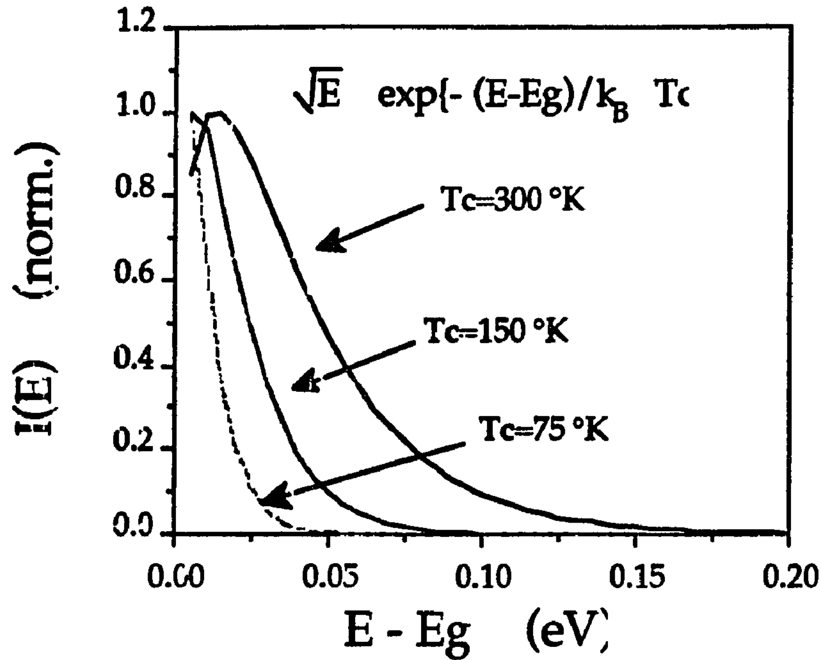

Fig. 3.6.2. Spontaneous emission PL spectrum for a conduction to valence band transition calculated at various carrier temperature using Eq. 3.6.12a for a non-degenerate direct band gap semiconductor.

the momentum of photon is negligibly small) and from the energy conservation which requires,

$$\hbar^2 k_c^2/2m_c + \hbar^2 k_v^2/2m_v = E - E_g \quad . \qquad (3.6.11d)$$

Letting

$$E_c = \hbar^2 k_c^2/2m_c \quad , \qquad (3.6.11d)$$

$$E_v = E_c{}^* m_c/m_v \quad . \qquad (3.6.11e)$$

Substituting Eq.s 3.6.11d and e into Eq.3.6.11d, Eq.3.6.11b and c are obtained.

To obtain an entire spectrum, the spontaneous emission rates r(E)s times

photoexcitation volume V_c for all transition have to be integrated with a condition of transition selection rule and an electron and hole distribution functions. Therefore, the spectrum I(E) is given by,

$$I(E) = \int_{V_c} r(E)\ dv \qquad . \qquad (3.6.12a)$$

For a non-degenerate direct band gap semiconductor case, the carrier distribution function is approximated by Boltzmann distribution function. The fundamental PL spectrum I(E) can be approximated to be,[14)]

$$I(E) \sim \exp\{-(E-E_g)/k_B T_c\} \bullet (E-E_g)^{1/2} \qquad (3.6.12b)$$

where T_c is the carrier temperature. Since the high energy tail arises from high kinetic energy carriers in the bands, one can determine the carrier temperature from the high energy tail of the PL which is single exponential curve as function of carrier kinetic energy.

For a non-degenerate indirect band gap semiconductor, the high energy tail is given as,[14)]

$$I(E) \sim \exp\{-(E-E_g)/k_B T_c\} \bullet (E-E_g)^2 \quad . \qquad (3.6.12c)$$

Fig.3.6.2. illustrated a spontaneous emission PL spectrum arising from a transition between a parabolic conduction and a parabolic valence band with a band gap E_g. The high energy tails indicate their carrier temperatures clearly. The higher the carrier temperature, the larger the high energy tail in the spontaneous emission spectrum.

3.6.2. Spontaneous emission from QWs

In a GaAs quantum confined structure, the band structure along the growth direction is quantized into discrete energy levels as shown in Fig.3.6.3. The dispersion curve in the xy plane perpendicular to the growth direction is still considered to be parabolic for both conduction and valence subbands around k=0. The number of electron or hole states per unit area in the xy plane in conduction subband is given by,

$$\rho_i \, dE = \frac{2 \, d^2 \vec{k}}{(2\pi)^2} \qquad (3.6.13)$$

where ρ_i is the electron or hole areal density of states in the xy plane and $\vec{k}$ is the electron or hole wave vector along the xy direction.

For the parabolic band in the xy direction, the areal density of state is given by,

$$\rho_i = \frac{m_{ci}}{\pi h^2} \qquad (3.6.14)$$

because of $E=\hbar^2 k^2/2m_{ci}$ and $d\vec{k}^2=2\pi k dk$, where m_{ci} is the effective mass of electron or hole in i-th subband. Therefore, the density of state per unit volume of i-th subband is given using the well width L_z by,

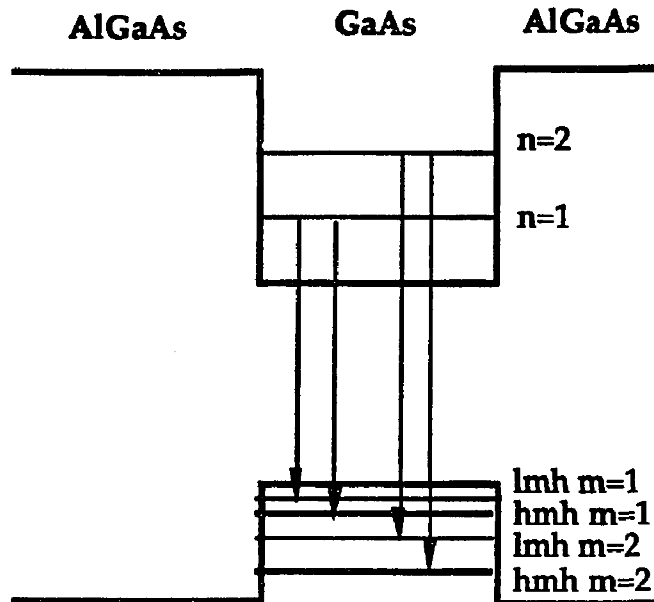

Fig.3.6.3. Radiative transitions in a GaAs/AlGaAs QW showing n=m transitions determined by selection rule. (n=m or n-m=even)

$$g_{ci} = \frac{\rho_i}{L_z} = \frac{m_{ci}}{\pi h^2 L_z} \quad . \qquad (3.6.15)$$

A density of states in a bulk GaAs was proportional to square root of the energy as given by Eq. 3.6.9b. It is obvious that the density of states in quantum structure is energy independent and thus the total density of states in a quantum well increases stepwise at each i-th subband and the density of states is proportional to the effective mass and inverse proportional to the well width L_z. Fig.3.6.4 schematically shows (a) a potential structure, (b) dispersion curve along the z-axis and xy-plane, and (c) the densities of states in the conduction and valence bands of a GaAs/AlGaAs QW/Si. The densities of states are steplike functions increase at each quantized subbands. Note, the density of states in a narrower well is larger than the wider well.

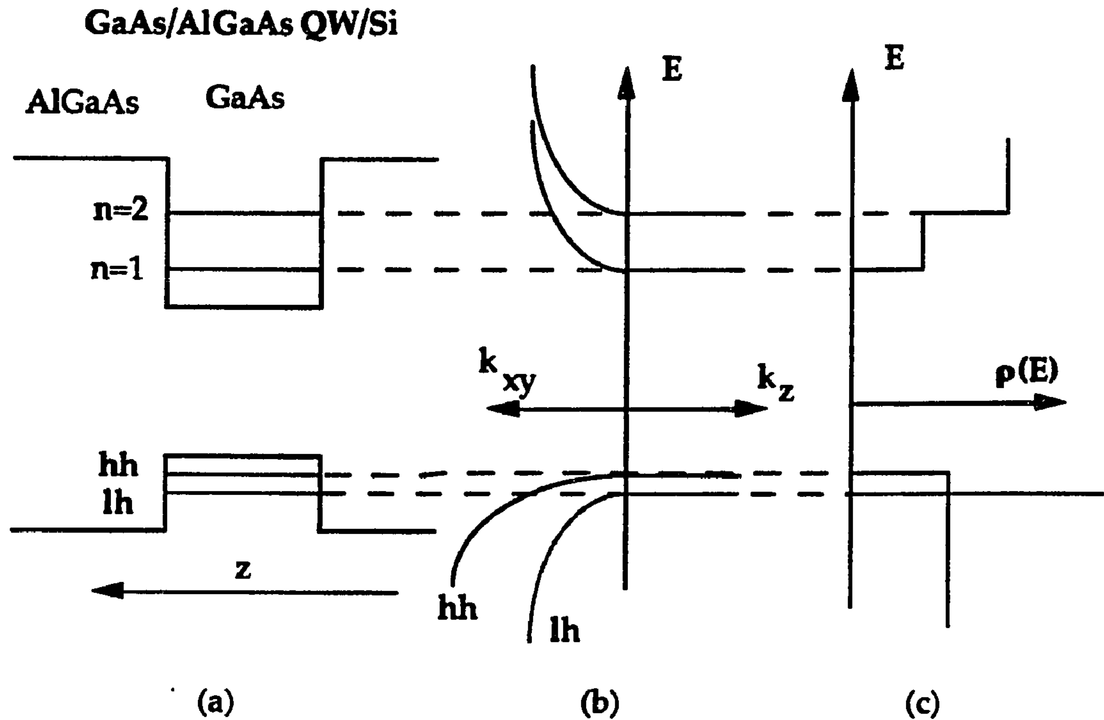

Fig. 3.6.4. (a) potential structure along z-axis and its quantized states, (b) dispersion curves along z-axis and in xy-plane, and (c) density of states in a biaxially tensioned GaAs/AlGaAs QW/Si.

The Fermi level in the quantized conduction band can be determined by integrating a product of the density of states and the electron distribution functions for entire subbands as similar manner as the bulk case discussed in section 3.6.1. The electron distribution function may be approximated to be a Boltzmann distribution. Once the Fermi level is determined, the electron distribution function at a lattice or carrier temperature is determined uniquely. Experimentally, the product of density of states and distribution function can be evaluated from an absorption spectrum or a PL excitation spectrum because the absorption spectrum is proportional to the product.

A spontaneous emission spectrum from a quantum well structure is determined from the transition rate W of the entire subbands. The matrix element $|M_{if}|^2$ is given by,

$$|M_{if}|^2 = |M_b|^2 \frac{(2\pi)^2}{A} \delta(k_c - k_v)\, \delta_{nm} \quad , \qquad (3.6.16)$$

where $|M_b|$ is an average matrix element for the Bloch states of the bands in xy plane, A is a unit area, and the delta function δ_{nm} arises from selection rules for the confined states (n, m) in the growth direction(n=m or n-m=even). The even eigen states to even eigen states and odd states to odd states transitions are allowed in the quantum well transitions and even to odd or vice versa are forbidden because a spatial overlap integral of the wavefunction for an even and an odd quantized states are zero. The average matrix element $|M_{bi}|^2$ for an n to m transition is given by (similar as Eq. 3.6.8. except $Eq=Eg+\Delta E_c+\Delta E_v$ where ΔE_i (i=c,v) are eigen states in conduction and valence bands)

$$|M_{bi}|^2 = \frac{m_0^2\, E_q (E_q + \Delta)}{12 m_{ci}\, (E_q + 2\Delta/3)} \quad , \qquad (3.6.17)$$

where Δ is the spin orbit split-off energy and Eq is the energy separation of eigen state energies in the allowed transitions between conduction and valence bands.

Using Eq.s 3.6.15, 3.6.16, and 3.6.17, parabolic subband structures in the xy plane, E_c and E_v for the energies from the conduction and valence band edges, the emission spectra for the quantum structure is given by,

$$r_{sp}(E) = \frac{16\pi^2 \bar{\mu q}^2 |M_{bi}|^2 m_r}{m_0^2 \varepsilon_0 h^4 c^3 L_z} f_c(E_c) f_v(E_v) \tag{3.6.18a}$$

with

$$E_c = \frac{m_r}{m_c}(E - E_q) \quad , \quad E_v = \frac{m_r}{m_v}(E - E_q) \quad , \tag{3.6.18b}$$

and

$$m_r = \frac{m_c m_v}{m_c + m_v} \quad , \tag{3.6.18c}$$

where $f_i(E_i)$ (i = c and v) are Fermi distribution functions of the conduction electrons and the valence holes. Eq.s 3.6.18b and c are obtained from the momentum and energy conservation of carrier and photon by assuming parabolic band structure for both conduction and valence bands as same manner as the bulk case discussed in the previous section.

Taking into account all (n,m) transitions, the entire PL spectrum can be calculated by integrating Eq. 3.6.18 for individual transitions.

3.6.3 Real spectrum

To fit the measured PL spectrum, the line shapes arising from homogeneous and inhomogeneous broadening have to be taken into account. The homogeneous line broadening arises from finite band width of the energy states and transition lifetime. The faster the transition rate, the wider the line width broadening. The broadening is usually fit with a Lorentzian. The

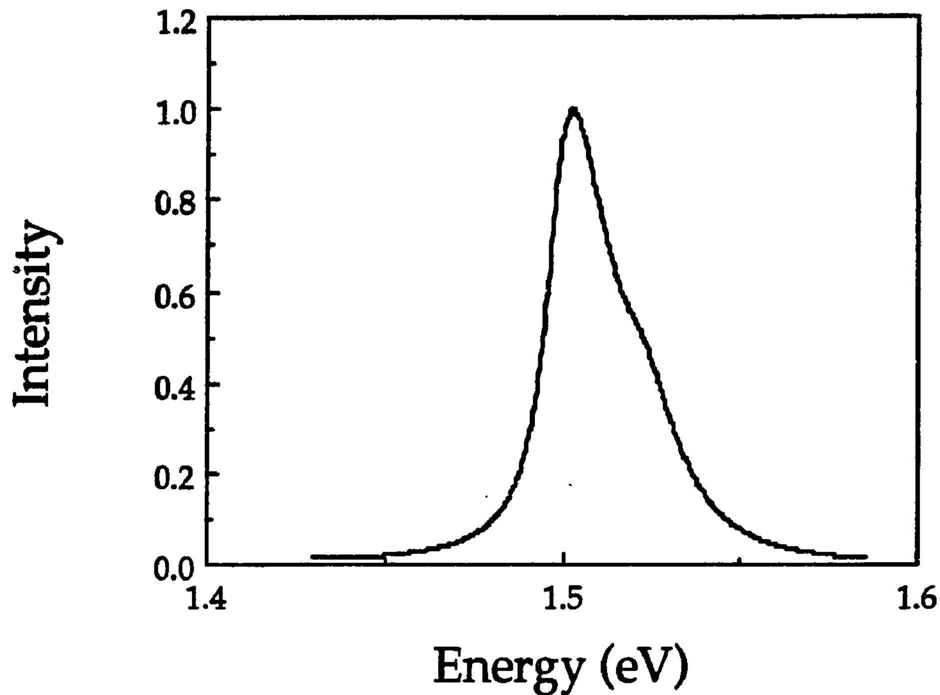

Fig. 3.6.5. PL emission spectrum with homogeneous and inhomogeneous line broadening.

inhomogeneous broadening arises from many factors. For a bulk case, the spectral resolution of system mainly dominates the line broadening. For a QW case, an interface roughness due to monolayer fluctuation causes the broadening which is usually given by Gaussian distribution function. Therefore, the spectrum I(E) measured is expressed as a comvolution formula as,

$$I(E) = \int_{V_c} \{ \Sigma\, r(E) * L(E) \} * G(E) dv \qquad (3.6.19a)$$

where L(E) and G(E) are the homogeneous and inhomogeneous broadening and $*$ denotes convolution.

To calculate the spectrum convoluted with the broadening factors, one needs to take Fourier transforms of the r(E), L(E), and G(E) and calculate the product of them because the Fourier transform of the spectrum I(E) is given by the products of the Fourier transforms of each component as,

$$\mathcal{F}\{I(E)\} = \mathcal{F}\{r(E)\} \bullet \mathcal{F}\{L(E)\} \bullet \mathcal{F}(G(E)\} \quad . \qquad (3.6.19b)$$

After calculating the product $\mathcal{F}\{I(E)\}$, one needs to take an inverse Fourier transform of the product to obtain convoluted spectrum I(E).

As an example, a spectrum is shown in Fig.3.6.5. The spectrum shows a low energy tail arising from the line broadening factors and a high energy tail due to the hot carrier temperature. If the broadening are not wide, one still can extract the carrier temperature from the high energy tail using a, single exponential function of T_c. That is,

$$I(E) \sim \exp\{ -(E - E_g)/k_B T_c\} \quad . \qquad (3.6.20)$$

3.7 Reference in Chapter 3

1). Nag, in R. R. Alfano edit. "Semiconductor Probed by Ultrafast Laser Spectroscopy" , Academic Press (New York,1984)

2). K. Kash and J. Shah, Appl. Phys. Lett. 45, 401 (1984)

3). J. Shah and R.F. Leheny, in "Semiconductor Probed by Ultrafast Laser Spectroscopy" edited by R.R.Alfano, Academic Press, 1984

4). S. Hiyamizu, T. Mimura, T. Fujii, and K. Nambu, Appl. Phys. Lett. 37, 805 (1980)

5). for example, C. L. Cesar, M.N. Islam, C.E. Soccolish, R.D. Feldmann, R.F. Austin, and K.R. German, in "Ultrafast Phenomena VII", Springer-Verlag, (1990)

U. Keller,W. H. Knox, and H. Roskos, in "Ultrafast Phenomena VII", Springer-Verlag, (1990)

6). C. Weisbuch, R. Dingle, A. C. Gossard, and W. Wiegmann, Solid State Comm. 38, 709 (1981)

7). J. P. Leburton, J. Appl. Phys. 56, 2850 (1984)

8). H. Iwamura, T. Saku, H. Kobayashi, and Y. Horikoshi, J. Appl. Phys. 54, 2692 (1983)

9). K. Hess, Appl. Phys. Lett. 35, 484 (1979)

10). E. M. Conwell edit. "High Field transport in semiconductor", Academic Press (New York, 1967)

11). Y. Masumoto, S. Shionoya, and H. Kawaguchi, Phys. Rev. B, 29, 2324 (1984)

12). T. C. Damen, J. Shah, D. Y. Oberli, D. S. Chemla, J. E. Cunningham, and J. M. Kuo, J. of Luminesc. 45, 181 (1990) and Phys. Rev. B, 42, 7434 (1990)

13).G. P. Agrawal and N. K. Dutta, "Long wavelength semiconductor lasers"

Van Nostrand Reinhold (New York, 1986)

14). S. S. Yao, Ph. D thesis at the City College of CUNY (1982)

CHAPTER 4

EXPERIMENTAL METHODS

In this thesis, two experimental techniques were used. These are : the steady state photoluminescence (PL) spectroscopy and the time-resolved PL spectroscopy at low sample temperatures. These methods were used in conjunction with mechanical uniaxial compression apparatus. The steady state PL spectroscopy is used to investigate and to characterize the optical properties of a semiconductor sample accurately. The time-resolved PL spectroscopy gives three dimensional information of the PL kinetics. These are time on a picosecond scale, PL energy in sub-meV accuracy, and PL intensity down to single photon counting level. A state-of-the-art femtosecond laser system was used for time resolved portion of this thesis. The time-resolved PL spectroscopy for a sample under externally applied uniaxial stress enables the investigation of the carrier and exciton dynamics within the stress tuned band structure.

4. 1. Steady state PL spectroscopy

A diagram of the steady state PL spectroscopy at low lattice temperature is shown in Fig. 4.1.1. A CW laser beam with a typical beam diameter of 3 mm is modulated with a mechanical chopper and is focused onto the semiconductor samples through a biconvex BK7 lens with a focal length of 20 cm. The laser spot diameter on the sample is 100 to 150 μm.

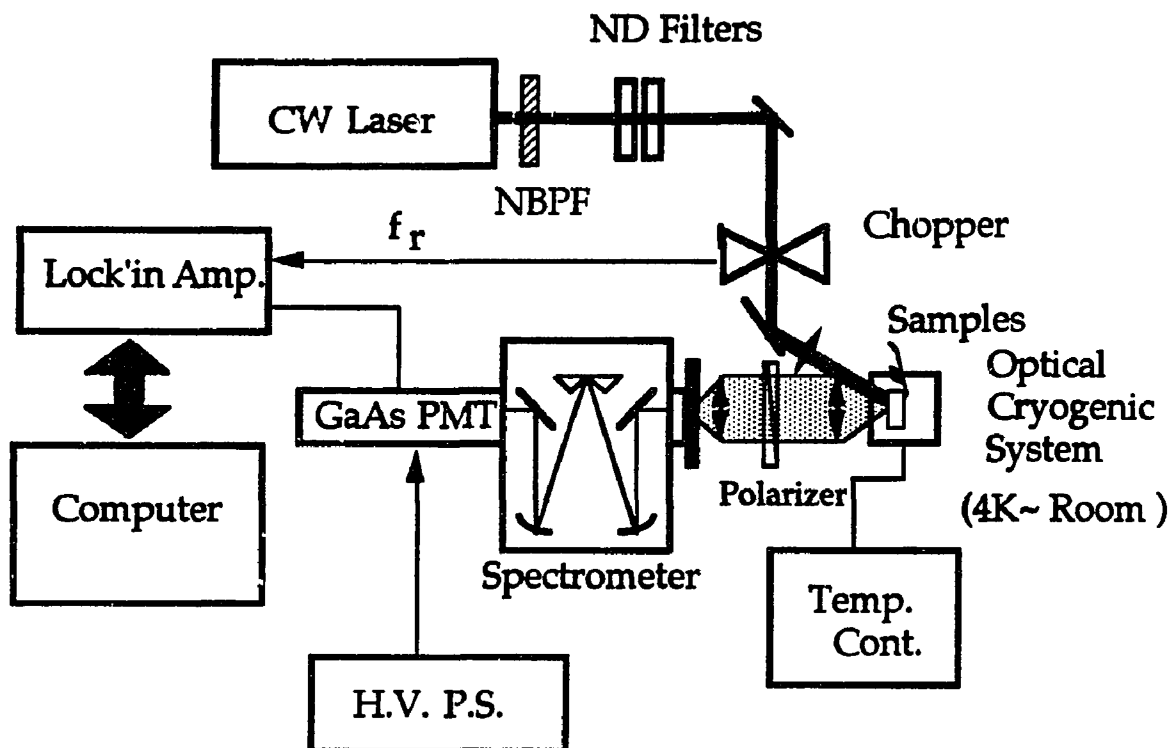

Fig.4.1.1 Steady State PL Measurement setup

The penetration depth of the laser beam depends on samples and photon energy of the laser. For example, the He-Ne laser can penetrate about 0.3 μm in GaAs bulk material. The intensity distribution I(t) of the penetrated beam in the GaAs is determined by incident laser intensity I_0 and the absorption coefficient α of the GaAs and is given by,

$$I(x) = I_0 \cdot \exp(-\alpha x) \tag{4.1.1}$$

where x is the penetration depth in the GaAs layer. Fig.4.1.2. depicts the photon absorption depth (1/α) in the GaAs layer as function of the incident photon energy. As the photon energy increases, the absorption depth decreases exponentially.

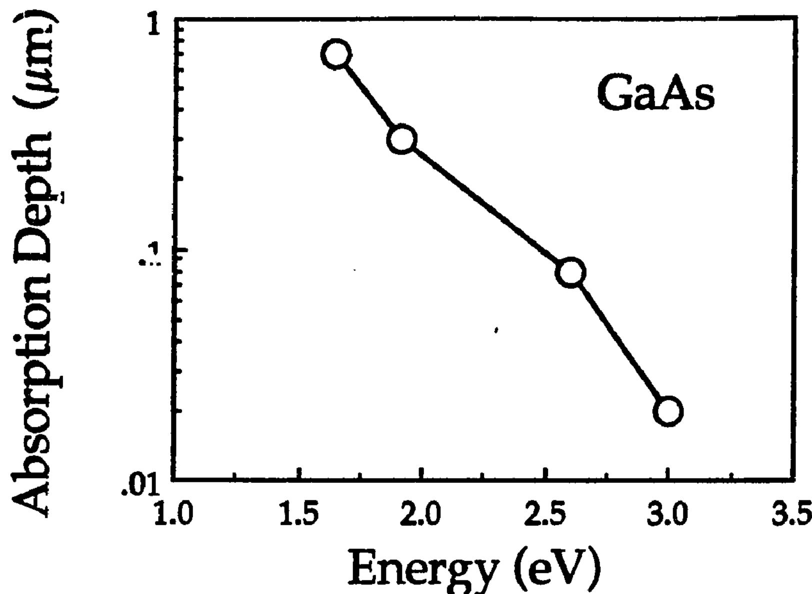

Fig.4.1.2. Photon absorption depth in a GaAs material[1)].

A central laser wavelength was selected using a narrow band pass filter(NBPF) and its incident laser beam intensity was varied using neutral density filters to investigate carrier density effects on the PL spectra. The photogenerated hot carriers thermalizes, becomes cool, recombine, and emit PL which energy corresponds to the sum of the kinetic and potential energy of the electrons and holes recombined. The PL from the samples are collected using a set of plano-convex lenses to avoid spectral aberration which reduces collection efficiency and distorts spectral information. The collected PL is introduced to a spectrometer (SPEX 1681B). To cut the scattered laser light, a color filter (a #7-59 filter to cut off λ <700 nm was mostly used in this research) is placed in front of the spectrometer. The PL signal at the output of the spectrometer is detected by a GaAs photocathode photomultiplier (PMT: Hamamatsu R943-02). This PMT has low dark noise characteristics to detect the red to near infrared PL spectrum. The excitation laser beam was chopped

at a frequency which determine a reference frequency for a lock-in amplifier. The modulated output electric signal from the PMT is connected to the Lock-in amplifier (Stanford SR575) that is controlled by a personal computer(IBM-PC). The PC computer software accumulates, analyzes, and displays the steady state PL spectrum on a TV monitor.

Since the lattice temperature determines the band structure and the carrier and exciton dynamics, the stability of the lattice temperature is very important. In this research, the samples were placed into an optical dewar with a temperature controller.

Polarization of the emitted PL can be also investigated by inserting a polarizer between the collection lenses. To avoid the polarization dependent reflection of the spectrograph, a de-polarizer is required to be inserted after the polarizer. By observing PL emission from a sample edge, one can determine the origin of PL spectrum(ie: from e-hh or e-lh transition) because the light wave propagation and absorption along the layer is determined by the selection rule of transitions available in the sample.

4.1.1. CW Laser

The CW lasers used in this thesis were a He-Ne and an Ar ion lasers. A CPM laser (see Chapter 4.2), a mode-locked YAG laser, second harmonics (SHG) of CPM laser, SHG of theYAG laser, SHG of the amplified CPM laser, and a synchronously YAG pumped dye laser were also used for the steady state experiments. Prior to the experiments, it was confirmed that the steady state PL spectra obtained by the CPM pulse laser photoexcitation at low intensity show similar features as those obtained from the PL excited by the

He-Ne laser which center wavelength of 632.8 nm is close enough to that of the CPM laser at 625 nm. The photoexcitation power was varied from 1 mW to few Watt depending on semiconductor samples to be investigated. A narrow band pass filter (NBPF) with a 10 nm band width (centered at the laser peak wavelength) was used to select only its central frequency component. Otherwise, the wide spontaneous emission components from the laser cavity contaminates the PL spectra from the samples. Especially, when an optical amplifier for the CPM laser is on, the amplified stimulated emission (ASE) from the amplifier cavity strongly distorts the PL spectrum.

4.1.2 Lock'-in amplifier detection

The lock'-in amplifier is an electronic device that works in frequency domain for electronic signal and requires a reference frequency f_r, which is provided usually as a mechanical chopping frequency of photoexcitation laser beam. Fig. 4.1.3 schematically shows a typical electronic signal spectrum from the PMT. There exists noise arising from background light, thermal emission from the photocathode of the PMT, and $1/f$ electronic noises generated in the electronic circuits. The lock'-in amplifier cuts all frequency components except the reference frequency components from the input signal. The filter band width is as narrow as 10Hz. As the result, the PL signal modulated at the reference frequency is extracted from the electronic input signal accurately and is amplified with a high gain electronic amplifier. To eliminate the electronic and optical background noise and achieve excellent signal to noise ratio, the lock'-in amplification is one of the powerful technique. To achieve best operation for the lock'-in amplifier, the PMT is required to use a 1MΩ load resistance R_L. Since the photoemitted and multiplied photoelectrons

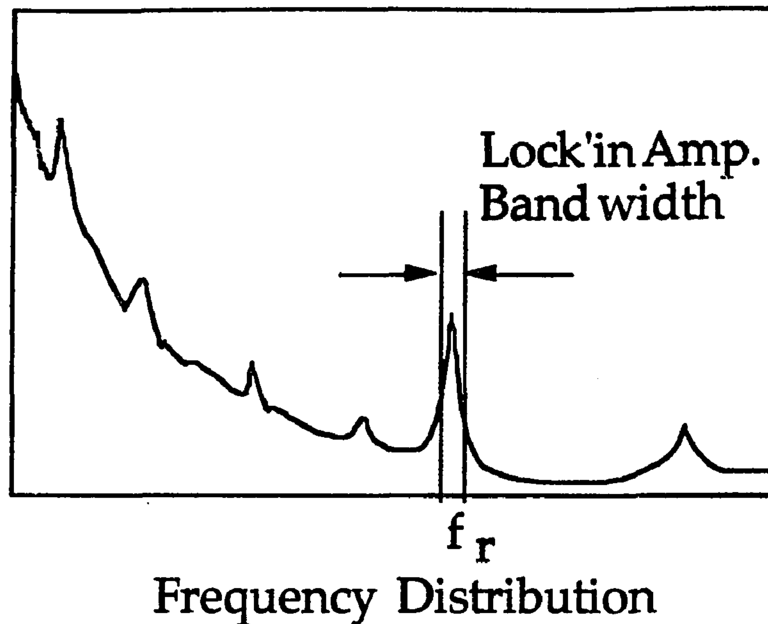

Fig.4.1.3. Frequency distribution of incident electronic signal into a lock'-in amplifier with a reference frequency f_r. The lock'-in amplifier has narrow band width as shown.

through the PMT act as a current source with a current I_{PMT}, the output voltage V_{out} from the PMT is converted by the load resistance R_L by Ohm's law, $V_{out}=I_{PMT}*R_L$. The temporal response of the PMT using 1MΩ load is as slow as 10 μs. The slow response does not affect the measurement as long as the reference frequency is lower than the PMT response frequency of around 100 kHz(=1/10μs). When a 50Ω load resistance is used instead, the output signal voltage becomes 20000 times lower but temporal resolution of the PMT is improved to be a few ns which is the ultimate time response of the PMT. The 50 Ω resistance is good to measure a ns PL decay profile of a sample directly on a high speed oscilloscope. In this thesis, 1MΩ resistance was used most of the time for the steady state measurements.

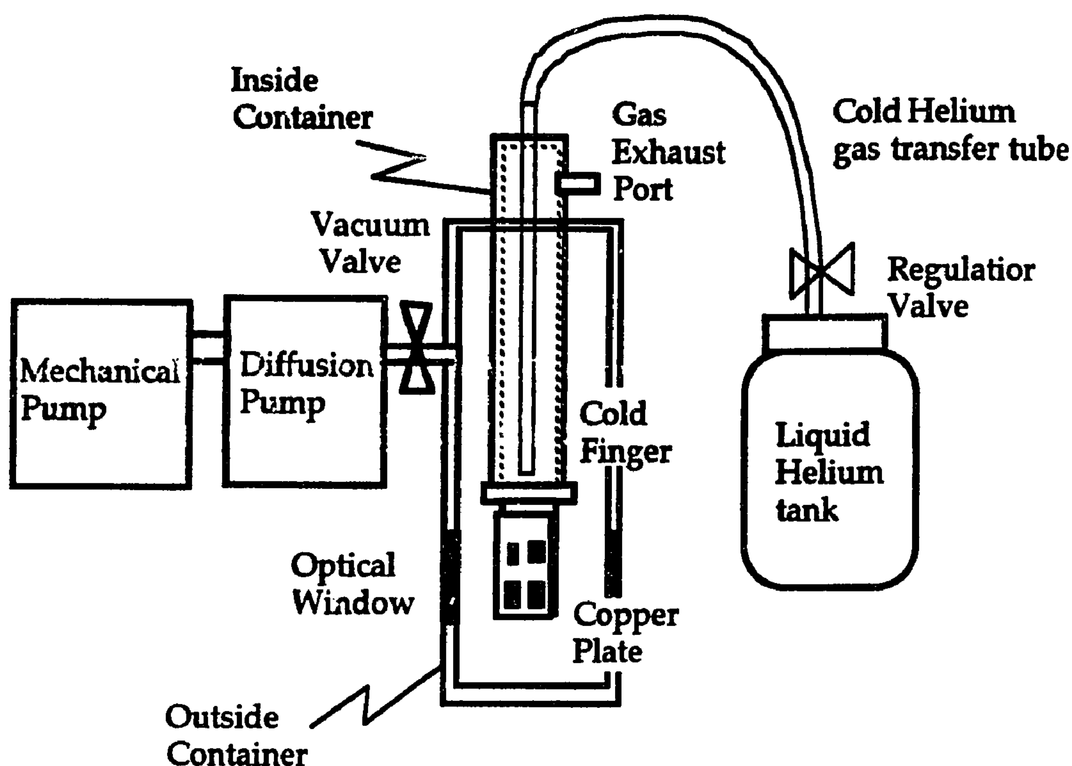

Fig. 4.1.4 Schematic diagram of optical cryostat, diffusion pump and liquid Helium tank.

4.1.3. Optical dewar

A stainless steel dewar from Janis Research Corp. (model #ST-4) was used in this research. Its structure is schematically depicted in Fig.4.1.4. The dewar consists of an outside stainless container with four quartz windows and of an inside stainless container attached to a cold finger. The sample house between the two containers is evacuated to maintain low sample temperature and to avoid water condensation and freezing of the samples. To avoid heating due to the infrared light goes into the sample region, an aluminum cylinder covers the sample and the cold finger. The inner surface of the cold finger which directly connected to the inside container is cooled by cold Helium gas transferred from liquid Helium reservoir tank placed outside the

dewar. Note that this dewar uses the cold helium gas not liquid Helium to cool the sample. Since the sample to be investigated is attached to the cold finger, the sample temperature can be cooled down quickly. To install samples, the inside container is removed from the outside container. The samples pasted on a copper plate is attached to the cold finger directly. One or multiple semiconductor samples cut into 5 mm x 5 mm pieces can be pasted by a glue on the copper plate. Then, the inside container is placed back into the outside container. The sample region is evacuated to 10^{-1} torr with a mechanical vacuum pump and then to 10^{-5} torr with a diffusion pump. It takes about 30 minutes to reach 10^{-6} torr from the atmosphere pressure. Once the vacuum reach 10^{-6} torr and the vacuum valve on the dewar is closed, the cold Helium gas is transferred to the dewar through the gas transfer tube inserted into the Helium reservoir tank. The "cryopump effect" lowers the vacuum to better than 10^{-7} torr. It takes about 5 minutes for the dewar to be ready to be cooled. When it is ready, it comes a booming sound from the gas exhaust port then the sample temperature starts going down. The sample temperature reaches to 4 °K within 20 minutes after the sound. Once the sample temperature shows 4 °K, one can close a valve on the transfer tube to regulate the a mount of Helium gas flow so that one can use 30 litters of liquid Helium in the reservoir tank for two to three days.

4.1.4. Temperature controller

A cryostat (LakeShore Cryotronics #805) temperature controller connected to the dewar is a key device to maintain sample temperature and can change the sample temperature from room temperature to near liquid Helium temperature. A built-in heater (high resistant wire) rounded

around the cold finger can raise the temperature by supplying electric current through it and heat it up. Using a semiconductor temperature sensor (Si diode sensor DT-470) and the current feedback circuit built-in the controller, the temperature at the sensor position, thus the sample temperature, can be maintained within 0.1 °K accuracy. It takes longer time to warm up the sample even ten degree with the built-in heater. During the warm-up, the sample temperature may be lower than the sensor temperature because the cold finger has certain heat capacitance which delays the warming up of the sample. After the controller indicates the desired temperature on the sample, it may take 5 more minutes for the sample to reach the temperature.

4.1.5. Glue

It may be worth write to discuss the glue used to paste samples onto the copper plate for the dewar. The glue must be a special glue that works at liquid helium temperature and is a non-fluorescent material. If the glue fluoresce around visible to near infrared, it affects the measurement and data analysis. One needs to be careful to select the glue for this purpose. In this research, GE 7031 adhesive & insulating varnish from Insulating Materials Department at St. Schenectady, N.Y. was used.

4. 2. Picosecond Time-resolved PL spectroscopy

In this section, I will discuss in detail the experimental setup for picosecond time-resolved PL spectroscopy. An experimental diagram is shown in Fig. 4.2.1. It consists of the CPM laser, a narrow band pass filter , neutral density filters, a laser beam focusing lens, an optical dewar and cryostat, a pair of PL collection lenses, a color filter, a spectrograph, and a

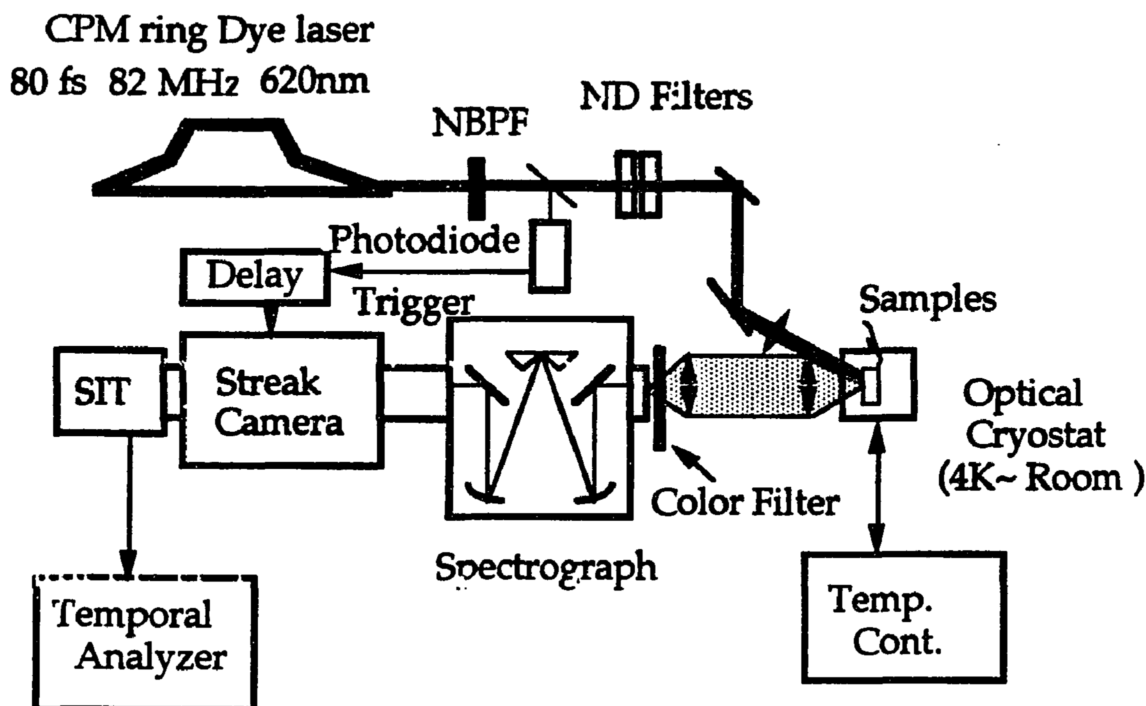

Fig.4.2.1 Time-resolved photoluminescence spectroscopy setup

streak camera system[2-7] with an electronic triggering photodiode and an electronic delay circuit. It is important to note that the difference in the setup between the steady state and the dynamic PL spectroscopies involves the lasers and the detectors. The steady state uses the CW lasers and the PMT with the lock'-in amplifier connected to the IBM-PC. The dynamic measurement uses an ultrafast CPM pulse laser system and a high speed temporal detector : a streak camera. It is quite easy to re-configure the experimental setup from the steady state to the dynamic measurement by removing an output slit of the spectrometer and replacing the PMT with the streak camera.

Laser pulses from the CPM laser photogenerates carriers in a semiconductor sample placed in the optical dewar. To eliminate contamination of amplified stimulated emission (ASE) from the CPM laser and

an optical amplifier, a narrow bandpass filter (NBPF) is inserted when an experiment is carrier out at around 670 nm where the ASE covers. The photoexcitation power is controlled by the neutral density filters to investigate carrier density effects on the carrier and exciton dynamics. The photoexcited carriers in a semiconductor sample recombine and emit PL after the short pulse optical perturbation. The PL from the sample is collected into the spectrometer (operates as a spectrograph) and is dispersed onto an input slit of the streak camera. To avoid artifact "Ghost" signal arising from the scattered light of the fundamental laser beam in the spectrograph, a color filter (#7-59) is set in front of the spectrograph to eliminate the CPM laser beam component and transmits near IR PL components. One has to be careful to select the color filter not to distort the PL spectrum.

A part of the laser pulse is fed into a photodiode to generate electronic trigger pulse for the streak camera to be synchronized with the laser pulses. The streak camera resolves time information of the PL spectrum giving three dimensional information; ie. time-wavelength-intensity of the PL. The carrier and exciton dynamics are investigated from the PL kinetics with 10 ps time resolution which is a typical time resolution of the synchroscan streak camera. The lattice temperature of the samples placed in the optical cryostat is controlled from liquid Helium temperature to room temperature to investigate temperature sensitive scattering mechanism in which phonon involved in the transition.

Following sections describe each experimental components in detail.

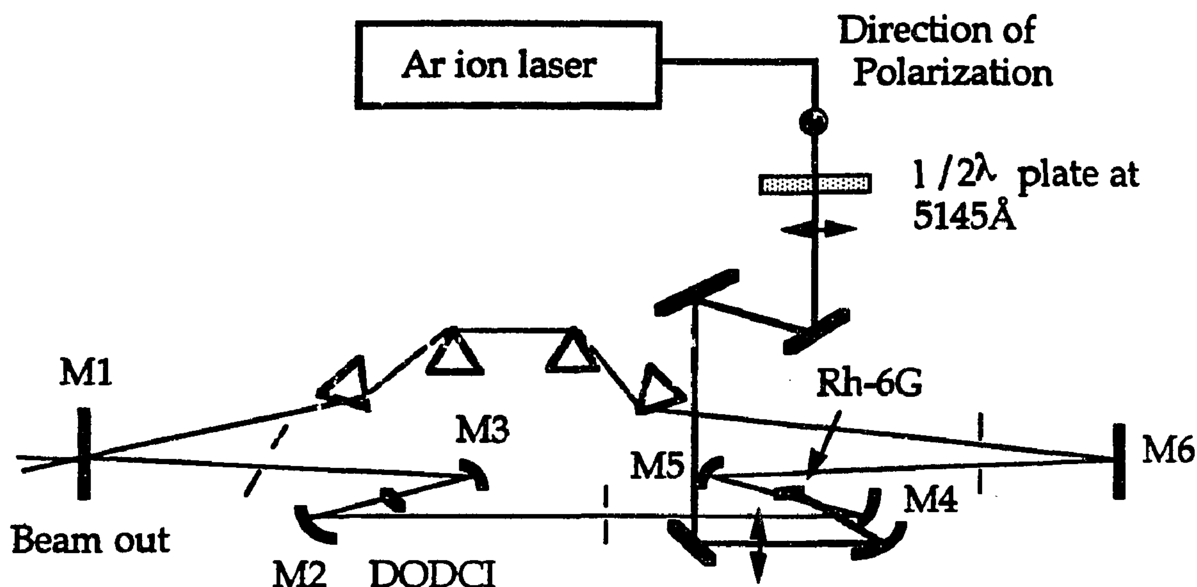

Fig.4.2.2. Colliding pulse mode-locked ring dye laser configuration

4.2.1 Ultrashort laser system

For an untrashort laser to photoexcite carriers in semiconductor samples, the pulse duration and laser intensity stability are very important parameters to obtain good results in the time-resolved PL spectra.

The configuration of the colliding pulse mode-locked (CPM) laser[7)] is shown in Fig. 4.2.2. The laser generates 80 fs pulses at a repetition rate of 82MHz. The central wavelength of the laser is 625 nm corresponding to 2.0 eV photon energy which is enough to excite the valence electrons into the conduction band in GaAs structured materials. The pulse duration is shorter than the time resolution of the streak camera and is shorter than the carrier interaction time with other carriers and lattice.

A gain medium, Rhodamine 6G dissolved in ethylene glycol (CH_2OHCH_2OH) solvent flowed as a jet stream, is photoexcited(pumped) by a polarization matched Argon ion laser beam with an average power of 3 W at 514.5 nm. The fluorescence from the gain dye is confined in a six mirror

cavity (M1 to M6) to lase. Two additional components are inserted in the cavity to mode-lock and to shorten the laser pulse duration.

First key component is a saturable absorbing dye jet which acts as ultrafast shutter. The dye is DODCI (,3'-Diethyloxadicarbocyaine lodide) dissolved in ethylene glycol and has non-linear absorption characteristics. The DODCI absorbs lasing photons until it saturates. Therefore, a high density photons can pass through the DODCI and weak photon such as background ASE (amplified stimulated emission) is absorbed. The non-linear absorption acts as an ultrafast shutter and shortens the pulse duration because the photons around the envelope of the pulse is absorbed. The shortened pulse will be amplified by the gain dye during second round trip in the cavity. Then, the pulse shortening will take place for the amplified pulse, again by the DODCI saturable absorber. The gain saturation shortens the tail of the pulses. After hundreds of round trips, the pulse duration becomes shorter than 100 femtosecond. The arrangement of the gain dye and the saturable absorber dye is determined to achieve stable amplification and absorption. The distance between the dye jets are set to be one fourth of the laser cavity length so that each pulse traveling counter directions in the cavity will be amplified at same gain and meet exactly at the saturable absorber jet to enhance the non-linear absorption effectively.

Next important additional component is a four prism pairs inserted in the cavity. Since the optical components such as mirrors, dye jets and air in the cavity are positive dispersion materials which broaden the pulse in time arising from group velocity dispersion and widen the spectrum due to non-linear Kerr effect in the dye jet where the photon density is high enough to

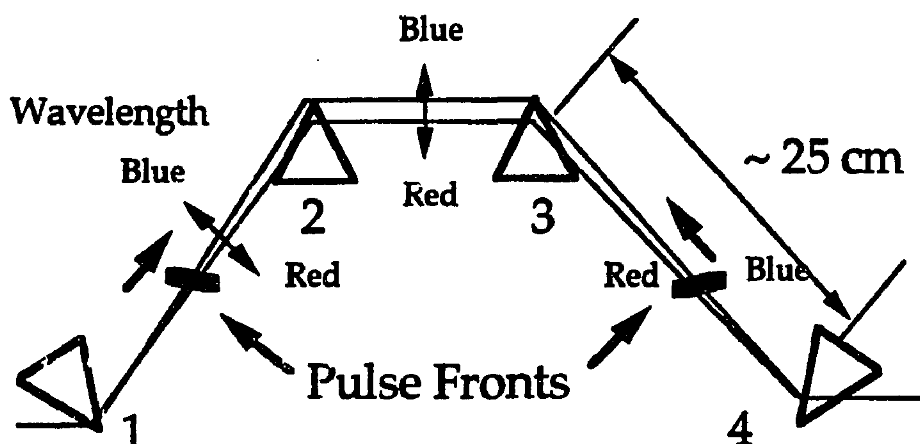

Fig. 4.2.3. Four prism configuration to create negative dispersion property.

cause non-linear optical effect. Since the dye solutions have small Kerr non-linearity in their refractive index, the laser pulses in the cavity are positively chirped. The linear dispersion effects arising from the group velocity dispersion occurs in optics such as glass plates, non-linear crystal plates, prism, and lenses are described in Appendix A.1 in detail. When the red component of light travels at leading edge of the pulse, the pulse is called positively chirped or up-chirped (because the frequency increases in time). A pulse with the blue component traveling at leading edge is called negatively chirped or down-chirped. When the positive chirp in the cavity is compensated by inserting a negative dispersion material in the cavity, the laser pulse can be compressed to be Fourier transform limited and be shortest for the band width of the laser cavity. Four prism pairs made of SF11 high refractive index glass acts as such negative dispersion element.

The four prism configuration is shown in Fig. 4.2.3. The amount of negative dispersion is mainly determined by separations between the prism #1 and #2 and between the prism #3 and #4. As discussed in Appendix A.1, the pulse fronts of the counter propagating pulses in the cavity are tilted after

the prism #1 and #4 because of the group velocity difference between the air and the prism glass. The spectrum of the pulse spreads along the spatial direction parallel to the optical table. The tilted and spectrally spread pulses enter the prism #2 or #3, respectively. Since the prisms #2 and #3 delay the red components of the laser pulse more than the blue part of the laser, the prism pairs #3 and #4 causes the negative dispersion and can compensate the positive dispersion of the laser pulses in the cavity. By tuning the position of the prism pairs, the CPM laser can generate pulses as short as 27 fs.[9] Using smaller refractive index prisms, one may compensate third order chirping components[10] and obtain an ultrashort pulse as short as 17 fs in a Ti:sapphire laser.

Since the CPM laser operates at a balanced wavelength determined by pumping power of Argon ion laser, gain of Rhodamine 6G, saturable absorption of the DODCI, mirror reflection, and prism configuration, the CPM laser does not allow wavelength tunability and can not be used for a resonant photoexcitation experiment.

4.2.2. Pulse duration measurement using an optical autocorrelator

A femtosecond optical autocorrelator is used to evaluate the pulse duration of the CPM laser pulses. The diagram of the dispersion free autocorrelator is depicted in Fig.4.2.4. The incident beam is split into two parts with a thin Pelicle beam splitter. The two beams travel different optical arms, reflected by the corner mirrors and focused onto a 100μm thick KDP crystal mounted on a quartz glass plate (shown in the inset of Fig.4.2.4) by a concave mirror. The radius of curvature of the concave mirror is 10 cm and the focal point becomes 5 cm. The generated SHG signal is reflected by a small piece of

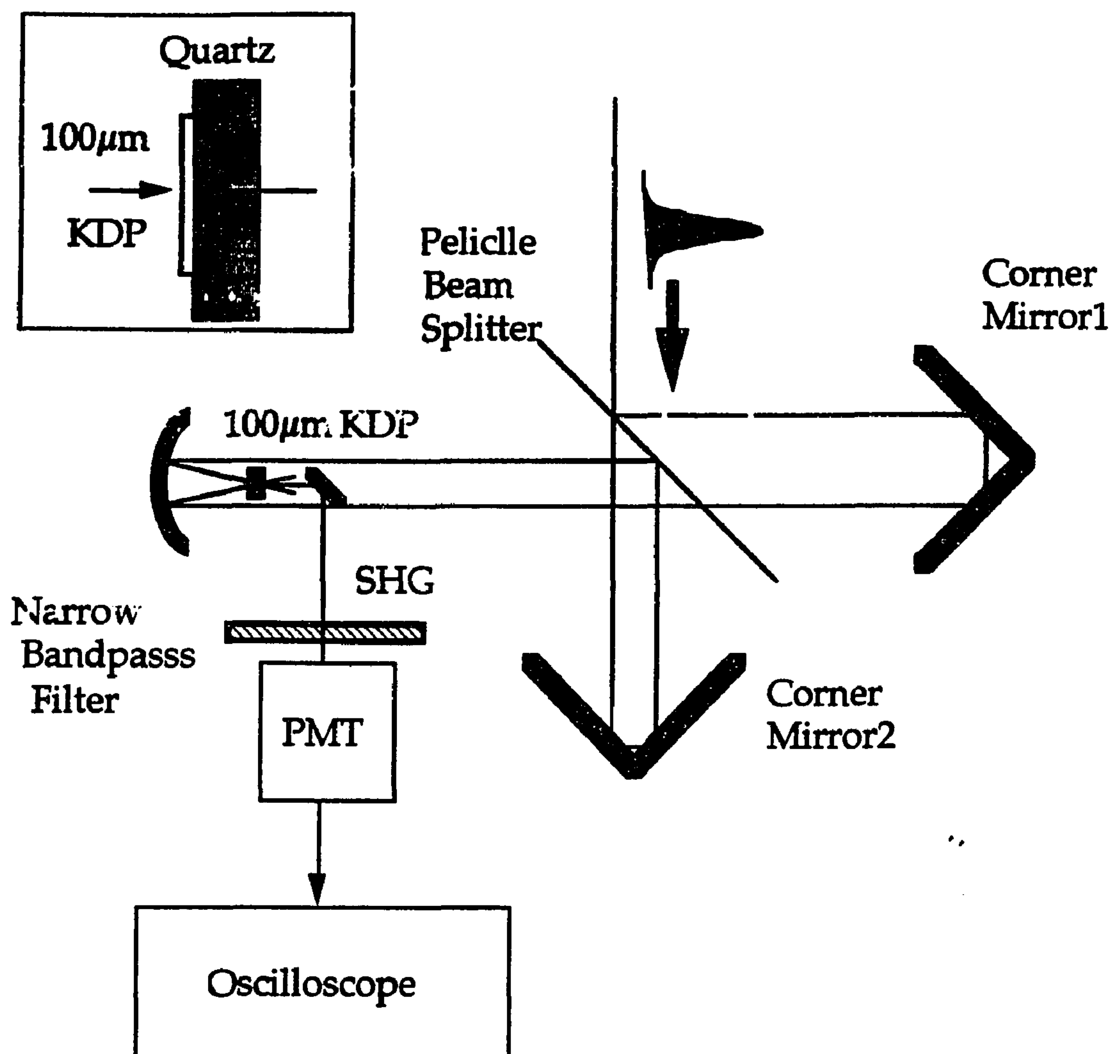

Fig. 4.2.4 Optical dispersion free autocorrelator configuration and a 100μm KDP crystal mounted (inset) on a quartz glass plate.

mirror toward a PMT through a SHG transmission narrow band pass filter. By varying one optical arm length with an electric shaker having μm accuracy, the autocorrelation function of incident laser pulse is generated as the intensity profile of the SHG signal as function of the arm length(which corresponds to delay time between two pulses overlapped on the KDP crystal). A 1.5μm arm length change corresponds to 10 fs delay time of the autocorrelation function. The output electronic signal from the PMT is lead

into an oscilloscope to obtain the SHG intensity profiles as function of time. In this case, the time is determined by the speed of vibration of the shaker and the amount of the arm length change. After the SHG intensity trace is obtained on the scope, one can determine the pulse duration by assuming a pulse intensity shape as a square of sech. The measured duration at full width at half maximum (FWHM) of the trace is divided by 1.55 (this value is determined from autocorrelation function of sec^2h) to obtain the pulse duration of the laser pulse. The typical pulse duration of the laser was 80 to 100 fs.

To determine the autocorrelation trace shape, the following calculation procedure is carried out. For a simple Gaussian pulse case, the electric field of the collinearly superposed laser beams on the KDP crystal is expressed as

$$E(t,\tau)_{tot} = E(t) + E(t+\tau) \quad . \tag{4.2.1}$$

The SHG intensity is given by

$$I(t,\tau)_{SHG} = E(t,\tau)_{tot} \bullet E(t,\tau)_{tot} \times (E(t,\tau)_{tot} \bullet E(t,\tau)_{tot})^*$$

$$= | I(t,\tau)_{tot} |^2 \quad . \tag{4.2.2}$$

The time integrated intensity $I(\tau)$ of the SHG on the scope can be obtained by integrating Eq.4.2.2. with respect to time t as,

$$I(\tau)_{SHG} = \int_{-\infty}^{+\infty} I(t,\tau)_{SHG} \, dt \quad . \tag{4.2.3}$$

The autocorrelation function as function of the delay time τ is given by,

$$I(\tau)_{SHG} = E_0^2 \sqrt{\pi}/2t_0 \; [\, 1 + 2\exp\{-(\tau/t_0)^2\}$$
$$+ 4\exp\{-\{A^2+3(\tau/t_0)^2\}/4\}\cos\{A(\tau/t0)^2/2\,\}\cos\omega\tau$$
$$+ \exp\{-(1+A^2)(\tau/t_0)^2\}\cos 2\omega\tau] \,. \qquad (4.2.4)$$

The first term 1 in the right hand side parenthesis is non-correlated term, the second term is the intensity correlation term, and the last two terms are coherent fringe terms.

By using slow detector or non-collinear configuration of autocorrelator, intensity autocorrelation function can be obtain by ignoring the coherent fringe terms from Eq. 4.2.4 and its shape is schematically shown in Fig. 4.2.5.

The intensity correlation curve is give by,

$$I(\tau)_{SHG} = E_0 2\sqrt{\pi} t_0/2[\, 1 + 2\exp\{-(\tau/t_0)2\}] \qquad (4.2.5)$$

From this equation, the delay time at half intensity of the peak SHG signal for the intensity correlated portion is expressed as,

$$t_0(FWHM)_{AC} = 2\,\text{lin}\,2\;\; t_0$$
$$= 1.38629\, t_0 \qquad (4.2.6)$$

using the incident pulse duration t_0. Therefore, one can determine the incident pulse duration with the measured SHG signal width $t_0(FWHM)_{AC}$.

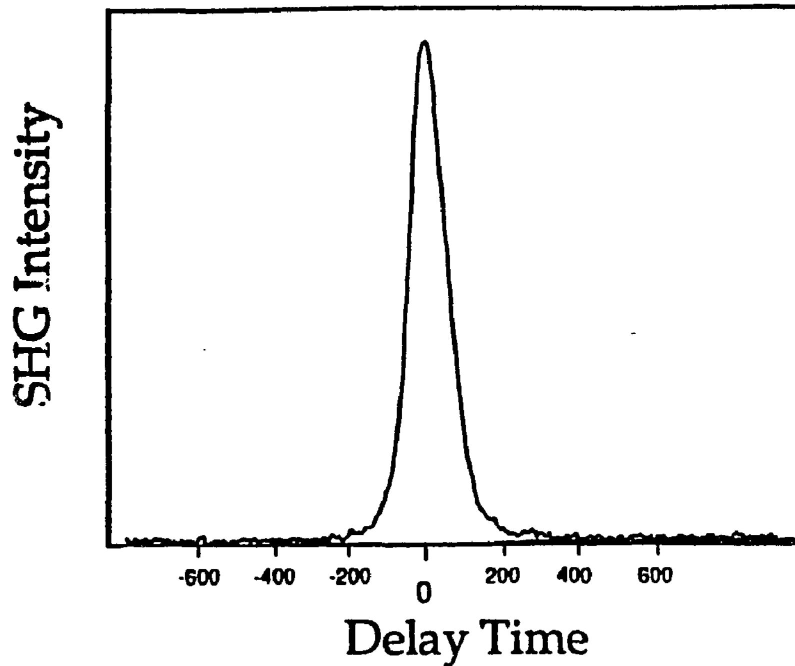

Fig. 4.2.5 Autocorrelation trace of femtosecond pulse obtained using a non-collinear autocorrelator.

Since the pulse duration and the spectrum bandwidth is related by the uncertainty principle (or Fourier transformation), one may use a spectrum analyzer to evaluate the spectral bandwidth of the laser at the same time as the auto-correlation is measured. The spectrum analyzer consists from a spectrograph which disperse the laser spectrum onto a Si photodiode array and electronic signal analyzer connected to the diode array (Hamamatsu Photonic Microchannel Analyzer: PMA). By tuning the position of four prisms in the laser cavity, one can see dramatic change in the spectrum and autocorrelation shape. At the optimum position achieving a shortest pulse duration, the spectrum analyzer shows a widest spectrum while the scope shows a narrowest SHG intensity trace at the same time.

4.2.3. Streak camera system

A streak camera system consists from a camera body, a SIT image pick-up camera, an image processing computer (temporal analyzer, TA) which digitizes and stores streak images (time-resolved PL spectra) into a memory to be analyzed. The schematic diagram with other peripherals are displayed in Fig. 4.2.6.

The streak camera body incorporates a streak tube which is a vacuum tube consisting of a photocathode, an acceleration mesh electrode, an electrostatic focus electrode, an anode aperture, a pair of deflection plates, a microchannel plate (MCP), and a phosphor screen as depicted in Fig.4.2.7. The photocathode instantly converts incident photons into photoelectrons through photoemission. The photoemission time has not been evaluated yet. However, it is believed that the time is in few tens of fs. The conversion efficiency is called as "quantum Efficiency(QE)" and is defined as a ratio between number of photoelectrons emitted and number of incident photons onto the photocathode. For a S-20 type photocathode, a typical photocathode quantum efficiency at 600 nm is about 20% which means that 1 photoelectron in average will be emitted when 5 photons at 600 nm illuminate the photocathode. Since the mesh electrode and the MCP have finite opening area of about 60% each, number of the photoelectron passing through the mesh and MCP decreases to be 36% of the incident photoelectrons. As the result, the total detectability at 600 nm is about 7% of incident photons.

The primary photoelectron has a kinetic energy of about 0.3 eV determined by the difference between the photon energy and the work function of the photocathode. The photoelectrons are accelerated toward the pair of deflection plates by the potential of about 10 kV applied between the

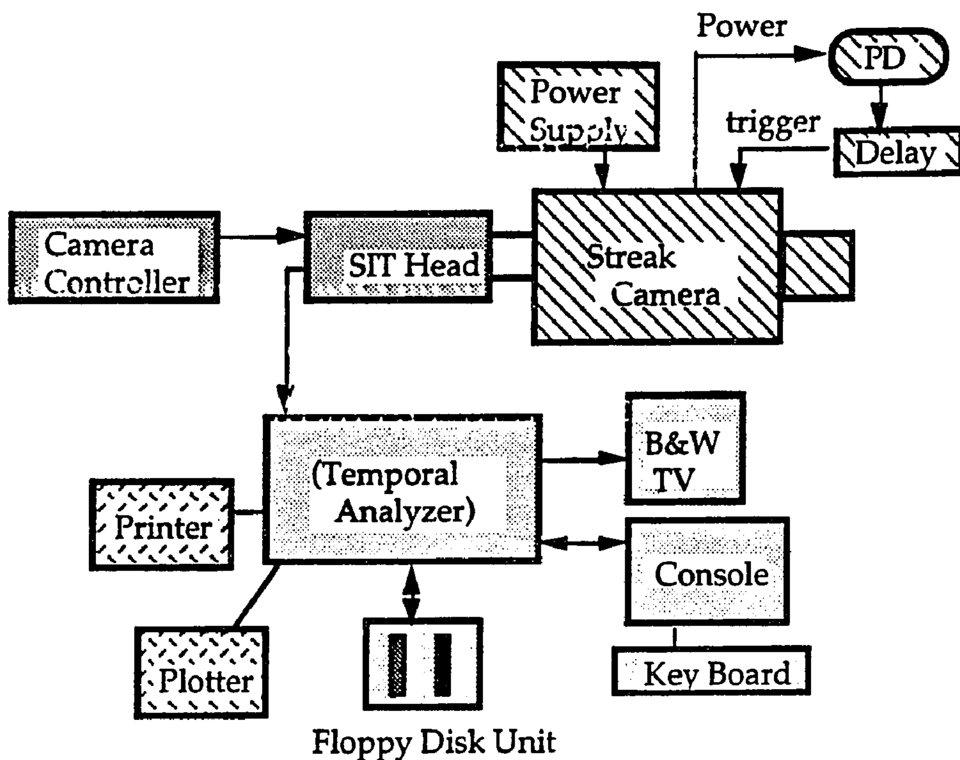

Fig. 4.2.6 Streak camera system block diagram

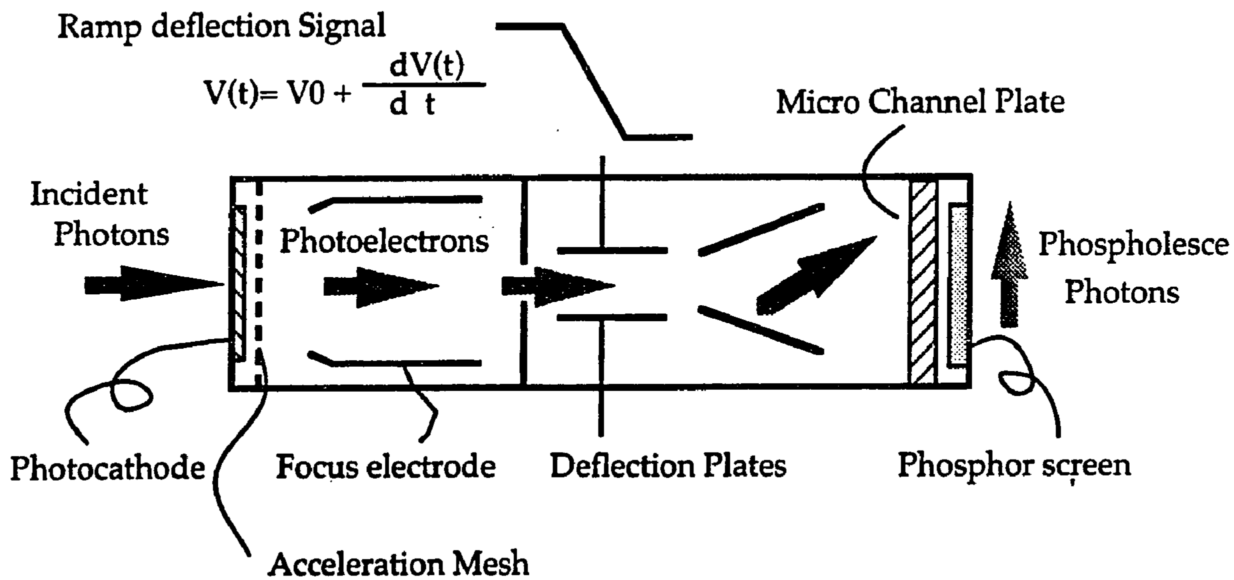

Fig.4.2.7 Streak tube structure

photocathode and the anode aperture electrode. The accelerated photoelectrons are focused onto a surface of the MCP by the electrostatic lens field created by the combination of the mesh, the focus electrode and the anode aperture at a focus mode of streak camera (no-deflection). The voltage applied to the focusing electrode is adjusted so that an image on the photocathode is projected onto the MCP. The MCP is a heavy glass plate with a lot of tiny through holes (microchannels) from its input to output surfaces. The diameter of each channel is 25μm which limits the time and spatial resolutions of the streak camera. A photoelectron entered into a channel is multiplied by secondary electron emission at the inner surface of the glass material. Since a high voltage is applied across the MCP, the electrons are kept being multiplied until they reach the output surface. The multiplication gain is around 1000 to 5000 and is determined by the applied high voltage. When two MCPs are arranged in tandem and applied twice the high voltage, the multiplication gain can be larger than 10^5 which enables single photoelectron counting. The multiplied electrons are accelerated again and hit the phosphor screen of the streak tube and gives fluorescence image(Streak image).

For streak mode (dynamic operation), rapid ramp or sinusoidal voltage is applied to the pair of deflection plates synchronously with the incident photons. The photoelectron reached the deflection field later is deflected more than the photoelectrons coming earlier. The dynamic deflection converts the time information at the photocathode into the spatial information on the output phosphor screen.

The following sections discuss in detail the key parameters of the streak camera.

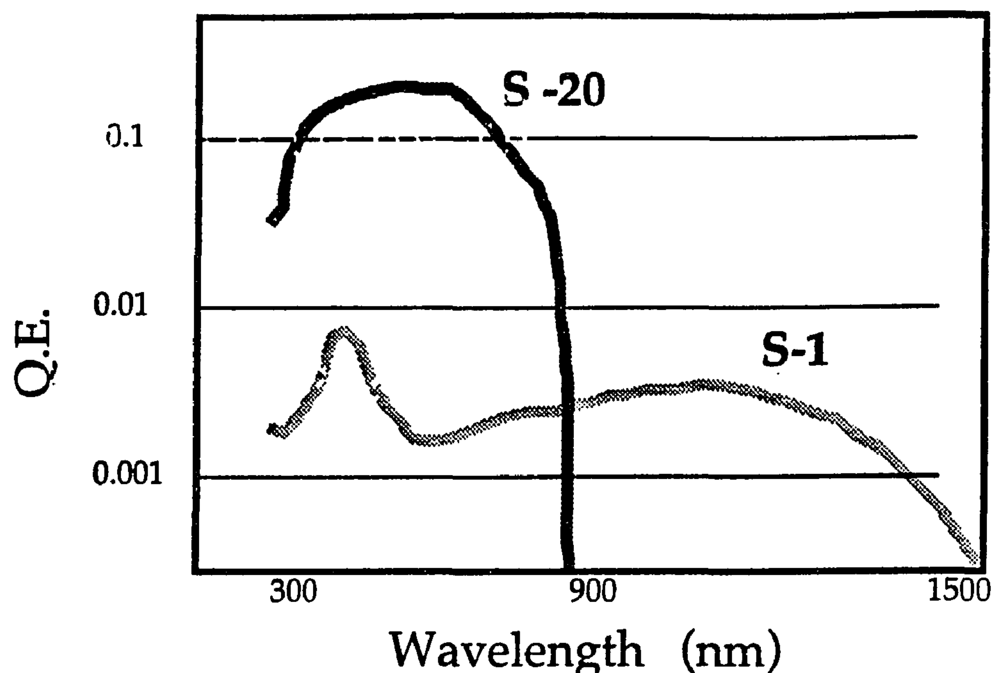

Fig. 4.2.8. Typical spectral sensitivity of S-20 and S-1 type photocathodes.

4.2.3.1. Spectral sensitivity

The spectral sensitivity is most important parameter to be specified. S-20, S-25, S-1 or other types of photocathodes can be incorporated in a streak tube. The photocathode can not be replaced The sensitive wavelength region were extended from X-ray[11] to far infrared[12]. Even 14 MeV fast neutrons generated by a laser fusion experiment were detected by a neutron streak camera with around 20 ps time resolution.[13] Once the photocathode type is selected, the quantum efficiency (QE) at different wavelength (given by a ratio between number of photoelectrons emitted and number of photons incident) and dark electron noise level are determined. Usually, S-1 photocathode emits more dark electrons because its work function is very low so that thermal electrons can escape from the photocathode with higher probability. Fig.4.2.8. shows the typical QE curves of S-20 and S-1 photocathodes used for Hamamatsu streak cameras. S-20 photocathode has sensitivity from 300 to 850 nm while S-1

photocathodes used for Hamamatsu streak cameras. S-20 photocathode has sensitivity from 300 to 850 nm while S-1 photocathode has sensitivity from 300 nm to 1.6 μm. In this research, both S-20 and S-1 type streak cameras were used.

4.2.3.2. Time resolution

Next important parameter is the time resolution. A synchroscan streak camera C1587 from Hamamatsu has four streak speed ranges. A fastest sweep range gives 8 to 10 ps time resolution and 600 ps time window on the output screen of the streak camera while the slowest sweep range gives about 30 ps time resolution and 1.8 ns time window. Since the synchroscan streak mode can accumulate the optical signal for a long time at a high repetition rate synchronized with the laser, it gives an excellent signal-to-noise ratio and the photoexcitation intensity can be weak as few tens μW. Therefore, high carrier density effects such as screening and carrier-carrier interaction can be neglected for the sample analysis under the weak photoexcitation.

A single shot streak camera plug-in for Hamamatsu C1587 gives 1.5 ps time resolution with 200 ps time window. For the single shot measurement, 360 fs time resolution was achieved experimentally.[3)] Since it is one shot measurement, the photoexcitation power becomes high to obtain reasonable PL signal from the sample to be investigated. For a case of semiconductor sample, such intense photoexcitation may introduce more complicated carrier density and hot phonon effects.

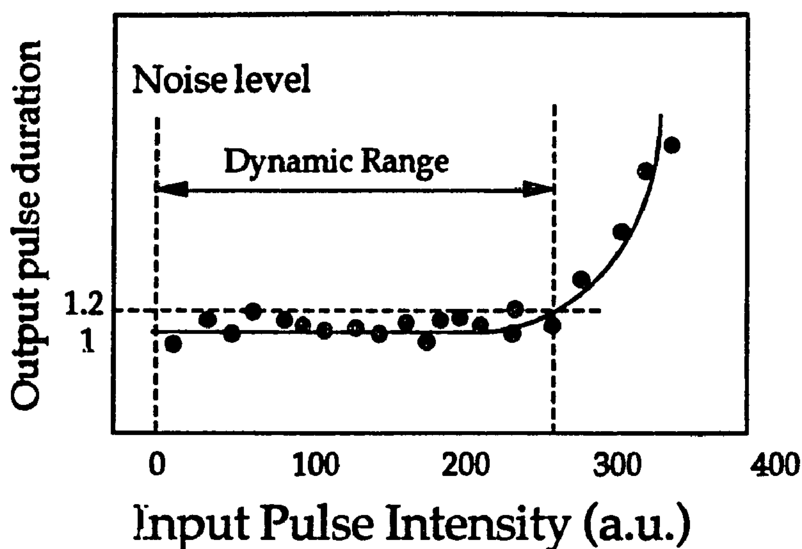

Fig. 4.2.9 Dynamic range of a streak camera defined as the range between the noise level to the incident intensity where the output pulse duration is appeared to be 20% wider.

4.2.3.3. Dynamic range

Another important factor to be taken into account is the dynamics range. When the peak power of the incident pulse increases, corresponding pulse width of the output time-resolved image becomes wider and degrades the time resolution. The time broadening arises from Coulomb electron-repulsion between the photoelectrons in the photocathode and during flight of the electrons in the streak tube. Therefore, it is safe to limit the incident light intensity within certain range. The range is called "dynamics range". The conventional dynamic range is determined from a weakest detectable signal intensity to an signal intensity which broaden the temporal profile 20% wider as shown in Fig.4.2.9. For the synchroscan streak camera, the dynamical range is very wide because the individual optical phenomena can

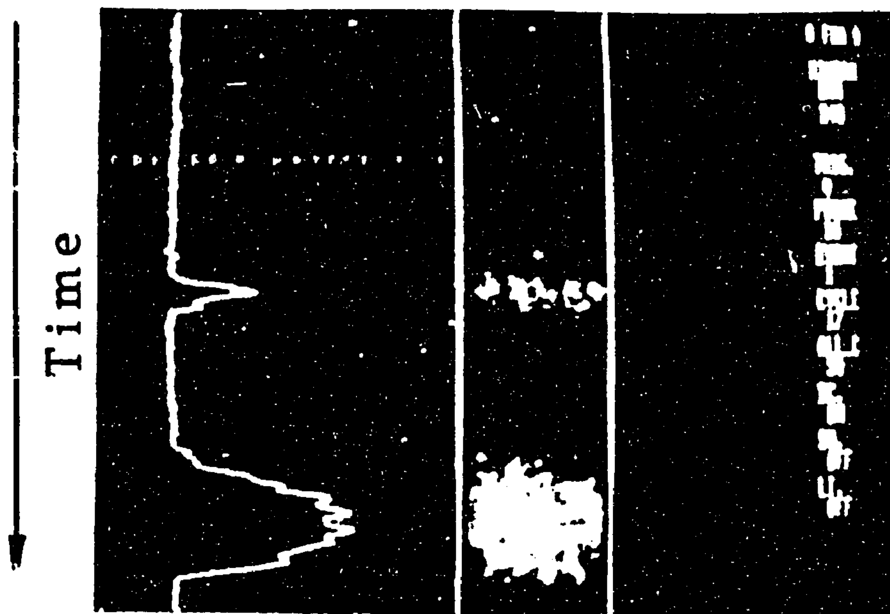

Fig.4.2.10 Time resolved pulse images within (pulse image obtained at early time) and out of the dynamic range (broadened pulse image at the later time) of a femtosecond streak camera(from Hamamatsu).

be very weak so that the electron repulsion will not take place. The lowest detectable signal level for the synchroscan streak camera is limited by the readout noise of the SIT camera. When a cooled CCD camera (which has very small noise level) is used to readout the streak image, the thermal electron noise from the photocathode (~ $2x10^{-10}$ electron/ps) limits the detectability. Thus, the dynamics range is more important characteristics for a single shot streak mode. A typical 2 ps single shot streak camera has dynamical range of 100. Fig.4.2.10 shows an example of un-broadened and broadened pulse images measured with a femtosecond streak camera. When the pulse intensity is out of the dynamic range, the pulse width becomes wide as shown at the later time of the streak time while the pulse within the dynamic range is shown to be narrow(early streak image).

4.2.3.4. Time spread in the streak camera

There are several parts of the streak camera which causes un-wanted time spread either optically or electronically. A total time spread is given by an equation as,

$$\tau_{total}^2 = \tau_1^2 + \tau_2^2 + \tau_3^2 + \tau_{jitter}^2 + \tau_{optics}^2, \qquad (4.2.7)$$

where each time spreading component is assumed to be Gaussian function, τ_1, τ_2, τ_3, are photoelectron dispersion term, time spread due to deflection electric field, and time spread due to finite slit width of the streak camera, respectively. The three parameters are determined by the streak tube structure and its operating voltage. τ_1 and τ_2 are within a picosecond and are negligible for a synchroscan streak camera. τ_3 depends on the slit width of the streak camera. τ_{jitter} arises from timing mismatch between the optical phenomena and the electrical pulse to trigger the streak camera. When the intensity of individual laser pulse fluctuates, the amplitude of electronic signal from the photodiode varies accordingly. Since the synchroscan streak camera amplifies the trigger signal from the photodiode directly to generate deflection signal applying to the deflection plates, the fluctuation causes a fluctuation on the deflection speed thus generates the jitter. τ_{optics} is the group velocity dispersion term occurs in the optical components of the streak camera.

Using the slit width of 30 μm, τ_3 is determined by the ultimate spatial resolution of the streak camera W (which is about 50 μm) and the sweep speed V of the streak camera, ie τ_3=W/V. The ultimate time spread τ_3 at fastest sweep speed of the synchroscan streak camera is around 6 ps.

The τ_{jitter} determines the time resolution of the measurement. To avoid the trigger jitter due to the mis-coupling between the laser and the photodiode, one requires adjustment of the photodiode position against the laser beam and the incident power of the laser into the photodiode. The laser beam is required to be incident perpendicular to the photodiode. The power required to achieve best trigger condition may be 1 to 3 mW. After setting the conditions, then fine position adjustment is the key to achieve best time resolution. For the synchroscan streak camera, one needs to set the streak speed to slowest first and obtain a streak image onto the TV monitor by optimizing the electric trigger delay. The pulse image duration on the monitor may be within 7 channel on the temporal analyzer. One rotates the photodiode to achieve 5 channel duration of the streak image. Then, one switches to the fastest sweep speed and repeats the same adjusting procedure until the pulse duration of the streak image at the fast sweep speed becomes within 10 channel(the best resolution achieved was 6.5 channel).

Optical time spread τ_{optics} occurs at the input optics of the streak camera and a window for the streak tube. Since the input optics is a complicate combination lens, the amount of glass for the optics is thick. Therefore, the femtosecond phenomena incident of the streak camera could be temporally spread by the wavelength dispersion characteristics (Group dispersion) of the input optics. The detailed measurement for the group time delay in the streak camera input optics was carrier out by Staerk at Max-Planck Institute using a tunable short pulse laser as shown in Fig. 4.2.11.[14) Fig. 4.2.12 shows a time profile of two pulses at 530 nm (second harmonics of Nd:YAG laser at 1.06 μm) and 320 nm (third harmonics of the 1.06 μm laser pulse). This figure displays the group delay effect caused by the input optics

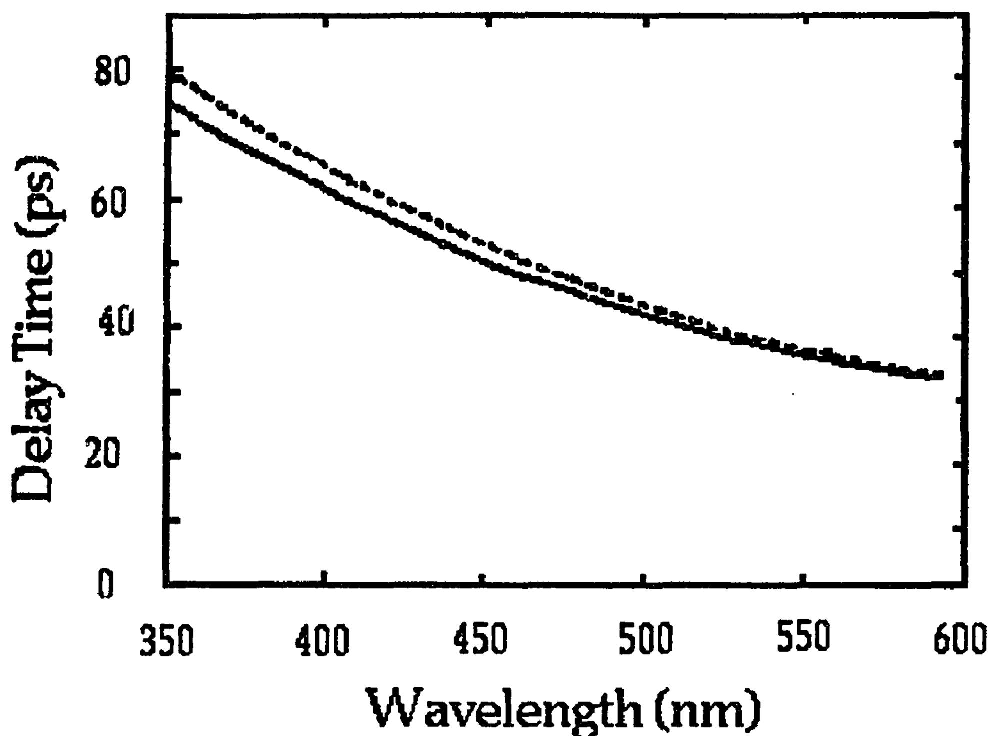

Fig.4.2.11. Optical pulse delay at different incident wavelength into input optics of streak camera measured by Staerk el al. at Max-Planck Institute.

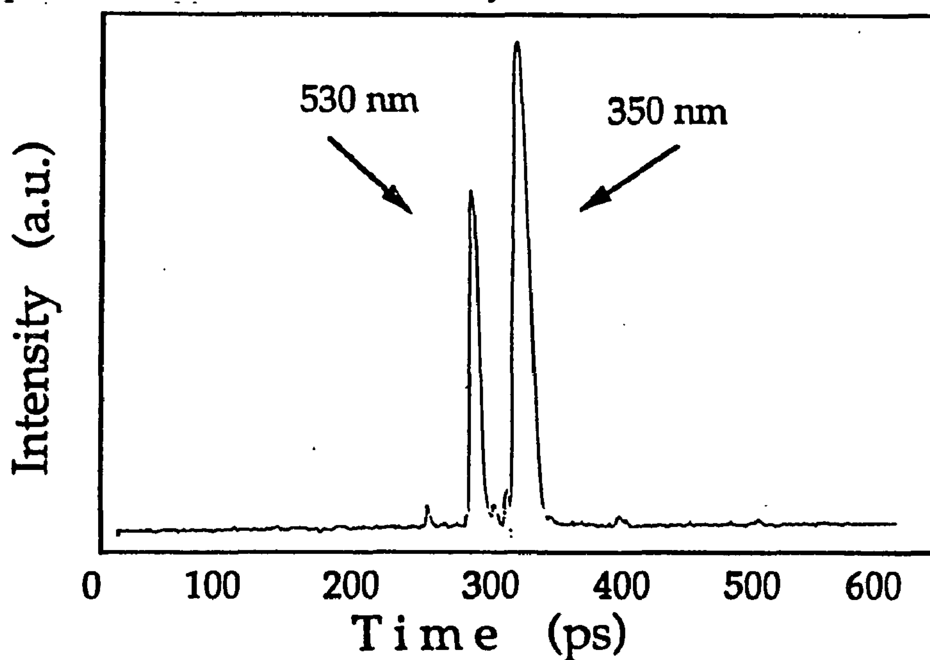

Fig.4.2.12. Group delay effect at 530 nm and 350 nm laser pulses, generated by taking second and third harmonics of a Nd:YAG laser, occured in an input optics of a 2 ps streak camera(Hamamatsu C1370).

of a streak camera.[15] Since the group refractive index at 530 nm is smaller than the value at 350 nm, the 530 nm laser pulse (strong light) arrived 40.2 ps earlier than the 350 nm pulse. This group delay was evaluated using a Nd:YAG laser and a 2ps streak camera(Hamamatsu C1370).

As seen in the figure, the blue light delays more than the red light as expected from the consideration in Appendix A1. Therefore, a careful time resolved measurement for blue ultrafast phenomena is required.

4.2.3.5. Streak trace overlap

When the streak camera is used at the synchroscan mode and measures a longer PL decay from a sample, the back trace of the synchroscan deflection can cause an overlap of the long decay tail on the initial sweep image resulting a requirement of complicated data analysis.

The regular synchroscan deflection uses a sinusoidal deflection along vertical direction synchronized with the incident laser pulses as shown in Fig.4.2.13. The deflection signal deflects the photoelectron downward first. After a half period of the laser repetition (it's 6 ns in the case of the CPM laser), the deflection returns upward and traces same location on the screen as the downward deflection trace. When the PL profile has longer decay than the half period of the laser repetition, the long PL tail on the upward deflection overlaps on the downward PL profile. As the result, the PL time profile is distorted by the overlap of the long PL decay tail. A circular scan operation solves this overlap problem. Two synchronized sinusoidal deflection signals are applied to both vertical and horizontal deflection plates incorporated in the streak tube so that the deflection trace shows either circle or ellipse depending on the streak speed and phase difference between the

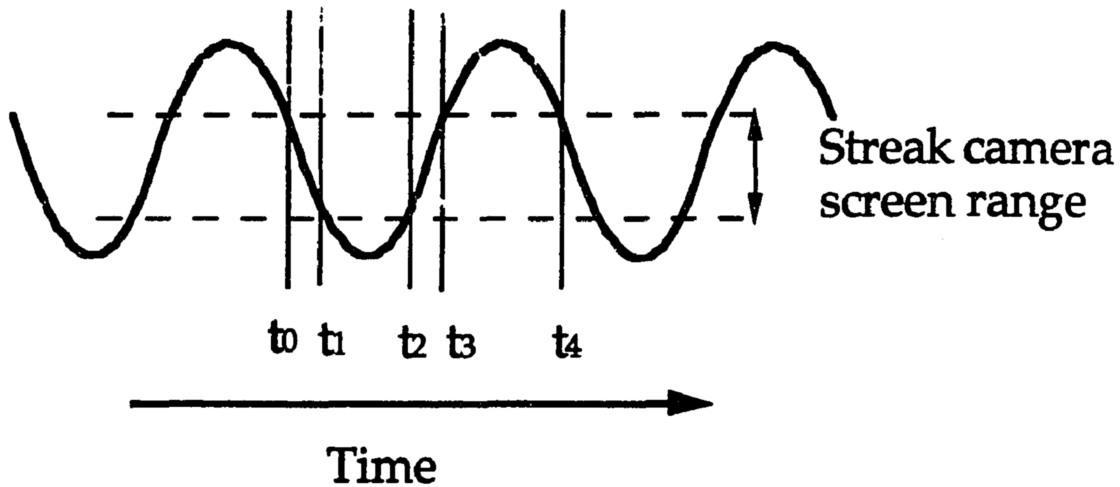

Fig.4.2.13. Synchroscan deflection signal and its linear region shown on the output screen of the streak camera.

vertical and the horizontal deflection signals as shown in Fig. 4.2.14. The circular scan operation shifts the long decaying PL upward trace to the outside of the streak image area so that the initial PL profile still remains original PL profile.

Fig.4.2.15. show the difference in the streak image profile incorporating a long decay component between that without circular operation(dashed line) and that with circular operation(solid line). To evaluate its overlap effect on the streak profile, a simple analysis was done as follows. Suppose an ideal profile was given by,

$$f(t)=\{2-\exp(-0.1t)-\exp(-0.03t)\}\bullet\{\exp(-0.0001t)+\exp(-0.03t)\} \qquad (4.2.8)$$

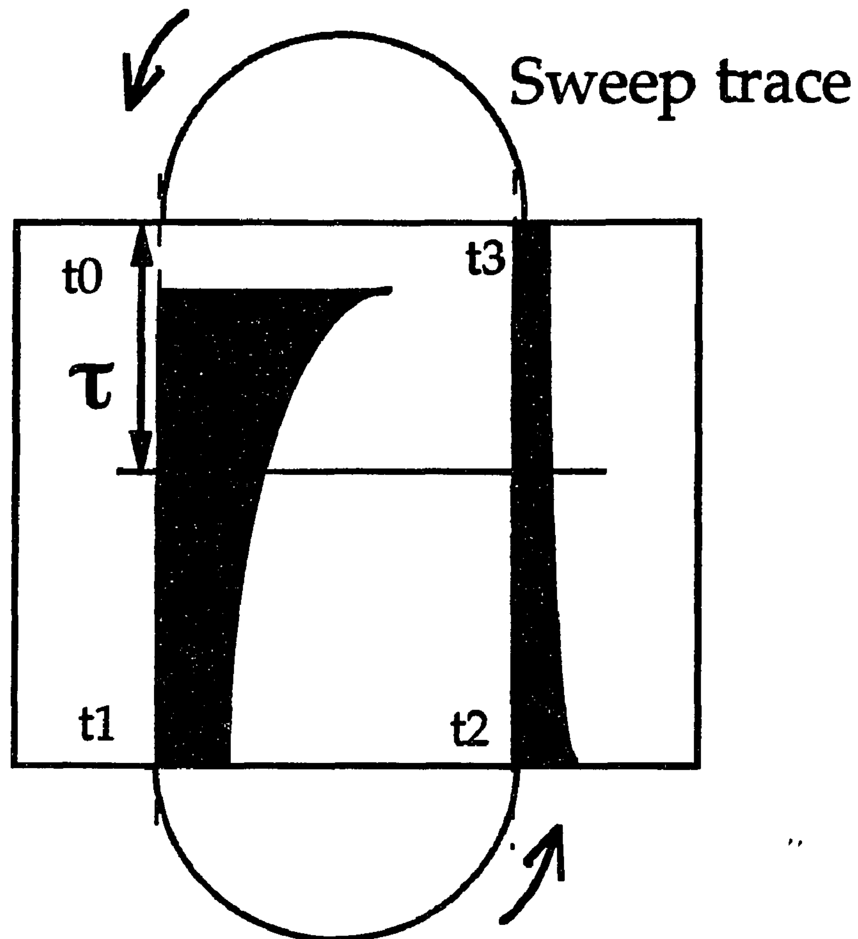

Fig. 4.2.14. Circular scan operation which enables to avoid overlap of long decay component from t_2 to t_3 on the initial sweep image during t_0 to t_1.

which contains 10 and 300 ps rising components and 300 ps and 10 ns decay components. The overlapped streak image at a delay time τ on the image is give by the summation of the intensities,

$$F(\tau) = f(t_0+\tau) + f(t_3-\tau) + f(t_4+\tau) + f(t_7-\tau) + \bullet\bullet\bullet\bullet\bullet \quad (4.2.9)$$

It is very hard to evaluate the original function f(t) from the overlapped streak profile $F(\tau)$ unless the function f(t) is well known function such as single

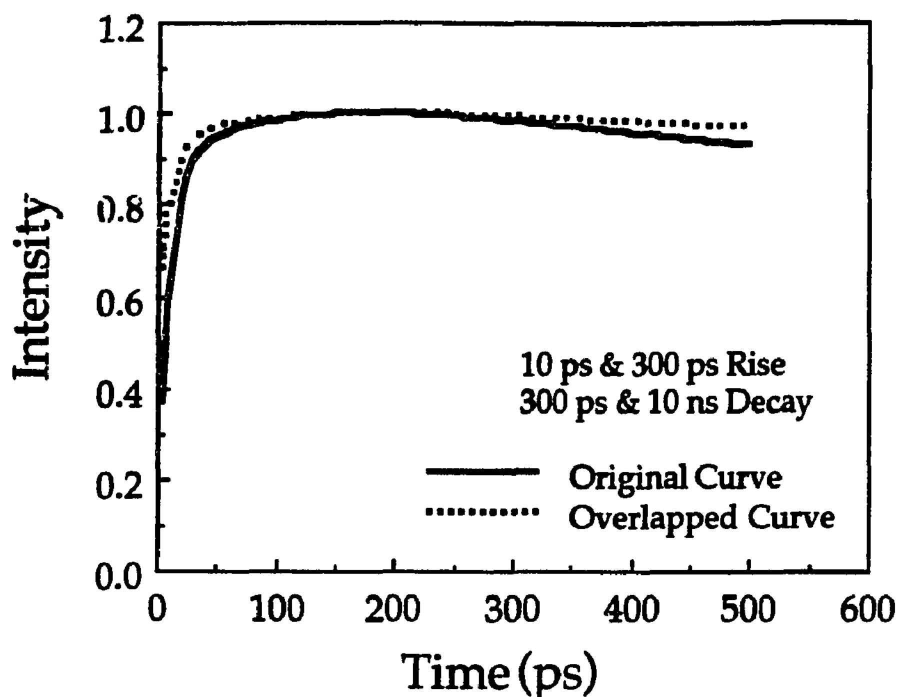

Fig. 4.2.15. Overlap effect of back trace of synchroscan streak mode when the PL decay time is as longer as 10 ns. Intensity profiles without circular scan(Dashed curve) and with circular scan(solid curve).

exponential decay curve. Therefore, when one expects to observe a long decay component from a sample, it is a key to use the circular scan operation.

Since the circular operation distorts the PL time axis because of the circular trace, there is a software to correct the temporal distortion. To correct the trace, one needs to take a continuous trace of CW light source. The software analyze the curvature of the trace and uses the obtained curvature to correct the streak image.

Using this circular scan and the software, one can measure long decaying PL profiles. However, if the decay time is longer than the period of

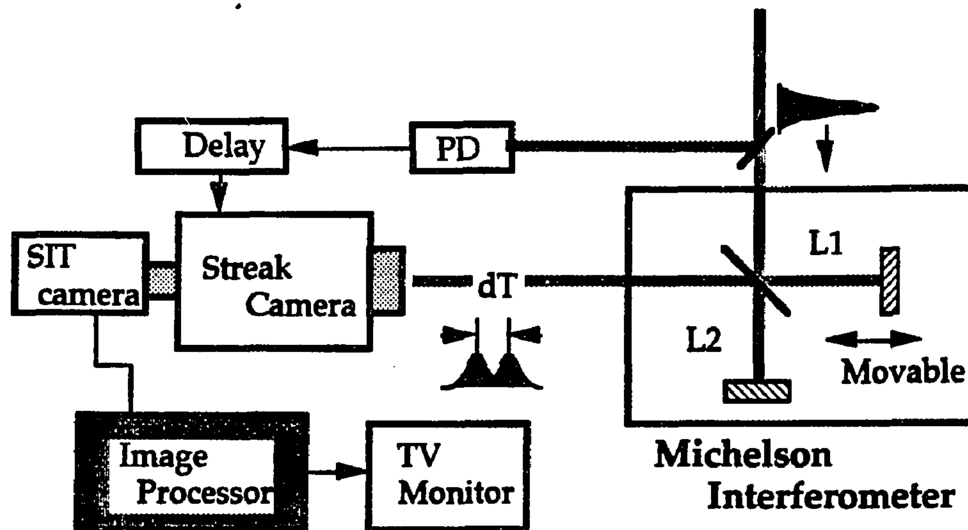

Fig. 4.2.16. Time axis calibration using a Michelson interferometer to obtain two pulses with well defined interval.

the laser repetition, it still hard to correct the overlap of the PL profile because of pile-up of the PL long tail.

4.2.3.6. Streak camera time axis calibration

A streak camera from Hamamatsu operates in either synchroscan or single shot mode by changing its plug-in unit. It is important to calibrate its time axis with short pulse trains of which separation is well defined with sub-picosecond time accuracy. A Michelson interferometer or an etalon can be used as the accurate train pulse generator.

A Michelson interferometer consists from one beam splitter and two plane mirrors as shown in Fig.4.2.16. An incident short pulse onto the beam splitter is split into two. The split beams travel each optical arm, and are reflected back to the beam incident direction. When the arm lengths are different with 1.5 mm, the traveling time of the two split beams within the arms is different with 10 ps. The two pulses obtained from the Michelson

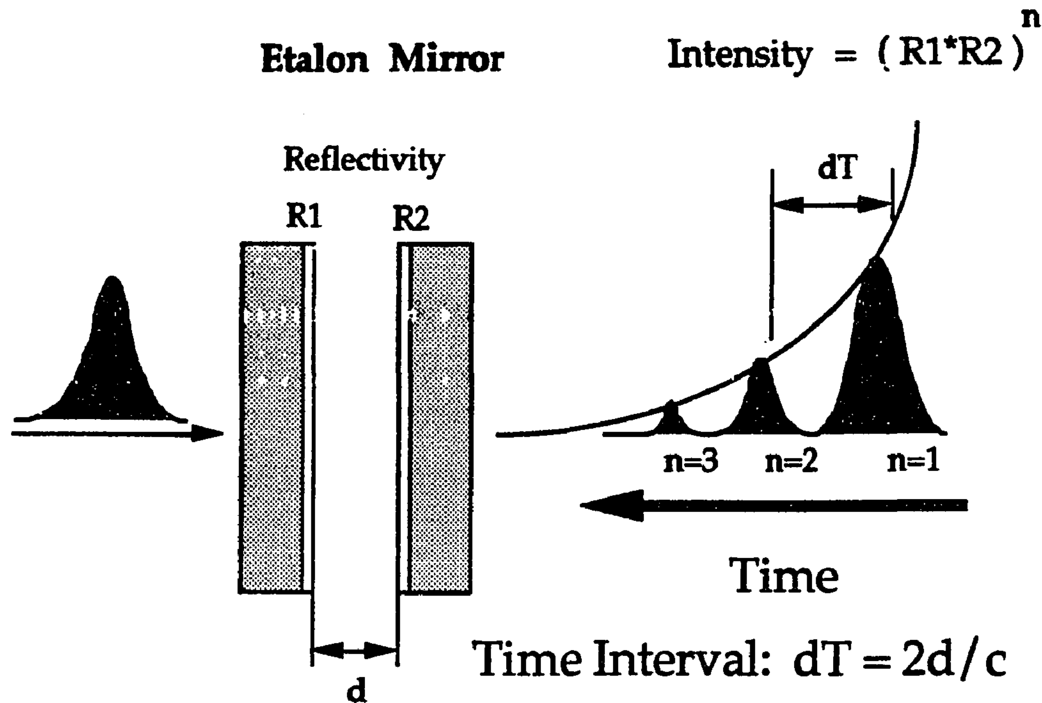

Fig. 4.2.17. Train pulse generation through etalon mirror.

interferometer can be well calibrated in time when an accurate translation stage is used for the displacement of one of the plane mirror.

The etalon consists of two mirrors facing parallel each other with a space d between them. The mirrors have reflections of R1 and R2, respectively. As a short pulse incident on the etalon as shown in Fig.4.2.17, some portion of the laser pulse transmits through the first input mirror and a part of it is reflected by the second mirror with reflection R2. The remaining part of the laser pulse through the second mirror gives a leading pulse of the train pulse (n=1). After the round trip in the etalon, a part of the reflected pulse from the second mirror toward the first mirror is reflected by the first mirror with reflection of R1. This process repeats until all photons escape from the etalon cavity. As the result, successive train pulses (n=1,2,3,——) are obtained through the second mirror. The interval between the successive

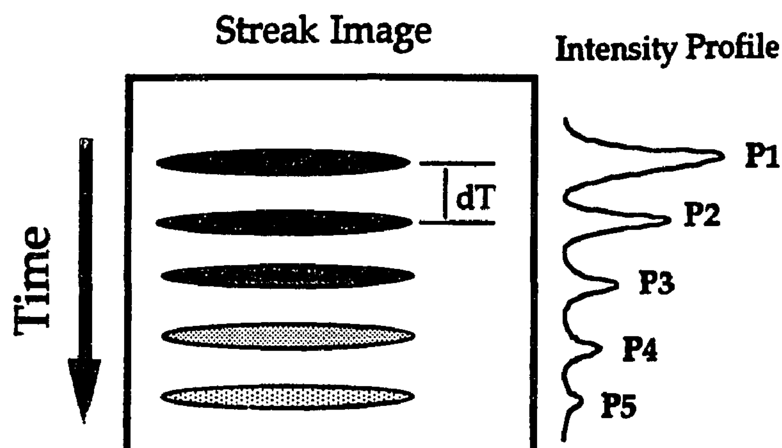

Fig. 4.2.18. Streak image and its intensity profile obtained for the train pulses from the etalon.

pulses are determined by the round trip time of the pulse in the etalon by $dT=2d/c$ where c is the velocity of light in the air. By changing the space between the mirrors accurately, pulse trains with a variable pulse interval can be obtained.

To calibrate the time axis of a streak camera using the train pulses from the etalon, the streak camera is synchronously triggered by the incidence pulse into the etalon and obtains an train pulse image on its output screen as schematically shown in Fig.4.2.18. First, one needs to measure the channel interval between the train pulse images p_1 and p_2, then the streak time (ps/ch) is calculated using the calibration time interval of the train pulses dT and the interval channel of the streak image of the train pulses p_2-p_1. The streak time obtained is given to the position at (p_1+p_2)/2 channel of the streak time axis. Repeat the procedure until peak position of the train pulse image (p_3, p_4, ---) can be hardly determined. Then, change the timing between the optical train pulses and the streak camera trigger by either optically or electrically. There is a delay box for the electric trigger signal to

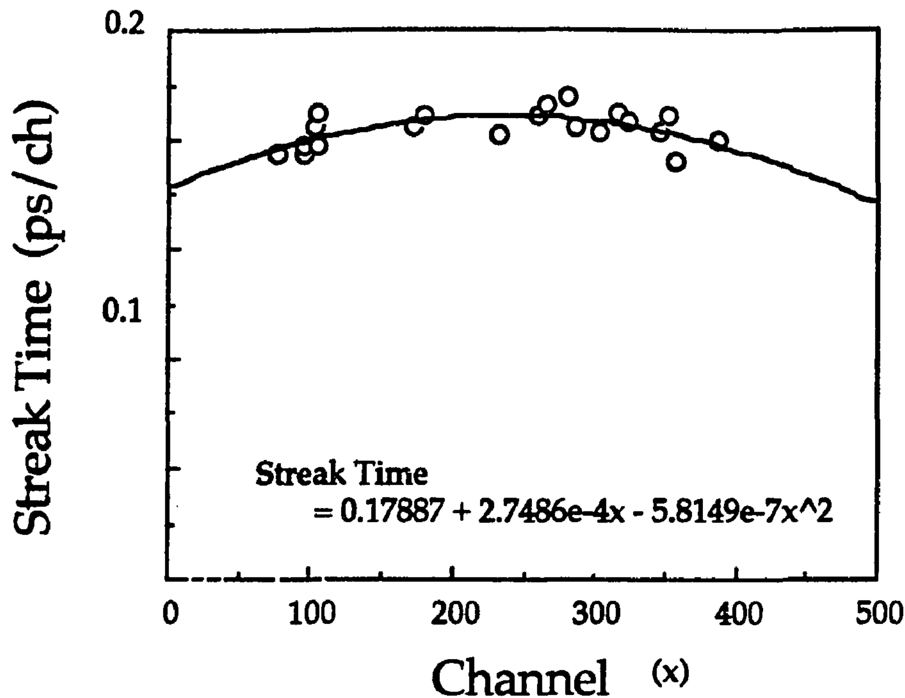

Fig.4.2.19. Time calibration curve obtained for a shynchroscan streak camera using a Michelson interferometer.

be delayed. One may increase the delay switch 250 ps. Then, obtain another shot of the train pulse image on the streak camera. Repeat the procedure at least 20 times so that entire screen of the streak camera output axis is filled with the calibration points.

Using a software "Criket graph" (a statistics program) on Macintosh computer, plot the streak time vs. the middle position of the train pulse images (p_1+p_2)/2. Use a second order polynomial to fit the streak time distribution of entire streak camera screen. The fit curve is the time calibration curve for the streak speed. If one needs another streak speed, repeat the whole sequence for the streak speed. Fig.4.2.19 shows an example of the streak time calibration curve measured for a synchroscan streak camera. The open circles are evaluated streak time and the solid curve is the

fit using a second order polynomial fit by a least square method. The equation of the second order fitting curve is given in the figure.

The time axis calibration is required when a new streak tube is installed, when a new SIT or CCD camera is attached to read out streak images, and when the laser repetition rate is changed by a laser re-alignment. When the laser repetition rate is changed, the streak camera is required to tune its RF amplifier to the resonance frequency to avoid non-linearity of the streak sweep speed. Turn the SWR and Power meter switch to SWR, and use insulated tuning screw driver to tune real(R) and imaginary(X) part of the amplifier to achive minimum SWR value. This procedure changes the streak speed. Therefore, the time axis calibration is required after the tuning.

For the synchroscan streak camera, the Michelson interferometer method usually gives accurate calibrations.

4.2.3.7. Photocathode sensitivity uniformity

The spectral sensitivity of the streak tube is supplied from Hamamatsu when the tube is shipped. The sensitivity will not change dramatically unless someone send strong laser beam into the streak camera and burn the streak tube photocathode or MCP. If one needs to know the degradation of the streak camera spectral sensitivity, ask Hamamatsu to calibrate it, again. In case, one wants to calibrate by oneself, it is important to have spectrally calibrated uniform light source such as a tungsten collimated lamp of which spectral distribution is determined by Black body radiation. Using well calibrated and spatially uniform narrow band pass filters to cover the input slit of the streak camera and a diffusing plate which scatters the light randomly as shown in Fig.4.2.20, one can accumulate the image to get the light incident on

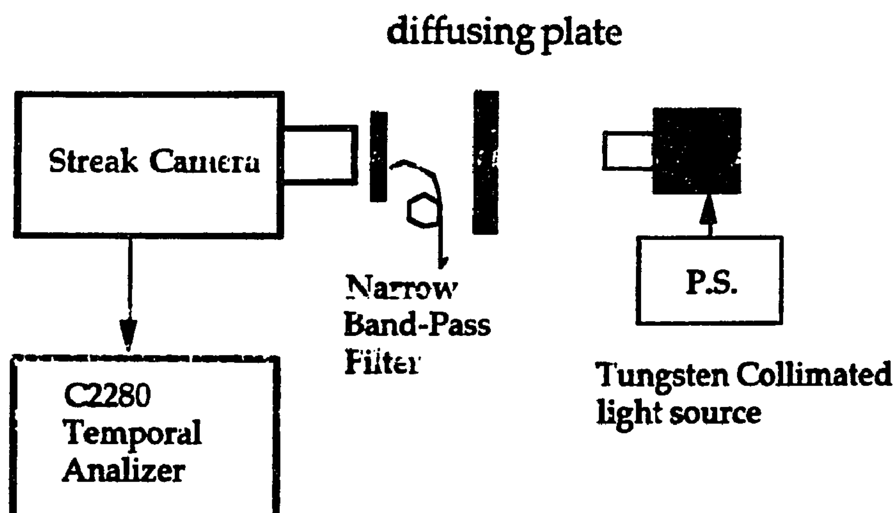

Fig.4.2.20. An experimental setup to evaluate uniformity of spectral sensitivity of the photocathode

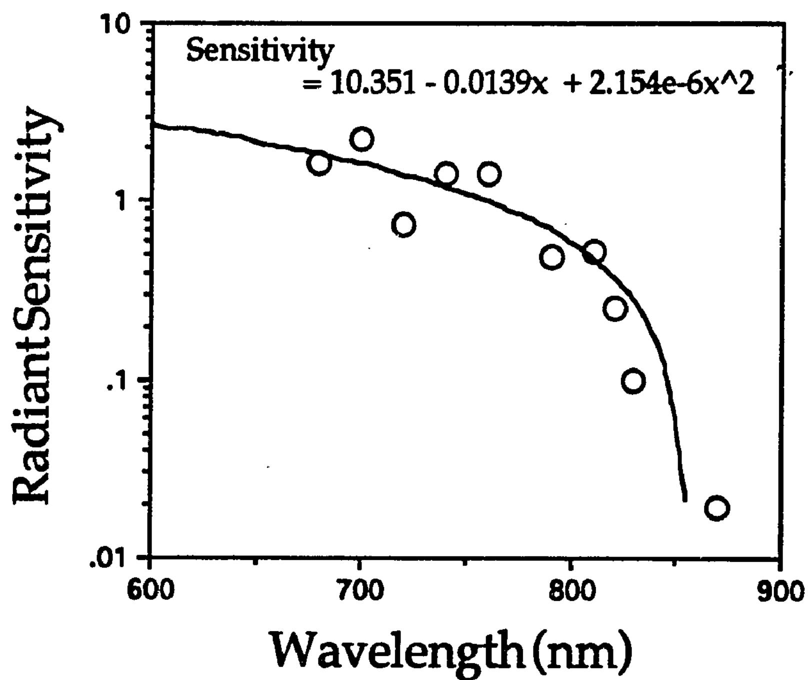

Fig.4.2.21 Spectral sensitivity of a synchroscan streak camera measured using a tungsten collimated lamp and calibrated narrow band pass filters.

the streak camera at the focus mode. The image displays the uniformity of spectral sensitivity of the photocathode. The intensity of output images at various wavelength determine a spectral sensitivity of the evaluated streak camera. Fig.4.2.21. shows an evaluated spectral sensitivity curve for a synchroscan streak camera using this method. The open circles are the measured output intensity while the solid curve was obtained by the second order polynomial fitting method.

4.2.4. Spectrometer and spectrograph

4.2.4.1. Operational principle

An spectrometer consists from an input slit, a collimating concave mirror, a ruled reflection or holographic grating, a focusing concave mirror, and an output slit. The light incident on the input slit is diffracted toward the collimating mirror to obtain parallel light beam incident onto the grating. The collimated light is diffracted by the grating. The diffracted monochromatic components is focused onto the output slit by the focusing concave mirror. In this case, aluminum concave mirrors are used to collimate and focus the light to avoid the color aberration. Since the diffraction angle for each wavelength component is different, the focus position for the each wavelength component is arranged along horizontal direction perpendicular to the output slit. When the output slit is removed, one can use the spectrometer as a spectrograph.

Using a set of collimating and focusing lenses in front of the sample, an image of the sample PL is projected onto the input slit. The image size on the input slit is around 100 μm determined by the laser beam diameter on the sample and the magnification factor of the set of collimating and focusing

lenses. To achieve highest coupling efficiency between sample and the spectrometer, a collection lens having same focal length of the concave mirror may be used.

4.2.4.2. Time spread of reflection grating

It is known that the spectrometer with a reflection or holographic grating causes time spread for ultrashort light pulses. The time spread is determined by geometrical optics for the incident beam and grating arrangement. As shown in Fig.4.2.22, the incident light is diffracted to certain direction that satisfy the Bragg's condition. The Bragg's diffraction is given by,

$$d(\sin\gamma - \sin\Phi_m) = m\lambda \qquad (4.2.10)$$

where d is the blaze width, θ_B is the blazed angle, γ is light incident angle, Φ_m is the diffraction angle from the normal to the grating, m is the order of diffraction, and λ is the diffraction wavelength. A grating is specified by a blazed wavelength where the diffraction efficiency is maximum of the diffraction spectral distribution function. The relationship between the blaze wavelength λ_B and blaze angle θ_B is given by

$$\frac{\lambda_B}{2\pi d} = \sin\theta_B \qquad (4.2.11)$$

Therefore, when one needs to purchase a grating, the blaze wavelength and number of grating grooves per mm g are the key parameters to determine which grating is suitable to the experiment. Once the Blaze wavelength and

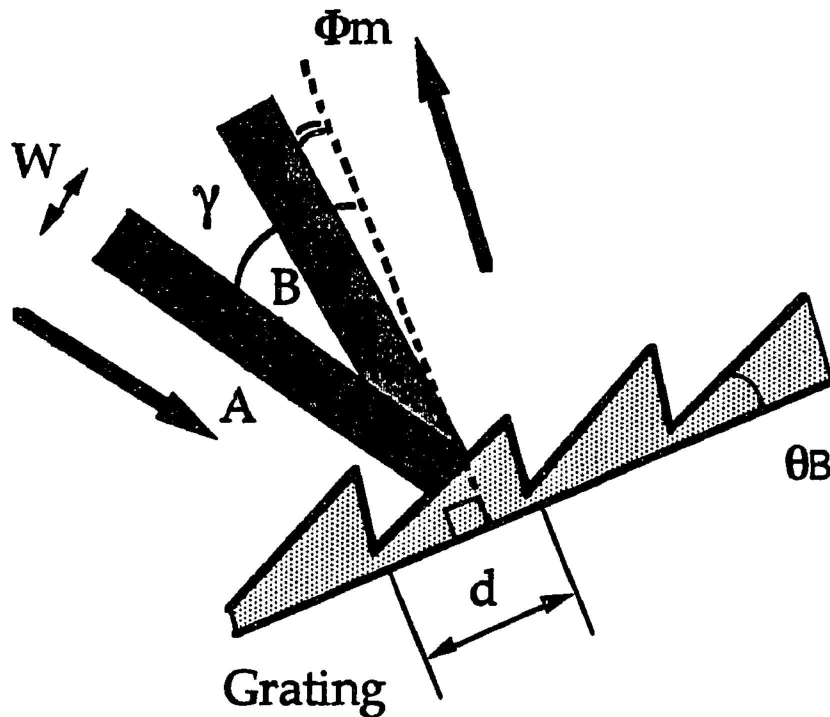

Fig. 4.2.22. Reflection grating structure and light diffraction.

number of grooves/mm are determined, the blaze angle is determined from Eq. 4.2.11.

Since the diffraction direction is not along reflection direction (Eq. 4.2.10), a time delay for a plane incident wave occurs. To evaluate the time spread, a plane wave incident on a square grating is considered as illustrated in Fig.4.2.22. From its geometry, the difference in flight distance between edges A and B are calculated and gives time delay Δt between the edges as,

$$\Delta t = \frac{(W \sin \gamma + W \sin \Phi_m)}{c} , \qquad (4.2.12)$$

Table 4.2.1 Time spread due to the square grating with different number of grooves and different grating width.

W / # of grooves	1 cm	$\sqrt{2}$ cm	2 cm
600	1.74 ps	2.46 ps	3.48 ps
1200	3.48 ps	4.92 ps	6.96 ps

where c is the velocity of light in the air and W is the grating width or light beam diameter in the unit of meter. Using Eq.s 4.2.10. and 4.2.12, the delay time Δt is derived to be,

$$\Delta t = W \bullet (2 \sin \gamma + \lambda g)/c , \qquad (4.2.13)$$

where g is the number of grating grooves per meter. Taking a derivative of Eq. 4.2.13 with respect to light wavelength λ, a time spread δt due to the wide spectrum of the incident light is evaluated as,

$$\delta t = W \bullet g \, \Delta\lambda \, / \, c \quad . \qquad (4.2.14)$$

The time spreads are calculated in Table 4.2.1 using $\Delta\lambda$=87 nm for 600 and 1200 grooves/mm square gratings with W=1, $\sqrt{2}$ and 2 cm. The larger the number of the grooves and the larger the grating size, the larger the time

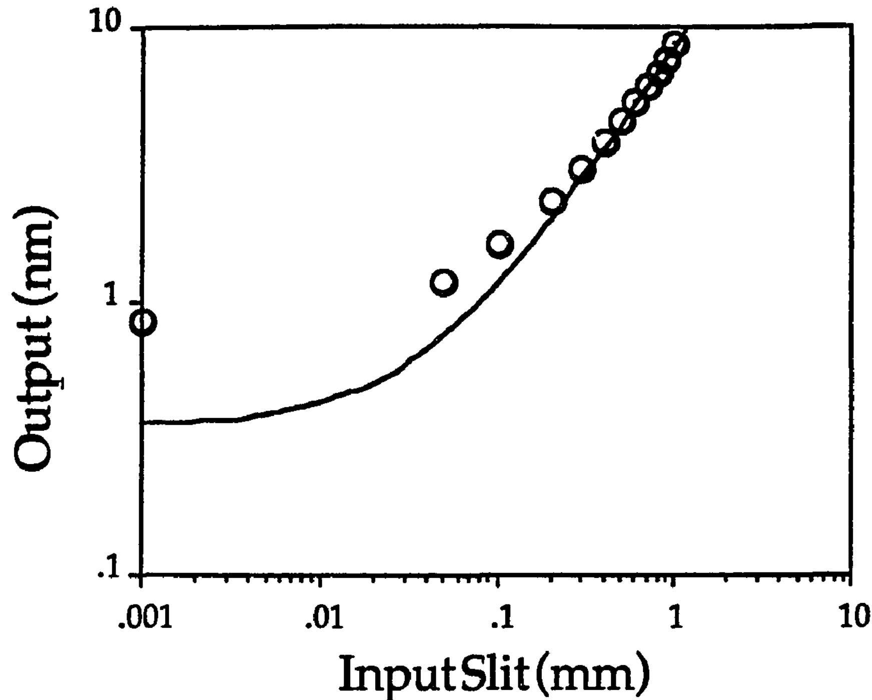

Fig.4.2.23. Ultimate spectral resolution determined by the streak camera and spectrograph resolutions

spreads. Therefore, the selection of a grating is important to obtain suitable time resolution for a time-resolved spectroscopic measurement.

4.2.4.3. Spectral resolution of the system

Spectral resolution of the time-resolved spectroscopy system is determined by the combined resolution of spectrograph and streak camera. The experimental results are shown in Fig. 4.2.23. When a 600 grooves/mm ruled reflection grating is used. The figure shows the relationship between the input slit width of the spectrograph (in μm) and the output spectral resolution of the streak image(in nm). The open circles are measured spectral resolution data at the slit widths and the solid curve indicates linear relationship between the output spectrum width and the input slit width.

Above 300 μm of the slit width, the spectral resolution is determined by the spectrograph while the resolution is determined by the spatial resolution of the streak camera below 300μm of the slit width. The minimum spectral resolution of the system is evaluated to be 0.9 nm for the 600 grooves/mm grating. Therefore, the optimum slit width to achieve relatively good resolution is 50μm input slit width. It is difficult to use a narrower slit width below 50 μm because the output signal intensity becomes too weak to observe. One can optimize the input slit width according to the signal intensity. At that time, the spectral resolution of the system may be degraded.

4.2.4.4. Spectral calibration

For the time-resolved spectroscopy, the spectral calibration is most important procedure. If one forgot to calibrate and move the streak camera, spectrograph or collection lenses, it may be impossible to achieve high spectral accuracy for the data analysis.

To calibrate the spectral axis on the streak image, one may use a Ne or Hg lamp which atomic emission lines are well established and their values are available on Nuclear Tables. The calibration light source is placed in front of the sample. The light source may be covered by a black paper with an aperture where a part of the light can pass through. This aperture enables to calibrate the spectral axis accurately. When the spectral lines are obtained on the TV monitor, fix the light source and integrate the image. Fig. 4.2.24. (a) to (c) show the spectral profiles of the integrated images at different central wavelengths such as 600, 700 and 800 nm using the 600 grooves/mm reflection grating for a Ne lamp. The numbers in parenthesis in the figures

are peak position on the TA and the numbers above for each position are the corresponding atomic line wavelength in nm for the Ne lamp. By fitting the peak positions on TA and the atomic lines (open circles) with a simple linear fit using a program "Criket graph" in a Macintosh computer, one can make a calibration curve (solid lines) as shown in Fig. 4.225. (a), (b) and (c) corresponding to the data in Fig. 4.2.24 (a), (b), and (c), respectively. To achieve higher accuracy for spectral axis calibration, several lamps or lasers may be used.

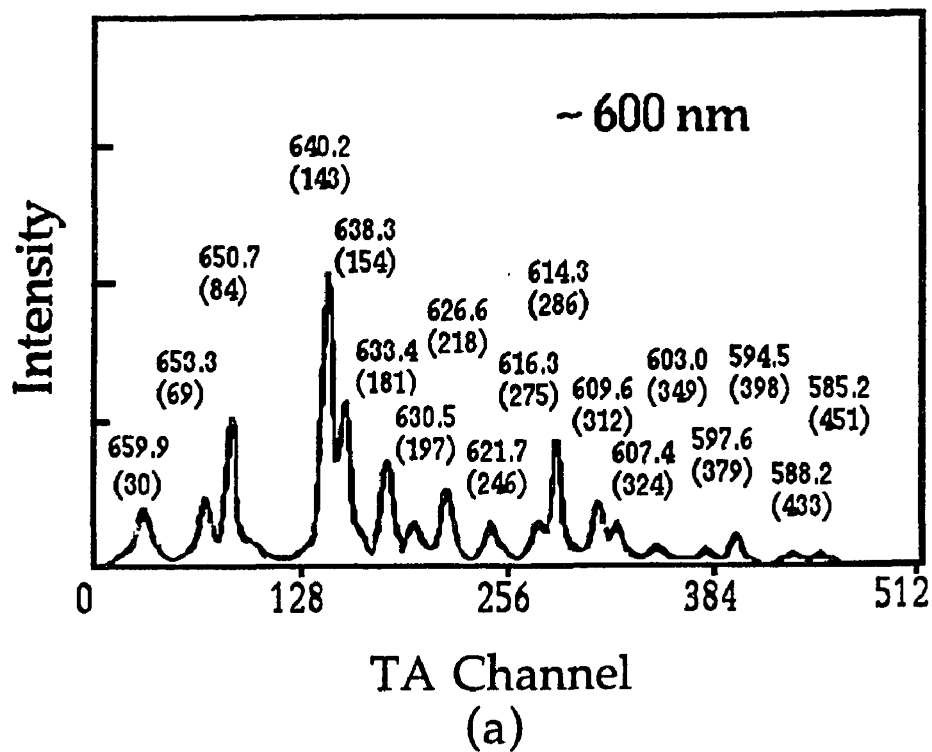

(a)

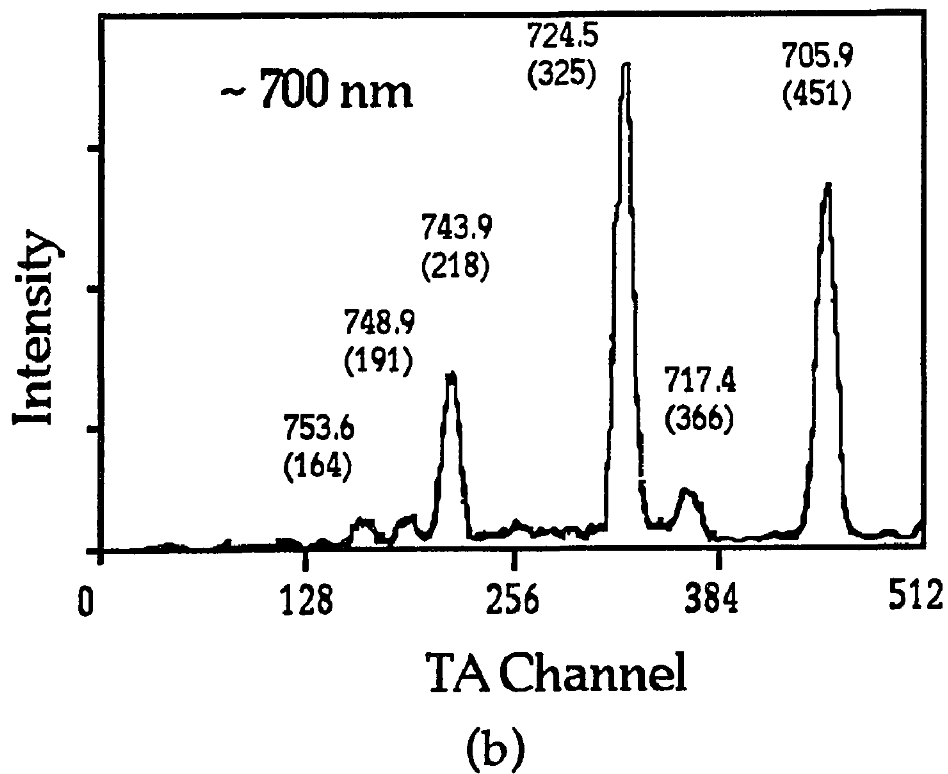

(b)

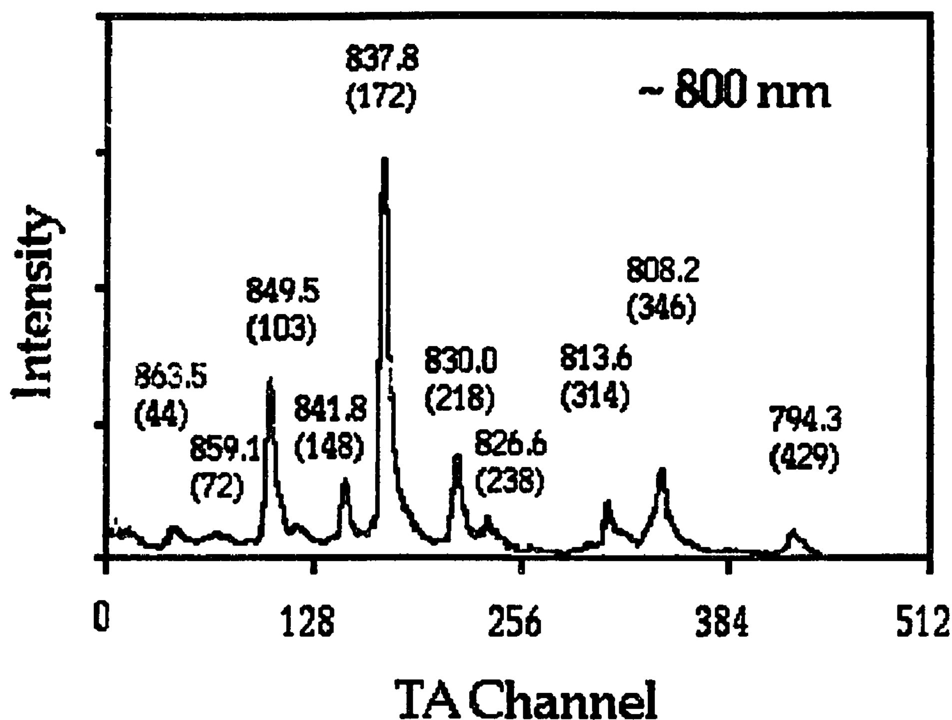

(c)

Fig. 4.2.24. Spectra of Ne lamp observed at (a) 600 nm, (b) 700 nm, and (c) 800 nm spectral regions, respectively, using 600 grooves/mm reflection grating in SPEX spectrometer 1681B. The numbers in parenthesis in the figures are peak positions on TA and the numbers above for each position are the corresponding atomic line wavelengths in nm.

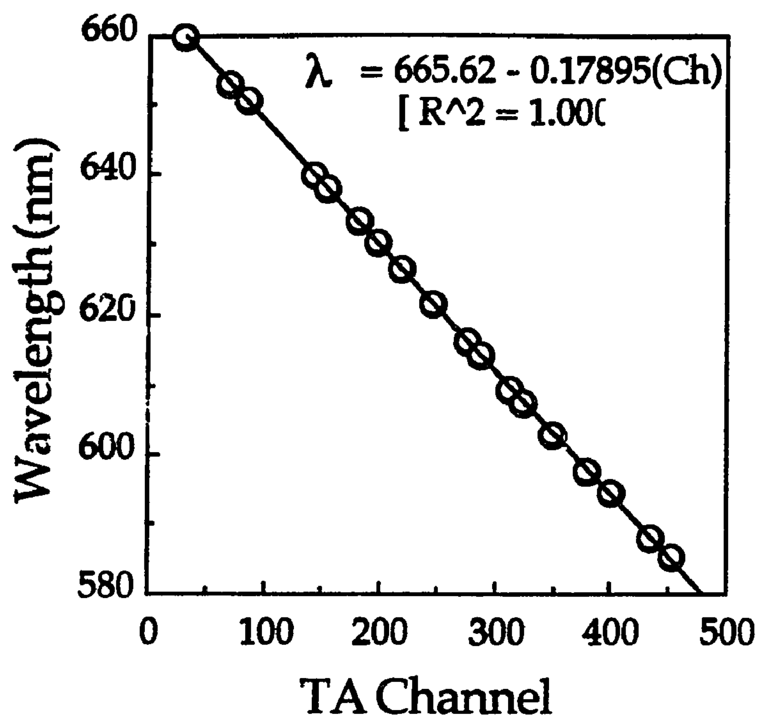

(a)

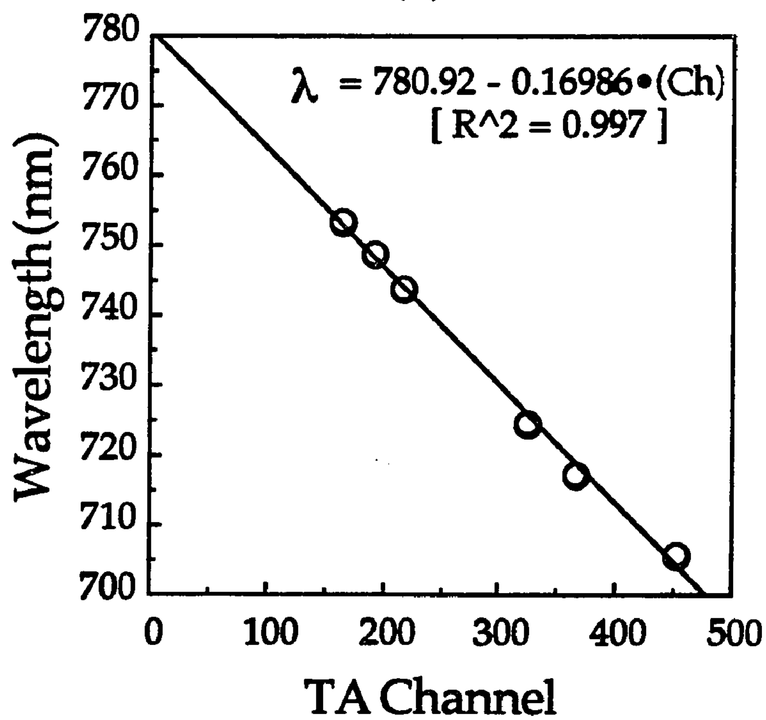

(b)

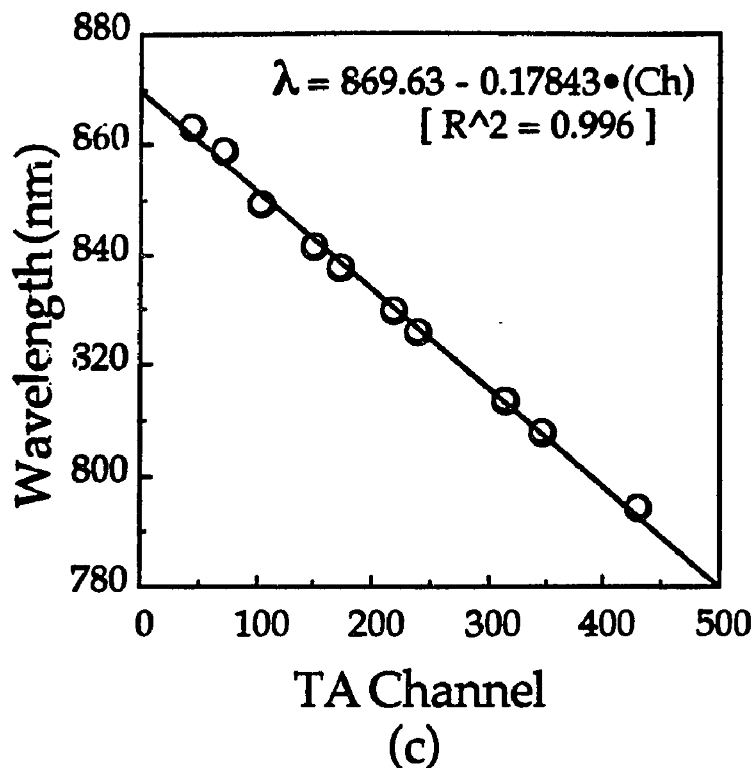

(c)

Fig. 4.2.25. Spectral calibration curves for Ne lamp obtained for the data shown in Fig. 4.2.24. (a), (b) and (c), respectively. Open circles are measured peak positions on TA and solid lines are fit curves by simple linear fitting with "Criket Graph" program in a Macintosh computer.

4.3. External pressure apparatus

Applying uniaxial external stress to semiconductor samples, the carrier and exciton dynamics under various deformed band structure has investigated in ps time domain at low temperature. This will give information on carrier-carrier scattering and carrier relaxation process under stress which are not extensively studied. The maximum stress obtained for a GaAs MQW/Si sample was 14 kbar along {001} direction. Typically, the maximum stress can be around 10 to 16 kbar which corresponds to more than 10000 times higher pressure than atmospheric pressure of 1.013 bar.

4.3.1. Cryostat with stress apparatus

The experimental setups for the steady state and the time-resolved PL spectroscopies under external stresses are the same as these discussed in previous sections 4.2.1 and 2 except for addition of a stress-cryostat dewar. A variable uniaxial stress can be applied onto semiconductor samples using the stress apparatus. The stress apparatus with dewar was obtained from Prof. Pollak of the Brooklyn college of CUNY. The operation of the stress apparatus and sample preparation for external stress experiments were performed with help of Mr. Hao Qiang from the Brooklyn College.

The stress cryostat (Janis Research Inc. Model# 8DT) also can vary sample temperature. However, since the heater locates on the high heat resistive material of the liquid Helium needle at the bottom of the cryostat, the heat-up is required to be very careful and takes a long time. Rapid heating process may destroy the cryostat. The solder between the heater plate and dewar is melt and breaks the vacuum sealing. In the experiments I have done, I broke the cryostat twice because the heater current was high

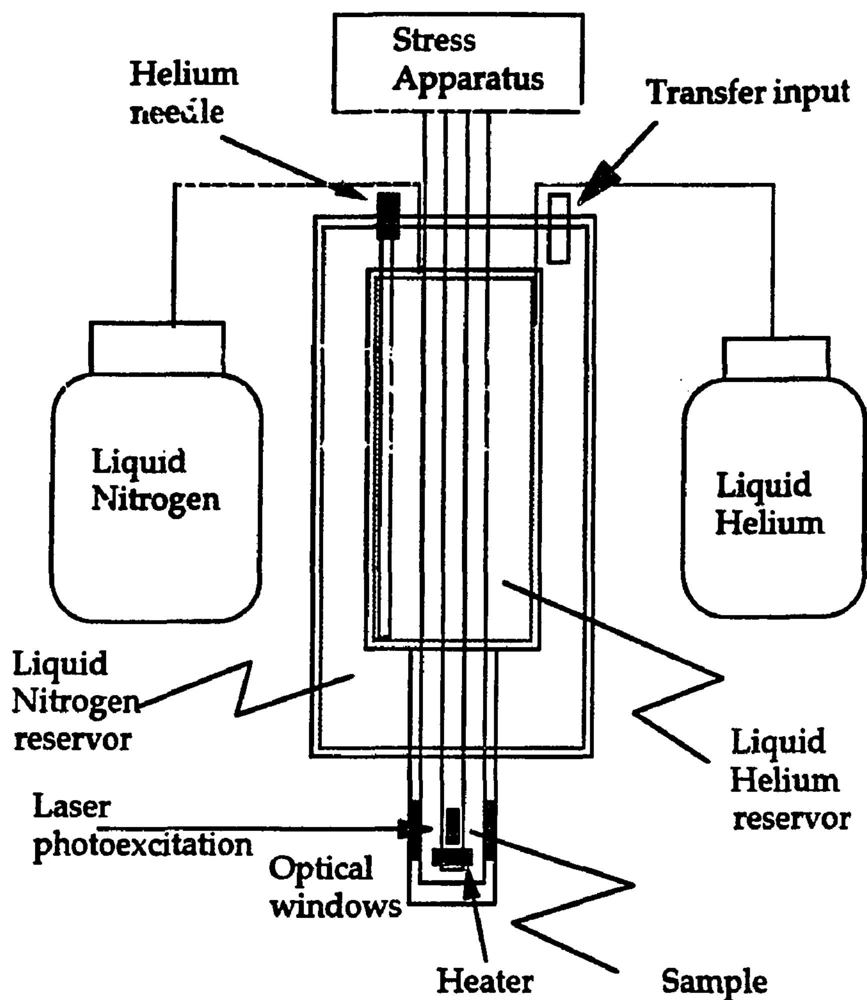

Fig. 4.3.1 Stress dewar structure.

while there was not enough liquid Helium flow. The damage can be repaired by using a high power solder iron and a solder without flux. In the experiments under external stress, I have used the dewar at liquid Helium temperature.

After a sample is mounted on a stress jig and is inserted into the dewar, the stress cryostat requires pre-cooling by using liquid nitrogen. To avoid water condensation and freezing of ice in the dewar, dry helium gas is necessary to be circulated to purge the wet air from the dewar for at least 30 minutes with Helium needle valve open so that the helium gas can dry the

inside of liquid helium tank. Then, liquid nitrogen is transferred into the liquid nitrogen tank and fill up to the top of the dewar. It may take 20 minutes. It is very important to pay attention to the stress arm while the sample is cooled. Because of the temperature difference from the room temperature, the stress arm shrunk and may damage the sample. Then, liquid Helium can be transferred to the Helium tank. At that time, the Helium needle valve should be closed but not tightly to avoid the freezing of the needle valve. One of the most simple but important process to maintain the liquid helium, one need to close the transfer input with a rubber cap. The tiny rubber cap prevents moisture and warm air to get into the Helium tank and enable to maintain the liquid helium cooled and clean. I have tried an experiment without the cap. It was very difficult to maintain a stable temperature. It also took a very long time to achieve 4 °K lattice temperature.

4.3.2. Stress apparatus

The PL from the strained sample is collected from the direction perpendicular to the strained axis and is time-resolved. Observing the PL from the sample while changing the magnitude of the external stress on the sample, the carrier and exciton dynamics is resolved spectrally and temporally at various lattice temperatures.

Fig. 4.3.2 shows a schematic diagram of the uniaxial stress apparatus. A sample is cut to 3 mm x 10 mm along certain crystal axis and is placed in the stress jigs (Fig. 4.3.3.) The sample placed between a pair of stress jigs is set on an arm of a lever. By changing a load applied on the another arm of the lever, the force applied onto the sample can be controlled mechanically and continuously. The load in the real case is given through a spring coil. The

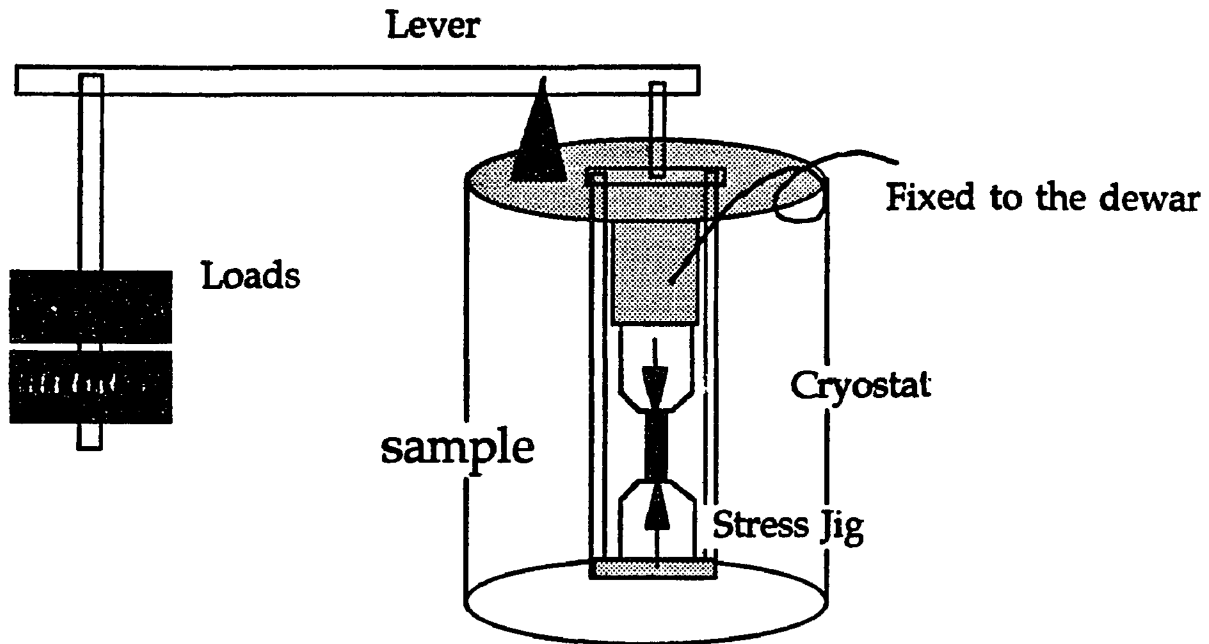

Fig. 4.3.2. Schematic diagram of compressive stress apparatus.

amount of force applied to the sample through the stress transfer rod is determined by the expansion of the spring coil and the ratio between the distance of the load to the support and the distance of support to the transfer rod. In this apparatus, the ratio is 10.

Because of Hook's law (F=kD where F is force, k is a spring constant with the gravity acceleration factor $g=9.8\ m/s^2$, and D is the displacement of the coil), the amount of force generated on the coil can be determined by the spring constant and the expansion D of the coil length. The spring constant is calibrated to be W/D=3.01 where W is weight loaded and D is the displacement of the spring. After the spring calibration, one just needs to measure the displacement of the coil D accurately to determine the amount of force F applied to the stress transfer rod. To determined the amount of stress applied onto the semiconductor sample, the cross section A of the

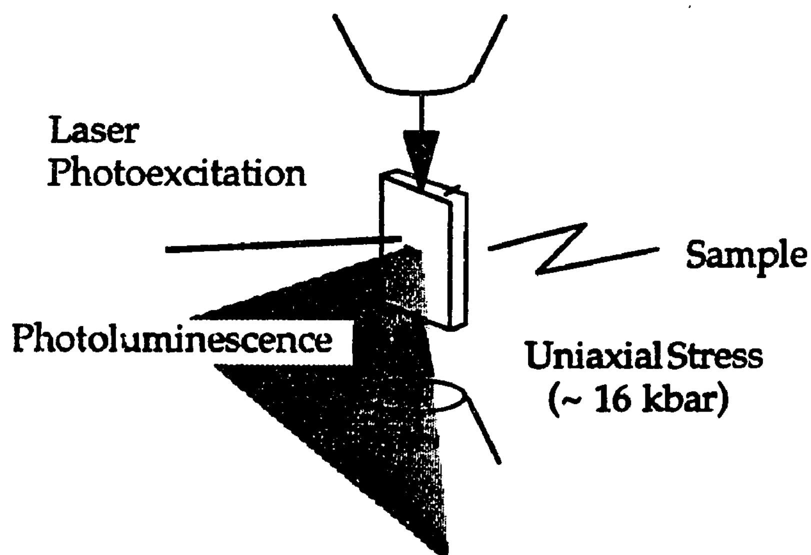

Fig. 4.3.3 Stress apparatus diagram. The stress can be applied to in-plane of samples.

semiconductor sample has to be measured accurately because the pressure is calculated by F/A. The stress X is calculate by,

$$X=10 \bullet F \bullet 9.8/A. \qquad (4.3.1)$$

The maximum stress one can apply is around 16 kbar which is much higher stress than any built-in stress of 3kbar.

4.4. Reference in Chapter 4

1). H. Unlu and H. Morkoc, Solid State Tech. March, 83 (1988)

2). D. J. Bradley, and W. Sibbett: Appl. Phys. Lett. 25, 382 (1975)

3). Y. Takiguchi, E. Inuzuka, K. Kinoshita, Y. Inagaki, and Y. Tsuchiya, Proc. SPIE 569, 167 (1985)

4). Y. Takiguchi, K. Kinoshita, M. Suyama, Y. Inagaki, and Y. Tsuchiya, Proc. SPIE 693, 105 (1986)

5). Y. Takiguchi, S. Aoshima, and Y. Tsuchiya, Proc. SPIE 693, 118 (1986)

6). N. H. Schiller, Y. Tuchiya, E. Inuzuka, Y. Suzuki, K. Kinoshita, K. Kamiya H. Iida, and R.R.Alfano, Optical Spectra 14, 55 (1980)

7). Y. Tuchiya, E. Inuzuka, and Y. Suzuki, Proc.13 the International Conference on High Speed Photography and photonics (Tokyo) (1978)

8). R. L. Fork, B. I. Breene, and C.V.Shank, Appl. Phys. Lett. 38,671(1981)

9). J.A. Valdmanis, R. L. Fork, and J. P. Gordon, Optics Lett. 10,131 (1985)

10). C. P. Huang, M. Asaki, S. Backus, H. Nathel, M.M. Murnane, and H. C. Kapteyn, Conf. Proc. "Ultrafast Phenomena", Th.E2(1992) Juan-Les-Pins, France

11). N. Nakano, H. Kuroda, E. Inuzuka, Y. Takiguchi, M. Sujiyama, Y. Tsuchiya, Y. Suzuki, SPIE proc. 491, 962 (1984)

12). Hamamatsu C1587-01 catalogue (1990)

13).K. Kinoshita, Y. Takiguchi, I. Hayashi, Y. Tsuchiya, K. Oba, M. Yamanaka, H. Niki, K. Miyanaga, T. Yamanaka, Y. Izawa, C. Yamanaka, SPIE proc. 693, 111(1986), and Rev. Sci. Instrum., 57, 1743 (1986)

14). This dispersion curve of an input optics of a streak camera was evaluated by Dr.Staerk at Max-Planck Institute under the collaboration

work with Hamamatsu Photonics K.K. Japan.

15). This result was obtained at Hamamatsu Photonics K.K. in Japan in 1987 using a Nd:YAG laser generating 5 ps and 1.06 μm pulses and a 2 ps streak camera.

CHAPTER 5

HOLE DYNAMICS IN GaAs/Si UNDER BIAXIAL STRESS

5.1. Introduction

A GaAs device grown on a Silicon substrate (GaAs/Si) is one of the important structure for future photonics devices. The hybrid of GaAs high speed opto-electronic devices and Si electronic devices enables diode-lasers and Si photodetectors to be integrated on a chip for ultrahigh speed computation and communication applications. Since the thermal expansion coefficients between GaAs epilayer and Si substrate are quite different, it generates a built-in biaxial tension in the GaAs epilayer. The stress alters the band structure of GaAs material, removes the degeneracy of the valence band, and thus alters carrier dynamics.

As discussed in Chapter 2, the light (lmh) and heavy mass holes (hmh) are degenerate at k=0 in the momentum-energy space for a non-strained GaAs bulk. The holes dominate optical and electrical characteristics for n-type doped GaAs bulk devices. Since the hole mass is heavier than the electrons in conduction band, the hole mobility is low and the response of the devices are slow. The hot hole dynamics photogenerated in the device is dominated by phonon emission, hole-hole, and hole-electron scattering processes. Since the lmh and hmh co-exist at the bottom of the valence band in the non-strained GaAs bulk, it was difficult to evaluate the separate interaction of heavy and light mass hole dynamics.

When a stress is applied to a GaAs bulk material, the band gap energy changes and the valence subbands are split according to the magnitude and the type of stress. The stress may be hydrostatic, uniaxial or biaxial and compressive or tensile stresses. As a biaxial tension (compression) is applied onto the GaAs bulk device, the band gap decreases (increases). The biaxial stress is a two directional stress in xy-plane perpendicular to the growth direction. The degenerate valence subband is split to the hmh and lmh subbands at k=0 by the stress. The lmh edge locates lower (higher) energy than the hmh edge. In this modified band structures, the hmh and lmh dynamics at the lowest energy can be separately investigated by analyzing a photoluminescence (PL) kinetics after photoexcitation by a short optical pulse.

In this chapter, the hole dynamics in 2μm and 4μm thick n-type GaAs separately grown on Si substrates (GaAs/Si) has been investigated using steady state and time-resolved PL spectroscopy techniques. The stronger PL was obtained from the 4μm thick GaAs/Si compare with the 2μm thick GaAs/Si. This indicates that the 4μm thick GaAs layer contains less non-radiative centers arising from dislocations caused by the strain.

5.2. 2μm thick n-type GaAs/Si

In this section, the hmh and lmh inter- and intra-valley thermalization processes in a 2 μm thick n-type GaAs/Si (in which a built-in biaxial tension splits the valence subbands) were investigated on a picosecond time scale.

5.2.1 Sample and experimental setup

A 2 μm intentionally Si-doped ($1x10^{16}$ cm^{-3}) n-type GaAs grown on five periods of $In_{0.5}Ga_{0.5}As$/GaAs (20 Å/20 Å) superlattice as buffer layers deposited on a {100} Si substrates cut 4° toward <110> (GaAs/Si) is used for this research. The arrangement of the Si substrate creates least amount of defect at the boundary.[1] This bulk GaAs/Si was grown by a MBE machine at Univ. of Illinois at Urbana-Champaign by Prof. Morkoc's group. The GaAs epilayer contains about 2.3 kbar of biaxial tension arising from the difference in thermal expansion between GaAs and Si substrate (as discussed in Chapter 2.2.2). Since the biaxial tension X(x,y,0) splits the valence subbands according to Eq.s 2.3.4a and b in Chapter 2, the separation energy between the hmh and lmh is given by $\Delta E_{hmh-lmh}$=-6.121•X (meV). From the steady state PL spectrum, the separation $\Delta E_{hmh-lmh}$ is measured to be 14 meV. Therefore, the biaxial tension incorporated in the sample is estimated to be 2.3 kbar. The hmh ($m_j=\pm1/2$) is located below the lmh ($m_j=\pm3/2$) by 14 meV as shown in Fig. 5.2.1. In this sample, although the superlattice is fabricated between Si and GaAs epilayer as buffer layers, the density of dislocation and defects may not be negligible.

The sample was mounted in an optical cryostat, was cooled down to 23 °K lattice temperature, and was photoexcited by a CW Ar laser beam (514.5 nm=2.4 eV photon energy) for steady state measurements and by a CPM laser pulses (2.0 eV photon energy with about 80 femtosecond pulse duration) for time-resolved PL measurements. The average photoexcitation powers were 10 mW for both cases. The laser beam was focused onto the sample by a lens with a 20 cm focal length. The focus spot diameter was around 100 μm. The photogenerated carrier density was estimated to be about $5x10^{15}$ cm^{-3} which

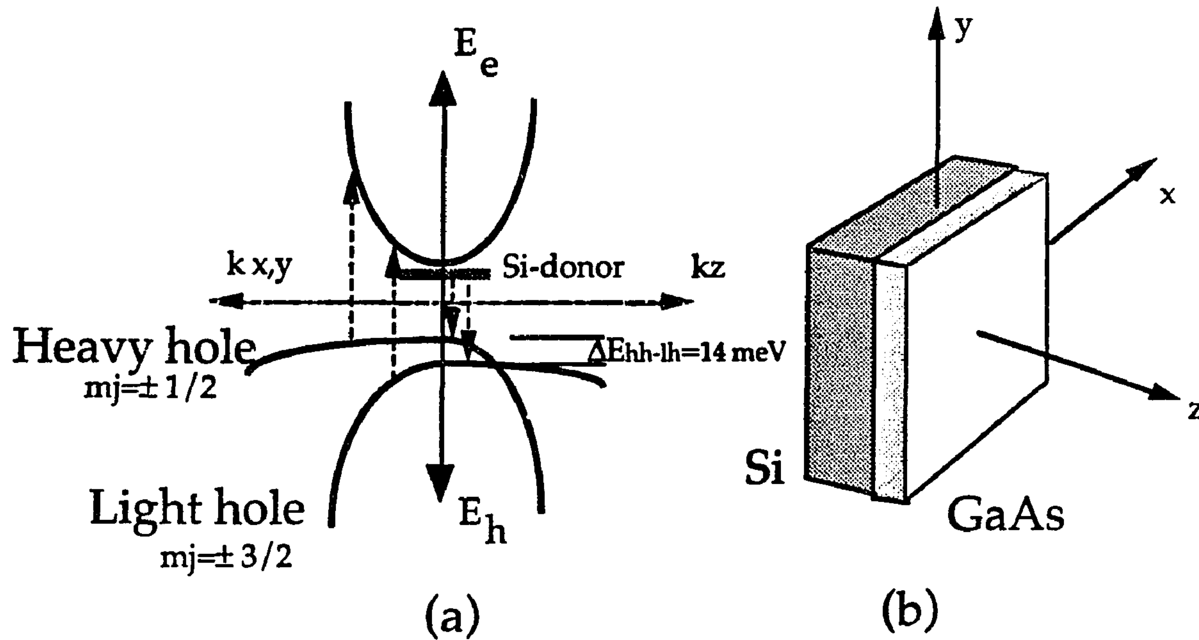

Fig. 5.2.1. (a) Band structure of biaxially tensile strained bulk GaAs with Si dopant and (b) structure of GaAs/Si sample.

was similar order of density of the dopant. The PL emitted from the sample was collected into a 25 cm spectrometer and spectrally resolved.

For the steady state measurements, a GaAs photocathode photomultiplier tube (PMT) detected the PL at the output of the spectrometer. The spectral resolution was about 5Å. The output signal was processed with a lock'-in amplifier and was analyzed with a personal computer.

For the time and spectrally resolved PL spectroscopy, the spectrometer in the steady state was modified to be a spectrograph by removing the output slit of the spectrometer. The spectrally dispersed PL was focused onto an input slit of an S-1 synchroscan streak camera with 10 picosecond(ps) time resolution.

To avoid the time spread due to the grating in the spectrograph, a 600 grooves/mm reflection grating was used for the time resolved measurements instead of 1200 grooves/mm used for the steady state measurements. The time

resolution of the 600 groove/mm grating was estimated to be 7ps as discussed in Chapter 4. A color filter (#7-59, which transmits longer wavelength above 700 nm) was used to cut the fundamental laser beam at 625 nm in front of the spectrometer (spectrograph).

5.2.2. Experimental results

5.2.2.1. Steady state PL spectrum

A CW Ar laser beam photoexcites electrons into the conduction band and creates holes in the valence subbands as shown by upward arrows in Fig.5.2.1.(a) The electrons in the donor level recombine with the photogenerated holes around k=0 shown by downward arrows and emit PL photons.

Since Si dopant is a type IV material, Si can be either donor (attached to Ga side) or acceptor (attached to As side) and its ionization process can be treated as hydrogen atom. The ionization energy E_{ion} for donor and acceptor can be determined by,[2)]

$$E_{ion} = - m^* q^4 / 8 n^2 h^2 (\varepsilon\varepsilon_0)$$
$$= -13.6 m^* / \varepsilon^2 m_0 \qquad (5.2.1)$$

where m^* is the effective mass of either conduction electron for the donor or hole for the acceptor, q is the electron charge, h is Planck constant, ε and ε_0 are dielectric constants of material and in air, and n determines the ionization level. Using ε=13.1 and $m_h^*=0.45m_0$, E_{ion}=35.6 meV for the acceptor while E_{ion}=5.3 meV for the donor with $m_e^*=0.067m_0$.

A steady state PL spectrum from the GaAs/Si sample at 4.3 °K lattice temperature is obtained as shown in Fig.5.2.2. The spectrum shows several PL

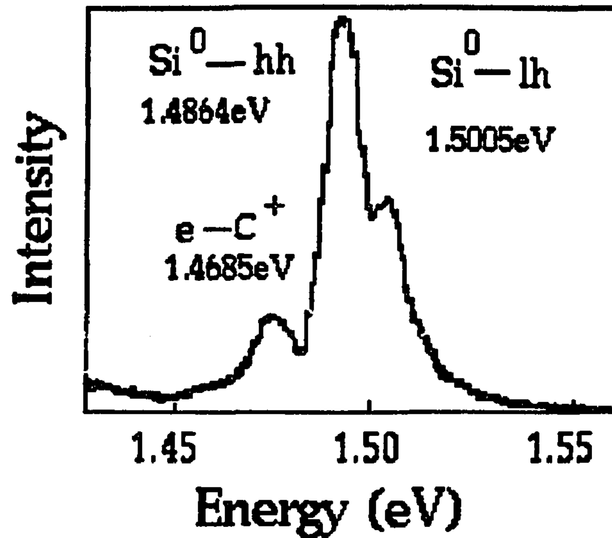

Fig. 5.2.2. A steady state PL spectrum from the 2μm GaAs/Si sample photoexcited by an Ar ion laser at 4.3 °K lattice temperature.

peaks. The major ones are at 1.5005 eV (826 nm), 1.4864 eV (833.8 nm), 1.4685 eV (844 nm), and 1.4515 eV (853.9 nm).

The peaks at 1.5005 eV (about 5 meV lower than band gap energy) and 1.4864 eV are attributed to the transition between Si donor level to lmh and hmh subbands, respectively. The energy separation between the peaks is 14 meV. The peak at 1.4685 eV (about 36 meV smaller than band gap energy) is arising from the transition between the conduction band and the redidual carbon acceptor level.

From the energy separation between Si-hmh and Si-lmh transitions of 14 meV, the magnitude of the stress X built-in the sample can be calculated by using relations of energy separations $\Delta E_{c\text{-hmh}, c\text{-lmh}}$ for conduction band to hmh and lmh subbands as(refer Chapter 2.2.2),

$$\Delta E_{c\text{-hmh}} = -10.36\, X \quad (\text{meV/kbar}) \qquad (5.2.2)$$

and

$$\Delta E_{c\text{-}lmh} = -4.239\,X \quad (\text{meV/kbar}). \tag{5.2.3}$$

Therefore, the energy difference $\Delta E(X) = \Delta E_{c\text{-}hmh}(X) - \Delta E_{c\text{-}lmh}(X)$ gives the amount of separation energy between the subbands under the tension X.

$$\Delta E(X) = -6.121 \bullet X \quad (\text{meV}) \tag{5.2.4}$$

From the measured separation of 14 meV, the magnitude of the biaxial tensile stress at 4 °K lattice temperature is estimated to be 2.28 kbar.

5.2.2.2. Time-resolved PL spectrum

As a result of the time-resolved PL spectroscopy using CPM laser pulses at 23 °K lattice temperature, a time- and energy-resolved PL image is obtained around 1.5 eV and is shown in a three dimensional (3D) display in Fig.5.2.3. The time-resolved 3D image is noisy because the PL intensity from GaAs epilayer was very weak and the S-1 type photocathode of the streak camera generates more thermal electrons. The GaAs epilayer might contain non-radiative recombination centers (misfit dislocation) and trap the photogenerated carriers. That may be why the PL decay time is faster compare with the PL decay time for a 4μm GaAs/Si sample. The 4μm GaAs/Si sample contains less dislocations as will be discussed in the section 5.2.

The time-resolved 3D PL spectrum in Fig. 5.2.3 is integrated in time between t=-7 ps and 520 ps. The time-integrated PL spectrum is shown in Fig. 5.2.4. to compare with the steady state PL spectrum to identify the transitions on the 3D PL spectrum. The PL peaks due to Si-donor to hmh and lmh transitions

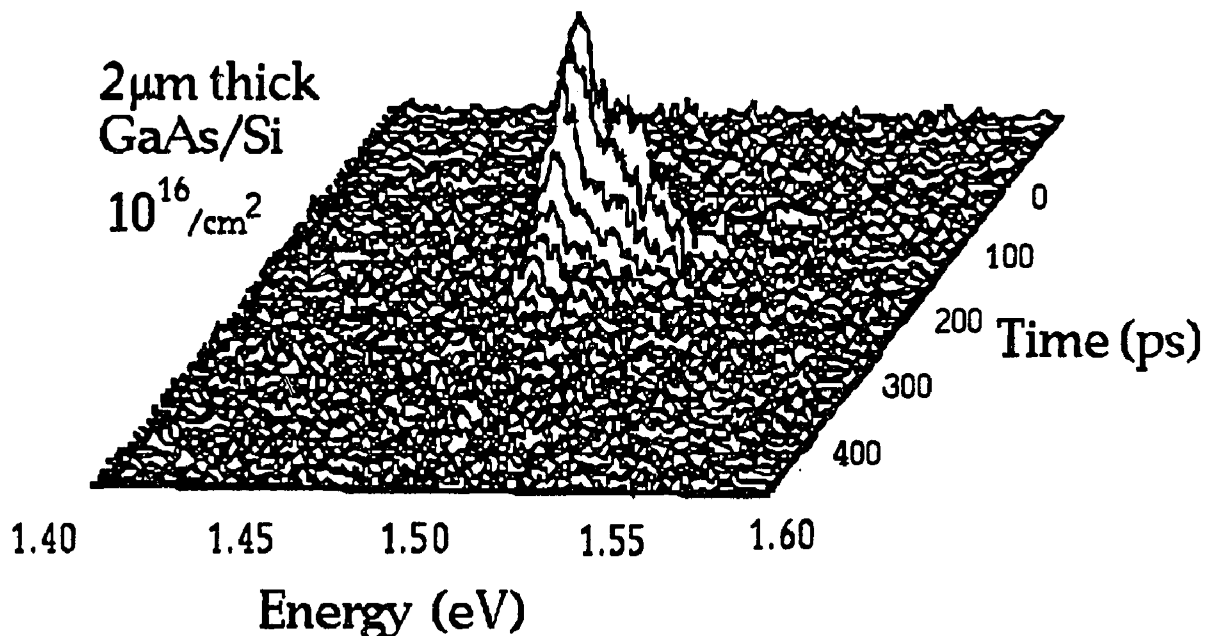

Fig. 5.2.3. Three dimensional display of the time-resolved PL spectrum from 2μm thick n-type GaAs epilayer grown on a Si substrate photoexcited by CPM laser pulses at the lattice temperature of 23 °K.

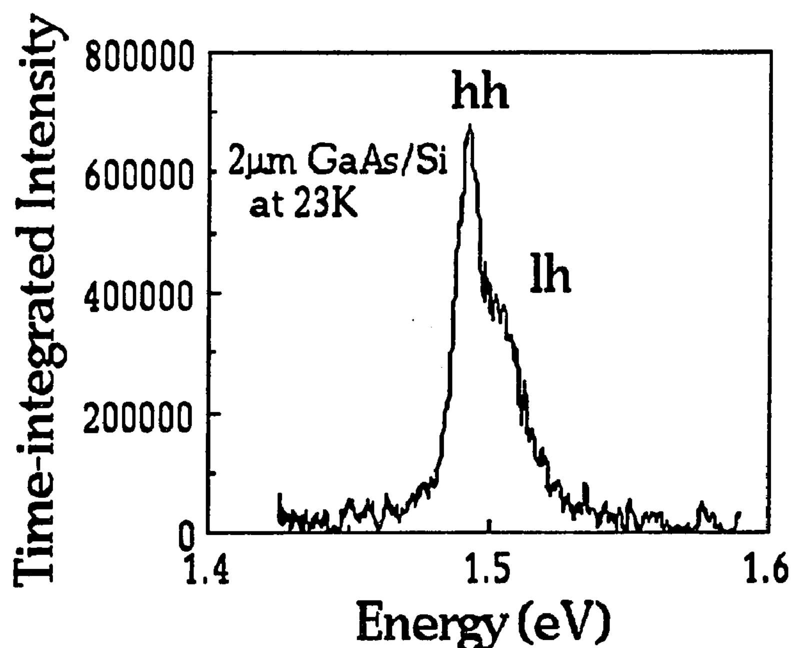

Fig. 5.2.4. The time integrated PL spectrum between -7 ps to 520 ps of the 3D PL image of 2μm GaAs/Si shown in Fig.5.2.3. at 23 °K lattice temperature.

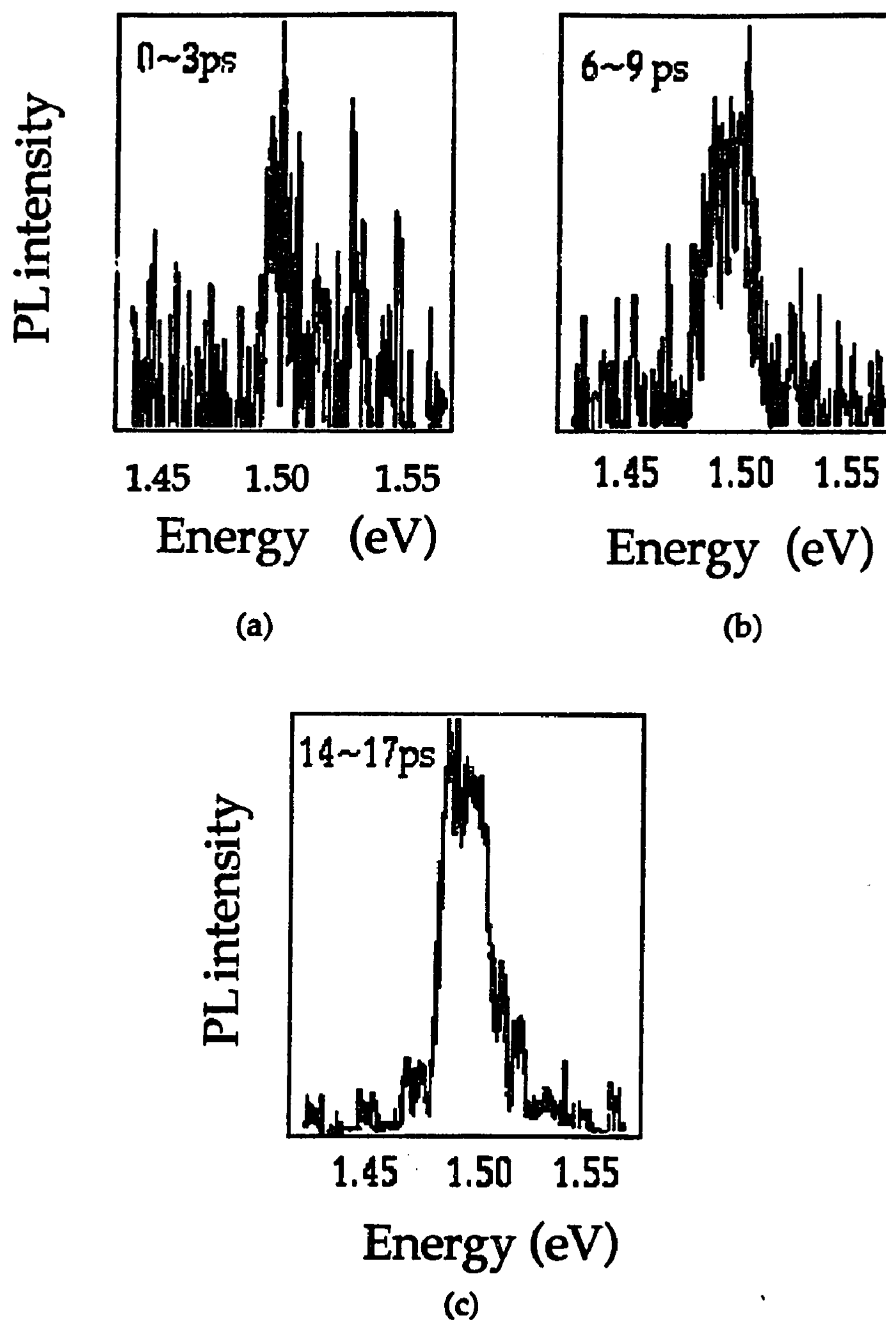

Fig.5.2.5. Initial PL kinetics from the 2μm GaAs/Si sample at 23 °K lattice temperature, integrated from (a).0 to 3 ps, (b).6 to 9 ps, and (c).14 to 17 ps, respectively.

are shown clearly while the other peaks are not seen in Fig.5.2.4. The lifetime of the acceptor and other impurity transitions might be longer than 5 ns so that most of the PL photons from the impurity transitions are out of the observing time window. Since the time window corresponds to 3% of laser pulse interval of 12.2 ns, 97% of the long decay PL is out of the time window. The time-resolved PL spectrum within the observing time scale mainly gives transition dynamics between the donor level to the hole subbands.

At the initial time after the photoexcitation, the PL intensity of the donor-lmh transition rises faster than that of the donor-hmh transition as shown in Fig. 5.2.5 (a), (b), and (c). Then, the peak intensities become same at 6 ps after the photoexcitation as shown in Fig. 5.2.5 (b). The peak intensities between hmh and lmh transitions remain similar until 17 ps as shown in Fig. 5.2.5 (c).

To verify the PL kinetics, the PL intensities between 1.482 and 1.499 eV for the hmh transition and between 1.499 and 1.529 eV for the lmh transition were integrated along the spectral axis and their PL intensity profiles are shown in Fig. 5.2.6 where the solid curve is the profile for the Si-domor to lmh transition while the dashed curve is for the Si-donor to hmh transition. There exists a noise on the Si-lmh PL profile around 6 ps. However, the rise time of the Si-lmh transition is indeed faster than that of Si-hmh transition. The rise times for the Si-hmh and the Si-lmh transitions assuming single exponential rising were evaluated to be 18.3ps and 11.0 ps, respectively. In Fig. 5.2.6, the PL intensity for the hmh reaches its peak about 5 ps later than that for the lmh subband. This peak delay will be explained in the section 6.2.4. The PL profiles showed single exponential decay curves and their decay times were evaluated to be 20.0 ps and 17.4 ps for the hmh and the lmh transitions, respectively.

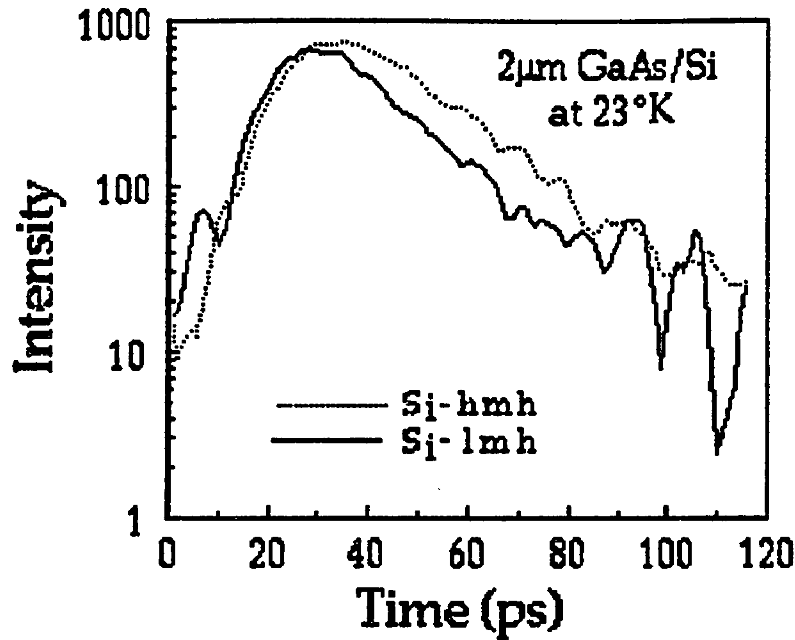

Fig. 5.2.6. Temporal profile of the donor to hmh transition integrated between 1.482 and 1.499 eV (dotted curve) and the donor to lmh transition integrated between 1.499 to 1.529 eV(solid curve) at the lattice temperature of 23 °K.

5.2.3. Discussion

5.2.3.1 Hot carrier dynamics model

A carrier transition model was used to explain the PL kinetics. When the laser pulse photogenerates electron-hmh or electron-lmh pair in the xy-plane as depicted in Fig. 5.2.7. At that time, the momentum ($k_c=k_v$) and energy for the photon-electron-hole system are conserved. Thus, the photoexcited e-hmh pair satisfies an energy conservation relation as,

$$h\nu = \hbar^2 k^2/2\, m_e^* + \hbar^2 k^2/2m_{hmh}^* + Eg(X) \qquad (5.2.5)$$

and the photoexcited e-lmh pair satisfies a relation as,

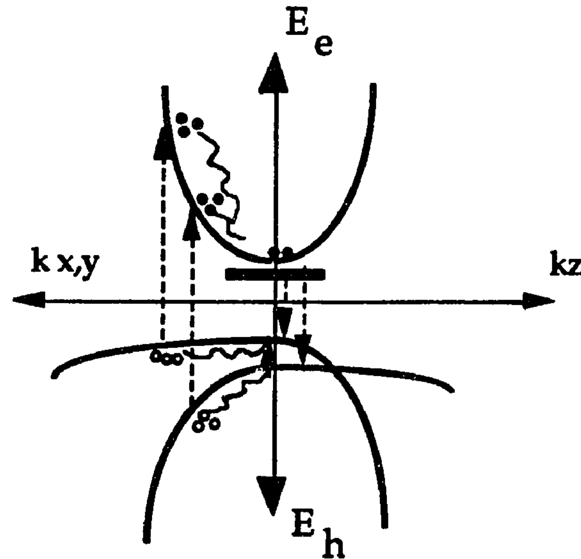

Fig. 5.2.7. Diagram of photogenerated electron and hole thermalization and PL emission dynamics.

$$h\nu = \hbar^2 k'^2/2m_e^* + \hbar^2 k'^2/2\, m_{lmh}^* + Eg(X) - \Delta E(X), \qquad (5.2.6)$$

where m^*_i (i=e, hmh, and lmh) are effective masses and $\Delta E(X)$ is the stress induced energy separation between the hmh and lmh subbands(~14 meV). The energy band gap Eg(X) is also stress dependent. Using the kinetic energies of electron $E_e = \hbar^2 k^2/2m_e^*$ for the e-hmh pair and $E'_e = \hbar^2 k'^2/2m_e^*$ for the e-lmh pair, Eq.s 5.2.5. and 5.2.6. are rewritten as,

$$h\nu = E_e/(1 + m_e^*/m_{hmh}^*) + Eg(X) \qquad (5.2.7)$$

and

$$h\nu = E'_e/(1+m_e^*/m_{lmh}^*)+Eg(X)-\Delta E(X). \qquad (5.2.8)$$

Therefore, the electron kinetic energy gained from the photoexcitation is determined by the band gap energy and the mass ratio between the electron and hole. The hmh and lmh gain the remaining kinetic energies. For 2.0 eV

photoexcitation, the electrons gain 280 meV and 450 meV for hmh- and lmh-electron transitions while the hmh and lmh gain 230 meV and 60 meV for the transitions, respectively.

The photogenerated hot carriers collide with residual cold electrons and relax toward the bottom of each subbands rapidly through carrier-carrier, carrier-impurity, and carrier-phonon scattering with conserving their momentum and energies.

When a hot electron incidents into residual cold electron gas, the kinetic energy E of the incident electron is transferred to the electron gas. The energy exchange rate due to the scattering process is given by,[3]

$$\left(\frac{dE}{dt}\right)_{e-e} = \frac{4\pi N_e q^4}{\varepsilon_0^2 \left(2m_e^* E\right)^{1/2}} \tag{5.2.9}$$

where N_e is the residual electron density, q is the electron charge, ε_0=8.854x10^{-14} (F/cm), E is the kinetic energy of incident electron, and m_e^* is the electron effective mass. From Eq.5.2.9, the heavier the mass and the lower the kinetic energy, the smaller the energy relaxation rate. The energy relaxation due to the hot lmh-cold electron interaction is much slower than that for hot hmh-cold electron because the in-plane mass of lmh is lighter than hmh.

The initial hot hmh can release six LO phonons to reach the bottom of valence band while the initial hot lmhs emit one to two LO phonons. During the relaxation, the lmhs scatter into the hmh subband by emitting phonons. The relaxation rates for the hmh and lmh through phonon interaction are different because of the effective mass dependence on the interaction as discussed in Chapter 3 . After the electrons and holes relax to low energies, the quasi-

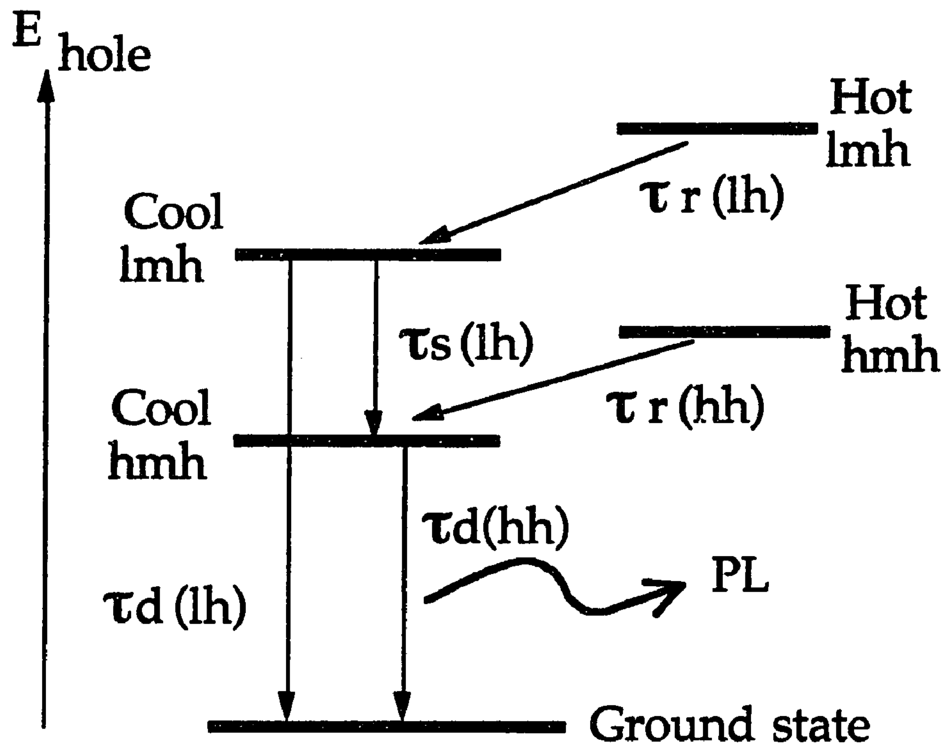

Fig. 5.2.8 Five energy level model including initial hole intra-subband thermalization, inter-subband scattering, and recombination scheme.

Fermi-Dirac distributions in both conduction and valence bands are established and are described using an electron and a hole temperatures, respectively. Finally, both electron and hole temperatures are cool down to the lattice temperature. The excess carriers recombine and emit PL photons.

5.2.3.2. Initial hot carrier thermalization model

Since there exists enough cool electrons at a low lattice temperature, the photogenerated hot electrons thermalize rapidly through electron-electron scattering and LO phonon emission within few ps. The photoexcited electron system establishes a quasi-Boltzmann distribution very quick after the thermalization is over as shown in Fig.3.4.1. However, since the minority

carrier in this system is the holes, the fast electron thermalization process can be hardly observed from the PL measurements.

Fig.5.2.8. depicts a simple five energy level model of the initial hole dynamics by intra-subband thermalization to the bottom of each subband, inter-subband scattering from the lmh to hmh subband, and recombination process. This model neglects inverse processes such as a cool hmh scatters into a cool lmh subband. The hot holes relaxed down to the bottom of each subband with time constants τ_r(hh, or lh) and become cool holes. The lmh scatters to the hmh subband with a scattering time τ_s(lh). The cool holes in each subband recombine with a decay time τ_d(hh, or lh). The PL intensities of the donor-hmh and donor-lmh transitions reveal the population of cool holes. Their rise and decay times are determined by combination of the relaxation, inter-subband scattering, and recombination decay times.

The carrier populations at these energy levels can be determined from a series of rate equations. For the hot lmh level, the population decreases by the thermalization as,

$$\frac{dN_{hot}(lh)}{dt} = -\frac{N_{hot}(lh)}{\tau_r(lh)} \tag{5.2.10}$$

while the hot hmh population decreases by the hmh thermalization as,

$$\frac{dN_{hot}(hh)}{dt} = -\frac{N_{hot}(hh)}{\tau_r(hh)} \quad . \tag{5.2.11}$$

The population of cool lmh increases by the lmh thermalization and decreases by the inter-subband scattering and recombination decay as,

$$\frac{dN_{cool}(lh)}{dt}=\frac{N_{hot}(lh)}{\tau_r(lh)}-N_{cool}(lh)\left(\frac{1}{\tau_s}+\frac{1}{\tau_d(lh)}\right) \tag{5.2.12}$$

The cool hmh increases due to the inter-subband scattering and the hot hmh thermalization and decreases by the recombination as,

$$\frac{dN_{cool}(hh)}{dt}=\frac{N_{hot}(hh)}{\tau_r(hh)}+\frac{N_{cool}(lh)}{\tau_s}-\frac{N_{cool}(hh)}{\tau_d(hh)} \tag{5.2.13}$$

where $N_{hot,cool}(lh, hh)$ are the population of hot or cool lmh and hmh states, respectively.

The rate equation was solved analytically to describe the population at each energy state. Since the PL time profiles observed are determined by the population at the cool hmh and the cool lmh states, the populations at the states are important. The population at the cool lmh level is derived to be,

$$N_{cool}(lh)=\frac{N_{hot}(lh)_{t=0}}{\tau_r(lh)}\bullet a\bullet \exp\left(-\frac{t}{\tau_x}\right)\left(1-\exp\left(-\frac{t}{a}\right)\right) \tag{5.2.14a}$$

with

$$\frac{1}{a}=\frac{1}{\tau_r(lh)}-\frac{1}{\tau_x} \tag{5.2.14b}$$

and

$$\frac{1}{\tau_x}=\frac{1}{\tau_s}+\frac{1}{\tau_d(lh)} \quad . \tag{5.2.14c}$$

The population of the cool hmh state is given by,

$$\frac{N_{cool}(hh)}{\exp\left(-\frac{t}{\tau_d(hh)}\right)}=\frac{N_{hot}(hh)_{t=0}}{\tau_r(hh)}\bullet b\left\{1-\exp\left(-\frac{t}{b}\right)\right\}+\frac{N_{hot}(lh)_{t=0}}{\tau_r(lh)}\bullet a\bullet c\left\{1-\exp\left(-\frac{t}{c}\right)\right\}$$
$$-\frac{N_{hot}(lh)_{t=0}}{\tau_r(lh)}\bullet a\bullet d\left\{1-\exp\left(-\frac{t}{d}\right)\right\}$$

(5.2.15a)

with

$$\frac{1}{b}=\frac{1}{\tau_r(hh)}-\frac{1}{\tau_d(hh)}\quad ,$$ (5.2.15b)

$$\frac{1}{c}=\frac{1}{\tau_x}-\frac{1}{\tau_d(hh)}\quad ,$$ (5.2.15c)

and

$$\frac{1}{d}=\frac{1}{\tau_r(lh)}-\frac{1}{\tau_d(hh)}\quad .$$ (5.2.15d)

From Eq.5.2.14, the PL profile for the Si-lmh transition should increase single exponentially with the combined rise time of **a**. The decay also be a single exponential with the decay constant of τ_x. Eq.5.2.15 determines the PL profile for the Si-hmh transition. It indicates that the profile decays single exponentially with $\tau_d(hh)$ and rises with the combination of the three time constant of **b**, **c** and **d** where **b** dominates the rise profile.

The data in Fig.5.2.5. (a) to (c) and Fig.5.2.6. indicate that the lmh population at the bottom increased faster than that for hmh. Since the PL intensity for the lmh increases within 6 ps after the photoexcitation as shown on the data in Fig.5.2.5, the lmh relaxation time should be around 6 ps. The data in Fig.5.2.6 shows that the rise time for the lmh subband is about 11 ps while that for the hmh subband is 18 ps.

By comparing these measured result displayed in Fig.s 5.2.5 and 5.2.6 with the population rate equation 5.2.14 (a), I find the decay and the rise times for the Si-lmh transition are,

$$a=11 \text{ ps} \tag{5.2.16a}$$

and

$$\tau_x=17.4 \text{ ps.} \tag{5.2.16b}$$

By substituting these value into Eq.5.2.14b, the lmh intra-band relaxation time is determined to be,

$$\tau_r(\text{lh})=6.7 \text{ ps.} \tag{5.2.16c}$$

For the hmh transition, the decay time is determined to be,

$$\tau_d(\text{hh})=20 \text{ ps.} \tag{5.2.16d}$$

Assuming $\tau_d(\text{lh})=\tau_d(\text{hh})=20$ ps, the inter-subband scattering time τs is determined from Eq.5.2.14c to be,

$$c=\tau s=133\text{ps.} \tag{5.2.16e}$$

Using $\tau_d(\text{hh})$ and $\tau_r(\text{lh})$ for Eq. 5.2.15d, d is determined to be,

$$d= 10.08 \text{ ps.} \tag{5.2.16f}$$

Since the rise components d and c do not contribute much as seen in Eq. 5.2.15a, the rise time of 18 ps for the hmh PL is dominated by b (the combination τ_r(hh) and τ_d(hh)). Therefore,

$$1/18(ps)=1/\tau r(hh)-1/\tau d(hh)\ . \qquad (5.2.16g)$$

The hmh intra-subband relaxation time τr(hh) is evaluated to be 9.5 ps.

The peak positions for the hmh and the lmh PL are found to be 4.5 ps different as shown in Fig. 5.2.6. This time delay arises from the slow hole feeding from the lmh subband through the slow inter-subband scattering. (the second term on the right hand side of Eq.5.2.15a)

The initial kinetic energies are 60 and 230 meV for the lmh and hmh, respectively. The average intra-subband energy relaxation rates are estimated to be 9 and 24.2 meV/ps for the lmh and hmh by dividing the initial kinetic energies by the τ_r(lh, hh), respectively. Assuming the intra-subband relaxation process is due to LO phonon interaction, the relaxation rate is depending on a square root of hole mass as given by Eq.3.3.8. The estimated relaxation rates for the hmh and lmh subbands are 2.7 times different while the square root of mass difference between the lmh and hmh is 2.3 times ($\sqrt{0.45/0.082}$=2.3) which is in reasonably agreement with the estimated energy relaxation rates.

Since the subband separation between hmh and lmh is about 14 meV due to the biaxial strain and the inter-subband relaxation time was evaluated to be 134 ps, the inter-subband thermalization rate is calculated to be about 0.1 meV/ps which may be dominated by acoustic phonon interaction.

Since the system time resolution is about 10 ps, further investigation is still required to conclude the relaxation times for the lmh and the hmh.

5.2.3.3 Hole temperature cooling

After the holes are thermalized and reached same hole temperature T_h, the hole cooling occurs. This process is evaluated by fitting experimentally obtained PL spectra sliced from 3D PL image at various delay times with calculated spontaneous emission PL spectra from Fermi's golden rule assuming an equilibrium hole temperature.

The GaAs band structure dispersion under a stress remains same and shifted to a lower energy. The band structures for the hmh and lmh are given by,

$$E_j = \frac{h^2}{2m_0}\left\{ a_j (k_x^2 + k_y^2) + b_j k_z^2 \right\} \qquad (5.2.17a)$$

where a_j and b_j are given by,

$$a_{j=\pm 1/2\,(\pm 3/2)} = \gamma_1 - \gamma_2 \quad (\gamma_1 + \gamma_2) \qquad (5.2.17b)$$

$$b_{j=\pm 1/2\,(\pm 3/2)} = \gamma_1 + 2\gamma_2 \quad (\gamma_1 - 2\gamma_2) \qquad (5.2.17c)$$

where $\gamma_1 = 6.85$, $\gamma_2 = 2.1$ are Luttinger parameters for GaAs.

The quasi-Fermi levels in the conduction and valence bands are determined using the relationship given by Eq.s 3.6.9 and 3.6.10.

For the conduction electrons, the electron distribution function f_c is determined by a Boltzmann distribution function because the electron density is much less than the effective density of state ~10^{21} cm^{-3} as,

$$f_c = N_c \exp\left(-\frac{E_{fc}}{k_B T_L}\right) \quad (5.2.18a)$$

with the effective density of states of the conduction band as,

$$N_c = 2\left(\frac{2\pi\, m_c^* k_B T_L}{h^2}\right)^{3/2} . \quad (5.2.18b)$$

The density of states is given by Eq. 3.6.9b. Therefore, the quasi-Fermi level E_{fc} in the conduction band is determined by,

$$N_D^+ + \Delta n = \int_0^\infty 4\pi\left(\frac{2m_c}{h^2}\right)^{3/2} E^{1/2} N_c \exp\left(-\frac{E - E_{fc}}{k_B T_L}\right) dE \quad (5.2.19)$$

where N_D^+ is the ionized donor density, Δn is photogenerated electrons, and E_{fc} is the quasi-Fermi level. The ionized donor density is determined by the lattice temperature T_L and is given by,

$$N_D^+ = \frac{N_D}{(N_D/N_c) \bullet \exp(E_d / k_B T_L) + 1} \quad (5.2.20)$$

where N_D is doping density and E_d is the donor ionization energy. At 23 °K lattice temperature, the effective density of states is 9.2×10^{21}. The density of ionized donor is negligibly small amount(7% of the total doped ions). The most donors are neutral(not ionized). The initial donor electron density of 10^{16} cm^{-3} and the injected electron-hole pair density of 5×10^{15} cm^{-3} are used. Substituting the electron density of 10^{16} into Eq.5.2.19, the quasi-Fermi level is determined to be E_{fc}= 135 meV.

The quasi-Fermi level in the valence band is determined as same manner as the quasi-Fermi level in the conduction band using Eq. 3.6.10. Since the Carbon acceptor may not be ionized at the lattice temperature, the photogenerated holes determine the quasi-Fermi level in the valence band by following equation as,

$$\Delta n = \sum_{i=hh,\,lh} \int_0^\infty 4\pi \left(\frac{2m_i}{h^2}\right)^{3/2} E^{1/2} N_{v,i} \exp\left(-\frac{E - E_{fv} + \Delta_i}{k_B T_L}\right) dE \tag{5.2.21}$$

where the summation runs for the hmh and lmh subbands, Δ_i for the hmh is zero and Δ_i for the lmh is 16 meV in this case. The calculation is rather complicate to determine the quasi-Fermi level in the valence band. Therefore, the quasi-Fermi level of the valence band was kept as a fitting parameter and was determined by the fit in the analysis. The quasi-Fermi level was 22 meV.

Once the quasi-Fermi levels in the conduction and valence bands are determined, the transition probabilities between the conduction and valence bands and between the Si donor to the valence band can be determined using Eq.3.6.11.

Since the measurement was carried out at the 23 °K lattice temperature, most of doped electrons located at the donor level. The density of electron in the conduction band was 7% of the total doped electrons. Therefore, the contribution of the conduction to valence band transition to the total PL intensity profile is small. The Si-lmh and Si-hmh transitions dominate the PL spectrum. Therefore, the following fitting calculation is only for the transition between the donor to the hmh and lmh subbands.

The matrix element of the donor to the valence band transition is given by Eq. 3.6.8b which is,

$$|M_{if}|^2 = 64\pi\, a^{*3} (1+a^{*2} k_b^2)^{-4} V^{-1} \bullet |M_b|^2 \qquad (5.2.22a)$$

where a* is the effective Bohr radius and is given by $a^* = 4\pi\varepsilon\hbar^2/m^*q^2$ and $|M_b|^2$ is given by Eq.3.6.8a which is,

$$|M_b|^2 = \frac{m_0^2 E_g (E_g + \Delta)}{12\, m_c (E_g + 2\Delta/3)}$$
$$= \xi\, m_0\, E_g \qquad (5.2.22b)$$

Therefore, the transition probability of the donor to the valence band is given by,

$$W(E) = A\left(\frac{4}{\pi}\right)^2 |M_b|^2 a^{*3} \left(N_D - N_D^+\right) \bullet$$

$$\left[\int d\vec{k_v}\,\delta(E-E_g-E_d)\frac{f_v(\vec{k_v})}{\left(1+a^{*2}k_v^2\right)^4} + \int d\vec{k_v}\,\delta(E-E_g-E_d-\Delta)\frac{f_v(\vec{k_v})}{\left(1+a^{*2}k_v^2\right)^4}\right]$$

(5.2.23)

where the Fermi distribution function f_V in the valence band is approximated to be a Boltzmann distribution function ($f_V=\exp\{-(E-E_{fv})/k_BT_h\}$) because the density of photogenerated holes are much less than the effective density of holes. The kinetic energy of holes is determined by the hole dispersion curve given by Eq. 5.2.17.

By integrating Eq.5.2.23 with respect to the wave vector along all crystal orientation within the valence band structure given by Eq.s 5.2.17a, b, and c, the total PL spectrum arising from the donor to the valence subbands can be evaluated using the transition probability function given by,

$$W(E)=AE_gE\frac{\Delta n}{N_{v\pm1/2}}\frac{1}{\left\{1+{m_{\pm3/2}}/{m_{\pm1/2}}\right\}^{3/2}\bullet\exp\left(-\Delta/k_BT_L\right)}\bullet\exp\left\{-\frac{E-E_{g\pm1/2}+E_d}{k_BT_h}\right\}$$
$$\bullet 64\pi a_B^3 N_D\bullet\left[\sum_{\pm1/2,\pm3/2}\frac{E-E_{gj}+E_d}{\left(a_j \text{ or } b_j\right)^{1/2}}\bullet G(E-E_{gj}+E_d)\right]$$

(5.2.24a)

with

$$G(x)=\int_0^1\frac{dy}{\left\{g_a-(g_a-g_b)y^2\right\}^4}$$

(5.2.24b)

where

$$g_{a(b)} = 1 + \frac{2m_0}{h^2} \frac{a_B^2}{a_j(b_j)} x \quad . \qquad (5.2.24c)$$

and the valence hole distribution function was approximated by a Boltzmann distribution because the density of carrier is much smaller compare with the effective density of valence states(non-degenerate).

For the fitting, the electron temperature T_e is assumed to be same as the thermalized hole temperature T_h. The calculated spectra were convoluted with a Lorentzian homogeneous line broadening factor Γ. Therefore, the number of fitting parameter is two: Th and Γ. The broadening factor was determined to be a constant value of 0.953 meV to fit the experimental spectra. Fig.5.2.9. (a) and (c) show the measured PL spectra sliced from the 3D PL spectrum at the time delay of 19~21 ps and 51~54 ps, respectively. The fitting curves are shown in Fig.5.2.9. (b) with T_h=140 °K and (d) with T_h= 85 °K calculated for the spectra (a) and (c), respectively. Since the density of states for the lmh is three times larger than the hmh subband, the difference in the hole temperature gives large difference in the lmh peak intensity. Therefore, T_h can be determined accurately by fitting the lmh intensity accurately.

The evaluated hole temperatures T_h at various delay times are depicted in

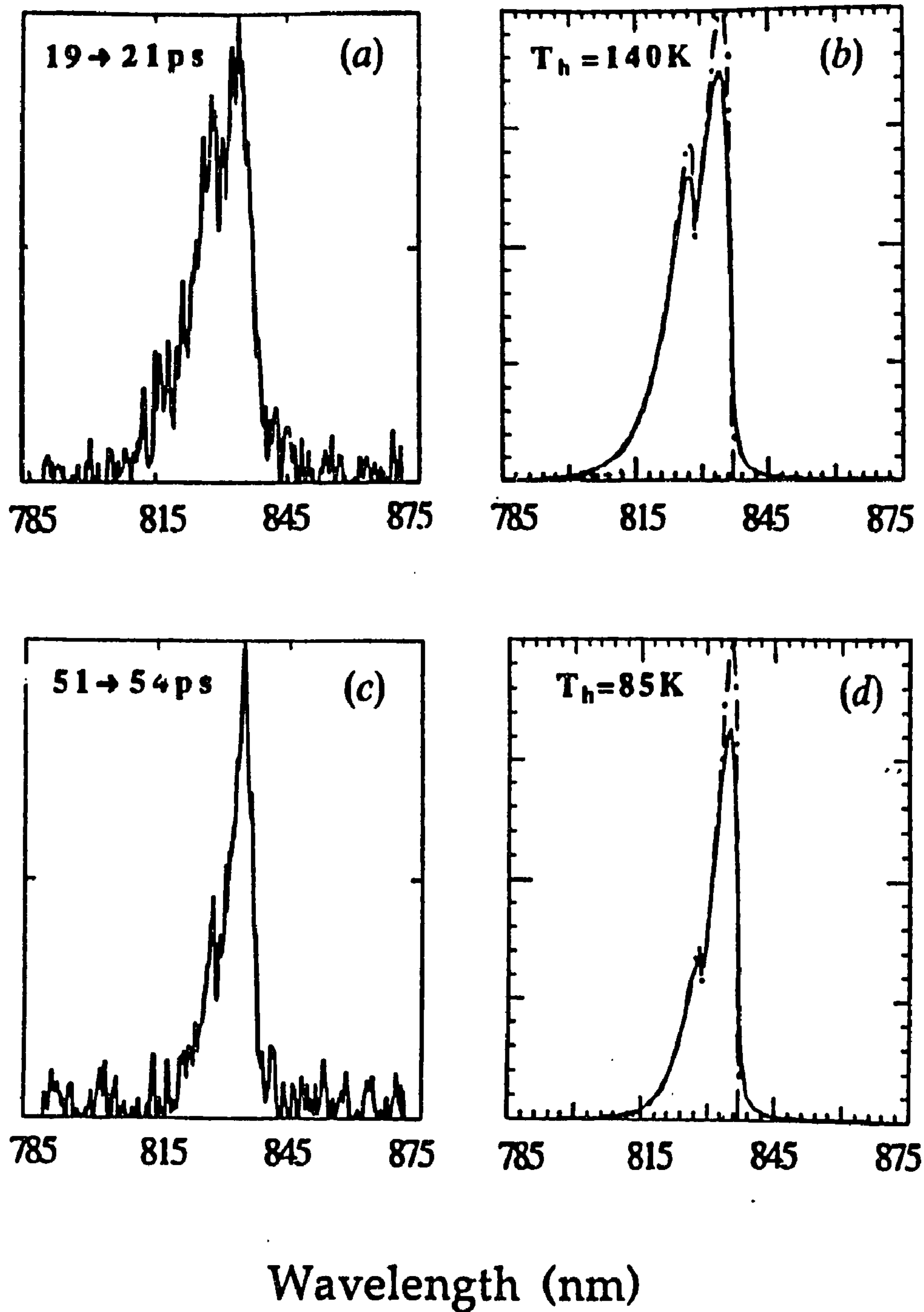

Fig.5.2.9. Measured PL spectra (a) at 19~21 ps (c) 51 ~54 ps and calculated curves using (b) Th=140 °K and (d) Th=85 °K to fit (a) and (c), respectively.

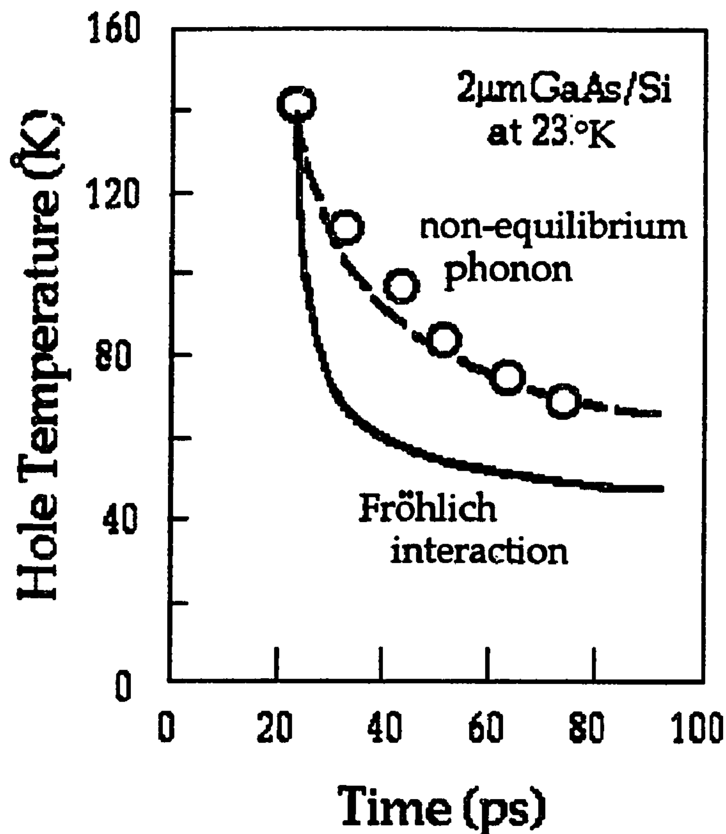

Fig.5.2.10. Hole cooling process analyzed with Fröhlich interaction equation (solid curve) and with non-equilibrium phonon taken into account(dashed curve).

Fig. 5.2.10. as open circles. The hole temperature cools down exponentially and reaches about 56 °K within 100 ps. Since the lattice temperature is 23 °K in this case, the hole temperature should becomes 23 °K after long enough delay time. To estimate energy relaxation time and rate, a single exponential function was fit to the subtracted curve after subtracting 56 °K from the data points. The energy relaxation time was found to be 28 ps. Fitting a simple linear relaxation, the energy relaxation rate (hole cooling rate) was determined to be 0.12 meV/ps. The order of this energy relaxation rate is due to LO phonon at a 80 °K carrier temperature as discussed in Chapter 3.

The Fröhlich interaction theory in a non-degenerate bulk semiconductor was investigated to understand this energy relaxation process. The average energy relaxation rate due to LO phonon interaction was given (for example, by Shah) as,[4)]

$$\left\langle\frac{dE_h}{dt}\right\rangle = k_B \left\langle\frac{dT_h}{dt}\right\rangle$$

$$= \frac{h\omega_{LO}}{3\beta} F(T_L, E_h) \quad , \qquad (5.2.25a)$$

with

$$F(T_L, T_h) = \left[\frac{1}{K_\infty} - \frac{1}{K_s}\right] \bullet \left[\frac{e^{x_L - x_h} - 1}{e^{x_L} - 1}\right] \bullet \left[(x_h)^{1/2} e^{x_h/2} K_0(x_h/2)\right] \qquad (5.2.25b)$$

where β is a factor determining oscillator strength for donor-lmh transition(β=0.4), E_h is the hole kinetic energy, T_L is the lattice temperature, and $F(T_L, E_h)$ is a function determined by T_L and E_h. $x_L=\hbar\omega_{LO}/k_BT_L$ and $x_h=\hbar$)ω_{LO}/k_BT_L. To compute the curve, an initial hole temperature T_{h0} was given first. Then, calculate the energy relaxation rate $<dT_h/dt>$ at T_{h0}. After 1ps, the hole temperature decreases with a value calculated by $<dT_h/dt>$x $1x10^{-12}$ °K. The hole temperature Th1 after the 1 ps delay time is determined to be $T_{h1}=T_{h0}-<dT_h/dt>$x $1x10^{-12}$. Continuously calculating the hole temperature as function of delay time, the hole temperature relaxation curve was obtained.

The solid curve is a theoretically expected curve. The experimentally obtained energy relaxation rate was found to be about 6 times slower than the expected energy relaxation time from the Fröhlich interaction theory.

The relaxation speed may be slowed down by non-equilibrium LO phonon or by acoustic phonon interaction. Suppose the electron system looses its average kinetic energy to lattice through LO phonon emission with a rate given by Eq.3.3.7. After the photoexcitation, the electron system temperature T_e decreases by the LO phonon interaction and is given as,

$$\frac{dT_e}{dt} = -\frac{1}{k_B}\left\langle\frac{dE_e}{dt}\right\rangle = -P_0F(T_e, T_p) \quad . \tag{5.2.26a}$$

where F(Te,Tp) is a function given by,

$$F(T_e,T_p) = \frac{\exp(x_p - x_e) - 1}{\exp(x_p) - 1} \bullet \left(\frac{x_e}{\pi}\right)^{1/2} \exp\left(\frac{x_e}{2}\right) \bullet K_0\left(\frac{x_e}{2}\right) \tag{5.2.26b}$$

where $x_{p,e}=E_{LO}/k_BT_{p,e}$ and K_0 is the Bessel function of zero order. The phonon system gains the energy from the electron system and looses the energy through LO phonon decay to acoustic phonons. The phonon temperature T_p is given by,

$$\frac{dT_p}{dt} = P_0F(T_e,T_p) - \frac{N_p(T_p)}{\tau_p} \bullet \frac{dT_p}{dN(T_p)} \tag{5.2.26c}$$

where $N_p(T_p)$ is the phonon occupation number at the phonon temperature T_p and τ_p is the LO phonon lifetime. As the phonon lifetime is assumed to be long, the energy transfer from the electron system to the phonon system is regulated by the non-equilibrium phonons.

Solving Eq.s 5.2.26 with respect to the electron temperature, the electron average energy relaxation process was investigated. Fig. 5.2.10. shows a slow (~8ps) phonon lifetimes shown in a dashed curve. The dashed curve fits to the obtained electron temperature cooling data. The non-equilibrium hot phonons are built-up due to the 8ps phonon lifetime in the hot electron gas. The cooling rate is equivalent to that of GaAs calculated from a material parameter and cooling rate was found to be six times smaller than that expected rate without non-equilibrium phonon effect.

To further investigate the hole energy relaxation process, average hole kinetic energy $<E_k(t)>$ was evaluated from the 3D PL spectrum using,

$$<E_k(t)> = \int_{E1}^{E2} I(E,t) \bullet E \, dE / \int_{E1}^{E2} I(E,t) \, dt - E_0 \qquad (5.2.27)$$

where E_1 and E_2 are low and high energy edges of the PL spectrum because the experiment is carried out within a certain PL energy region, and E_0 is the lowest donor-hmh transition energy determined from a steady state PL peak positions at the same lattice temperature. By subtracting E_0=1.4949 eV, the average hole kinetic energy $<E_k(t)>$ was calculated as shown in Fig. 5.2.11. The average hole energy relaxation time was evaluated from the $<E_k(t)>$ data to be 26.6 ps by fitting a single exponential curve as shown in Fig.5.2.11. This time constant agrees with the result of hole temperature cooling analysis using the spontaneous emission spectra fit as shown in Fig.5.2.10. Therefore, the hole cooling time was confirmed to be 27±2 ps. The average energy analysis

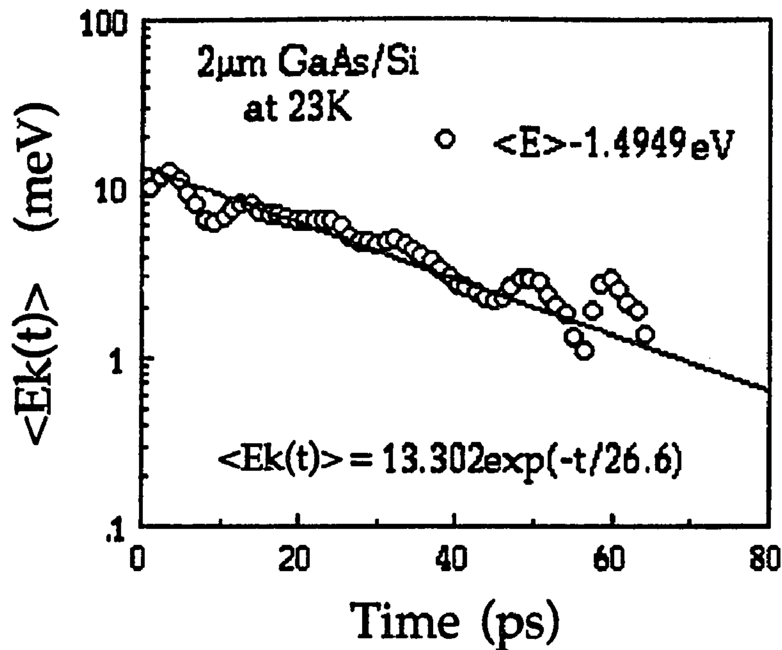

Fig. 5.2.11. Average hole kinetic energy relaxation for the 2μm GaAs/Si at 23 °K lattice temperature. The kinetic energy is calculated by subtracting 1.4949 eV from <E>.

(requiring no fitting procedure) was confirmed to be useful method to determined the hole cooling dynamics.

5.2.4. Summary

The hole dynamics in a 2μm thick n-type GaAs/Si under a built-in biaxial tension has been investigated. The internal stress enabled me to study the lmh and hmh dynamics separately in a GaAs bulk.

The hot lmh and hmh intra-subband relaxation (thermalization) times were evaluated to be about 6.7 and 9.5 ps, respectively. The hot hole thermalization rate was estimated to be between 9 and 24.3 meV/ps. The relaxation rates were found to depend on the hole mass as the Fröhlich interaction theory predicts. After the hmh and lmh thermalize to k=0, the warm

hole system is cooled to the lattice temperature with a hole cooling time of 27±2 ps and with a hot hole cooling rate (assuming linear energy relaxation to lattice) of 0.12 meV/ps. The hole cooling time were further confirmed using the average hole kinetic energy calculation. The hole cooling or energy relaxation rate was analyzed in terms of non-equilibrium LO phonon interaction and was found to be 6 times slower than the theoretically expected rate. I performed additional experiment on 4μm thick GaAs/Si sample to obtain better signal to noise ratio and make the dynamics discussed here more accurate.

5.3. 4μm thick n-type GaAs/Si

5.3.1. Introduction

Hole dynamics in the strained GaAs/Si with 2μm GaAs epilayer thickness has been investigated and discussed in detail in the previous section 5.2. Since the signal-to-noise ratio for the time-resolved PL spectrum for the 2μm GaAs/Si was poor, a thicker GaAs epilayer was required to repeat same experiment under higher signal-to-noise ratio. In this section, 4μm thick GaAs epilayer grown on a Si substrate was investigated as same manner as the 2μm thick GaAs/Si. This sample should have less non-radiative process because the photoexciting region is away from the interface between GaAs and Si substrate where defect density is higher. The built-in stress should be about the same order at 4 °K.

For the case of the 2μm thick GaAs/Si sample, I found that the lmh subband locates about 14 meV lower in energy in the valence band than the hmh subband at 4 °K lattice temperature. The energy separation arises from 2.3 kbar of the built-in tension. The initial hole intra-subband thermalization time, inter-subband scattering, and recombination with donor electrons were found to depend on the subband characteristics. The intra-subband relaxation times for the lmh and hmh subbands were determined to be 6.7 and 9.5 ps, respectively. The inter-subband transition from the lmh to hmh subbands is estimated to be 134 ps. The lmh and hmh recombination lifetimes including non-radiative recombination were assumed to be same and determined to be 20 ps.

Since the stronger PL from the sample was observed from the 4μm thick GaAs/Si sample, the hole dynamics can be investigated with higher signal-to-noise ratio in more detail.

5.3.2. Sample and experimental setup

The 4 μm thick GaAs epilayer doped with Si at 3.5 x 10^{16} cm^{-3} was grown on a {100} Si substrate 4° tilted toward <110> by a MBE machine and was annealed at 820°C for 10 minutes to release residual stress and to remove dislocations at the interface. The sample was fabricated by Prof. Morkoc's group at University of Illinois, Arbana-Champaign.

Only time-resolved PL spectroscopy was carrier out with the 4μm thick GaAs/Si sample. The CPM laser beam with 10 mW(2.0 eV photon energy and 80 fs laser pulse duration) photoexcited the sample placed in an optical cryostat dewar which was cooled to be 4 °K Helium temperature. The PL from the sample was collected into a 25 cm spectrograph (SPEX 1681B) incorporating a 600 grooves/mm reflection grating blazed at 1μm. The streak camera coupled to the spectrograph incorporated S-20 photocathode which generates much less thermal electron and has similar spectral sensitivity at the PL wavelength region compare with the S-1 type photocathode streak camera used for the evaluation of the 2μm thick GaAs/Si. The streak camera was synchronized with the laser pulses from the CPM laser operated at 82 MHz repetition rate.

5.3.3. Experimental results

A time-resolved PL spectrum of the 4μm GaAs/Si at 4 °K lattice temperature is shown in Fig. 5.3.1 in a 3D display. Comparing with the PL spectrum obtained for the 2 μm GaAs/Si as shown in Fig.5.2.3, it is clear that the PL signal intensity is much stronger and shows clear PL kinetics. The PL profile is similar to the 2μm GaAs/Si sample. This feature indicates the 4μm GaAs/Si contains less density of defects (which causes less non-radiative decay) in the

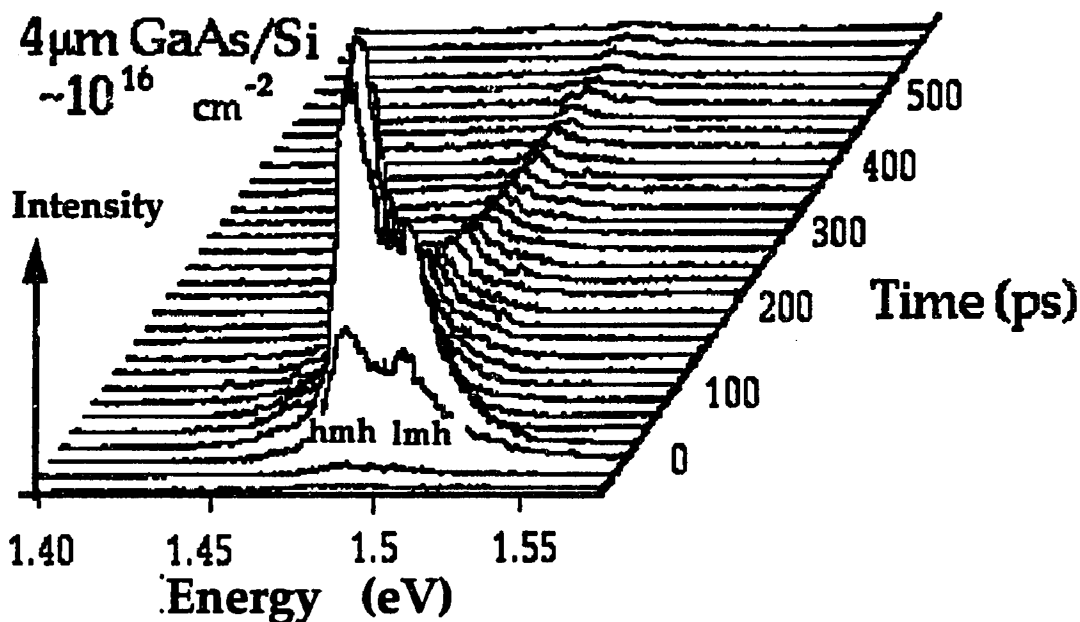

Fig. 5.3.1. Time-resolved PL spectrum in three dimensional display for the 4μm thick GaAs/Si sample obtained at 4 °K lattice temperature.

photoexcitation region. Two peaks arising from the Si-hmh and Si-lmh transitions were observed.

Integrating the 3D PL spectrum from t=0 to 500 ps, the time integrated PL spectrum shows three distinguish PL peaks originated from Si donor level to heavy mass hole (hmh) at 1.484 eV, Si donor level to light mass hole (lmh) at 1.501 eV, and a conduction band to Carbon acceptor transition at 1.4685 eV. The energy separation of the hmh and the lmh subbands is 17 meV. The spectrum clearly shows same features as 2μm GaAs/Si sample. Using an equation which determines the energy split arising from the biaxial tension X in kbar,

$$\Delta E_{c\text{-}hmh} - \Delta E_{c\text{-}lmh} = (-10.36 + 4.239) \bullet X$$

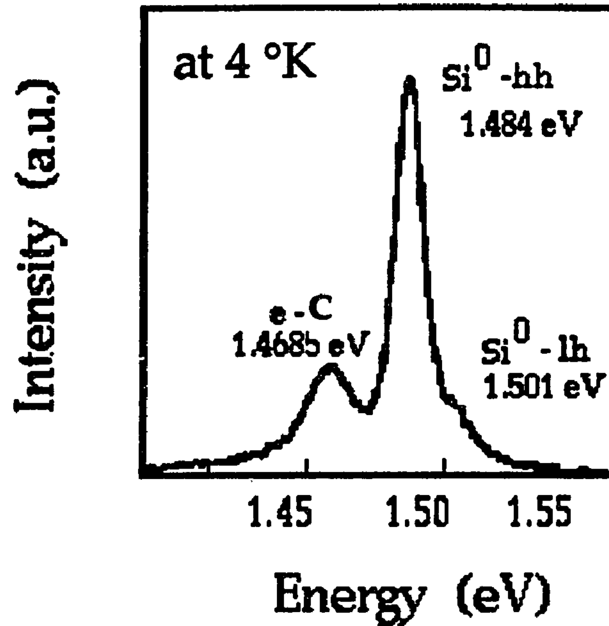

Fig. 5.3.2. Time integrated PL spectrum from t=0 to 500 ps for the 4μm GaAs/Si at 4 °K lattice temperature, showing three peaks corresponding to donor to hmh, donor to lmh, and conduction band to Carbon acceptor transitions.

$$= -6.02 \bullet X \quad (\text{meV}). \qquad (5.3.1)$$

The magnitude of built-in stress is calculated to be 2.8 kbar which is 0.5 kbar higher than that for the 2μm thick GaAs/Si case (2.3 kbar). Since the 4μm thick GaAs sample was annealed at 820°C for 10 minutes, the residual strain and the density of defects decreases. After the annealing, the sample was cooled down to the measurement temperature of 4 °K, the less density of defect may prevent to release its strain arising from the thermal expansion coefficients between GaAs and Si. As the result, the annealed 4μm thick sample contains higher strain than the 2μm thick sample without annealing.

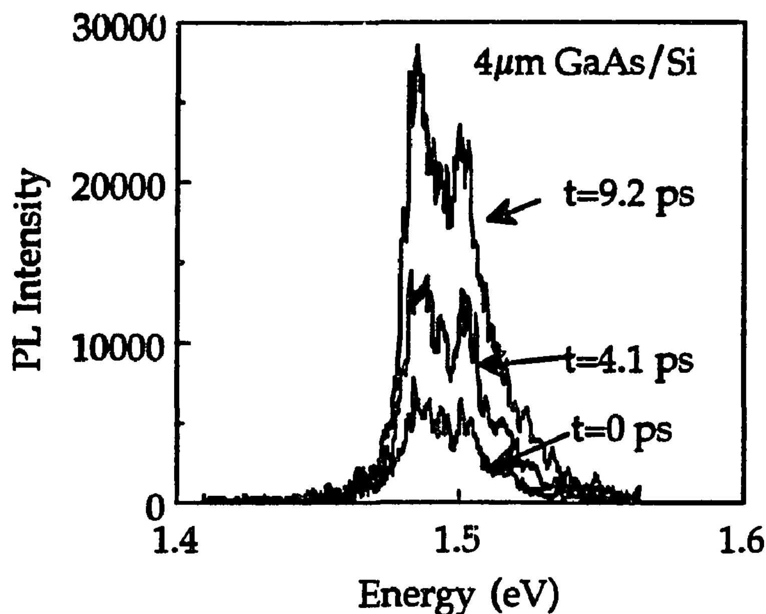

Fig. 5.3.3 Initial PL spectral change for the 4μm GaAs/Si at 4 °K lattice temperature.

To investigate initial hmh and lmh thermalization process, as discussed in the previous section 4.1, the PL spectral change at an initial time are obtained from the 3D PL spectrum (Fig.5.3.1.) is demonstrated in Fig. 5.3.3. The PL from the donor-lmh transition increases faster than the donor-hmh transition. The lmh and hmh PL intensities become same around 4 ps.

To observe the hmh and lmh thermalization process clear, the PL temporal profiles of the Si-hmh and Si-lmh transition peaks are shown in Fig. 5.3.4 (a) for short time window and (b) for long time window with the conduction band to the Carbon acceptor transition profile. The Si-lmh transition PL increases slightly faster compare with the Si-hmh PL. The rise times for the Si-hmh and the Si-lmh transitions were obtained by fitting a single exponential to the rising profiles and are determined to be 8.3 and 5.6 ps, respectively. The peak positions (indicated by arrows) differ about 6 ps as shown in Fig,.5.3.4 (a).

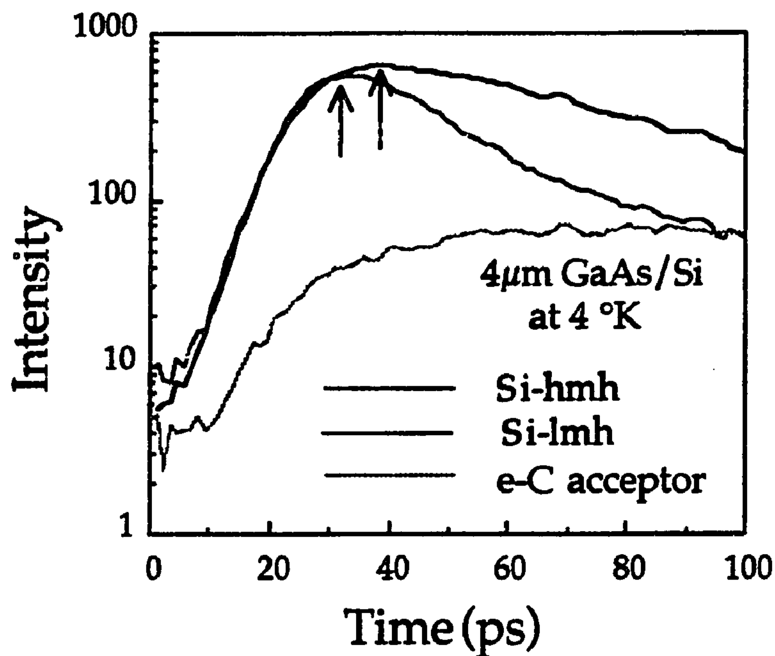

(a)

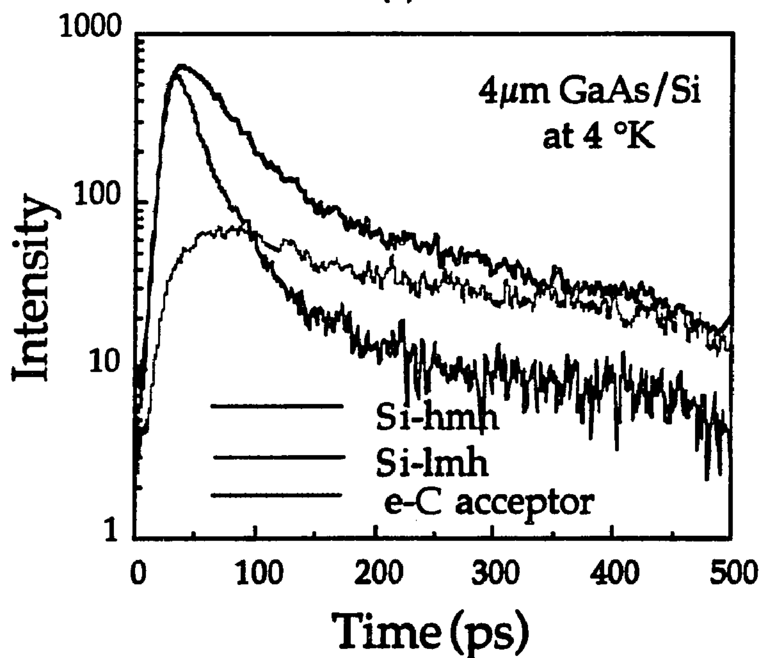

(b)

Fig. 5.3.4 Temporal profiles for the donor-hmh, the donor-lmh, and conduction electron-carbon acceptor transitions in the 4μm GaAs/Si (a) at the short time window and (b) for the long time window.

This feature was also observed for the 2μm GaAs/Si in the section 5.1. Another feature observed in Fig.5.3.4 (b) is that the PL profiles for the Si-hmh and Si-lmh transitions show two decay components while the conduction electron-Si acceptor transition profile shows almost single decay profile. Fitting a single exponential function to the PL profiles at early delay time and later time, the two decay components were determined. The fast decay components for the Si-hmh and Si-lmh transitions were evaluated to be 28.2 and 25.9 ps while the slow decay components to be 246 and 353 ps, respectively.

5.3.4.Discussion

To compare the hole dynamics investigated for the 2 μm thick GaAs/Si sample in section 5.1, the experimental data obtained for the 4μm thick GaAs/Si was examined using the similar model as the 2μm thick GaAs case.

5.3.4.1 Initial hole relaxation and slow recombination tail

Using same five energy level model as the 2μm thick GaAs/Si case, the intra- and inter-subband relaxation times, decay times were evaluated from the 4μm GaAs/Si PL time profiles. According to the solution of the rate equations Eq.s 5.2.14c, 5.2.15b, 5.2.15c, and 5.2.15d, the time constants are determined by following equations.

The rise time of the Si-lmh transition is determined as,

$$\frac{1}{\tau_r(lh)} - \frac{1}{\tau_x} = \frac{1}{5.58} \qquad (5.3.2)$$

where the decay time of the Si-lmh transition τ_x is given and was observed by,

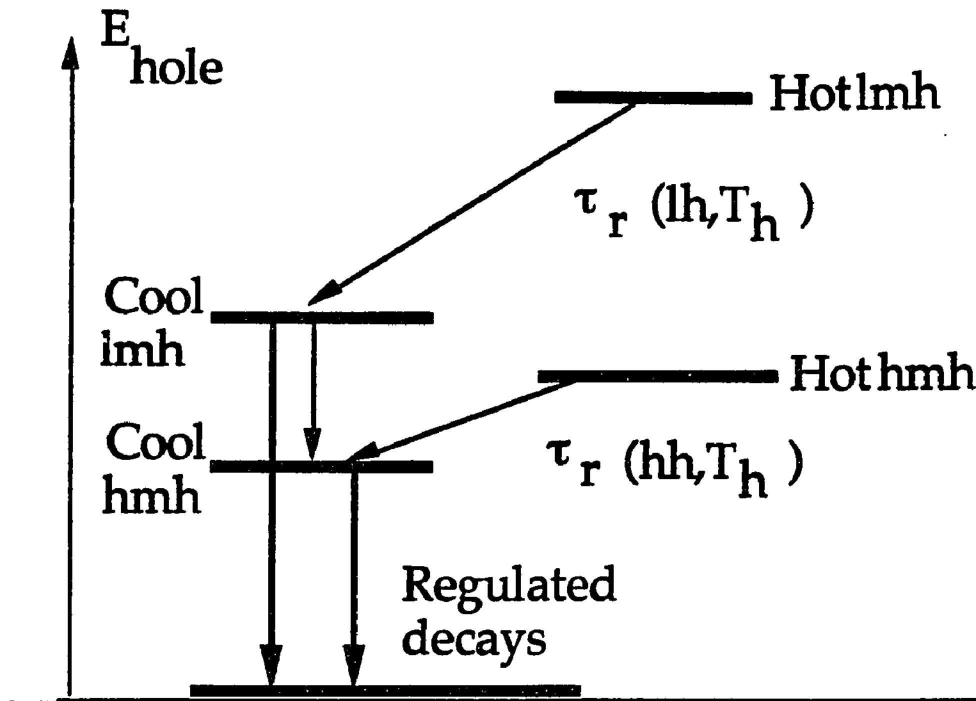

Fig.5.3.5. A hole temperature dependent intra-subband relaxation and recombination model.

$$\frac{1}{\tau_x} = \frac{1}{\tau_s} + \frac{1}{\tau_d(lh)} = \frac{1}{25.9} \qquad (5.3.3)$$

From the Eq. 5.3.2 and 5.3.3, the intra-subband thermalization time $\tau_r(lh)$ is determined to be 4.59 ps.

The rise time for the hmh transition is determined by,

$$\frac{1}{\tau_r(hh)} - \frac{1}{\tau_d(hh)} = \frac{1}{8.32} \qquad (5.3.4)$$

and the decay time is assumed to be $\tau_d(hh)$=28.2 ps(neglecting the slow decay component). Thus the intra-subband thermalization time for the hmh is solved

to be 6.42 ps. Assuming the lmh decay is same as that of the hmh of 28.2 ps, the inter-subband scattering time is estimated from Eq. 5.3.3 to be 318 ps.

The PL time profiles in Fig. 5.3.4.(b) show two decay components for the hmh and lmh transitions. In the 2μm thick GaAs/Si sample, I have adopted a five energy level model which describes direct transitions between the donor level to the bottom of the valence subbands and showed single and fast decay components. This five energy level model with simple relaxation processes can not explain the slow decay components.

When the hole temperature dependence on the intra-subband hole relaxation processes is taken into account as schematically depicted in Fig.5.3.5, the fast and slow decay components can be understood as follows.

At the initial time, the hole system is hot and interacts with LO phonon. The hot holes becomes warm and relax to the bottom of the valence band. As the hole temperature becomes cooler, acoustic phonon interaction becomes dominating process. Since the acoustic interaction is slow process, the relaxation time determines the PL decay time not the lifetime of the holes. Namely, the acoustic phonon interaction becomes the bottle neck for the PL time kinetics. Using this model, the slow and fast PL decay profiles are explained. For the 2μm thick GaAs/Si case, this process might be present. However, the signal to noise ratio was so poor that it was hardly resolved.

5.3.4.2. Average energy relaxation

The non-equilibrium phonon effect on the PL long decay profiles and the average energy relaxation process were investigated. The average hole energy

<E(t)> for the 4 μm GaAs/Si at 4 °K lattice temperature was calculated from the 3D PL spectrum using the equation,

$$<E(t)> = \int_{E1}^{E2} I(E, t)\bullet E \, dE / \int_{E1}^{E2} I(E, t) \, dt \qquad (5.3.5)$$

where E_1 and E_2 are low and high energy edges of the PL spectrum. The average energy (thick curve) evaluated is shown in Fig. 5.3.6. with the spectrally integrated PL time profile(thin curve) between E1 and E2. The fast energy relaxation was found to be over within 100 ps. The non-equilibrium phonon must be established within the time scale and the accumulated LO phonon should decay quick after the energy relaxation is over because the LO phonon lifetime is a few ps.

To determine the average hole kinetic energy $<E_k(t)>$ relaxation time, the PL peak energy 1.487 eV is subtracted from the average hole energy <E(t)> as shown in Fig. 5.3.7. By fitting a single exponential curve to the evaluated average hole kinetic relaxation curve between 55 and 75 ps delay times, the average energy relaxation time was extracted to be 12.6 ps. The average hole energy relaxes down from 1.497 eV to 1.487 eV within 50 ps. The rapid average hole energy relaxation is due to LO phonon interaction as same as the 2μm GaAs/Si case in which the energy relaxation time was 28 ps. The relaxation time for the 4μm GaAs/Si is found to be twice faster than the 2μm GaAs/Si. Since the density of dislocations in the 4μm thick GaAs/Si are much less than the 2μm GaAs/Si, the non-radiative process generates much less phonons in the 4 μm GaAs/Si. The reason why the energy relaxation becomes faster may be due to the LO phonon density is lower for the 4μm GaAs/Si case so that the phonon re-absorption effect is negligible.

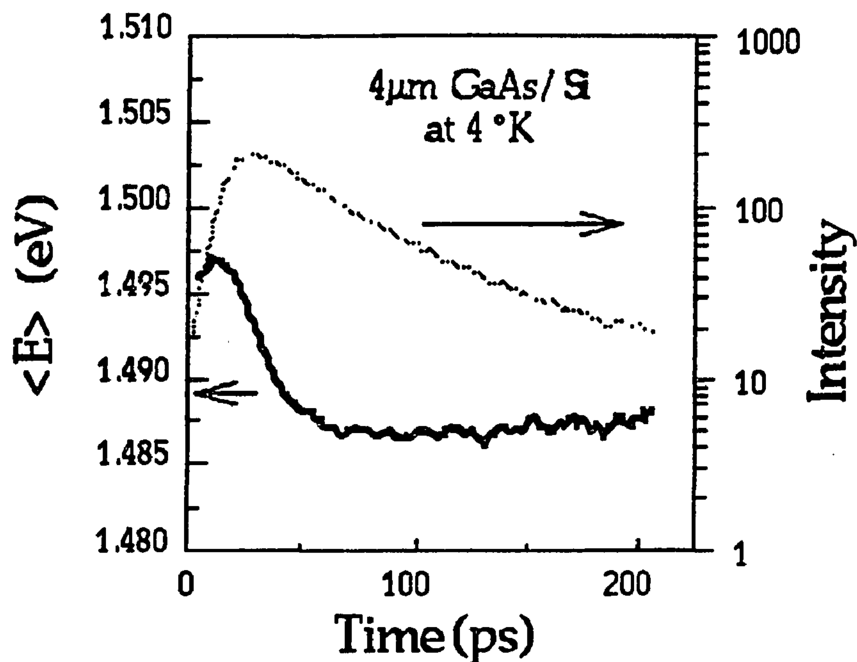

Fig. 5.3.6. Average hole energy and PL intensity profiles for the 4µm GaAs/Si at 4 °K lattice temperature.

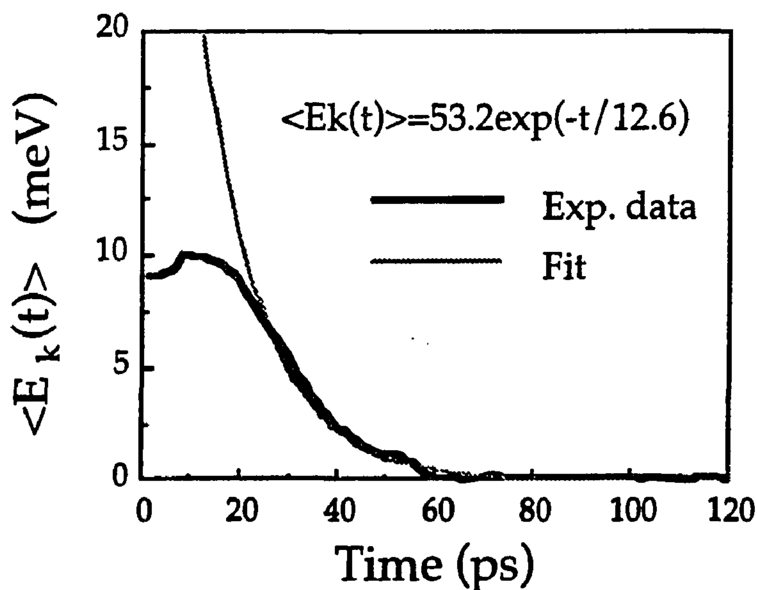

Fig.5.3.7. Average hole kinetic energy relaxation within 100 ps delay time. Experimental data are shown in thick solid curve while a single exponential fit between 55 and 75 ps delay time is shown in thin dotted curve.

Assuming a linear energy relaxation, the hole energy relaxation rate is calculated to be 0.2 meV/ps which corresponds to the energy relaxation rate for LO phonon interaction and is larger than that of the 2μm GaAs/Si.

5.3.5. Summary

Hole dynamics under a built-in biaxial tension in a 4μm thick GaAs bulk grown on a Si substrate has been investigated using the time-resolved PL spectroscopy at a low lattice temperature to confirm the hole dynamics investigated in the 2μm GaAs/Si as discussed in the previous section.

The intra-subband hole thermalization time for the hmh and the lmh subbands were estimated to be 8.5 and 5.6 ps, respectively and the feature that the lmh relaxes faster than the hmh to the bottom of the subband was confirmed to be true. The inter-subband transition time was found to be very slow compare with the intra-subband thermalization times. The recombination time for the 4μm GaAs/Si was found to be slower than that of the 2μm GaAs/Si sample. The difference in the decay times was attributed to the difference in the density of dislocations which causes non-radiative decay. By using thicker epilayer, the effects of the non-radiative transition on the PL kinetics can be reduced. The fast and slow decay profiles were explained in terms of LO and acoustic phonon interactions during the hole intra-subband relaxation processes. The hole average energy relaxation time was evaluated to be 12.6 ps assuming single exponential relaxation from the average hole energy calculation. The hot hole cooling rate was determined to be 0.2 meV/ps which was twice larger value than that in the 2μm GaAs/Si because the number of dislocation is less in the 4μm GaAs/Si sample and the LO phonon density is low to be reabsorbed by the holes.

5.4. Conclusion

In this chapter, the hole thermalization and cooling process in the n-type GaAs/Si have been investigated. It has been demonstrated that the built-in tension removed the valence subband degeneracy and enabled the separate evaluation of the hmh and lmh dynamics.

Tables 5.4.1 and 5.4.2. summarizes the measured rise and decay time constants and the evaluated hole intra- and inter-subband relaxation, recombination times, and average energy relaxation times for the 2μm and the 4μm GaAs/Si samples, respectively.

Table 5.4.2 clearly shows qualitatively the same hole dynamics between the 2μm and 4μm GaAs/Sis. The hot hole intra-subband thermalization time for the lmh subband is about 1.5 times faster than that of the hot hmh. The energy relaxation rate during the intra-subband relaxations for the lmh and the hmh subbands were estimated to be 9 and 24.2 meV/ps which revealed the rates were determined by the LO phonon scattering which depends on the hole mass. The inter-subband transition from the lmh to the hmh subband was found to be about ten times slower process than the intra-subband relaxations. The donor-hole recombination were fast process with a lifetime of around 20 to 30 ps. The 2μm GaAs/Si shows faster recombination time which can be understood from the difference in the density of dislocation (creates non-radiative decay channel) in the photoexcited region. The slower recombination time for the annealed 4 μm GaAs/Si indicated that the 4 μm GaAs/Si has less non-radiative centers.

Table 5.4.1 Experimentally evaluated time constants from the PL time profiles for the 2μm and 4μm thick GaAs/Sis.

	Rise Time (ps)		Fast Decay (ps)		Slow decay (ps)	
	hh	lh	hh	lh	hh	lh
2μm GaAs/Si	18.0	11.0	20.0	17.4	—	—
4μm GaAs/Si	8.32	5.58	28.2	25.9	246.3	353.2

Table 5.4.2. Estimated hole intra-subband relaxation times and recombination times using the cascading energy relaxation model and the average energy relaxation times for the 2μm and 4μm thick GaAs/Si.

	τ_r (hh) (ps)	τ_r(lh) (ps)	τ_s (ps)	τ_d(hh) (ps)	τ_d(lh) (ps)	τ relax (ps)
2μm GaAs/Si	9.5	6.7	134	20	20	26~28
4μm GaAs/Si	6.42	4.59	318	28.2	28.2	12.6

5.5. Reference in Chapter 5

1). H. Unlu and H. Morkoc, Solid State Tech. March, 83 (1988)

2). Sorab K. Ghandhi "VLSI Fabrication Principle" Wiley-International, New York (1983)

3). E. M. Conwell "High Field Transport in Semiconductor", Academic Press, New York (1967)

4). R. R. Alfano edit. "Semiconductor Probed by Ultrafast Laser Spectroscopy" Academic Press (New York, 1984)

CHAPTER 6

2D ELECTRON DYNAMICS IN Be MODULATION-DOPED GaAs MQW/Si UNDER STRESS

6.1 Biaxially tensioned Be modulation-doped MQW/Si

6.1.1 Introduction

Electron dynamics governs the transport and optical properties in a p-type photonic semiconductor devices. Hot electrons can be generated in the semiconductor by electric field or by light. These hot electrons release their excess energies through carrier-carrier scattering and phonon emission. When the kinetic energy of the electrons are higher than 500 meV above the conduction band edge in GaAs, the electrons scatter into the X- and L-valleys through inter-valley scattering which lowers the electron mobility because of the larger effective masses in the X- and L-valleys. The electron energy relaxation processes in bulk materials and 2D systems (such as QW and superlattice) have been extensively investigated theoretically and experimentally. With the recent progress of femtosecond time resolved spectroscopy techniques, ultrafast electron-phonon interaction process is being studied. The energy relaxation time in a GaAs bulk varies from sub-picosecond to few tens ps depending on the electron and lattice temperatures. The fastest energy relaxation of 0.35 ps was measured at 77 °K lattice temperature with 150 °K carrier temperature. Shank et al.[1,2] investigated the electron energy relaxation under strong photoexcitation using the femtosecond laser pulse pump and supercontinuum probe method and found electron re-distribution to

quasi- Boltzmann distribution within few ps. When electrons are confined in a quantum well structure, the movement of the electron is allowed only in-plane direction perpendicular to the well growth direction and becomes two dimensional (2D) electron gas. The energy relaxation process of such 2D electron gas has also been investigated by Shank et al. in 1982.

The hybrid between GaAs and Si devices are very important for future photonic application to achieve high speed and efficient photonic devices. When the p-type GaAs QW device is grown on a Si substrate, the strain induced by the difference in the thermal expansion between GaAs and Si alters the quantized band structures and the electron dynamics that has not been studied in ps time scale, yet.

In this section, the hot electron cooling dynamics has been investigated using two modulation Be-doped GaAs multi-quantum well samples grown on Si substrates (p-type MQW/Si). By changing the well widths of the QW structures, the change in the electron energy relaxation dynamics interacting with cool light or heavy holes at the lowest valence subband was investigated. The modulation doping is known to cause band warping due to the charge transfer to well region. However, the warping effect is neglected in my discussion.

6.1.2. Samples

Fig.6.1.1. shows schematic band structures of two QW samples with primary radiative transitions indicated by downward arrows. The multiple QW (MQW) with well widths of 188Å (in Fig.6.1.1.(a)) and 40Å (in Fig.6.1.1.(b)) were

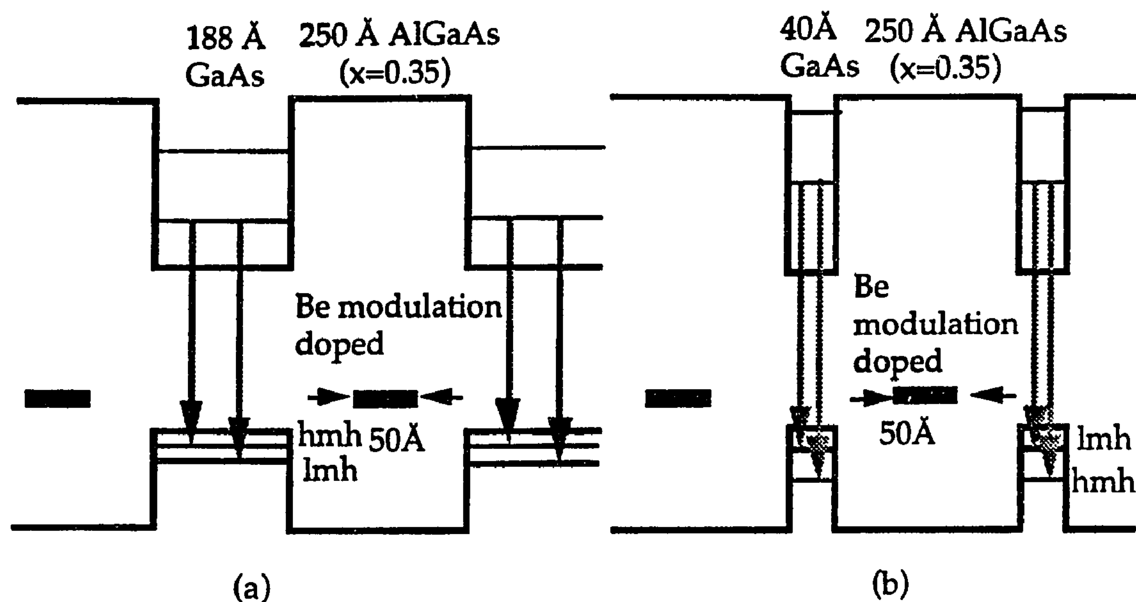

Fig. 6.1.1 Band structures of the (a) 188Å and (b) 40Å multiple QW grown on Si substrates. The central 50Å regions of the AlGaAs barriers are Be modulation doped.

fabricated individually on {100} Si substrates tilted 4° toward <011> direction with a 2μm of GaAs buffer layer. One sample consisted from 20 periods of MQW with 40Å well widths separated by 250Å $Al_{0.35}Ga_{0.65}As$ barriers in which central 50Å were doped with Be atoms to supply enough holes to the valence band in the wells. The density of light holes (lmh) in the well is estimated to be 1.9×10^{12} cm^{-2}. The another sample consisted of 20 periods of multiple QWs with the 188Å well widths and 250Å AlGaAs barriers in which central 50Å regions were also doped with Be. The heavy hole density in the 188Å MQW is about 2.5×10^{12} cm^{-2}. Since the impurity was doped only in the barrier, the impurity scattering which dominates energy relaxation at a low lattice temperature is negligible for the dynamics analysis. The samples were grown by a MBE machine at Univ. of Illinois at Urbana-Champaign by Prof. Morkoc's group.

The MQWs are under about 3 kbar of built-in biaxial tensile stress at 4 °K lattice temperature as same as a GaAs/Si sample. The hmh subband (m_j=±1/2) located at lower energy in the 188Å MQW while the lmh subband (m_j=±3/2) located at lower energy in the 40Å MQW as the results of the combination of the stress and the quantum confinement effects. The band structure in the 40Å MQW is similar as regular QWs where the lmh subband is located at lower energy.

6.1.3 Experimental method

To evaluate the electron dynamics, the time-resolved PL spectroscopy technique with 10 ps time and 1 nm spectral resolutions was used to analyze PL kinetics.

The two samples were placed together in an optical cryostat at 4 °K lattice temperature and photoexcited separately by CPM laser pulses with 100 fs pulse duration and 2.0 eV (625 nm) photon energy. The PL from each sample was collected into a 25 cm spectrograph incorporating a 600 grooves/mm ruled reflection grating blazed at 1μm. The PL was spectrally dispersed and coupled into an input slit of a streak camera to be time-resolved. The streak camera operated synchronously with the laser pulses at 82 MHz repetition rate. The photocathode of the streak camera was S-20 type which has higher quantum efficiency around 700 to 800 nm than S-1 type photocathode as shown in Fig.4.2.8. The temporally and spectrally resolved PL spectra at various lattice temperatures were stored into an image processing computer (TA) to be analyzed.

6.1.4 Experimental results

The experimental 3D PL spectral profiles for the 188Å and the 40Å MQWs at 4 °K lattice temperature are displayed in Fig. 6.1.2(a) and (b), respectively.

Fig. 6.1.2.(a) for the 188Å MQW shows a strong peak arising from the conduction band to the hmh (e-hmh) transition and a shoulder on high energy side of the PL profile is due to the transition between the conduction band to the lmh subband(e-lmh). The e-hmh transition PL has a long decay profile while the e-lmh transition shows a fast decay. The initial PL spectrum shows two features. First, the initial PL spectrum is very wide which indicates that the carriers in the system is hot. Since there are two primary transitions, the high energy tail of the spectrum shows two exponential structures. Next, the PL shoulder due to the e-lmh transition increases faster than the e-hmh transition. The feature is similar to that in the n-type GaAs/Si discussed in Chapter 5.

For the 40Å QW in Fig.6.1.2 (b) shows two distinguishable peaks arising from the conduction band to lmh (e-lmh) at low energy and hmh subband transitions (e-hmh) at high energy. The energy separation between the subbands for the 40 Å QW was measured to be 41 meV. The e-lmh transition of the PL spectrum at the initial time after the photoexcitation is found to increase faster than the e-hmh transition. The PL spectral profiles are similar as those for regular QWs because the band structure of the 40Å MQW/Si is similar as the regular QWs except the subband separations are altered by the tension.

6.1.5. Discussion

To explain the PL kinetics mentioned above, the electron cooling process (electron energy relaxation process) in the strained QW will be modeled.

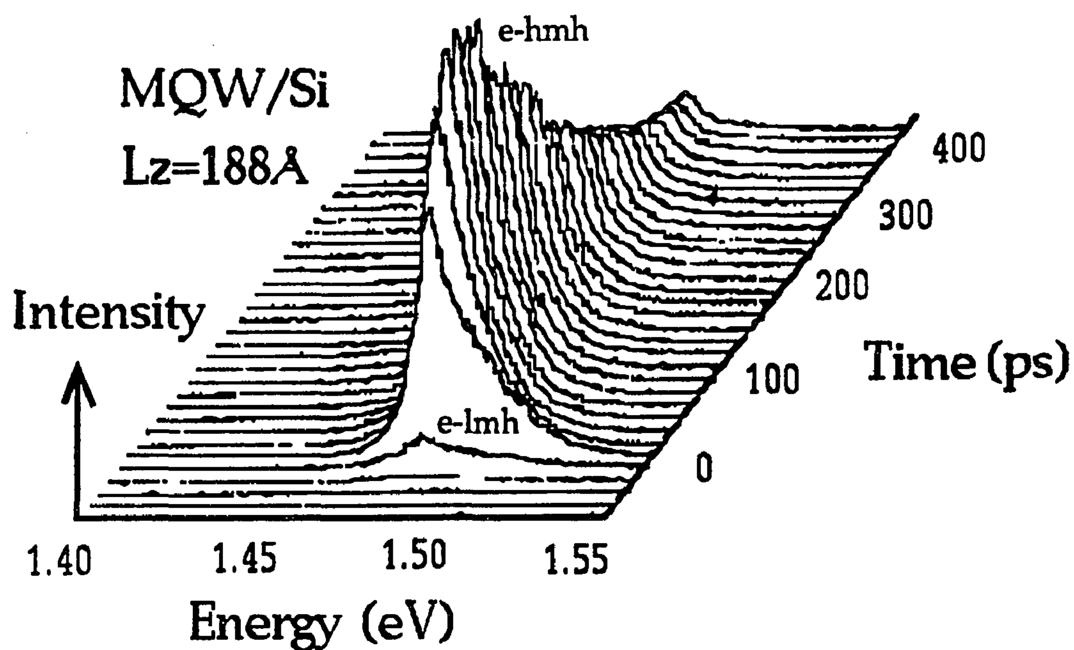

(a)

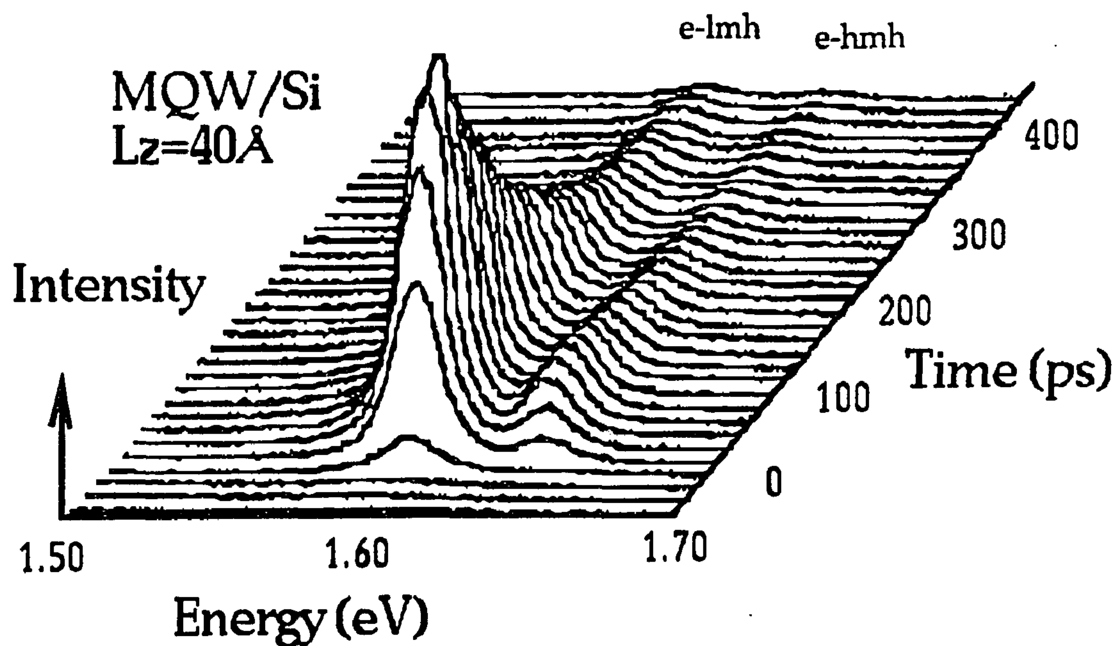

(b)

Fig. 6.1.2. Three dimensional display of the time-resolved PL spectrum from (a) the 188Å MQW/Si and (b)the 40 Å MQW/Si at the lattice temperature of 4 °K.

Fig.6.1.3. (a) and (b) schematically show the band structures (neglecting band mixing) and photoexcitation scheme of the 188Å and 40Å MQW/Si samples. In the figures, n and m_i(i=hmh and lmh) represent quantum numbers for the conduction and valence bands, respectively. The upward arrows indicate photoexcitation. The arrows along the dispersion curves correspond to the carrier relaxation process. The downward arrows represent the transitions with PL emission. During the photoexcitation, the photon energy is conserved as carrier potential and kinetic energies. The energy relaxation occurs through carrier-carrier scattering and phonon scattering. The PL transition between the conduction and valence subbands are determined by the transition selection rule. The shadow represents the modulation doped cool holes. The valence subband structures are different between Fig.6.1.3. (a) and (b). The m_{hmh}=1 subband (m_j=±1/2) locates at the lowest energy in the 188 Å MQW/Si while the m_{lmh}=1 subband (m_j=±3/2) locates at lowest energy in the 40 Å MQW/Si. The higher subbands in the valence bands in the 188Å and 40 Å QWs are overlapped complicatedly. A detail valence band structure in a 200 Å GaAs QW including the band mixing effect was given by J. Lee.[5,6] In this thesis, the simple band structure model shown in Fig. 6.1.3. was used to explain the electron and hole dynamics in these QWs.

For the 188 Å MQW/Si, the weak quantum confinement lifts the subbands to higher energy from the bulk GaAs/Si band structure. Along the growth direction, the energy levels are quantized. The electrons and holes can move only along xy-plane (plane perpendicular to the sample growth direction). Since there exists about 2.5×10^{12} /cm^2 cool hmhs in the well, the photogenerated hot carriers collide with these cold hmhs

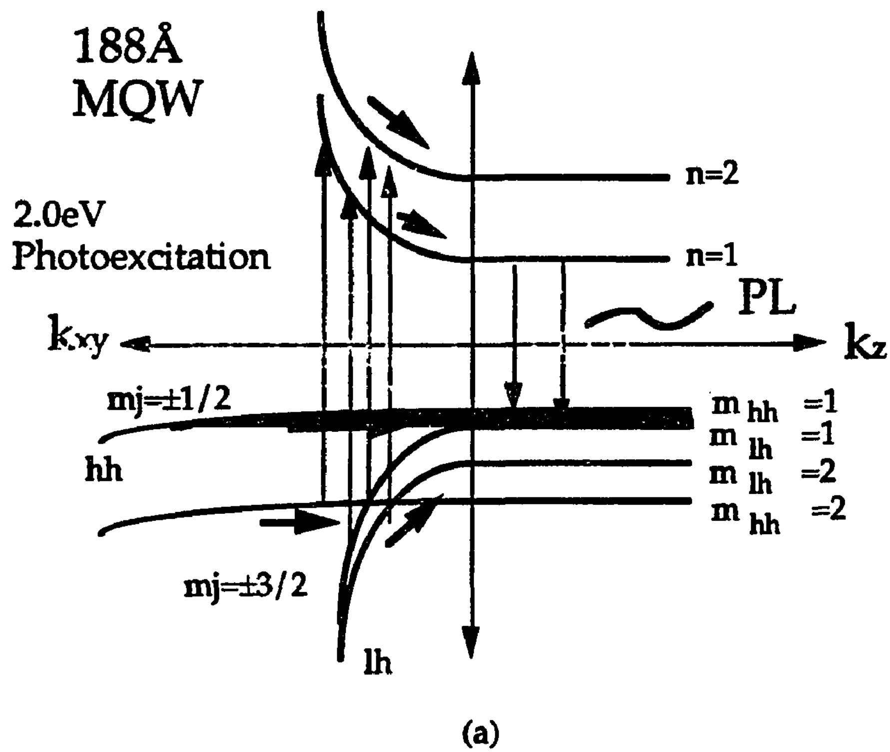

(a)

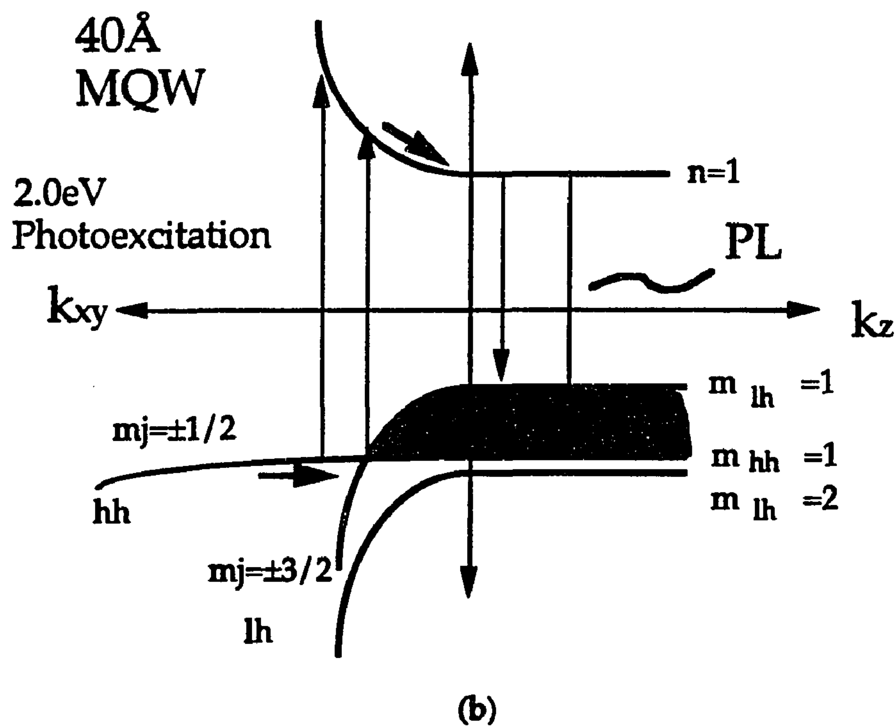

(b)

Fig. 6.1.3. Band structures of the (a) 188Å MQW/Si and (b) 40Å MQW/Si with modulation doped-in holes in the valence bands.

and transfer their energies to the cold hole system. In the conduction band, the electrons also collide with the cold holes and transfer their energies to the cold hole system. The collision can not transfer the kinetic energy of electron to the heavy weighted holes efficiently because the effective masses between the electrons and holes are much different. The electrons mainly release their energies to lattice through electron-phonon interaction. After the carrier thermalization, the hole system becomes warm and can be represented by a warm hole temperature. The thermalized electrons are also warm at the electron temperature and cooled down to the lattice temperature by emitting phonons.

In the 40 Å MQW/Si, the quantization lifted up the subbands and compensates the tension effects. The band structure becomes similar as regular QWs in which the lmh subband are located lower energy. Due to the modulation doping, there exist cold lmhs at 4 °K with 1.2×10^{12} cm^{-2} density. The photogenerated hot carriers are scattered by the lmhs, emit phonons, and be thermalized. The holes in the higher quantized subbands relax down to the lowest subband through hole-hole scattering or emission of phonons. After the carriers are thermalized, the whole electron and hole system is cooled down to the lattice temperature.

The average electron cooling processes for the MQW/Si were investigated with the system time resolution of 10 ps. To understand the carrier cooling process, the electron and hole temperatures at various delay time were extracted from the 3D PL spectra by fitting calculated spontaneous emission spectra assuming an electron (T_e) and hole temperatures (T_{hmh} and T_{lmh}).

The spontaneous emission spectrum W(E) of a conduction electron at E transiting to the valence subbands is calculated from a Fermi's golden rule under the energy and momentum conservations as,

$$W(E) = 2\pi/\hbar \bullet |M_{cv}|^2 \rho(E_v)\, \delta\,(E-E_c+E_v) \qquad (6.1.1)$$

where $|M_{cv}|^2$ is the transition matrix element, $\rho(E_v)$ is the density of states of the valence subbands, and the delta function represents the energy conservation. To obtain whole spectrum, the distribution of the conduction electron is required to be taken into account.

First, the Fermi level in the conduction band is determined by using an integration of electron population in the conduction band with the electron temperature T_e as,

$$n_0 + \Delta n = \int \rho_c(E) / \{1+\exp(E - E_f)/k_B T_e\}\, dE \qquad (6.1.2)$$

where n_0 is the residual electron density (n_0=0 in this case), Δn is photogenerated electron density, E is the energy measured from the conduction band edge, E_f is the quasi-Fermi level to be obtained, and k_B is the Boltzmann constant. $\rho_e(E)$ is the density of states of conduction band in a QW and is given by,

$$\rho_c(E) = m_e^* / \pi \hbar^2 L_z \bullet y(E) \qquad (6.1.3)$$

where m_e^* is the effective electron mass, $\hbar$ is Planck constant divided by 2π, L_z is the well width, and y(E) is a step function which increases at each quantized level. In case that the photogenerated electron density is low enough compare with an effective density of states of conduction band (non-degenerate), the Fermi-Dirac distribution can be replaced by a simple Boltzmann distribution function ($f_c(E)=\Delta n/N_c \bullet \exp(-E/k_BT_e)$ where $Nc=\rho_c(E)k_BT_L$ is effective density of states at the lattice temperature T_L). Solving E_f using Eq.6.1.2. and 6.1.3, the electron distribution function is determined. A quasi-Fermi level in the valence band is also calculated with same manner as for the conduction band. Since the valence band consists from quantized hmh and lmh levels, the quasi-Fermi level is determined by integrating the hole distribution in the subbands.

The matrix element for the transition between the conduction and valence subbands is given as,[3]

$$|M_{cv}|^2=8\pi^3/V \bullet |M_b|^2 \delta (k_c - k_v) \tag{6.1.4}$$

where V is a volume of the semiconductor, $|M_b|$ is the average matrix element for the Bloch states. The delta function represents the selection rule and is non-zero when $k_c=k_v$. According to the k•p theory by Kane, the average matrix element for the Bloch state is given by,

$$|M_b|^2=\frac{m_0^2 E_q(E_q+\Delta)}{12m_c(E_q+2\Delta/3)} \tag{6.1.5}$$

where Δ is the split-off separation energy and E_q is the energy gap between the quantized conduction and valence subbands. The average matrix element depends on the transition energies governed by the selection rule.

Using Eq.s 6.1.1, 6.1.3, 6.1.4, and 6.1.5, the spontaneous emission spectrum between a conduction and a valence subband is given by,

$$W(E) = 16\pi^2\bar{\mu}\, q^2 E\, |M_b|^2 m_r^* / (m_0^2\, \varepsilon_0 h^4\, c^3 L_z)\, f_c(E_c)\, f_v(E_v), \qquad (6.1.6)$$

where

$$m_r^* = m_e^*\, m_h^* / (m_e^* + m_h^*)\,, \qquad (6.1.7)$$

$$E_c = m_r^* / m_e^* (E - Eq), \qquad (6.1.8)$$

and

$$E_v = m_r^* / m_h^* (E - Eq). \qquad (6.1.9)$$

To obtain whole transition spectrum, W(E) is summed over the individual transitions.

Therefore, a fitting spectrum $I(E, T_e, T_{hmh}, T_{lmh})$ at a delay time is given by,

$$I(E, T_e, T_{hmh}, T_{lmh}) = [\,\Sigma\ W(E, T_e, T_{hmh}, T_{lmh})] \cdot L(E) \cdot G((E)\ , \qquad (6.1.10a)$$

with

$$L(E) = E_\gamma / (E^2 + E_\gamma^2) \qquad (6.1.10b)$$

and

$$G(E)=\exp(-E^2/E_{ih}^2), \qquad (6.1.10c)$$

where E_γ and E_{ih} are the broadening factors due to the homogeneous and inhomogeneous line width broadenings, respectively.

To fit the data with the model, a measured PL spectrum at a time delay is selected from the 3D PL image, normalized after the spectral sensitivity correction of the system, and is compared with the Eq.6.1.10 assuming the line broadening factors (E_γ and E_{ih}) and the electron and hole temperatures (T_e, T_{lmh}, and T_{hmh}). Since the determination of the quasi-Fermi level in the valence band is not straight forward, I assumed a quasi-Fermi level for the valence band to compute the spectrum. The program was written for Hamamatsu temporal analyzer and listed in Appendix 2.

The transitions to be considered in the 188Å MQW/Si are n_c=1 to n_{hmh}=1, n_c=1 to n_{lmh}=1, and n_c=1 to n_{lmh}=3 while those for the 40Å MQW/Si are n_c=1 to n_{hmh}=1 and n_c=1 to n_{lmh}=1 where n_i=j denotes quantized subband i (c for conduction and hmh and lmh for the valence subbands) with the quantum eigen state number j determined from the selection rule(odd number of quantized electron states to odd number of quantized valence band states or even number conduction bands to even number valence quantized states.)

Fig. 6.1.4. (a) and (c) show the measured PL profiles of the 188Å MQW/Si at a delay time of 37 ps and of 40 Å MQW/Si at a delay time of 29 ps, respectively. The fitting results for these experimental PL spectra are shown in Fig.6.1.4. (b) and (d) corresponding to the PL spectra (a) and (c), respectively. The parameters used for the fitting curve (b) were T_e= T_{lmh}=67 °K and T_{hmh}=4.3 °K while those for the fitting curve (d) were T_e=15.3 °K and

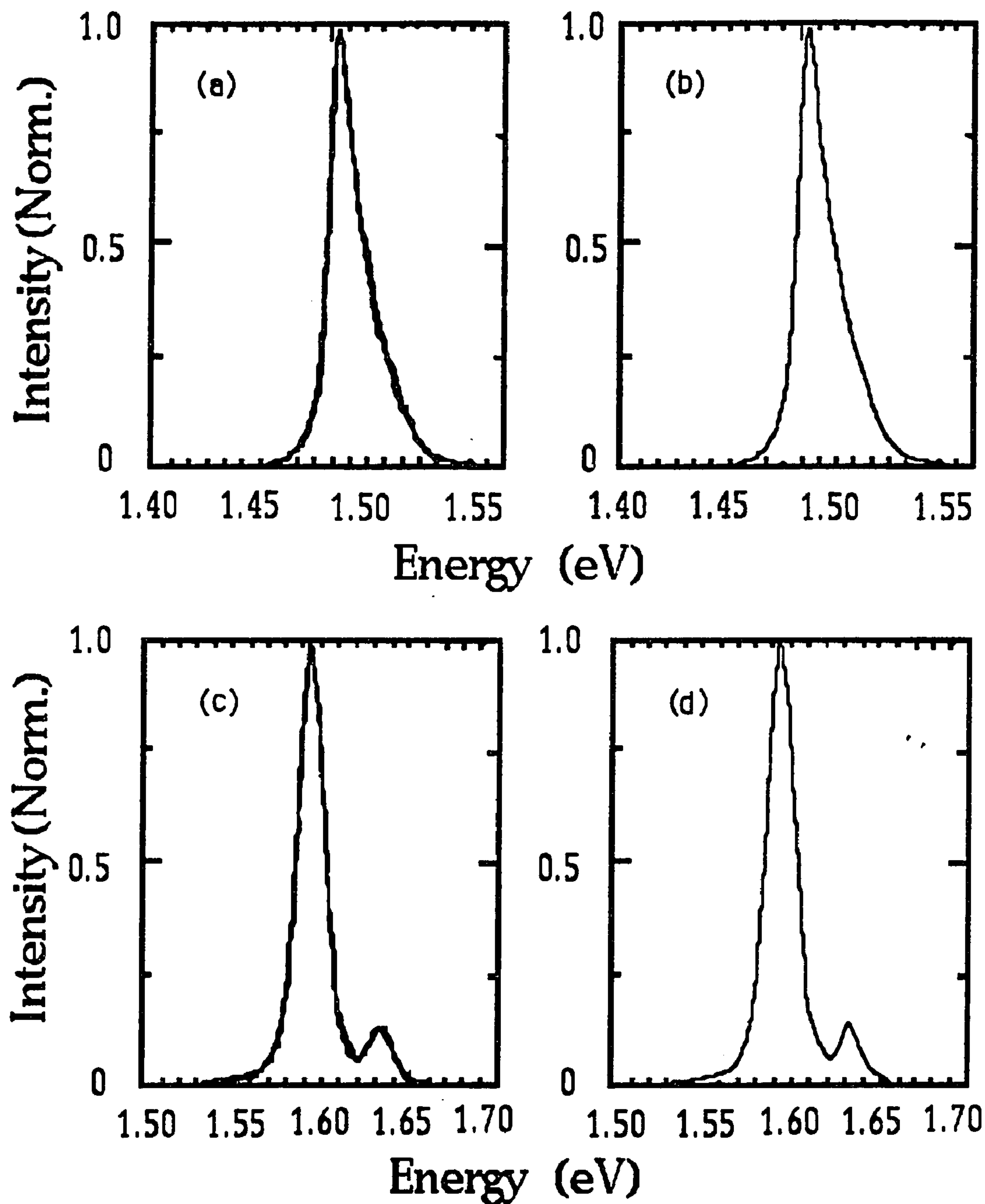

Fig. 6.1.4. Experimental PL spectra for (a) the 188Å QW and (c) the 40Å QW, respectively, and fitting curves (b) and (d) for (a) and (c), respectively, using spontaneous emission curves convoluted with inhomogeneous line broadening and well width fluctuation.

T_{lmh}=T_{hmh}=7.3 °K. The fit were so exact that the fitting curve and experimental data can not be distinguished when these curves are superimposed. Fitting the calculated spectra to the measured PL spectra at various delay times, the electron temperature as function of the delay time were evaluated.

The electron temperatures in both MQWs are depicted in Fig. 6.1.5. with open circles for the 188Å MQW and with squares for the 40Å MQW, respectively. The electron cooling from 100 °K to 40 °K takes 150 ps in the 188Å MQW while it takes 100 ps in the 40 Å MQW to be cooled from 30 °K to 4 °K. The electron cooling time assuming a single exponential cooling for the 188Å MQW was evaluated to be 43.7 ps while that for the 40Å MQW was 29.9 ps. The initial electron temperatures for the MQWs were found to be 103 °K and 79 °K for the 188 Å and the 40 Å MQWs, respectively. The initial temperature difference between the 188 Å and 40 Å MQWs arises from the difference in the electron-hole interaction and from different well width. The hot electrons collide with cold lmh in the 40 Å MQW and with cold hmh in the 188 Å MQW as discussed previously. Since the coupling between a hot electron and a lmh is stronger than that between a hot electron and a hmh due to the mass difference, the cooling rate of hot electron in the 40 Å MQW is larger. After the thermalization, the electron and hole system cooled down by transferring the energy to the lattice through phonon interaction.

Using LO phonon Fröhlich interaction and energy transfer rate equation between the electron system and LO phonon system, the cooling processes for the MQWs were simulated as same manner as the 2μm GaAs/Si case discussed in Chapter 5.2.

After the photoexcitation, the electron system looses its average kinetic energy to lattice through LO phonon emission with a rate given by Eq.3.3.7 and

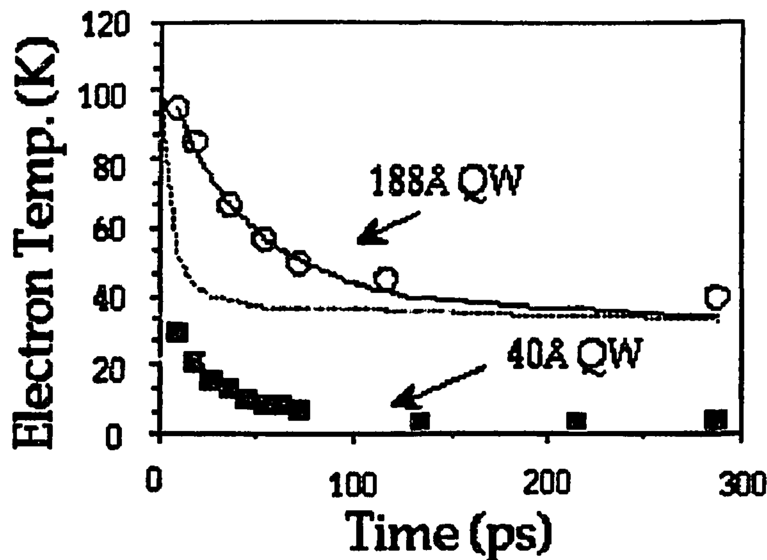

Fig. 6.1.5. Electron thermalization in the modulation Be-doped GaAs MQW/Si with Lz=181Å (dots) and Lz=40Å (squares). Non-equilibrium LO phonon is taken into account (solid line) while dashed line is without the non-equilibrium phonon effect.

the electron system temperature T_e decreases. The average energy relaxation rate is given as,

$$\frac{dT_e}{dt} = \frac{1}{k_B}\left\langle \frac{dE_e}{dt} \right\rangle = -P_0 F(T_e,T_p) \qquad (6.1.11a)$$

where F(Te,Tp) is a function given by,

$$F(T_e,T_p) = \frac{\exp(x_p - x_e) - 1}{\exp(x_p) - 1} \bullet \left(\frac{x_e}{\pi}\right)^{1/2} \exp\left(\frac{x_e}{2}\right) \bullet K_0\left(\frac{x_e}{2}\right) \qquad (6.1.11b)$$

where $x_{p,e}=E_{LO}/k_BT_{p,e}$ and K_0 is the Bessel function of zero order. The phonon system gains the energy from the electron system and looses the energy through LO phonon decay to acoustic phonons. The phonon temperature T_p is given by,

$$\frac{dT_p}{dt} = P_0F(T_e,T_p) - \frac{N_p(T_p)}{\tau_p} \bullet \frac{dT_p}{dN(T_p)} \qquad (6.1.11c)$$

where $N_p(T_p)$ is the phonon occupation number at the phonon temperature T_p and τ_p is the LO phonon lifetime. As the phonon lifetime is assumed to be long, the energy trasfer from the electron system to the phonon system is regulated by non-equilibrium phonons.

Solving Eq.s 6.1.11 with respect to the electron temperature, the electron average energy relaxation process was investigated. Fig. 6.1.5. shows the calculated curves using a fast (~0 ps, shown in a dashed curve) and a slow (~8ps, shown in a solid curve) phonon lifetimes. The solid curve fits to the obtained electron temperature cooling data. The non-equilibrium hot phonons are built-up due to the 8ps phonon lifetime in the hot electron gas in the 188Å QWs. The cooling rate is equivalent to that of GaAs calculated from a material parameter was found to be six times smaller than the rate without non-equilibrium phonon effect.

The average electron energy <E(t)> was evaluated from the PL data as shown in Fig. 6.1.6. to confirm the energy relaxation process for the 188 Å MQW. The average energy <E(t)> for the 40 Å MQW/Si was not given here because the interface roughness was found to dominate the average energy relaxation process. By subtracting the steady state PL peak energy 1.480 eV

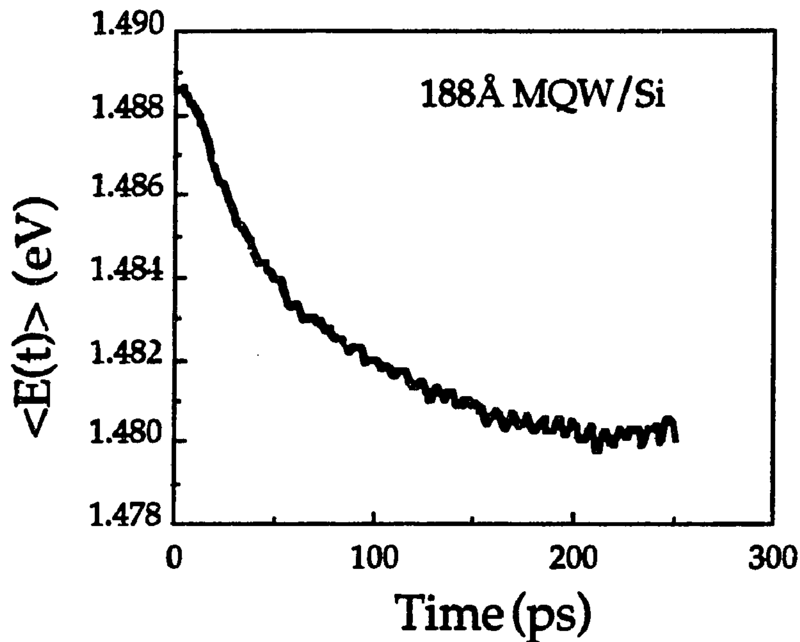

Fig. 6.1.6. Average electron energy relaxation in the 188 Å MQW/Si sample at 4 °K lattice temperature extracted from the PL data.

from the <E(t)> and fit a single exponential curve for the average electron kinetic energy, the average electron kinetic energy relaxation time was determined to be 50ps which is close to the electron cooling time evaluated from the spontaneous emission spectra fit. Therefore, the electron cooling time in the 188 Å Be-modulation doped MQW/Si is confirmed to be 46±4 ps. The initial energy relaxation rates are calculated from the evaluated cooling time and the relaxation energy which is defined by the energy difference between the initial and the cooled carrier kinetic energies. The rates are evaluated to be 8.6 (meV)/43.7 ps=0.197 meV/ps and 3.4 meV/29.9 ps =0.1137 meV/ps for the 188Å and the 40Å MQW/Si samples, respectively.

6.1.6. Conclusion

Differences in the hot electron thermalization processes through e-lmh and e-hmh interaction has been investigated using the 188Å and 40Å MQW/Si samples. It was confirmed that the combination of stress and quantum confinement altered the lowest valence subband to be hmh and lmh for the samples. The electron thermalization processes are found to be much different between the samples because of interaction carrier mass difference and hot-phonon effect co-existing within the well. The electron cooling times were determined from the spectral fit to be 44 ps and 30 ps for the 188Å MQW and the 40Å MQW samples, respectively. The average energy relaxation time assuming a single exponential were evaluated to be between 46±4 ps for the 188Å MQW. The energy relaxation rate in the 188Å MQW/Si was evaluated to be about 0.197 meV/ps which is 1.7 times larger than that in the 40Å MQW.

6.2. External uniaxial stress on Be-modulation doped 188Å MQW/Si

6.2.1. Introduction

It is well known that the stress generated in a semiconductor material alters its band structure and the carrier dynamics. The lattice mismatch between the epilayer and the substrate causes not only defects or dislocations but also a strain at the interface. When the heterostructured sample is cooled to a room temperature from its growth temperature around 700°C, the difference in the thermal expansion coefficients of the layers causes the biaxial stress along the interface plane. Further, external compressive stress can be applied onto the semiconductor sample hydrostatically or uniaxially.

When uniaxial compressive stress is applied to a quantum well (QW) structure whose valence band is already split into hmh and lmh subbands, the quantized energy gap further increases and the valence subbands are lifted up to higher hole energy. Since the hmh subbands ($m_j=\pm1/2$) are more sensitive to the compressive stress, the lowest hmh subband catches up the lowest lmh subband ($m_j=\pm3/2$) at a certain magnitude of the stress (crossover stress). At the crossover stress, the valence band becomes degenerate at k=0 (if no band mixing occurs) as similar as a bulk GaAs except the quantization flattens the band structure along the QW growth direction. The electron and hole thermalization and cooling processes in a semiconductor QW device under stress are important processes and determine the electronic and optical characteristics of the strained QW. The carrier dynamics under the stress has not been studied in picosecond time scale yet. Since the band structure can be tuned by externally applied stress, one can In this section, the electron cooling process in a semiconductor QW structure under both biaxial tension and was investigated. The photoluminescence (PL) kinetics from the sample was

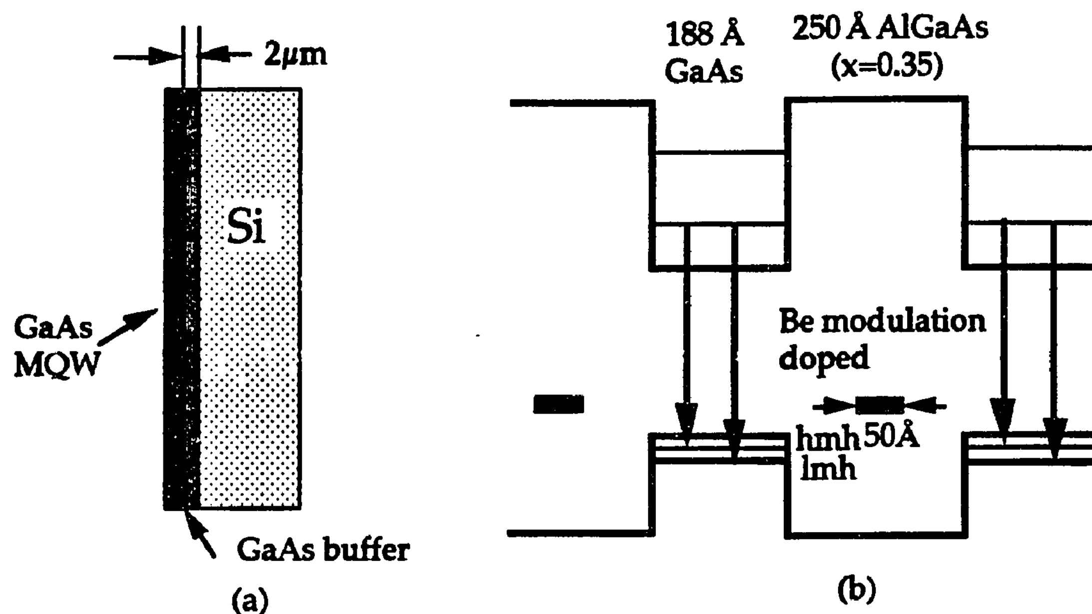

Fig. 6.2.1. (a) Sample and (b) band structures

external uniaxial compression control the carrier dynamics if the carrier thermalization and cooling processes under the stress is understood.

analyzed using picosecond time-resolved PL spectroscopy technique.

6.2.2. Sample and experimental setup

The sample was a Be-modulation doped 188Å multiple QW grown on a Si substrate (MQW/Si) which was also used to investigate the electron dynamics under built-in biaxial tension in the previous section. The 188Å MQW structure was fabricated on {100} Si substrates tilted 4° toward <011> direction with a 2μm of GaAs buffer layer as shown in Fig.6.2.1.(a). The MQW consists from 20 periods of QWs with 188Å well widths separated by 250Å $Al_{0.35}Ga_{0.65}As$ barriers in which central 50Å regions were modulation-doped with ion-inplanted Be atoms to supply enough holes to the valence band in the wells as

shown in Fig.6.2.1.(b). The density of heavy holes (hmh) in the well is estimated to be $2.5x10^{12}$ cm^{-2}.

The sample was cut to a 3 mm x 8 mm size to fit into a stress apparatus placed in an optical dewar. The sample cooled to 4 °K lattice temperature was photoexcited by laser pulses from a CPM dye laser at 82 MHz with 100 fs pulse duration and 2.0 eV photon energy. Since the dewar is large and heavy, the dewar was placed on the floor. The laser beam was sent down to the floor and focused onto the sample through 20 cm focal length BK7 lens. The laser spot size on the sample was around 200μm. The photogenerated carrier density was estimated to be about $2x10^{8}$ cm^{-2}. The PL from the sample was collected into a 25 cm spectrograph using two plano-convex lenses. One lens was placed on the floor and collimated the PL from the dewar. The collimated PL was reflected upward to the optical table on which the spectrograph and a streak camera were set. Another lens focused the collimated PL into the input slit of a spectrograph which incorporated a 600 grooves/mm reflection grating blazed at 1μm. To cut the fundamental scattered laser beam, a #7-59 visible cut and IR transmitting color filter was placed in front of the spectrograph. The spectrograph dispersed the PL spectrum onto the input slit of a streak camera which time-resolves the PL spectrum. The time resolution was 10 ps and the spectral resolution was 1 nm. Since the compressive stress applied onto the sample lifts the quantized band edges to higher energies, the spectrograph was initially set to show the PL at the lower energy side on the streak image so that the observing spectral region could cover the shifted PL spectra at a higher stress. The stress machine was operated with a help of Dr. Hao Qiang from the

Brooklyn college. The 188Å MQW/Si sample was compressed up to 14 kbar. Then, the sample destroyed.

6.2.3. Experimental results

The steady state band edge shift due to the uniaxial stress was measured prior to this time-resolved measurement using an intrinsic 188Å single QW at room temperature by a modulated photoreflection spectroscopy by Hao Qiang[4] at the Brooklyn College. The modulated photoreflection spectra under various stresses along [100] direction are depicted in Fig. 6.2.2. and reveal several important features. Since the built-in tension lowered the subbands and the quantum confinement lifts the subbands to higher energy, the lowest hmh subband located about 20 meV below the lmh subband at the external stress X=0. As the uniaxial stress increases, the hmh subband (11HH transition) moves to higher energy in valence band and finally across the lmh subband(11LH). At the cross over stress of 1.3 kbar at room temperature, the hmh and lmh subbands showed anti-cross arising from the band mixing.[5,6] Further increasing the stress, the hmh subband across the $n_c=2$ to $n_h=2$ transition (22LH) at 10 kbar. It is interesting to know what is happening on the carrier dynamics at the crossover stress region where the carrier masses may not be ordinary heavy or light hole masses. The energy gap between the conduction and valence subbands under uniaxial stress along [100] direction are given in first order approximation as discussed in Chapter 2.3 as,

$$\Delta E_{c\text{-}hmh} = \{ a(S_{11}+2S_{12}) - b(S_{11}-S_{12}) \}\bullet(-X)$$

$$= -0.6024\bullet(-X) \text{ (meV/kbar) for strained GaAs,} \quad (6.2.1)$$

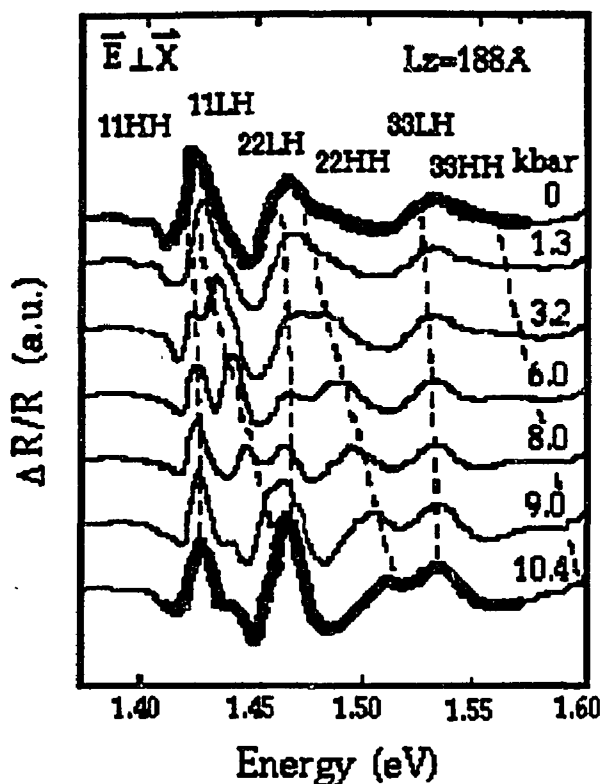

Fig. 6.2.2. Band edge energy shifts due to the externally applied uniaxial stress measured with modulation PL spectroscopy by Hao Qiang[5].

and

$$\Delta E_{c\text{-}lmh} = \{ a(S_{11}+2S_{12}) + b(S_{11}-S_{12}) \}\bullet(-X)$$

$$= -6.722\bullet(-X) \text{ (meV/kbar) for strained GaAs.} \qquad (6.2.2)$$

where S_{11}, S_{12}, a, b, and X are compliance coefficients, hydrostatic and shear deformation potentials, and external uniaxial stress in kbar, respectively. Since the positive direction of X is tensile stress, the compressive stress of X is negative value. $S_{11}=11.6\times10^{-4}$ kbar^{-1}, $S_{12}=-3.7\times10^{-4}$ kbar^{-1}, a= -8.7 eV, and b= -2.0 eV are used to calculate the shifts in a strained GaAs[7].

The transition energies at 4 °K lattice temperature have been calculated by Hao Qiang [7,8] and are shown in Fig. 6.2.3. The anti-crossing stress for the hmh and lmh subbands moves to around 2 kbar (it was 1.3 kbar at room temperature). At 7.5 kbar, the 11HH transition acrosses 13LH transition showing anti-crossing. Fig. 6.2.4. shows the calculated valence subband structure by Hao Qiang. The hole subband structure around 2 to 3 kbar is complicated and may contribute a change in the hole dynamics. Note that the notation for the transitions are different from those by Hao Qiang. The transitions dominating the PL kinetics after the carrier thermalization are thought to be two or three lowest transitions in my cases.

The time-resolved PL spectra in 3D displays under uniaxial compressive stresses of 0, 2.2, and 7.6 kbar are shown in Fig. 6.2.5. (a), (b), and (c), respectively. The PL spectra show some differences between them. Especially when the stress is 7.6 kbar where the lowest subband are supposed to be same as that under 2.2kbar, the higher energy PL peak intensity remains strong for a longer time than that under 2.2 kbar stress.

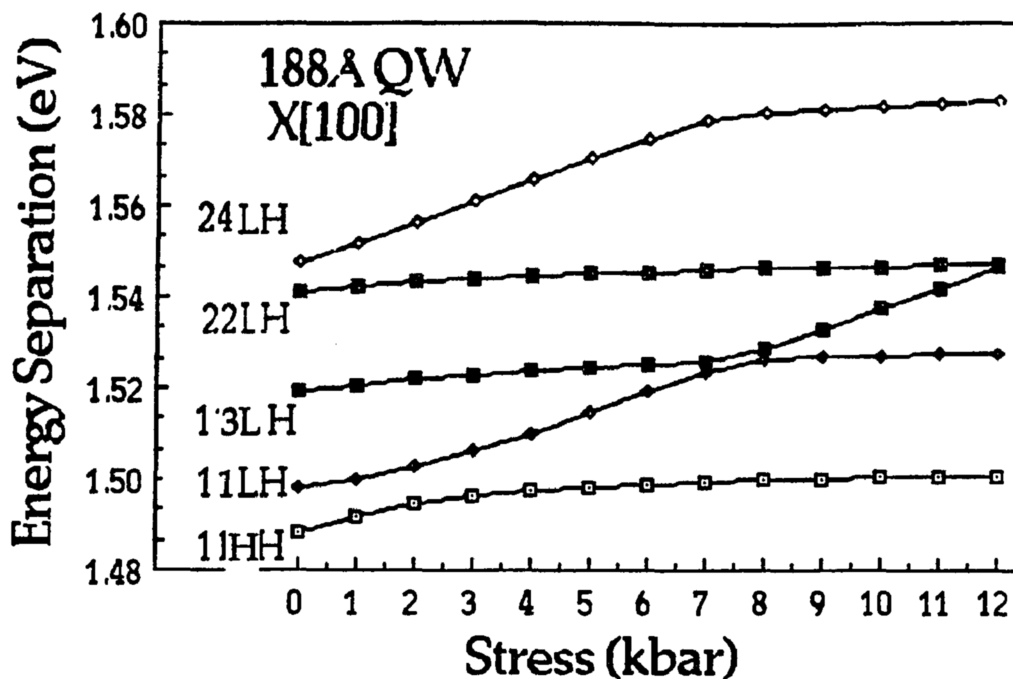

Fig. 6.2.3. Calculated transition energies between conduction and valence subbands under different uniaxial stresses for the 188Å MQW/Si at 4 °K lattice temperature (by Hao Qiang).

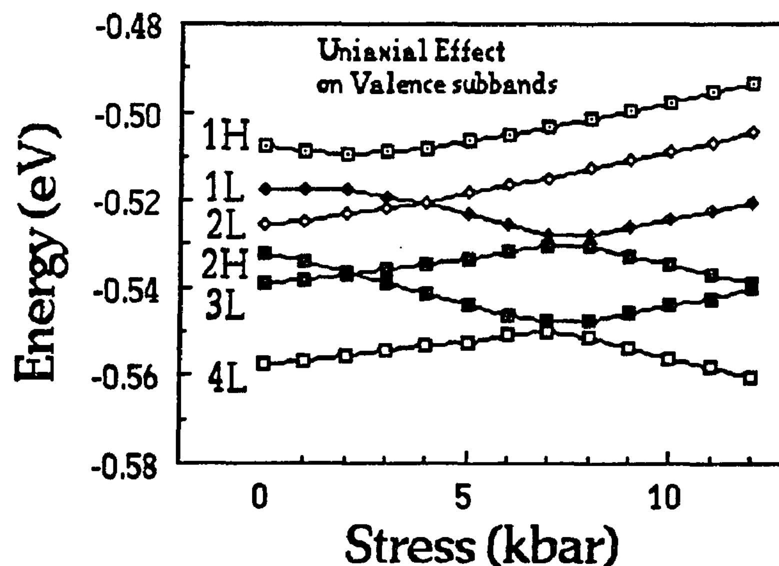

Fig. 6.2.4. Calculated valence subband structure under uniaxial compressive stress along [100] direction(by Hao Qiang).

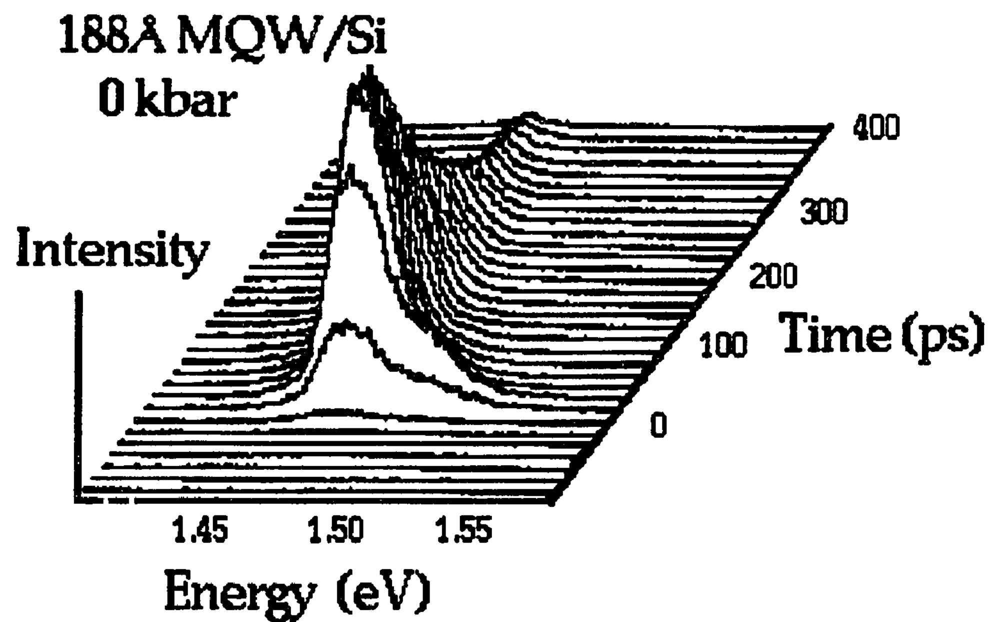

(a)

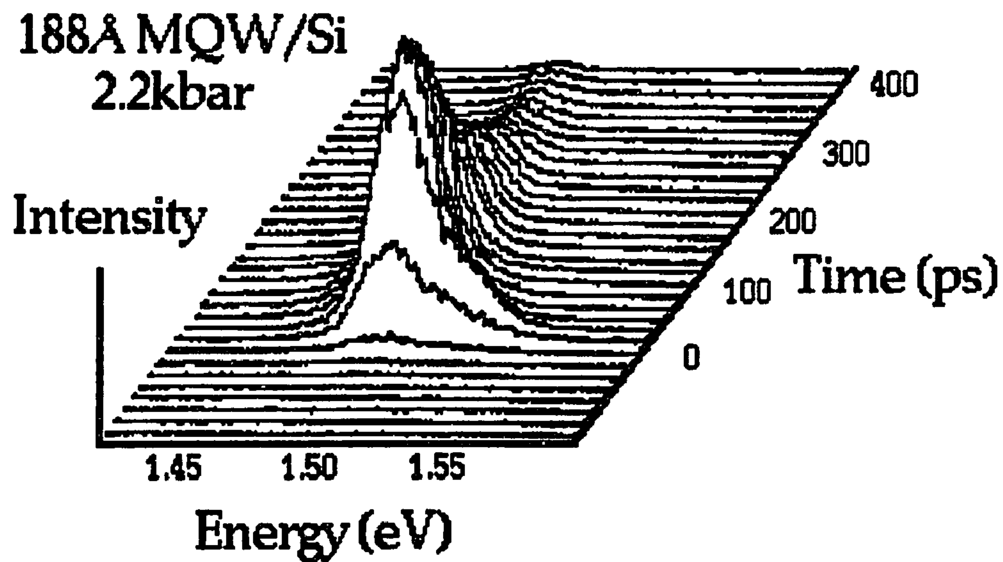

(b)

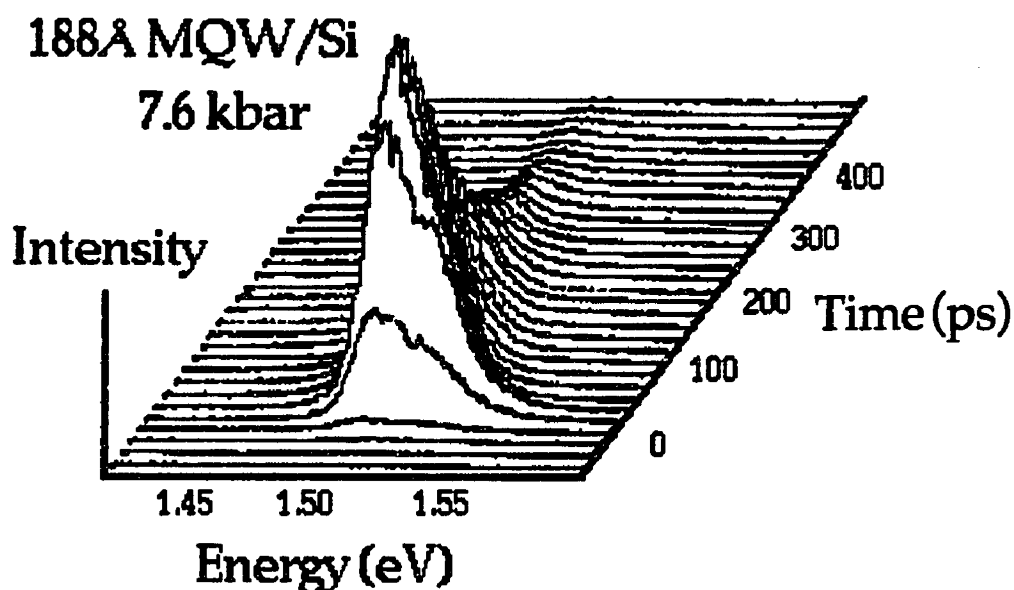

(c)

Fig.6.2.5. 3D time-resolved PL spectra under (a) 0 kbar, (b) 2.2 kbar, and (c) 7.6 kbar of uniaxial compressive stresses at 4 °K lattice temperature.

6.2.4. Discussion

To evaluate electron temperature cooling process under the uniaxial stress, I have used the spontaneous emission spectral fit procedure to the obtained PL time profiles. The spontaneous emission spectra are calculated using the same equation described in the previous section. Since the band structure is altered by the uniaxial compression, the transitions at 9.6 kbar of the stress are 11LH and 13 LH. The fitting results are shown in Fig.6.2.6 (a) and (b). The gray curves are experimental results and the solid curves are the fitting curves. It is clear that the initial spectral profile is wide compare with the spectrum at t=110 ps. Within 100 ps, the electron temperature cooled down to 40 °K. The electron temperature as function of delay time is plotted in Fig. 6.2.7. The open circles are the electron temperatures under 9.6 kbar of stress determined from the fit while the gray dots are those without the external

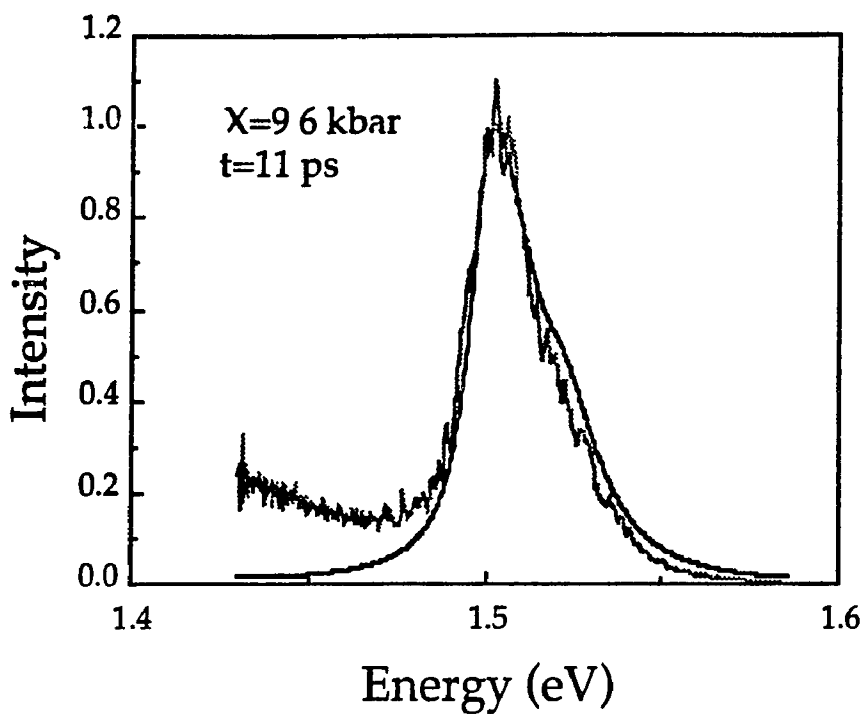

(a)

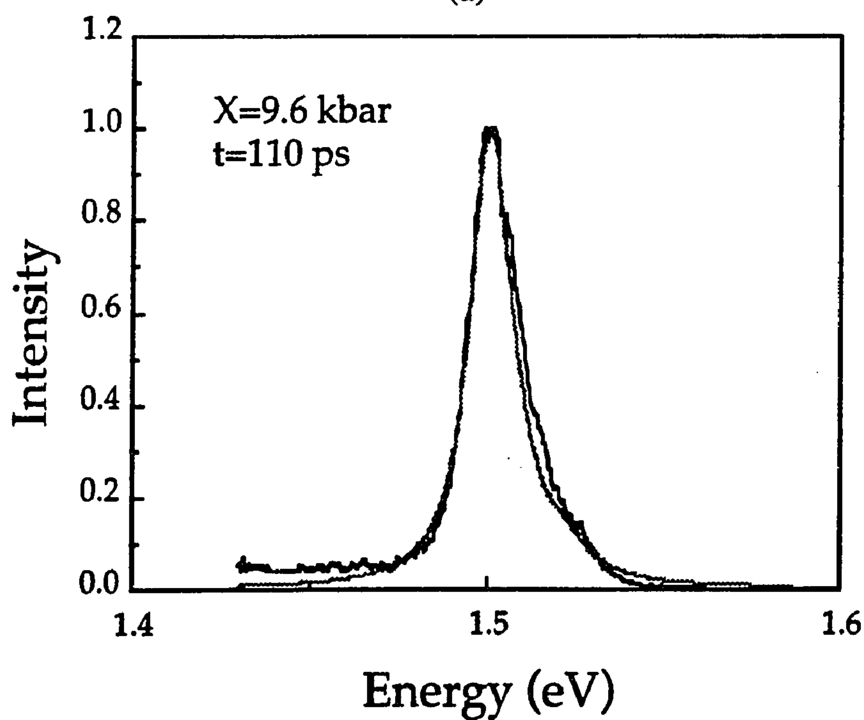

(b)

Fig.6.2.6. Spontaneous emission spectral fit at (a) t=11 ps and (b) 110 ps.

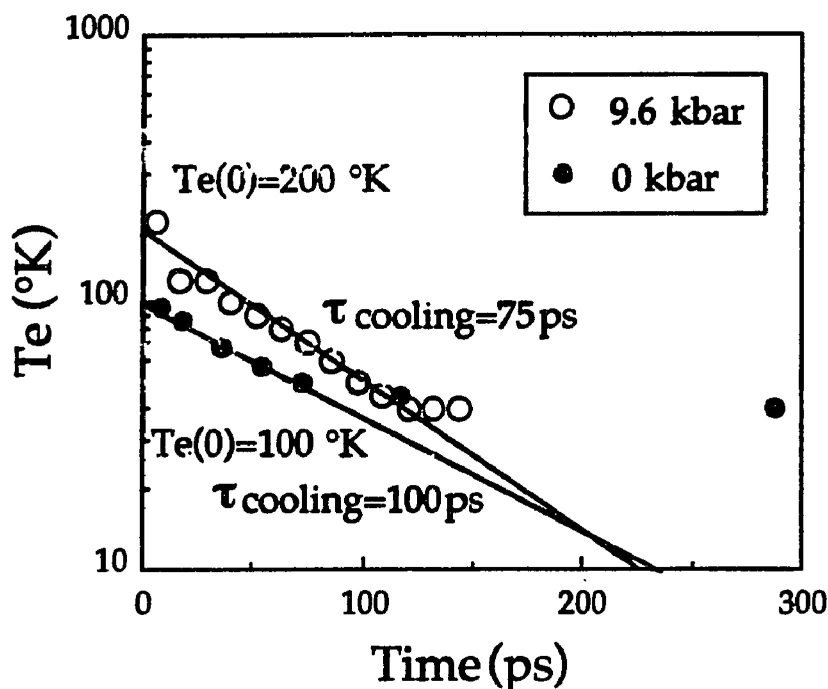

Fig.6.2.7 Electron temperature cooling under 0 and 9.6 kbar of uniaxial stress.

stress. The solid lines are exponential fits for the electron temperature coolings. It is clear that the electron temperature cooling time of 75 ps under 9.6 kbar of stress is faster than that of 100 ps without stress.

The band structure under 9.6 kbar of stress is similar as the 40Å MQW/Si as discussed in the previous chapter. Since the well width is different from the 40Å case, it is not straight forward to compare the electron cooling process in the 188Å MQW under 9.6kbar of stress. However, the electron cooling time becomes faster when the lowest subband was altered to lmh band as similar as the 40Å MQW/Si case.

To further evaluate the electron cooling dynamics under various compressive stresses, average electron energies as function of delay time were calculated from the time-resolved PL spectra obtained at 4 °K lattice temperature. A 2D PL spectrum I(E,t) at a delay time t is selected from the 3D

time-resolved spectrum and determines the average carrier energy at the delay time by using,

$$\langle E(t)\rangle = \int_{E_1}^{E_2} I(E, t)\bullet E \, dE / \int_{E_1}^{E_2} I(E, t) \, dt \qquad (6.2.3)$$

where E_1 and E_2 are the low and high energy edges of the PL spectrum at the delay time t because the experiment was carried out within a certain PL energy region.

The time-resolved PL spectra were analyzed using Eq. 6.2.3 and the average electron energies as function of delay time under various stresses are depicted in Fig. 6.2.6. (a) and (b). The figures show several features on the average energy relaxation process under the external stresses.

As the magnitude of stress increases, the average energies shift to higher energies because the band edge energies are lifted. After 7 kbar of stress, the transition energy does not move much. This indicates that the lowest transition has become the conduction band to the lmh subband which is less sensitive to the compressive stress.

Another noticeable feature is that the initial average energies above 9 kbar of stress increase, first reach their peaks, and then start relaxing their energies to lower energies within 30 ps after the photoexcitation.

Subtracting the values $\langle E(t)\rangle$ at 300 ps delay time from the $\langle E(t)\rangle$ curves under different stresses, the initial average electron kinetic energies under the stresses were evaluated and are shown in Fig.6.2.9.(a) and (b) corresponding to the original $\langle E(t)\rangle$ data in Fig. 6.2.8. (a) and (b), respectively.

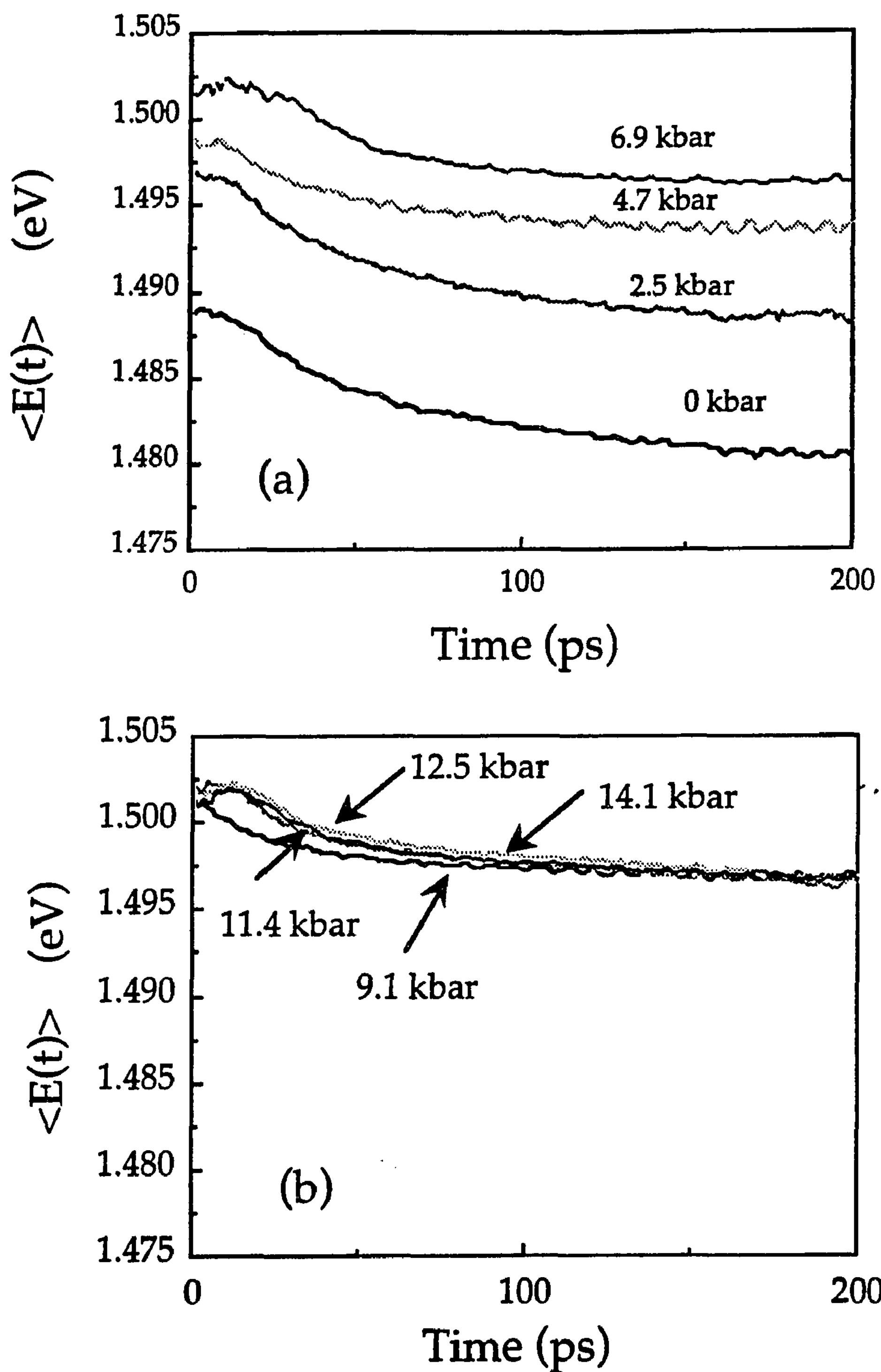

Fig. 6.2.8. Average carrier energy (a) under and (b) above 9 kbar of uniaxial stress at 4 °K lattice temperature.

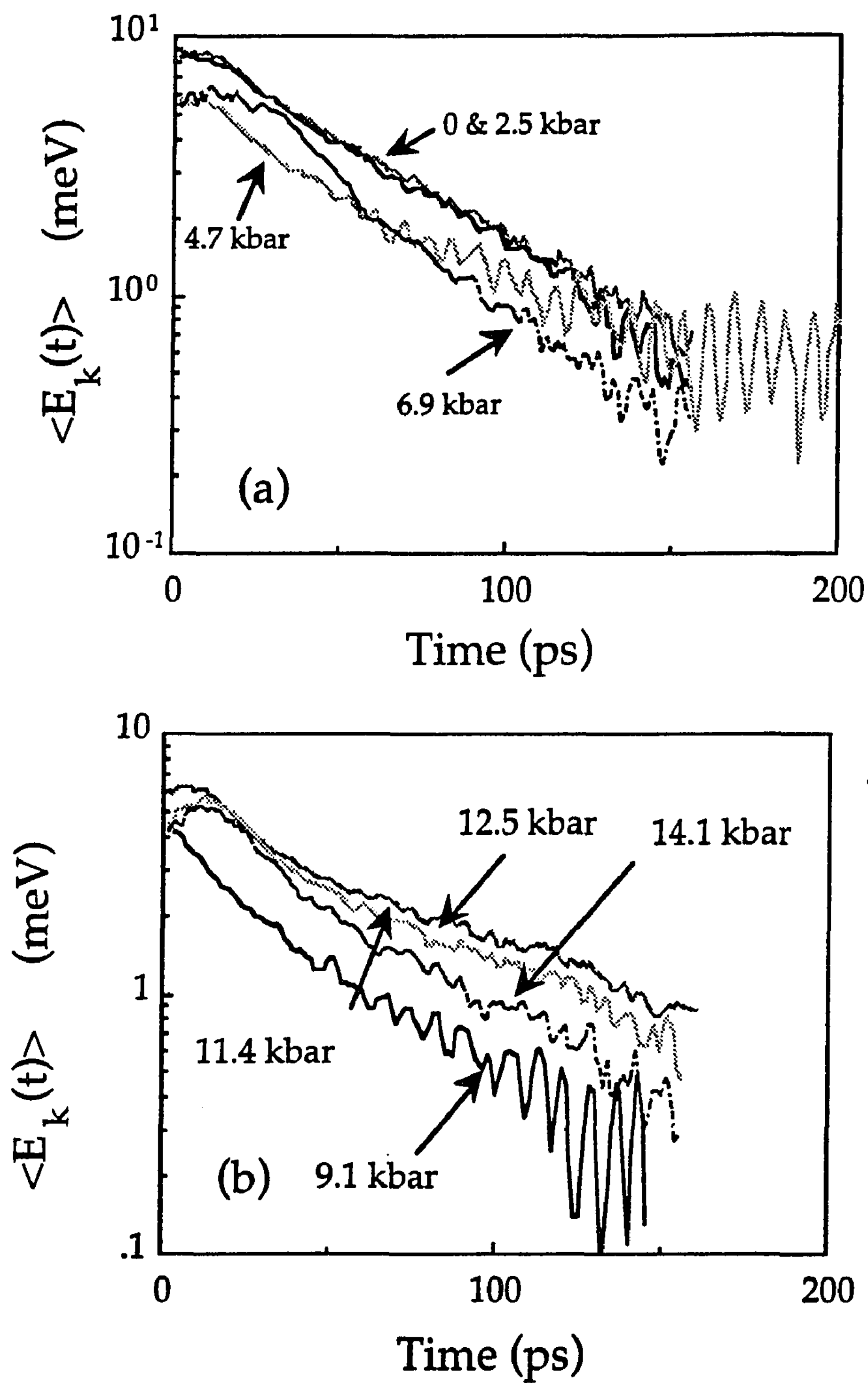

Fig.6.2.9. Average carrier kinetic energy after subtracting the long relaxation components under various uniaxial stress.

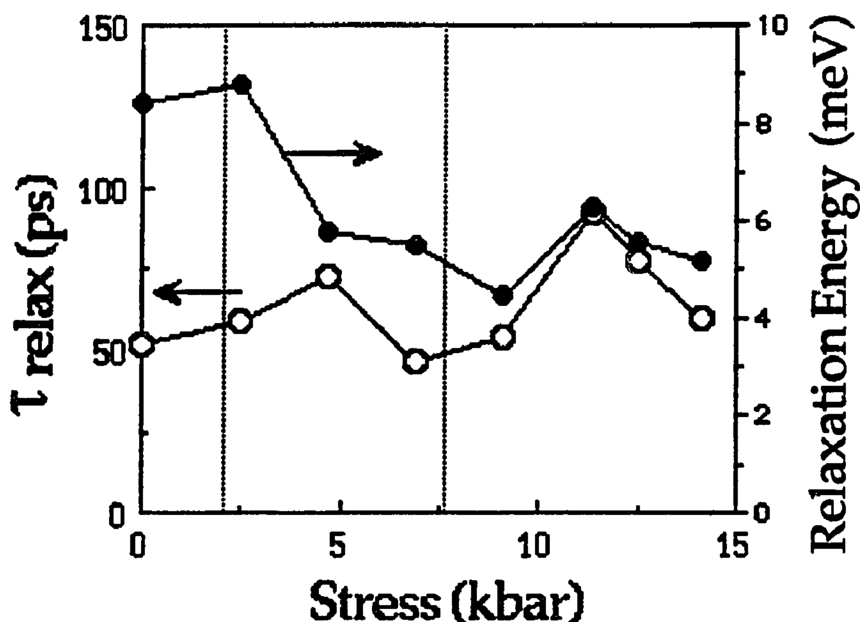

Fig. 6.2.10. Average carrier energy relaxation time and the relaxation energy under various uniaxial stress. The dashed lines correspond to cross over points in valence subbands.

The average kinetic energies under 0 and 2.5 kbar stresses are single exponential relaxation curves while those under higher stresses becomes non-single exponential. The highly stressed (X>9 kbar) average kinetic energy curves show the initial energy peaks as discussed previously.
It is clearly observed that the carrier relaxation process after 2.5 kbar is changed.

To estimate the energy relaxation rates under the stress, the average electron kinetic energy relaxation times were determined using simple exponential fits to the evaluated curves although they show fast and slow relaxations. The relaxation energies ΔEs which are defined as the energy difference between the peak $<E_k(t)>$ and $<E_k(t')>$ at a long delay time t'. The

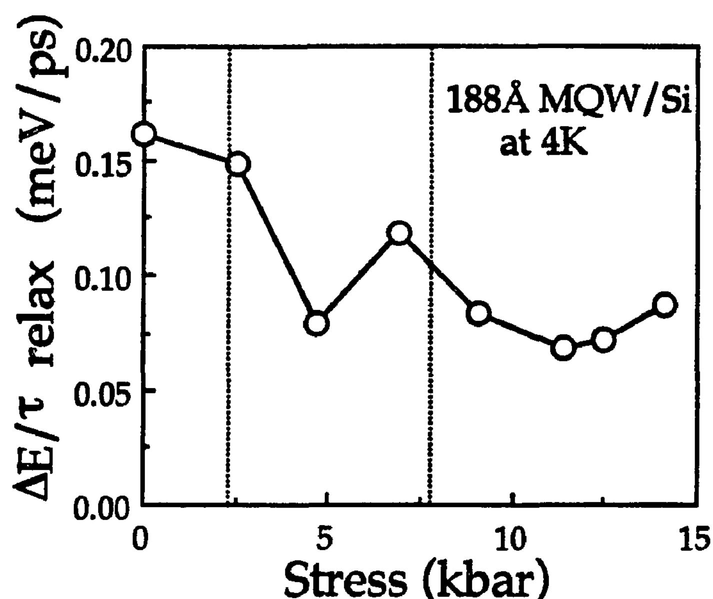

Fig.6.2.11. Average kinetic energy relaxation rates under various compressive stresses.

evaluated energy relaxation times and the relaxation energies ΔEs are shown in Fig. 6.2.10. The open circles are average energy relaxation times while the dots are the relaxation energies as defined above. The dotted lines in Fig. 6.2.10. indicate the anti-cross stress (between the m=1 hmh and m=1 lmh subbands) and crossover stress (m=1 hmh to m=3 lmh subband), respectively. As the stress increases from 2 to 5 kbar, the relaxation time becomes slower and then fast again between 6 to 10 kbar. Around 12 kbar the relaxation time becomes slowest. The relaxation energy decreases as the stress increases from 2 to 5 kbar and stays almost same energies.

Fig.6.2.11. depicts the average kinetic energy relaxation rates obtained by taking ratio between the relaxation energies ΔE and the relaxation times τ_{relax} at the various stresses. The dotted lines indicate the anti-crossing and crossover stresses between subbands as depicted in Fig. 6.3.8. After the crossover of the

lowest hmh and lmh transition, the relaxation rate drops down to about half of that before the crossover and increases when the 11HH and 13LH subband anti-cross. The uniaxial compression lifts the conduction subbands linearly. Such linear shift may not cause this complex change of the relaxation process. On the other hand, the stress lifts the valence subbands complex way as depicted in Fig. 6.2.4. Therefore, the energy relaxation during the cooling depends on the valence subband structure and the relaxation rate becomes larger when the hmh subband located at a lower energy.

To understand the energy relaxation kinetics, a five energy level model was adopted. The model energy diagram is depicted in Fig. 6.2.12. The higher energy levels E_1 to E_4 contains numbers of carriers N_1 to N_4, respectively. The carriers in the levels relax to lower energy levels as depicted by arrows with time constants τ_{r1} to τ_{r4}. The carriers in the E_3 level scatter to E_4 level with a scattering time τ_s. When this model is compared with the real carrier relaxation process, the E_1 to E_3 and the E_2 to E_3 relaxations correspond to hot carrier intra-valley thermalizations in two different subbands, the E_3 to E_4 transition corresponds to inter-subband scatterings, the E_3 and E_4 to the ground level are radiative recombination processes.

These carrier relaxation processes are simulated by following rate equations to determine carrier populations at the levels.

The change in the carrier population at E_1 level is given by,

$$\frac{dN_1}{dt} = -\frac{N_1}{\tau_{r1}} \qquad (6.2.4a)$$

and that at E_2 level is equated as,

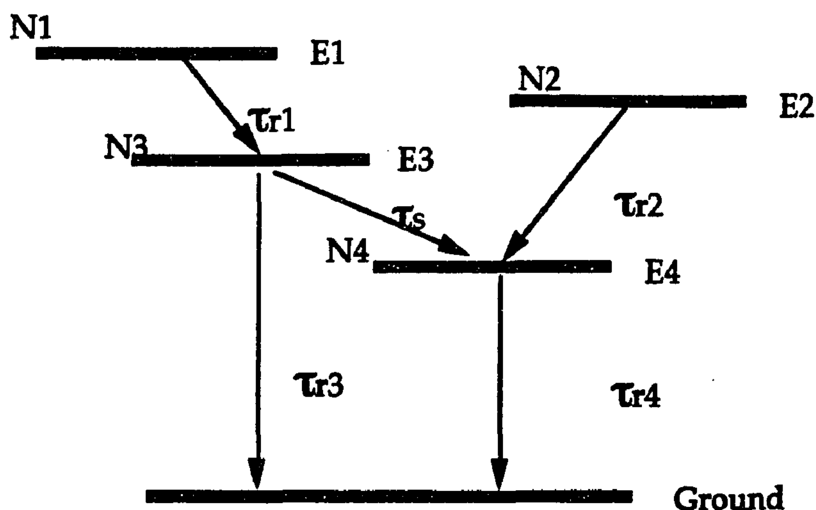

Fig.6.2.12. Five level energy relaxation model

$$\frac{dN_2}{dt} = -\frac{N_2}{\tau_{r2}} \quad . \qquad (6.2.4b)$$

The carriers at the E_1 and E_2 levels relax to lower energy levels single exponentially.

The carrier population in the E_3 level increases due to the relaxation from the E_1 level and decreases due to the scattering to E_4 levels and the recombination to the ground level. The rate equation is given by,

$$\frac{dN_3}{dt} = -\frac{N_3}{\tau_{r3}} - \frac{N_3}{\tau_s} + \frac{N_1}{\tau_{r1}} \quad . \qquad (6.2.4c)$$

The carrier population in the E_4 level increases due to the relaxations from the E_3 and E_2 levels and decreases only by the recombination process. The population is equated as,

$$\frac{dN_4}{dt} = -\frac{N_4}{\tau_{r4}} + \frac{N_3}{\tau_s} + \frac{N_2}{\tau_{r2}} \quad . \qquad (6.2.4d)$$

When one determines an average carrier energy from a PL spectrum, the radiative energy levels are considered to be taken into account. Since the E_1 and E_2 levels correspond to hot carrier states which were assumed not to give radiative recombinations. The average carrier energy in this five level model is determined by the populations in the E_3 and E_4 levels. The average carrier energy is given by,

$$\langle E(t) \rangle = \left(\frac{N_3 E_3 + N_4 E_4}{N_3 + N_4} \right) . \qquad (6.2.5)$$

Solving these rate equations, the populations at the levels are determined to be the followings as,

$$N_1(t) = N_{10} * \exp(-t/\tau_{r1}), \qquad (6.2.6a)$$

$$N_2(t) = N_{20} * \exp(-t/\tau_{r2}), \qquad (6.2.6b)$$

$$N_3(t) = N_{30} * \exp{-t/\tau_x)} + N_{10}/\tau_{r1} * \tau_c * (\exp(-t/\tau_x) - \exp(-t/\tau_{r1})), \qquad (6.2.6c)$$

and

$$N_4(t) = [\, N_{40} + N_{30}/\tau_s * \tau_a * \{1 - \exp(-t/\tau_a)\}$$
$$+ N_{20}/\tau_{r2} * \tau_b * \{1 - \exp(-t/\tau_b)\}$$
$$+ N_{10}/\tau_{r1} * \tau_c * \{\tau_a * \{1 - \exp(-t/\tau_a)\} - \tau_d * \{1 - \exp(-t/\tau d)\}\}] \bullet \exp(-t/\tau_{r4}),$$

$$(6.2.6.d)$$

with

$$1/\tau_x = 1/\tau_{r3}+1/\tau_s \ , \qquad (6.2.7a)$$

$$1/\tau_a=1/\tau_x-1/\tau_{r4} \ , \qquad (6.2.7b)$$

$$1/\tau_b=1/\tau_{r2}-1/\tau_{r4} \ , \qquad (6.2.7c)$$

$$1/\tau_c=1/\tau_{r1}-1/\tau_x \ , \qquad (6.2.7d)$$

and

$$1/\tau_d=1/\tau_{r1}-1/\tau_{r4} \ , \qquad (6.2.7e)$$

where N_{i0}s (i=1,2,3, and 4) are the initial carrier populations at the energy levels E_1 to E_4, respectively. Substituting Eq.s 6.2.6 and 6.2.7 into Eq. 6.2.5, the average carrier energy in the five level system is determined.

The initial carrier populations are assumed to be constants as N_{10}=10, N_{20}=30, N_{30}=0, and N_{40}=200. Since the calculated average carrier energies will be normalized later, the numbers for the initial carriers are relative values but not absolute carrier populations. The hot carrier relaxation times τ_{r1} and τ_{r2} are assumed to be 5 ps and 8 ps, respectively. The carrier recombination times τ_{r3} and τ_{r4} are assumed to be 300 ps and 20 ps, respectively. The most important parameter to determine the average energy relaxation process is the carrier scattering time τ_s which is kept as a variable.

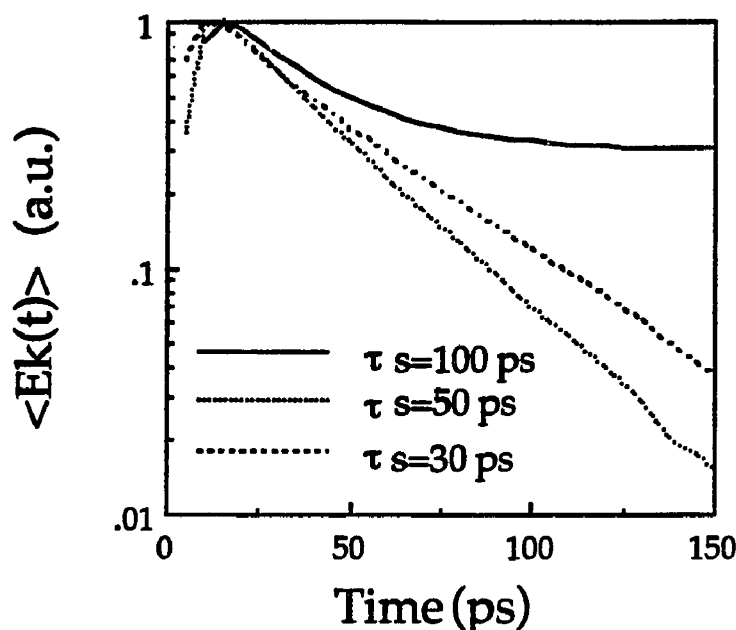

Fig.6.2.13. Calculated average energy using the five level model with the scattering time τs as a variable.

Fig. 6.2.13. shows the calculated curves using τ_S=100, 50, and 30 ps with a solid, a dotted, a dashed curves, respectively. The figure shows several important features. First, the average energies change non-single exponentially. Next, the average energy curves become a single exponential as the scattering time becomes shorter from 100 ps to 30 ps. And the initial average energy peak delays as the scattering time becomes longer. Although the model is too simple using only discrete five levels, the real average energy relaxation process is simulated.

Comparing these calculated curves with the measured data shown in Fig. 6.2.9, the following concepts are deduced.

First, for the energy relaxation under 0 and to 2.5 kbar stress, they showed simple exponential and no initial peak as similar case as the fast

scattering time case as τs=30 ps in the simulation. This implies that the inter-subband scattering time for the lmh to hmh subbands under these stresses is fast. As the stress increases, the measured average energy relaxation curves shown in Fig. 6.2.9. (b) become similar as the calculated curve with τs=100 ps. Thus, the inter-subband scattering time from the hmh to lmh subband becomes slower. The inter-subband scattering under 0 to 2 kbar stress is the transition from the lmh to the hmh subband in the valence subband while that under higher stress is the hmh to the lmh subband or the higher hmh to the lower hmh subband. Although the simulation is preliminary, the inter-subband scattering process from the lmh to hmh subband was suggested to be slow while that from the hmh to the lmh subband is faster.

6.2.5. Conclusion

The carrier energy thermalization and cooling dynamics in a 188Å MQW/Si sample under various external uniaxial compressive stresses has been investigated using picosecond time-resolved PL spectroscopy. The electron cooling time under 9.6 kbar of compressive stress becomes faster than that under 0 stress. The energy exchange between hot electron and lowest valence hole (either hmh or lmh) determines the electron cooling process as similar mammer as the previous 188Å and 40Å MQW/Si results. The average electron relaxation process was found to depend on the lower valence subband structure under different stresses.

Using a simple five energy level model to simulate the inter-subband scattering time effect on the average energy relaxation process, it was found that the non-single exponential process and the average energy peaking

behavior were due to the slow inter-subband scattering time. The slow inter-subband scattering causes the peak average energy positions to be delayed.

Therefore, the stress altered band structure causes the carrier energy relaxation times to be changed. The average carrier relaxation times were affected by the slow inter-subband scattering from a lmh to a hmh subband.

6.3 Reference in Chapter 6

1). C.V.Shank, R. L. Fork, B. I. Greene, C. Weisbuch, and A.C. Gossard, Surf. Sci. 113,108(1982)

2). C.V. Shank, R. L Fork, R. Yen, J. Shah, B.I. Greene, A.C. Gossard, and C. Weisbuch, Solid State Commun. 47, 981 (1983)

3). G. P. Agrawal and N. K. Dutta, "Long-wavelength Semiconductor Lasers", Van Nostrand Reinhold (New York, 1986)

4). Hao Qiang, F. H. Pollak, Kai Shum, Y. Takiguchi, R. R. Alfano, Appl. Phys. Lett. 60, 2651 (1992)

5). Johnson Lee and M. O. Vassell, Phys. Rev. B. 37, 8855 (1988)

6). Johnson Lee and M. O. Vassell, Phys. Rev. B. 37, 8861 (1988)

7). Hao Qiang, F. H. Pollak, and G. Hackman, Solid State Commun. 76,1087 (1990)

8). Hao Qiang, will be submitted to a journal.

CHAPTER 7

2D EXCITON DYNAMICS IN INTRINSIC GaAs SQW/Si

7.1. Introduction

Quasi-two dimensional (2D) exciton dynamics in GaAs single QW and MQW has been studied extensively. 2D exciton formation time in a 80Å MQW was determined to be shorter than 20 ps by T. C. Damen et al. [1] and in a 50Å QW to be 14.4 ps by R. Strobel et al. [2] The light mass hole inter-subband exciton relaxation time to heavy mass hole exciton was evaluated to be 90 ps in a 86 Å MQW, heavy mass hole exciton formation time to be 190 ps, and exciton localization time to be 130 ps by J. Kusano et al.[3] using a rate equation analysis fit to the PL time profiles. Takagahara theoretically studied the 2D exciton dynamics considering various phonon interactions[4]. The 2D exciton recombination process was extensively studied by Feldmann et at.[5] both experimentally and theoretically. Exciton decay times were found to vary from 200 ps to 2 ns depending on well width, exciton photoluminescence linewidth (related to exciton binding energy) and exciton masses (exciton binding energy is also determined by the exciton mass).

Exciton dynamics in an intrinsic GaAs QW determines optical and electronic properties of the QW at a low lattice temperature below 100 °K where the excitons can exist because of the exciton binding energy of 10 to 20 meV which is higher than the lattice thermal vibration energy. When a stress is applied to the QW structure either internally (built-in) or externally (from outside), the exciton dynamics can be altered because of the band structure

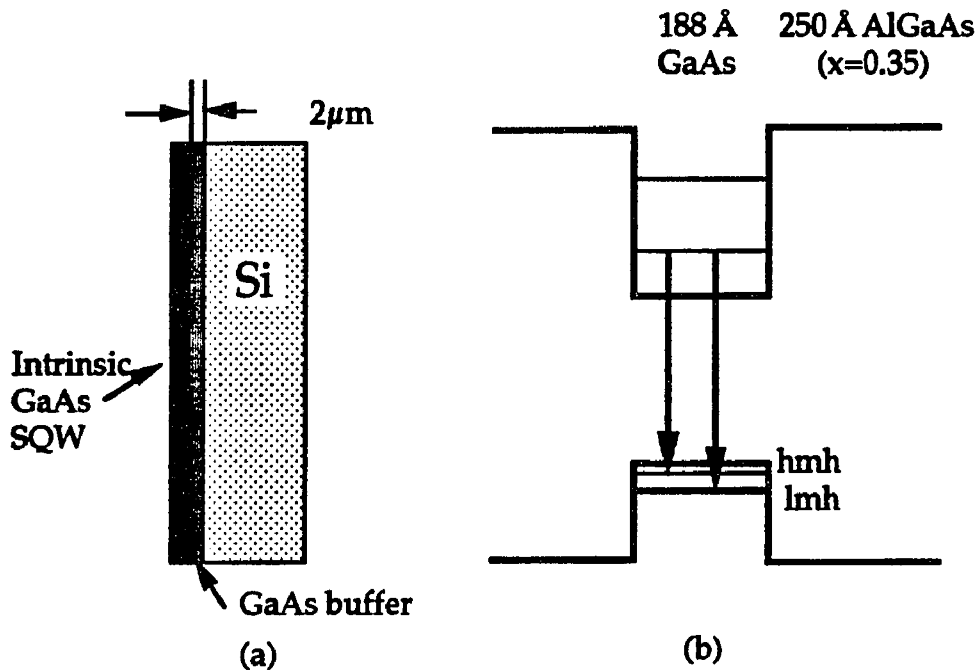

Fig.7.2.1. (a) Sample and (b) band structures of the 188Å SQW/Si

change. There is a need to understand the effect of stress on exciton dynamics to improve the intrinsic device.

In this chapter, the exciton dynamics under built-in biaxial and external uniaxial stress in an intrinsic GaAs single QW with 188Å well width grown on a Si substrate was investigated using the time-resolved PL spectroscopy with a stress apparatus.

7.2. Sample and experiments

An intrinsic 188Å single QW structure sandwiched by 250Å $Al_{0.35}Ga_{0.65}As$ barriers was fabricated on a (100) Si substrates tilted 4° toward <011> direction with a 2μm of GaAs buffer layer as shown in Fig.7.2.1 (a) for the sample structure and (b) for the band structure along growth direction. As the result of the difference in the thermal expansion coefficients between GaAs and Si

substrate, the GaAs QW is strained biaxially about 2 kbar as same manner as MQW/Si samples investigated in Chapter 6 except the barrier for the SQW/Si was not modulation doped. This SQW/Si sample was grown by MBE at Univ. of Illinois, Arbana-Champaign by Prof. Morkoc's group. The band structure as function of uniaxial stress at room temperature was determined from the modulated photoreflection spectroscopy as shown in Fig. 6.2.2. under collaboration with Hao Qiang and F. H. Pollak[6)] at the Brooklyn College.

The sample was placed in a stress apparatus and inserted into an optical dewar to cool the sample to 4 °K under a compressive stress. The sample was uniaxially compressed up to 14 kbar. The sample in the dewar was photoexcited by laser pulses from a CPM dye laser operated at 82 MHz with 10 mW average power, 100 fs pulse duration, and 2.0 eV photon energy. The laser beam was focused onto the sample through 20 cm focal length lens to obtain 2.5×10^{12} cm^{-2} photogenerated carrier density. The PL arising from the exciton annihilation was collected into a 25 cm spectrograph connected to a streak camera with an S-20 photocathode which has high sensitivity at observing region of 800 nm. The time- and spectrum-resolved PL was stored into an image processor (TA) to analyze the exciton dynamics from the PL kinetics.

7.3. Experimental results

As the compressive stress increases, the PL peak shifts to high energy and the time-resolved PL spectra did not show dramatic change as same manner as doped- MQW/Si case. Fig. 7.3.1 shows the PL spectra under 0 and 9.3 kbar stresses. The 0 kbar spectrum shows three peaks at 1.486, 1.4997, and 1.5109 eV while the 9.3 kbar PL spectrum shows two peaks at 1.5006 and 1.5134 eV. These

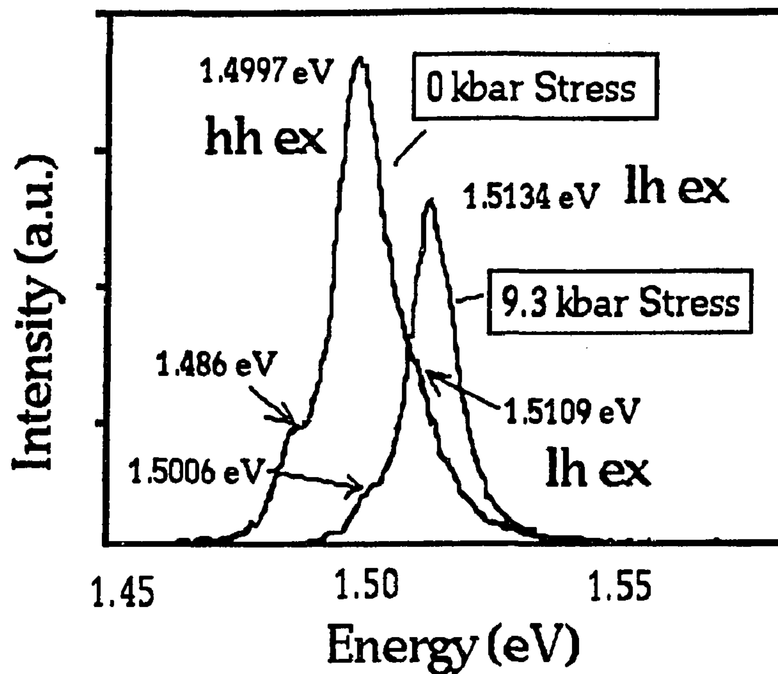

Fig.7.3.1. PL spectra for the SQW/Si under uniaxial stress of 0 kbar and 9.3 kbar at 4 °K lattice temperature.

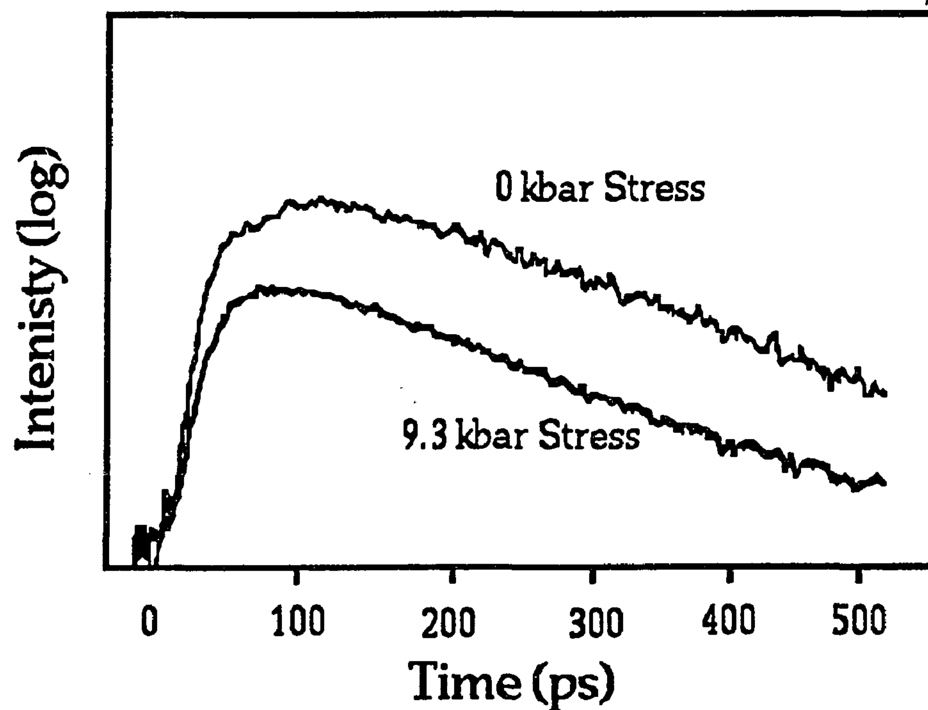

Fig.7.3.2. PL intensity profiles for the SQW/Si under uniaxial stress of 0 kbar and 9.3 kbar.

transitions can be identified from the calculated transition energies. For the 0 kbar stress, the peak at 1.4997 eV arises from the annihilation of hmh exciton while the peak at 1.5109 eV arises from the annihilation of lmh exciton. For the 9.3 kbar PL spectrum, the peak at 1.5134 eV arises from the lmh exciton annihilation. The low energy peaks for both cases may be unknown impurity bound exciton annihilation or conduction to valence bands transitions of the GaAs buffer layer. It is clear that the hmh subband moves to high energy but the lmh subband is in-sensitive to the compressive stress and stays at almost same energy level.

Fig.7.3.2. shows the PL time profiles integrated between high and low energy PL edges under 0 and 9.3 kbar of stresses. The rise time for the profile under 9.3 kbar is faster than that at the 0 stress. The PL time profile of the 0 kbar case shows slow rising component in contrast to the 9.3 kbar profile. The exciton annihilation decay time is found to be un-changed by the stress and estimated to be 170 ps.

7.4. Discussion

7.4.1. Initial exciton dynamics

The band structures in the xy and z directions without stress (0 kbar) and under 9.3 kbar of uniaxial compressive stress are schematically shown in Fig. 7.4.1. The lowest subband for the 0 kbar case is the hmh while that under 9.3 kbar stress is the lmh because the compression lifted the hmh subband to higher hole energy and exceeded the crossover stress. The 2.0 eV photons from the pump laser photoexcite the carriers(solid arrows). The hot carriers ($\varepsilon > k_B T_L$) thermalize towards the bottom of each subband shown by the thick arrows in

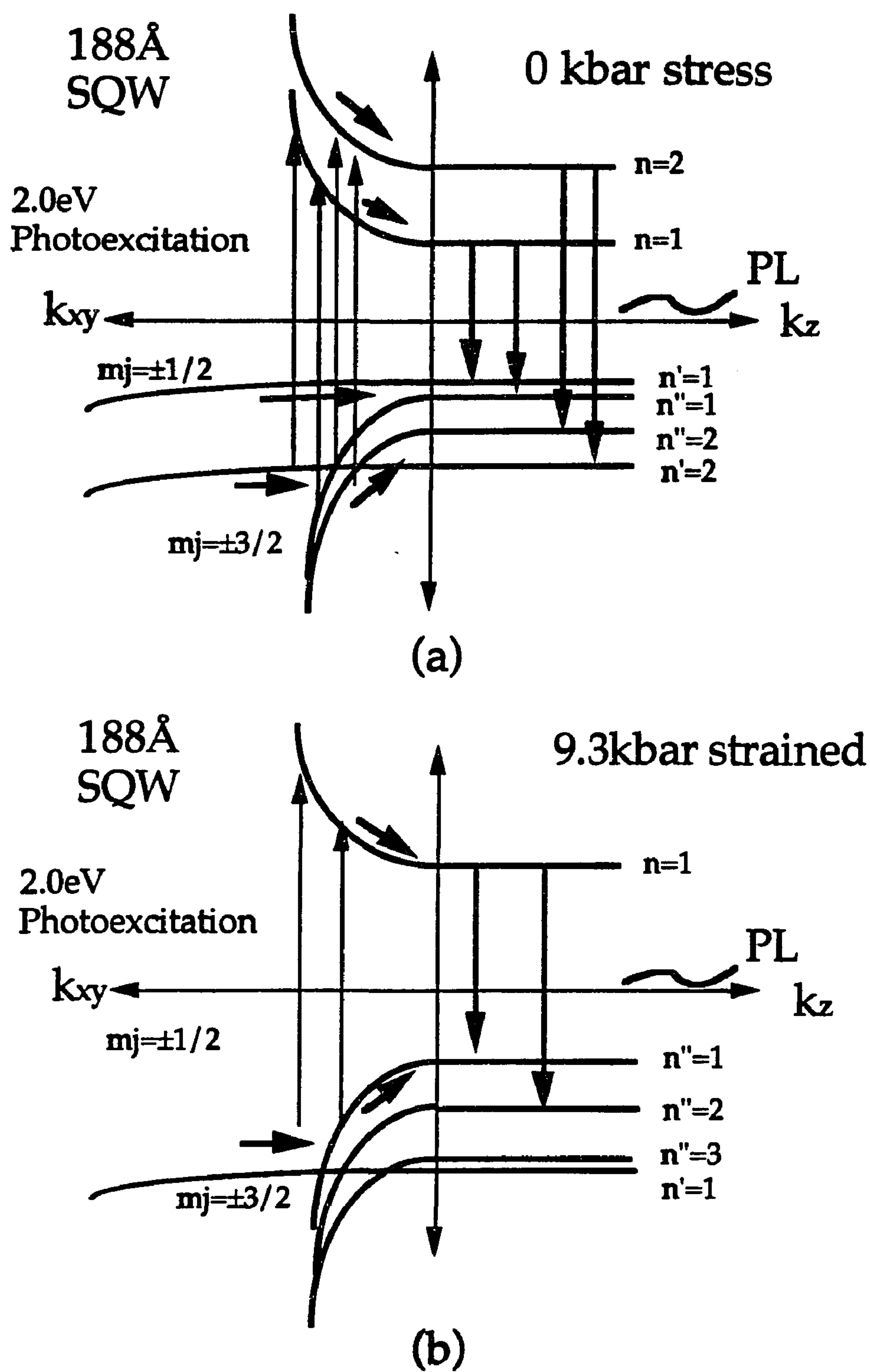

Fig. 7.4.1. Band structures of the 188Å SQW/Si (a) under 0 kbar and (b)under 9.3 kbar uniaxial compressive stress at 4 °K.

Fig.7.4.1. The carriers in high energy subband scatter to lower energy subbands. During the thermalization and cooling, these carriers form excitons. These warm excitons release energies by emitting phonons and reach the lowest exciton levels near k=0. The excitons recombine and annihilate photons as depicted by the downward gray arrows. The difference in the exciton dynamics between the 0 kbar and 9.3 kbar cases mainly arises from the structure change in the lowest exciton bands.

The PL rising profiles in Fig. 7.3.2 are different because the hole thermalization and inter-subband scattering time are different. In the previous section 6.1, it was found that the lmh thermalization is faster than the hmh thermalization. The inter-subband scattering is one order of magnitude slower than the thermalization time for the scattering from the lmh to the hmh subband. The slow scattering time is determined from the slow rising portion of PL profile. In the strained SQW/Si, the 9.3 kbar stress PL profile did not show a clear slow rising component. This observation means that the inter-subband scattering from the hmh to the lmh subband is faster than that from the lmh to the hmh. The band structure under 9.3 kbar has less bottlenecks (band mixing) on the hole dynamics than the lower stress structures (Fig.7.4.1) The faster loss rate can be expected for highly strained sample. This effects will be discussed in the next section.

7.4.2. Exciton average energy relaxation

To determine the exciton energy relaxation process, the average exciton energy was calculated from the PLs using the equation (as discussed in Chapter 3.5) given by,

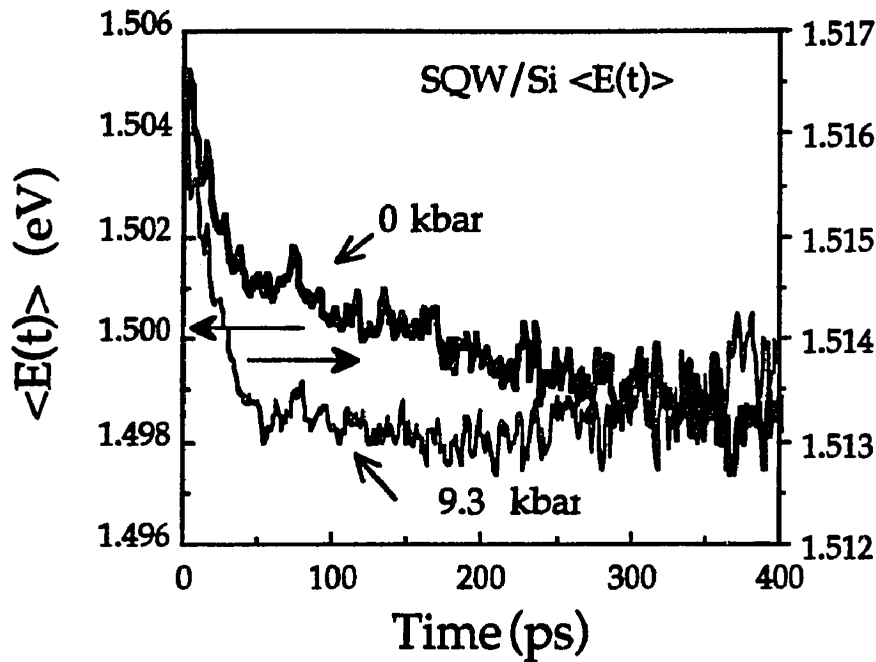

Fig. 7.4.2. <E(t)> for the SQW/Si without stress and under 9.3 kbar of stress at 4 °K lattice temperature.

$$\langle E(t) \rangle = \int_0^{\infty} E \bullet I(E, t)\, dE \Big/ \int_0^{\infty} I(E, t)\, dE \quad , \qquad (7.4.1)$$

where I(E,t) is a 2D PL spectrum at a delay time selected from the 3D time-and spectral resolved PL image, and ε is the exciton annihilation energy. Fig. 7.4.2. shows the calculated average exciton energies as function of the delay time under 0 kbar stress (thick solid line) and under 9.3 kbar stress (thin solid line) for the QW at 4 °K. The average exciton energy relaxation under 0 kbar stress clearly shows a fast and slow relaxation components while that under 9.3 kbar stress shows only fast relaxation process.

Fitting exponential curves (single and double) to each average exciton relaxation curves, a fast and slow relaxation times and the relaxation energies (defined as the energy difference at the initial time and at the end of the

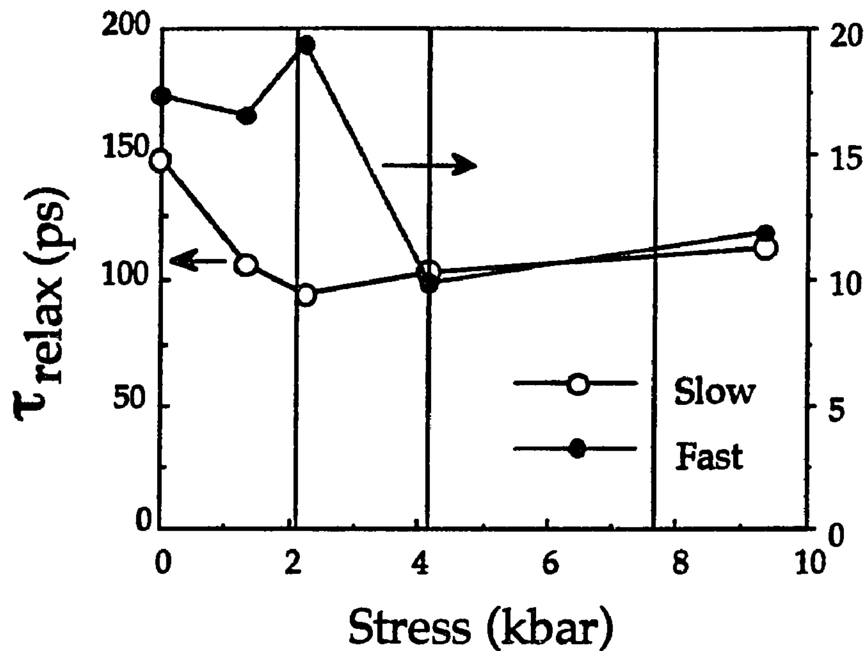

Fig. 7.4.3. The fast and slow relaxation rates under various uniaxial compressive stresses. The open circles are for fast relaxation rates and the dots for the slow relaxation rates.

relaxation) are evaluated. Fig. 7.4.3 shows the evaluated fast and slow relaxation times. From this figure, there is one order of magnitude difference between the relaxation times for the fast and slow relaxation components. In the band calculation result, there occurs a band mixing around 3 kbar, the bottleneck on the hole dynamics are expected. The fast relaxation component changes its time around 3 kbar to be slower while the slow component changes its time around 1 kbar. The fast relaxation time becomes slowest at the 2.3 kbar stress. The 3 kbar stress corresponds to the stress where the lmh and hmh subbands cross over. The fast component becomes slower after 4 kbar of stress where the lowest valence subband changed from hmh to lmh subband tuned by the uniaxial stress. The difference in the fast relaxation process can be due to the exciton mass difference.

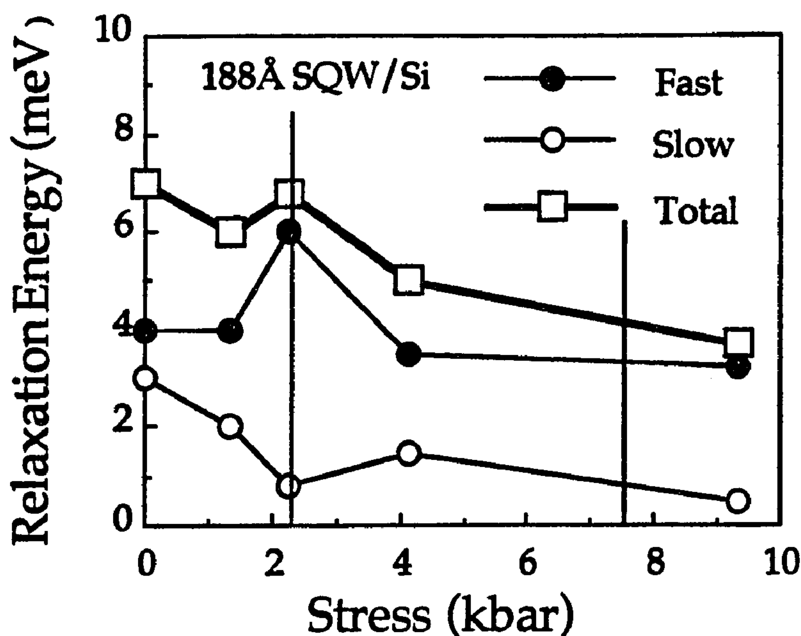

Fig.7.4.4. The exciton relaxation energy for fast (dots) and slow (open circles) relaxation profiles. The open squares are total relaxation energies.

The relaxation energies extracted from various PL spectra under different uniaxial stresses are depicted in Fig. 7.4.4. The dots correspond to the fast relaxation energies measured from the peak average energy to the end of fast relaxation process around 100 ps while the open circles are for the relaxation energies due to the slow relaxation process. The open squares are the total relaxation energies. At 2.3 kbar of compressive stress, the fast relaxation energy reaches its peak and then becomes lower. On the other hand, the relaxation energy for the slow component becomes the lowest at the 2.3 kbar stress.

Taking the ratios between the evaluated relaxation times τ_{relax}s and the relaxation energies ΔEs, the average exciton energy relaxation rates ($\Delta Es/\tau_{relax}$) are calculated and shown in Fig. 7.4.5.

The following model explains the fast energy relaxation component which was attributed to exciton-LO phonon interaction.

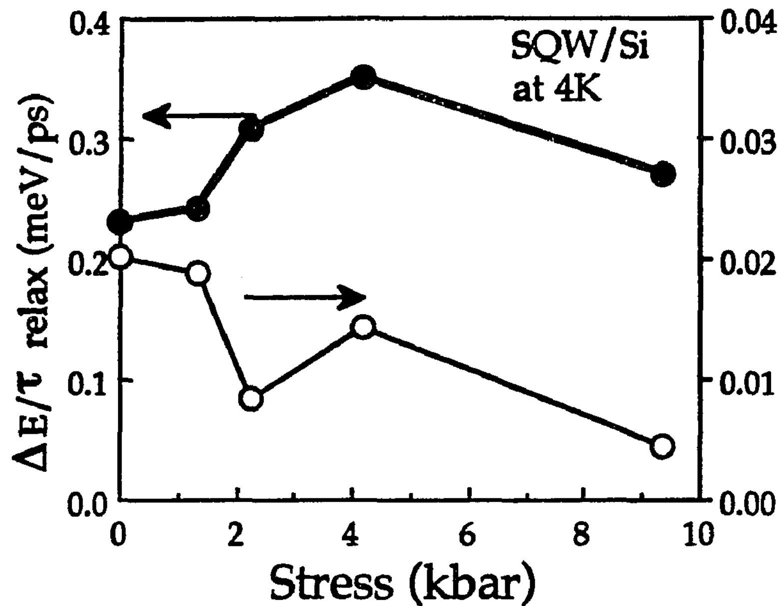

Fig.7.4.5. Average exciton energy relaxation rates for the fast and slow components in 188Å SQW/Si under various compressive stress.

Lee et al.[7] discussed 2D exciton energy relaxation process through various phonon interaction mechanisms. Spector[8] introduced an exciton linewidth Γ_{op} arising from exciton-LO phonon interaction and is given by,

$$\Gamma_{op} = 4Nq^2M\omega_{op}b^6/\hbar K L_z^2 \bullet I\{2\pi/L_z,(2M\omega_{op}/\hbar)^{1/2}\} \bullet f_0(2M\omega_{op}/\hbar) \quad (7.4.2a)$$

with

$$I(x,y)=(\pi^2/xy^2) \bullet [1+y^2/2(x^2+y^2)-x^5/2py(x^2+y^2)^2\{1-\exp(-2\pi y/x)\}] \quad (7.4.2b)$$

and

$$f_0(z) = [\ \{\beta^2+(2m_h{}^2z/M^2)\}^{-3/2} - \{\beta^2+(2m_c{}^2z/M^2)\}^{-3/2}]^2 \quad , \quad (7.4.2c)$$

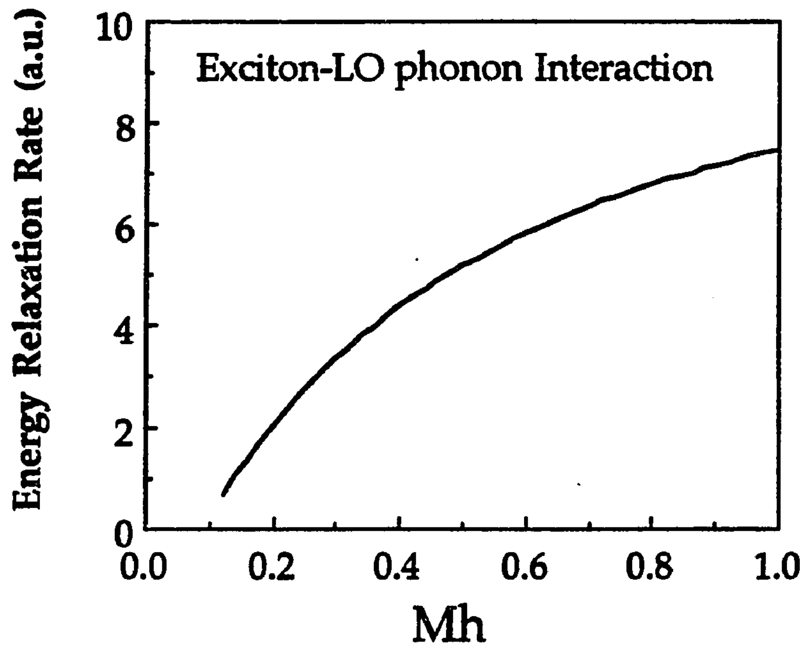

Fig. 7.4.6. Exciton energy relaxation rate as function of hole mass

where N is the number of thermal phonon(Bose-Einstein factor), q is the electron charge, $M=m_c+m_h$ (m_c: conduction electron effective mass, m_h : hole effective mass), L_z is the well width, β is a variable with an order of $3/a^*$ (a^*: Bohr radius), $1/K'=1/K_\infty-1/K_s$ (K_∞ : optical dielectric constant, K_s: static dielectric constant), and ω_{op} is the LO phonon angular frequency.

The energy relaxation rate due to this interaction is given by,

$$d\langle E_k(t)\rangle/dt = 2\Gamma_{op}\bullet\omega_{op} \quad . \qquad (7.4.3)$$

Using Eq.s 7.4.2 a,b, c and 7.4.3, the energy relaxation rate due to the exciton -LO phonon interaction is calculated as function of exciton mass as shown in Fig.

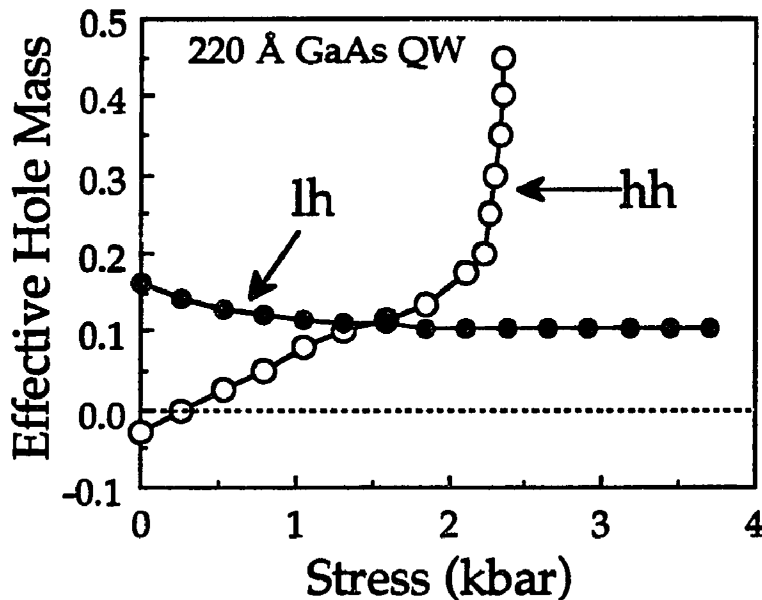

Fig. 7.4.7. Effective hole mass in a 220 Å QW under [100] uniaxial compressive stress calculated by J. Lee[9,10)]

7.4.6. The figure shows that the heavier the exciton mass, the larger the energy loss rate.

To understand the experimentally measured energy relaxation rate, a band structure calculation by Lee et al.[9,10)] gives an important aspect on the lowest energy hole subband mass. According to the band structure calculation for a 220 Å quantum well under uniaxial compressive stresses, the lowest valence subband changes from the hmh to lmh subband after a cross over stress as shown in Fig. 7.4.7. Note, their notations for the hmh and lmh subbands are different from my notations. The hmh effective mass increases linearly above the crossover stress while the lmh effective mass decreases slowly and does not change much after the crossover stress. This exciton mass change, which alters the energy exchange rate, exactly matches to the change in the fast energy relaxation process as shown in Fig. 7.4.5. Namely, the energy relaxation

increases up to the crossover stress and becomes unchanged after the crossover stress. Therefore, I can conclude that the fast energy relaxation process arises from exciton-LO phonon interaction which depends on the lowest exciton mass.

The slow energy relaxation component was attributed to a slow inter-subband exciton scattering process. As discussed above, the inter-subband scattering time from the lmh to the lower hmh exciton subband is slow as 130 to 300 ps. Although the exciton energy relaxation due to LO phonon interaction is fast, the inter-subband scattering time slower down the energy relaxation. This process is proved by the faster energy relaxation rate after the crossover stress where the lmh subband becomes the lowest valence subband.

7.5. Conclusion

The exciton dynamics in an intrinsic 188Å GaAs SQW/Si has been investigated. The exciton energy relaxation was found to consist of a fast and a slow relaxation processes. The fast relaxation is attributed to the LO phonon scattering with exciton showing the lowest exciton mass dependence and is explained by the exciton-LO phonon interaction model. The heavier the lowest exciton mass, the larger the average exciton relaxation rate. The slow energy relaxation process is attributed to the result of slow inter-subband scattering in the valence band. Since the lmh to hmh inter-subband scattering time is slow as 130 to 300 ps, the exciton relaxation rate at later time is dominated by the inter-subband scattering time. In addition, the lmh thermalization time is also confirmed to be faster than the hmh thermalization time. This result is consistent with the hole dynamics in the n-type GaAs/Si cases.

7.6. Reference in Chapter 7

1). T. C. Damen, J. Shah, D. Y. Oberli, D. S. Chemla, J. E. Cunningham, and J. M. Kuo, J. of Luminesc. 45, 181 (1990) and Phys. Rev. B, 42, 7434 (1990)

2). R. Strobel, R. Eccleston, J. Kuhl, and K. Kohler, Phys. Rev. B 43, 12564 (1991)

3). J. Kusano, Y. Segawa, Y. Aoyagi, S. Namba, and H. Okamoto, Phys. Rev. B 40, 1685 (1989)

4). T. Takagahara, Phys. Rev. B, 31, 6552 (1985)

5).J. Feldmann, G. Peter, E. O. Gobel, P. Dawson, K. Moore, C. Foxon, and R. J. Elliott, Phys. Rev. Lett. 59, 2337 (1987)

6). Hao Qiang, F. H. Pollak, Kai Shum, Y. Takiguchi, R. R. Alfano, Appl. Phys. Lett. (1992)

7). Johnson Lee, E. S. Koteles, and M. O. Vassell, Phys. Rev. B, **33**, 5512 (1986)

8). H. N. Spector, Johnson Lee, and Paul Melman, Phys. Rev. B **34**, 2554 (1986)

9). Johnson Lee and M. O. Vassell, Phys. Rev. B. **37**, 8855 (1988)

10). Johnson Lee and M. O. Vassell, Phys. Rev. B. **37**, 8861 (1988)

CHAPTER 8

2D EXCITON DYNAMICS IN BIAXIALLY STRAINED GaAsP QWS

8.1. Introduction

Quasi-two dimensional (2D) exciton dynamics in intrinsic GaAs quantum wells (QWs) are important to determine the operation of intrinsic optical and electronic devices. Recent progress in ultrafast optical computation techniques has been realized using ultrafast non-linear optical phenomena associated with exciton screening and exciton Stark effects when a voltage is applied along the growth direction of a QW. The following 2D exciton dynamics in various kinds of QWs has been extensively studied. The 2D exciton formation time in a 80Å multiple QW (MQW) has been determined to be shorter than 20 ps by T. C. Damen et al.[1,2] and that in a 50Å QW to be 14.4 ps by R. Strobel et al.[3] Kusano et al.[4] photoexcited an intrinsic 86 Å GaAs MQW with a wavelength tuned laser and observed initial carrier kinetic energy dependence on the exciton PL time profiles. They modeled the exciton formation, inter-subband scattering, localization (migration into interface islands arising from monolayer fluctuations during the sample fabrication), and recombination processes using a coupled rate equation and determined the rates of the individual process in the MQW. The light mass hole (lmh) exciton inter-subband relaxation time to heavy mass hole (hmh) exciton was evaluated to be 90 ps, hmh exciton formation time to be 190 ps, and the localization time to be 130 ps. After the 2D exciton is formed, the exciton localization is the dominant energy relaxation process and strongly

affects the PL kinetics. K. Fujiwara et al.[6,7] discussed the 2D exciton localization process by using roughness controlled samples by growth interruption method. The inter- and intra-island exciton localization processes were found to give strong effects on the PL kinetics. Bacher et al.[8] also observed that the exciton localization process is the dominant process below 40 °K lattice temperature in a series of very thin InGaAs/InP QWs. Masumoto et al. investigated an average exciton energy relaxation process in a growth interrupted GaAs/AlGaAs MQW and analyzed in terms of acoustic deformation potential (ADP) interaction of the localized 2D exciton with the cool lattice[9] by extended a theory of surface carrier kinetics by Hess and Sah[10]. They found one order of magnitude difference in a localized exciton energy relaxation rates between the experimental result and the ADP interaction theory. The theory further predicts that the exciton relaxation rate through ADP interaction depends on well width, exciton mass, material density and ADP value. Takagahara theoretically studied the exciton localization dynamics into the interface roughness considering various phonon interactions with the exciton.[11] Basu et al.[12] extended Takagahara's work and showed that the longitudinal optical phonon interaction at low lattice and exciton temperatures does not rule the exciton localization process into the island and ADP interaction dominates the process. The 2D exciton recombination process was extensively studied and discussed by Feldmann et at.[5] and its recombination rate was theoretically derived. Exciton decay times were determined to be from 200 ps to 2 ns depending on well width, exciton photoluminescence(PL) linewidth, exciton binding energy, and exciton mass.

In this chapter, exciton dynamics under biaxial tension in an intrinsic $GaAs_{1-y}P_y/Al_xGa_{1-x}As$ QWs(GaAsP QWs) with different well widths and phosphor concentrations were investigated using the time-resolved

spectroscopy, exciton population rate equations, and average exciton energy relaxation calculations. The dynamics investigated are exciton formation, exciton inter-subband relaxation, localization into interface islands, and exciton annihilation recombination. The acoustic deformation potential interaction of localized 2D excitons at interface islands was studied using y=0.05 GaAsP QWs with various well widths at various lattice temperatures.

8.2. Sample

Two samples were grown on (100) GaAs semi-insulating substrate oriented 2° off toward (110) by atmosphere pressure MOCVD with growth interruption at 750°C substrate temperature.[13] Each sample consists of a 1 μm un-doped GaAs buffer layer, a 0.4 μm $Al_{0.35}Ga_{0.65}As$ barrier layer, single 121Å wide GaAs QW, and a series of $GaAs_{1-y}P_y$ QWs with nominal widths of 48, 79, and 121Å separated by 400Å $Al_{0.35}Ga_{0.65}Al$ barriers as shown in Fig.8.2.1(a) for the sample structure and (b) for the band structure along the growth direction. Two samples contain either 5% or 8% of phosphor in the GaAsP well materials. Because of the lattice mismatch between GaAsP and AlGaAs as discussed previously, the stress in the GaAsP wells is tensile while that in AlGaAs barrier is compressive. The magnitude of the tension in the well depends on its phosphor composition and well width. The samples were grown at Univ. of Massachusetts at Amherst by Prof. K. M. Lau's group and were obtained under collaboration with Dr. E. S. Koteles of GTE.

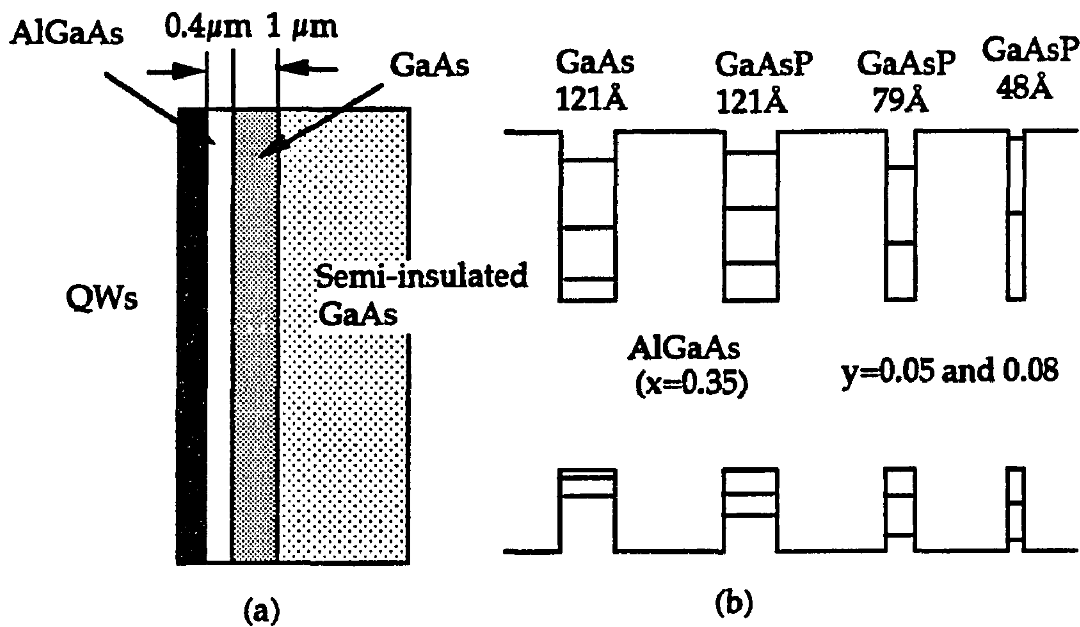

Fig. 8.2.1. (a) Sample and (b) band structures of the GaAsP QWs

8.3. Experimental setup

The samples were placed in an optical cryostat and were photoexcited separately by the laser pulses from a CPM laser. The laser pulses were 100 fs pulse duration with 2.0 eV photon energy at 82 MHz repetition rate. The laser beam with 10 mW average power was focused onto the samples through 20 cm focal length lens. The spot size was around 150 μm. The photogenerated carrier density was an order of 1×10^{16} cm^{-3}. The PL from the sample was collected into a 25 cm spectrograph, dispersed onto an input slit of a streak camera(S-20), and time-resolved. To avoid the scattered laser beam to get into the spectrograph, a color filter (#7-59) was placed in front of the spectrograph. To evaluate fast and slow PL kinetics, the time-resolved PL was measured at two sweep speeds of the streak camera. The observed time windows were 600 ps and 1.8 ns, respectively. The sample temperature were varied from 4 °K to room temperature to investigate the exciton dynamics at different lattice temperatures.

8.4. Experimental results

8.4.1. Steady state PL and PLE spectra

The steady state PL and PL excitation (PLE) spectra of the two samples at a low lattice temperature were measured by my collaborator E. S. Koteles[14] at GTE for y=0.05 and y=0.08 QWs as shown in Fig.8.4.1(a) and (b), respectively. The dotted curves are the PLE spectra and the solid curves are the PL spectra. The strong excitonic absorption features in the QWs were clearly demonstrated on the PLE spectra. Since the tension lifts the hmh subbands to higher hole energy than the lmh subbands, the lowest exciton subband in the QW can be either degenerate, heavy or light mass exciton[13,14] determined by the balance of the stress effect and the quantum confinement. Namely, the exciton levels in the 121Å GaAsP QW with y=0.05 and 79Å GaAsP QW with y=0.08 are degenerate because the stress effect compensated the quantum confinement energy. For the 121Å GaAsP QW with y=0.08, the hmh subband locates lower than the lmh. Other QWs have similar band structures as an ordinary QW except their eigen states are lowed by the stress. That means the lmh subband locates at a lowest energy. The peaks of the PL spectra shift around 10 meV from the lower PLE exciton absorption peaks indicating exciton localization to interface islands arising from well width fluctuation during the sample growth procedure.[15] The absorption profiles reveal the transition selection rule clearly. Namely, the lmh subband ($m_j=\pm3/2$) transition rate is three time larger than that of the hmh subband ($m_j=\pm1/2$). From the difference, one can tell which absorption peak corresponds to hmh or lmh exciton transition.

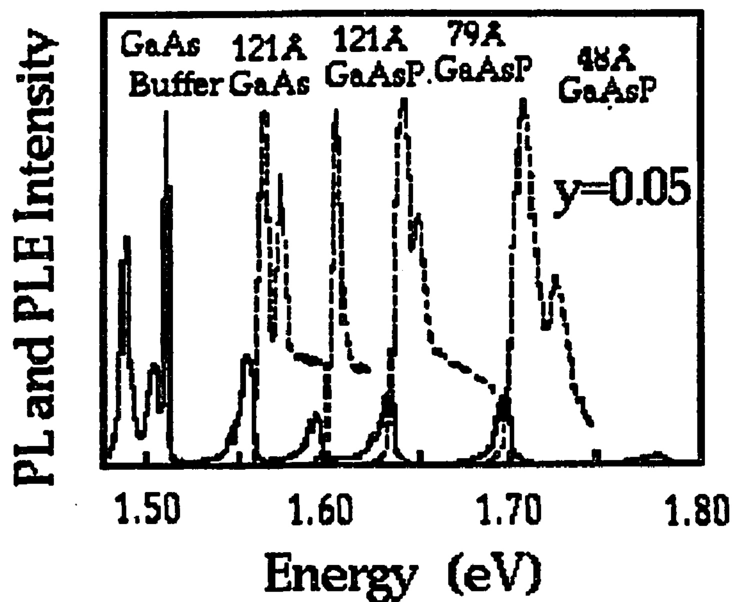

(a)

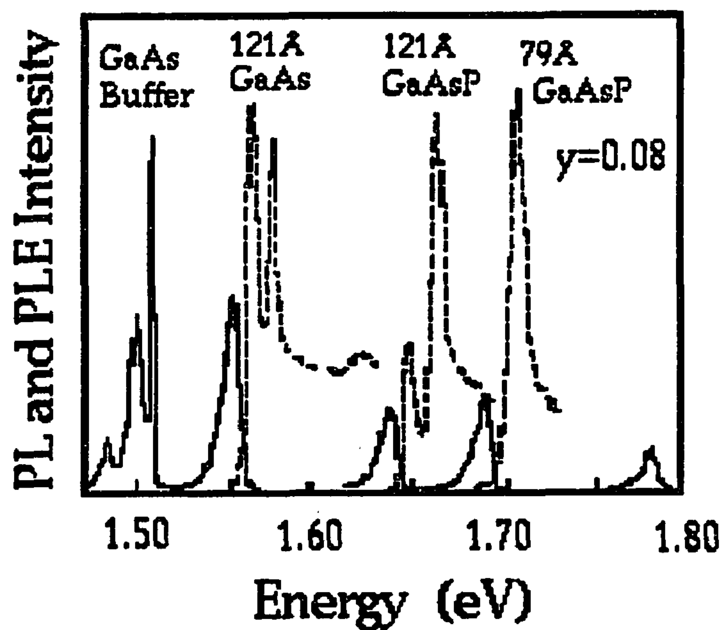

(b)

Fig. 8.4.1. The steady state PL and PLE spectra for 121Å GaAs and GaAsP QWs (a) with y=0.05 and (b) y=0.08 phosphor concentrations, respectively.

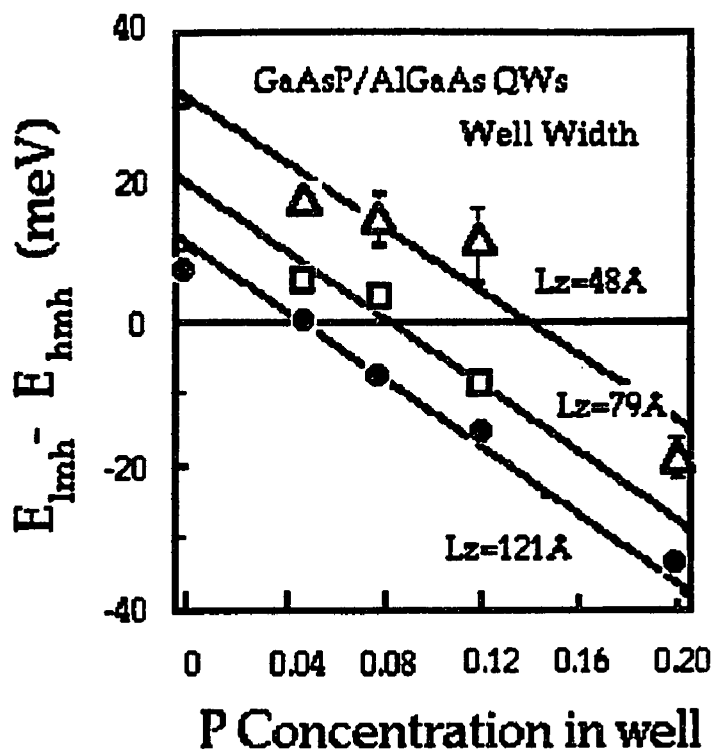

Fig. 8.4.2. Energy separation between the lowest hmh and lmh subbands with various phosphor concentrations in the well materials.

The energy separation between the lowest hmh and lmh subbands were evaluated from the PLE spectra and are depicted in Fig. 8.4.2. with expected curves which take into account the stress with various well widths.[14]

Since one monolayer (ML~2.83 Å) well width fluctuation changes its eigen state energy about 1 meV for a 121Å QW case and the lateral size of the interface islands may be around the Bohr radius of the excitons, the exciton PL peaks from the island having different ML widths are not separated with the spectral resolution of the experimental setup.

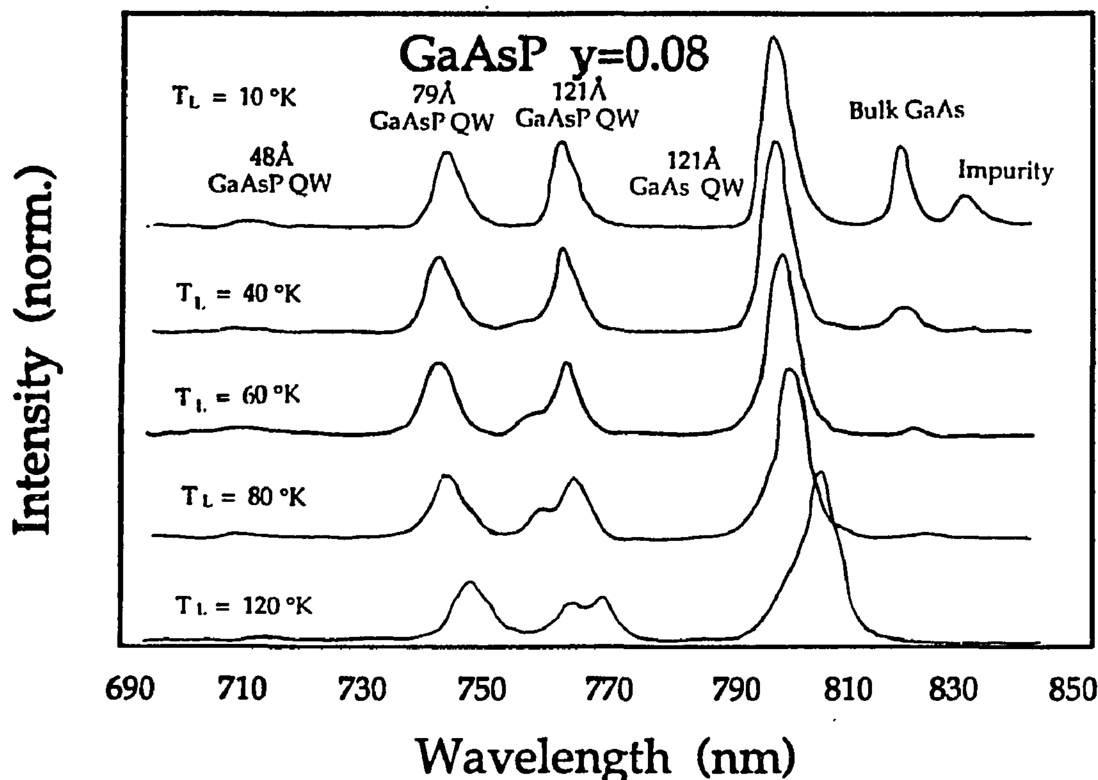

Fig.8.4.3. Temperature dependence on the PL spectra of the y=0.08 GaAsP QWs.

The steady state PL spectra at various lattice temperatures from 4 °K to room temperature were also measured. The PL intensities decrease as the lattice temperature increases as shown in Fig. 8.4.3.

8.4.2. Time-resolved PL spectra

The time-resolved PL spectra of the two samples are shown as three dimensional (3D) displays in Fig.8.4.4. (a) for y=0.05 QWs and (b) for y=0.08 QWs, respectively. Since the 3D PL spectra were obtained at a spectral region where all PL spectral range for the four QWs could not be covered, Fig. 8.4.4.(a) shows three peaks originated from e-hmh transition from the 121Å GaAs QW, 121Å and 79Å GaAsP QWs with y=0.05 while (b) shows only two peaks originated from the 121Å GaAs QW and 121Å GaAsP QW with

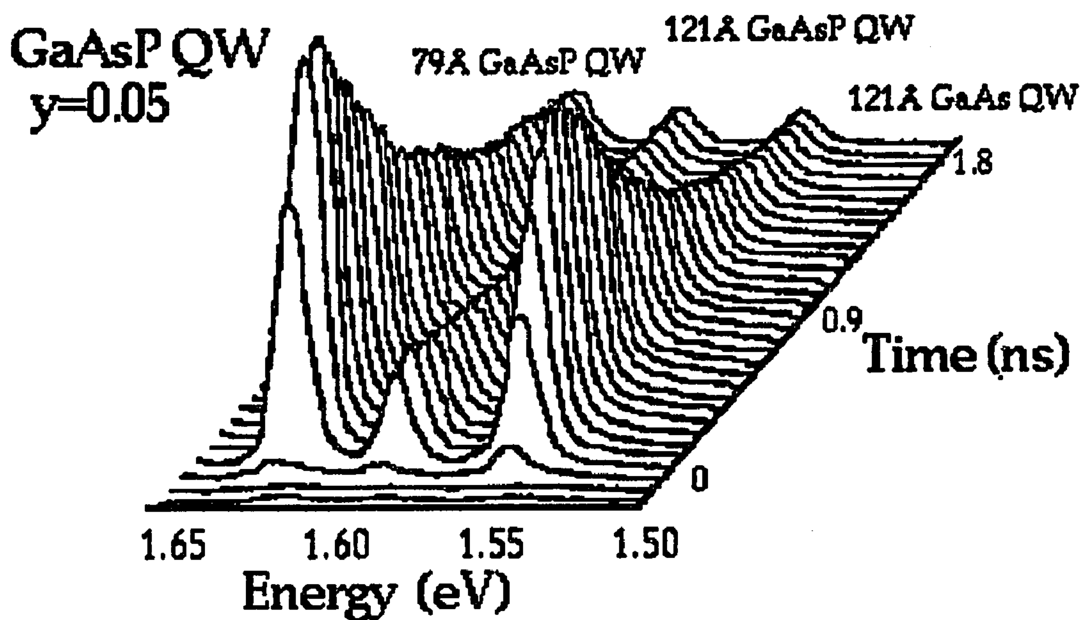

(a)

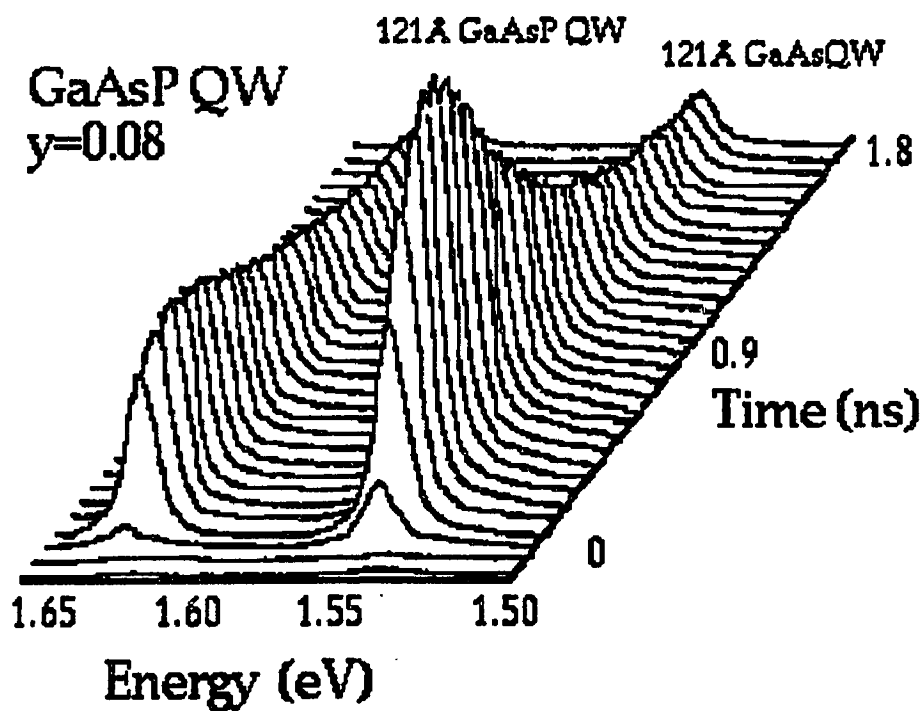

(b)

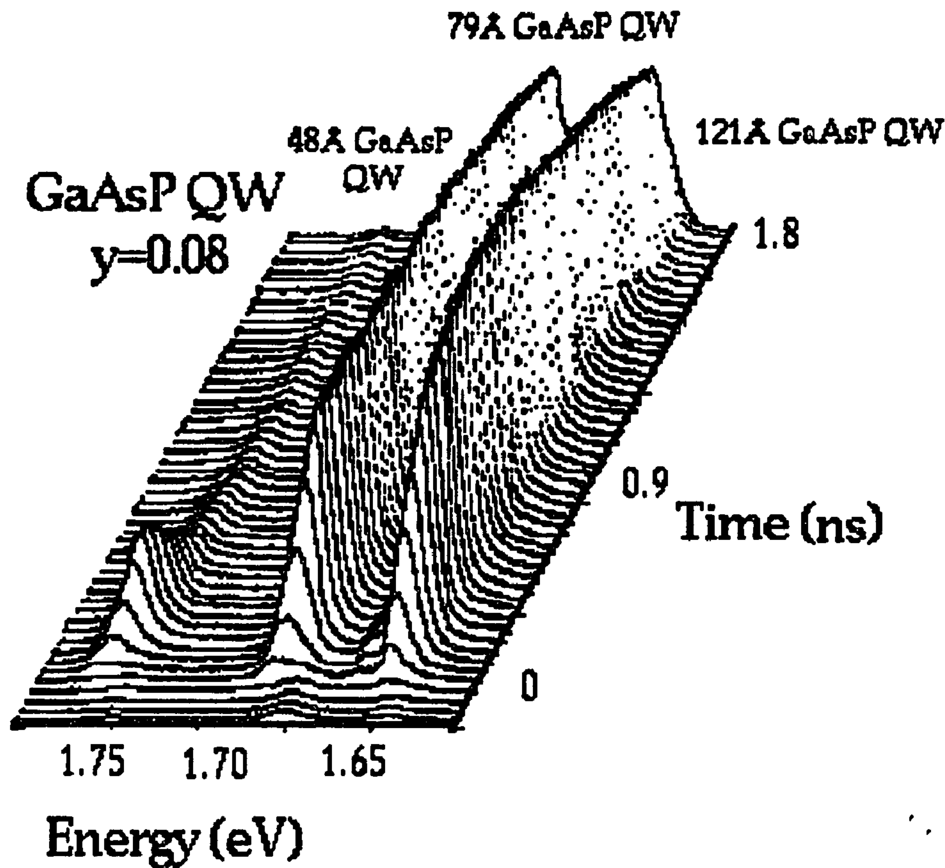

(c)

Fig.8.4.4. Three dimensional time-resolved spectra of (a) the 121Å GaAs QW, the 121Å and 79Å GaAsP QWs with y=0.05, (b)the 121Å GaAs QW and the 121Å GaAsP QW with y=0.08, and (c) the 79Å and the 48Å GaAsP QWs with y=0.08.

y=0.08. The PL 3D spectra for the 121Å, 79Å, and 48Å GaAsP QWs with y=0.08 are shown in Fig. 8.4.4(c) at a different spectral range. The observed time windows were 1.8 ns.

The sample qualities between the two samples were found to be almost same because the PL and PLE behaviors of the 121Å GaAs QWs on both samples were similar. Each PL shows differences in rise and decay profiles. The differences arise from the differences in exciton formation, thermalization,

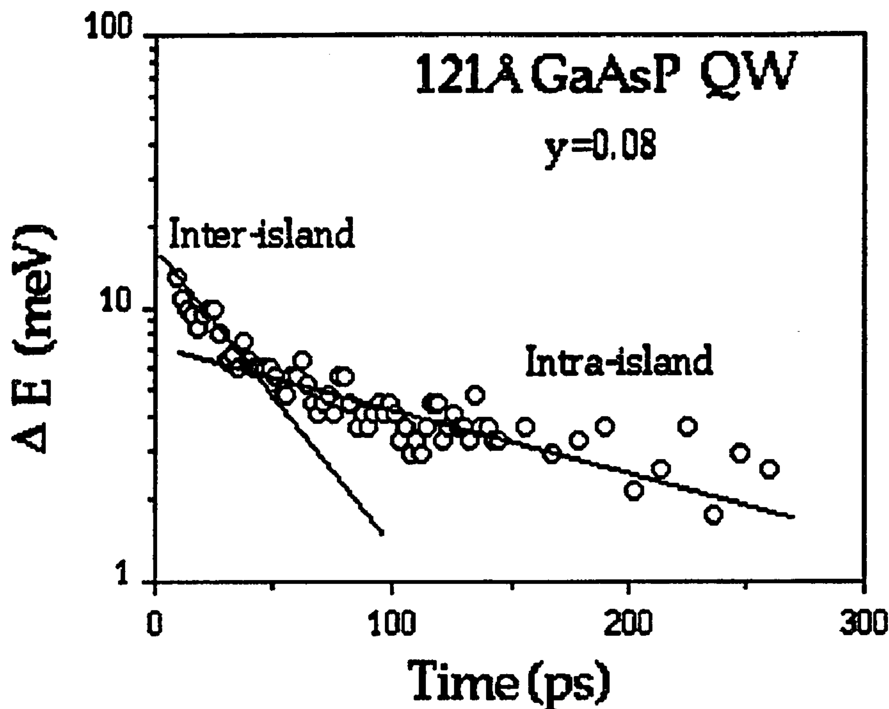

Fig. 8.4.5. Dynamic Stokes shifts of the PL peak energy observed for the 121Å GaAsP QW with y=0.08.

localization and recombination processes determined by the well materials, well widths, and the stress altered band structures. These processes will be explained in the following section.

8.4.3. Dynamic Stokes shift

For the initial time after the photoexcitation, it was found that the PL emission peak energies $E_p(t)$s red-shift as function of delay time which are called dynamic Stokes shifts.[16)] The dynamic Stokes shifts $\Delta E(t)=E_p(t)-E_p(\infty)$ for these QWs show double exponential shift behaviors in time as shown in Fig.8.4.5. Fig.8.4.6. schematically depicts the interface structure of a GaAsP/AlGaAs QW with localized and delocalized excitons shown as a circle and an oval,

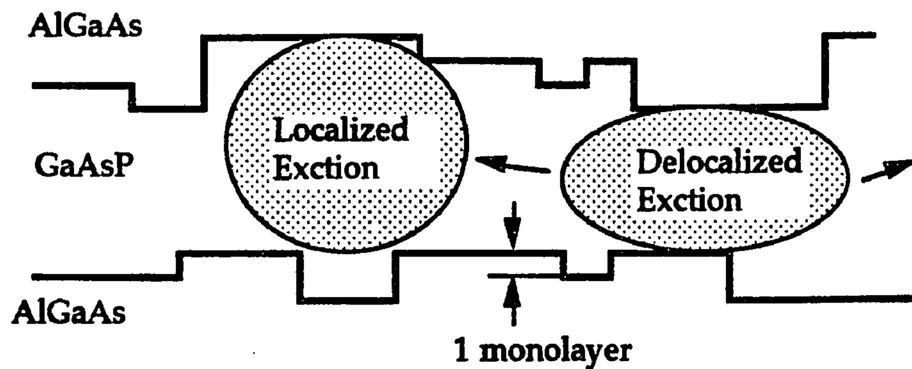

Fig.8.4.6. Monolayer fluctuation of interface in GaAsP/AlGaAs QW structure and schematic view of localized and delocalized excitons.

respectively. The ML fluctuation generates interface islands which lateral size can be same order of the well width. As a photogenerated electron-hole pair looses their energies and form an exciton, the exciton moves in the QW and reaches a widest well arising from the ML fluctuation of the GaAsP material. Since the widest well has the lowest energy states among the entire well structure, the localized exciton further looses its energy in the wider well. These energy relaxation processes are called localization. The origin of the two shifts components were attributed to the inter-islands (the free exciton moves around and finds a wider well) and intra-island localization (the localized exciton looses its energy in the wider well) processes to either widest islands, defects or impurities as discussed by Fujiwara et al.[6,7] The localized exciton may be trapped at an interface impurity or a defect state in the widest well. Since the energy states of the impurity and defect states are lower than the quantized state of the widest well, the exciton looses the kinetic energy further. The most dominating exciton energy relaxation process after exciton formation was determined to be exciton localization process. To estimate the localization times for the 121Å GaAs, 121Å GaAsP QWs with y=0.05 and y=0.08, single exponential shift curves were fit to the data by a least square fitting method although there

were fast and slow localization processes. The localization times were determined to be 31±5 ps, 36±5 ps, and 68±5 ps for the 121Å GaAs, 121Å GaAsP QWs with y=0.05 and y=0.08, respectively.

8.5. Discussion

8.5.1. Exciton binding energy

As the lattice temperature increases, the excitons delocalize and dissociate by the thermal lattice vibration. The exciton delocalization is the process that the localized excitona are kicked out from the localized state to free moving exciton state. The process does not change the PL intensity much. When $k_BT_L>E_b$, the excitons dissociate. Since the dissociated electron-hole pairs show weak radiative recombination strength compare with the excitons, the PL intensity arising from the dissociated electron-hole pairs are weak. As the result, the annihilation PL intensity decreases depending on the exciton binding energy. Exciton binding energies E_b in these samples were evaluated from temperature dependences on the steady state PL intensities (shown in Fig.8.3.4). The exciton PL peak intensities were plotted as function of $1/T_L$ (T_L: the lattice temperature) as shown in Fig.8.5.1. If the exciton binding energy is high, the PL intensity remains strong at higher T_L because the excitons are hardly dissociated. Fig.8.5.1. shows the binding energy difference clearly between the excitons of the bulk GaAs and those in the QWs. Using an exciton dissociation equation, the exciton binding energies were estimated as follows.

Exciton population is determined by the balance between exciton formation, decay, and dissociation. The exciton population increases due to the exciton formation from photogenerated electron-hole pairs with a generation

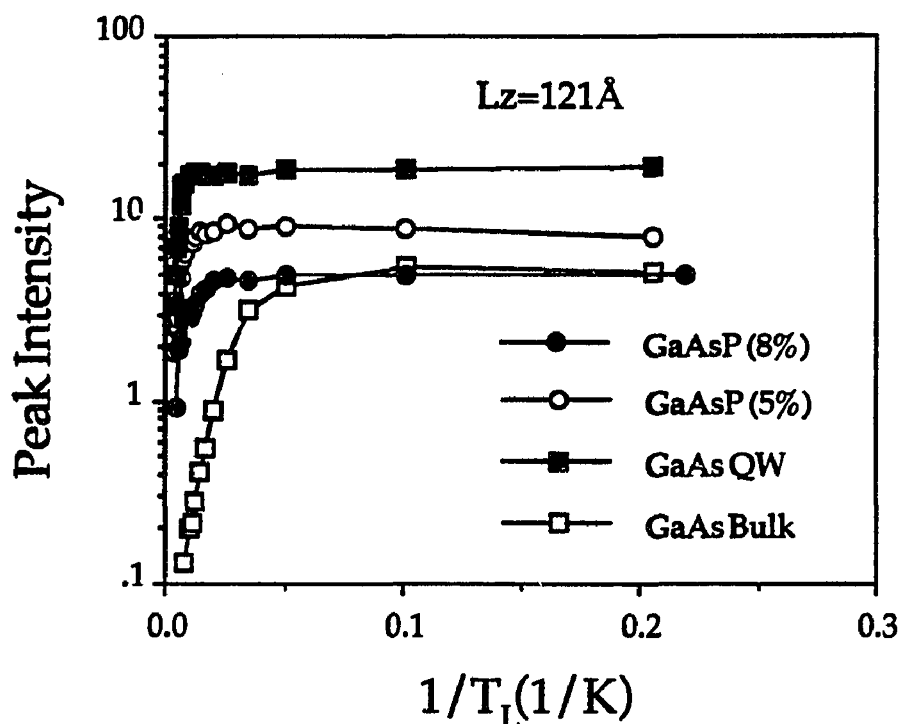

Fig. 8.5.1. Exciton PL peak intensities as function of inverse of lattice temperatures.

rate g. The exciton population decreases due to exction recombination and dissociation. Assuming the excitons having kinetic energy higher than the exciton binding energy E_b, the exciton population rate equation is given by,

$$\frac{dc}{dt} = -\frac{c}{\tau} - \frac{c \bullet \exp\left(-\frac{E_b}{k_B T}\right)}{\tau_0} + g \quad , \tag{8.5.1}$$

where c is the exciton population, τ is the exciton annihilation decay time, g is the photogeneration rate, and τ_0 is the fitting parameter to be determined. For a steady state, dc/dt=0, thus,

$$c(T) = \frac{g \bullet \tau}{1 + \frac{\tau}{\tau_0} \bullet \exp\left(-\frac{E_b}{k_B T}\right)} . \tag{8.5.2}$$

Fitting the calculated curve using Eq.8.5.2 to the experimentally obtained exciton dissociation curves shown in Fig. 8.5.1, the exciton binding energies were determined. The exciton binding energies for the 121Å GaAs QW and the 121Å GaAsP QWs with y=0.05 and bulk GaAs were evaluated to be, 18, 28 and 6 meV, respectively.

For the bulk GaAs, the exciton binding energy can be estimated assuming a hydrogenic model which gives a series of ionization energies E_n as,

$$E_n = -R^*y / N^2 \tag{8.5.3}$$

with a Rydberg constant given by,

$$R^*y = \mu q^2 / 2\varepsilon\varepsilon_0^2 \hbar^2 , \tag{8.5.4}$$

where N is 1,2,3—, $\mu^{-1} = m_e^{-1} + m_h^{-1}$, q is the electron charge, $\varepsilon\varepsilon_0$ is the dielectric constant of GaAs, and $\hbar$ is the Planck constant divided by 2π. For a 2D exciton in a QW, the binding energy is given by,

$$E_n^{2D} = -R^*y / (N+1/2)^2 \tag{8.5.5}$$

where N=0,1,2,3,—. Therefore, the 2D exciton binding energy for the QW is four times larger than that for the bulk. From the Rydberg constant, the heavier the exciton mass, the higher the exciton binding energy. Using Eq.s 8.5.4 and

8.5.5, the 2D exciton binding energies for the confined hmh and lmh excitons and that in the bulk are theoretically expected to be 11, 19 and 4.7 meV, respectively. Although the evaluated energies are slightly different from the theoretical values, the features agree qualitatively. Therefore, the exciton in the 121Å GaAsP QW with y=0.05 is hmh exciton.

8.5.2. Exciton dynamics model

In this section, I am going to evaluate the exciton formation time, inter-subband scattering time, and annihilation decay time from the time resolved PL spectra as shown in Fig.8.4.4. Especially, when the PL intensity profiles at the lowest emission energy is analyzed(the PL arises from the localized 2D exciton annihilation), these time constants determine the PL profiles. Therefore, I will analyze the PL profiles at the lowest emission energies using a following exciton dynamics model.

The 2.0 eV photons excite electrons and holes high above from each subband edge. The hot carriers relax down toward the bottom of each subband and form excitons. The excitons further relax their energies and scatter to lower subbands. At the lower subband, the excitons localize to the lower energy states which are in the wider islands. During these processes, the excitons annihilate and emit PL photons. The PL spectrum is determined by the population of excitons (determined by the exciton density of state and exciton distribution function) and the recombination rate at the energy.

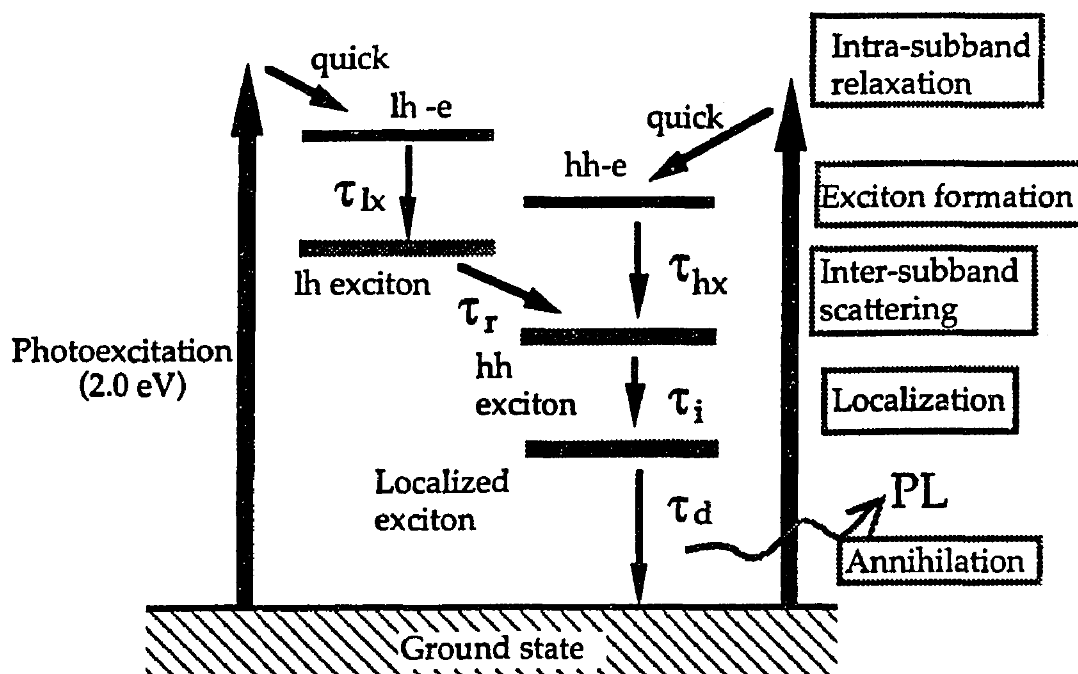

Fig. 8.5.2. Energy diagram of the six level model transition schematics.

When the time-resolved PL spectra profiles at the lowest exciton annihilation recombination energies are analyzed, the rise times of the PL temporal profiles are determined by the free carrier intra-subband relaxation, exciton formation, exciton inter-subband scattering, excitonlocalization processes while the decay is determined by the exciton annihilation recombination and unknown non-radiative recombination.

This exciton dynamics was analyzed with a set of six coupled rate equations evaluating the population of electron-hole gas, the lmh and hmh excitons, and the localized excitons as shown in Fig.8.5.2. By fitting the PL time profiles obtained for the QWs at the lowest emission energies (correspond to localized exciton recombination) using the solution of the rate equations, time constants for each relaxation process were determined.

The six energy level model was the similar approach as Kusano et al.[4] The energy levels consist of a free lmh-electron level, a free hmh-electron level, lowest lmh and hmh exciton levels, localized exciton level at the interface islands, and a ground state.

For the calculation, several assumptions were made following:

(1) the hot free carriers relax down to each band edge rapidly within system response time.

(2) there is no inter-subband scattering during the hmh or lmh exciton formation.

(3) the relaxed excitons only in the lower subband localize at the interface islands.

(4) the ratio between the photogenerated lmh-electron and the hmh-electron populations are introduced as 1 to 3 which is determined by the transition selection rule. The initial populations at the hmh and lmh excitons and at the localized state are zero.

(5) the hmh and lmh exciton formation times in a QW are assumed to be same(τ_{lx}=τ_{hx}).

(6) the exciton annihilation times are much slower than other energy relaxation times so that the excitons annihilate only within the wide islands.

In the following rate equations, the parameters $N_{lb}(t)$, $N_{hb}(t)$, $N_{lx}(t)$, $N_{hx}(t)$, and $N_i(t)$ are the populations of free lmh-electron pairs, free hmh-electron pairs at each subband edges, lmh and hmh excitons, and localized excitons, respectively. The τ_{lx}, τ_{hx}, τ_r, τ_i, and τ_d are the exciton formation times from free carriers to hmh or lmh excitons(τ_{lx}= τ_{hx} from assumption (5)),

the exciton inter-subband scattering time from a high to a lower subband, the exciton localization time, and the exciton annihilation decay time, respectively.

Assuming the lmh subband locates at higher energy than the hmh subband, the carrier population of the free lmh-electron state $N_{lb}(t)$ decreases to form lmh excitons:

$$\frac{dN_{lb}(t)}{dt} = -\frac{N_{lb}(t)}{\tau_{lx}} , \qquad (8.5.6)$$

with a formation time τ_{lx}. The population of the free hmh-electron state $N_{hb}(t)$ decreases to form hmh excitons with a formation time τ_{hx}. The rate equation is given by:

$$\frac{dN_{hb}(t)}{dt} = -\frac{N_{hb}(t)}{\tau_{hx}} . \qquad (8.5.7)$$

The population of the lmh exciton $N_{lx}(t)$ increases due to the formation from the free carriers and decreases due to the inter-subband scattering to the lower hmh exciton state. $N_{lx}(t)$ is given by:

$$\frac{dN_{lx}(t)}{dt} = \frac{N_{lb}(t)}{\tau_{lx}} - \frac{N_{lx}(t)}{\tau_{r}} . \qquad (8.5.8)$$

The hmh exciton population $N_{hx}(t)$ increases because of the lmh exciton inter-subband scattering, and exciton formation from the free carriers and decreases due to the exciton localization to the interface islands. The rate equation is given by:

$$\frac{dN_{hx}(t)}{dt} = \frac{N_{lx}(t)}{\tau_r} + \frac{N_{hb}(t)}{\tau_{hx}} - \frac{N_{hx}(t)}{\tau_i} \quad (8.5.9)$$

The population of the localized excitons $N_i(t)$ is given by:

$$\frac{dN_i(t)}{dt} = \frac{N_{hx}(t)}{\tau_i} - \frac{N_i(t)}{\tau_d}, \quad (8.5.10)$$

where first term is from the hmh exciton localization and the second from the localized exciton annihilation. The values of τ_is for the QWs have been determined from the dynamic Stokes shifts discussed above.

The coupled rate equations Eq.s 8.5.6 to 8.5.10 are solved analytically and their solutions determined the population as function of delay time as:

$$N_{lb}=N_{lb0}\bullet\exp(-t/\tau_{lx}) \quad , \quad (8.5.11a)$$

$$N_{hb}=N_{hb0}\bullet\exp(-t/\tau_{hx}) \quad , \quad (8.5.11b)$$

$$N_{lx}=(N_{lb0}/\tau_{lx}{}^{*}a+N_{lx0})\bullet\exp(-t/\tau_{lh})-N_{lb0}/\tau_{lx}{}^{*}a\bullet\exp(-t/\tau_{lx}), \quad (8.5.11c)$$

$$\begin{aligned}N_{hx}=N_{hx0}\bullet\exp(-t/\tau_i)&+b/(1/\tau_{hx}-1/\tau_i)\bullet\{\exp(-t/\tau_i)-\exp(-t/\tau_{hx})\}\\ &+c/(1/\tau_{lh}-1/\tau_i)\bullet\{\exp(-t/\tau_i)-\exp(-t/\tau_{lh})\}\\ &-d/(1/\tau_{lx}-1/\tau_i)\bullet\{\exp(-t/\tau_i)-\exp(-t/\tau_{lx})\}, \quad (8.5.11d)\end{aligned}$$

and

$$\begin{aligned}N_i=N_{i0}\bullet\exp(i/\tau_d)&+1/\tau_i{}^{*}N_{hx0}/(1/\tau_i-1/\tau_d)\bullet\{\exp(-t/\tau_d)-\exp(-t/\tau_i)\}\\ &+e/(1/\tau_{hx}-1/\tau_i)\bullet\{\exp(-t/\tau_i)-\exp(-t/\tau_{hx})\}\\ &-e/(1/\tau_i-1/\tau_d)\bullet\{\exp(-t/\tau_d)-\exp(-t/\tau_i)\}\\ &+f/(1/\tau_{lh}-1/\tau_i)\bullet\{\exp(-t/\tau_i)-\exp(-t/\tau_{lh})\}\end{aligned}$$

$$-f/(1/\tau_i-1/\tau_d)\bullet(\exp(-t/\tau_d)-\exp(-t/\tau_i))$$
$$-g/(1/\tau_{lx}-1/\tau_i)\bullet\{\exp(-t/\tau_i)-EXP(-t/\tau_{lx})\}$$
$$+b1/(1/\tau_i-1/\tau_d)\bullet\{\exp(-t/\tau_d)-\exp(-t/\tau_i)\} \quad (8.5.11e)$$

with

$$a=1/(-1/\tau_{lh}+1/\tau_{lx}) \quad , \quad (8.5.12a)$$

$$b=N_{hb0}/\tau_{hx} \quad , \quad (8.5.12b)$$

$$c=N_{lb0}/\tau_{lx}{}^*a+N_{lx0} \quad , \quad (8.5.12c)$$

$$d=N_{lb0}/\tau_{lx}{}^*a \quad , \quad (8.5.12d)$$

$$e=b/\tau_i/(1/\tau_d-1/\tau_{hx}) \quad , \quad (8.5.12e)$$

$$f=c/\tau_i/(1/\tau_d-1/\tau_{lh}) \quad , \quad (8.5.12f)$$

and

$$g=d/\tau_i/(1/\tau_d-1/\tau_{lx}) \quad . \quad (8.5.12g)$$

The localized exciton PL time profile I(t) observed at the localization state is given by:

$$I(t) = \frac{N_i(t)}{\tau_d} \quad . \quad (8.5.13)$$

From Eq. 8.5.11e, the PL profiles consist from seven rising components and one decay component. The PL profiles of the 121 Å GaAs and 121 Å GaAsP QWs with y=0.05 and 0.08 were evaluated and compared to the exciton dynamics under different band structures but with the similar well configuration.

To determine the exciton formation, relaxation, localization and annihilation decay times, the calculated curves using Eq.s 8.5.11e and 8.5.13 were fit to the measured PL time profiles with four fitting parameters such as τ_{lx}, τ_{hx}, τ_r, and τ_d. The exciton localization times τ_is were already determined from the

dynamic Stokes shifts as discussed in section 8.4.3. Since the time scale of the annihilation decays are one order of magnitude slower than those of exciton formation, relaxation or localization processes. Once τ_ds are obtained by the fits accurately, τ_{lx}, τ_{hx}, and τ_r are the remaining parameters to be obtained. As mentioned above, the τ_{lx} and τ_{hx} are assumed to be same for the fitting. Therefore, there are two fitting parameters, τ_{lx} and τ_r, to be obtained after the determination of the τ_ds. The fitting results for the three time profiles are shown in Fig.s 8.5.3 (a) to (c). The measured PL profiles are displayed with thick solid curves while the fitting curves are in thin solid or dashed curves. To demonstrate the fitting accuracy, there show several fitting curves with slightly different fitting parameters.

The localized exciton annihilation decay times in the 121 Å GaAs QW, the 121 Å GaAsP QW with y=0.05, and the 121 Å GaAsP QW with y=0:08 were found to be 650, 1400, and 950 ps, respectively.

The 2D exciton lifetime was evaluated by Feldmann[5] as,

$$\tau_d \propto (1/E_b^{2D}) \bullet (M/\mu) \bullet \Delta(T)/\{1-\exp(-\Delta(T)/k_B T)\} \qquad (8.5.14)$$

The exciton formation times were estimated to be 70, 10, and 5 ps, respectively. The exciton formation times for the 121 Å GaAsP QWs with y=0.05 and y=0.08 were within 20 ps and consistent with the result obtained by Damen et al.[1] and similar to the result obtained by Strobel et al.[3] On the other hand, the formation time of the 121 Å GaAs QW was found to be longer than the other formation times and was similar to the result obtained by Kusano et al.[4] The lmh to hmh in the 121 Å GaAs QW and hmh to lmh exciton inter-subband scattering times in the 121 Å GaAsP QW with y=0.08 were found to be

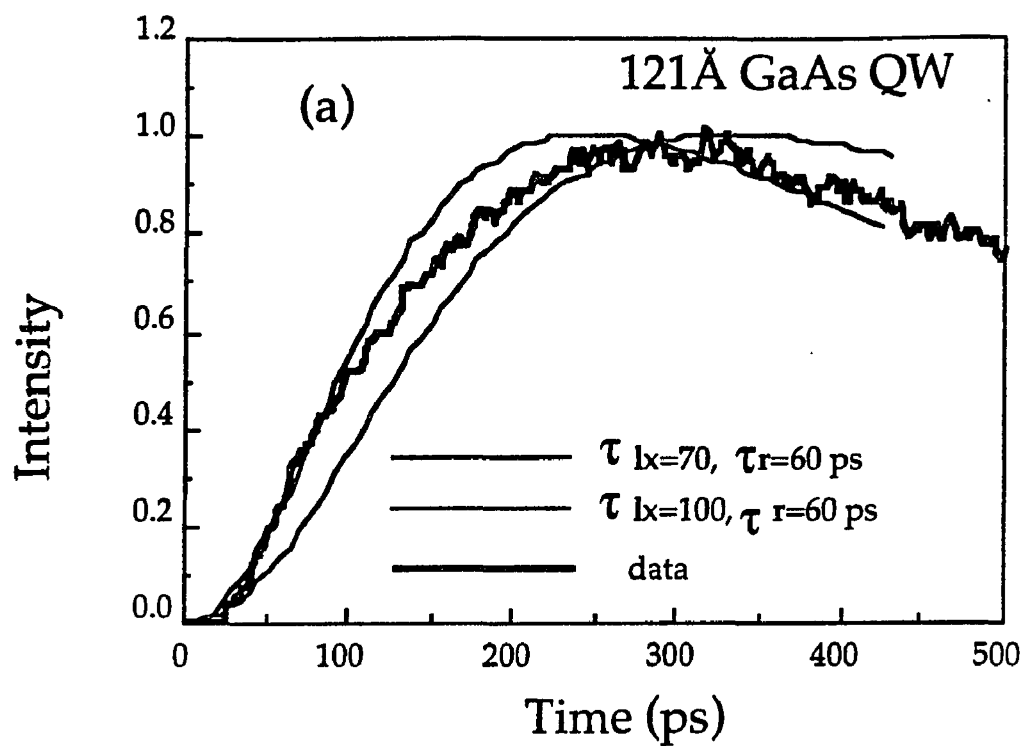
121Å GaAs QW
(a)
τ lx=70, τr=60 ps
τ lx=100, τ r=60 ps
data
Intensity
Time (ps)
1.2
1.0
0.8
0.6
0.4
0.2
0.0
0
100
200
300
400
500

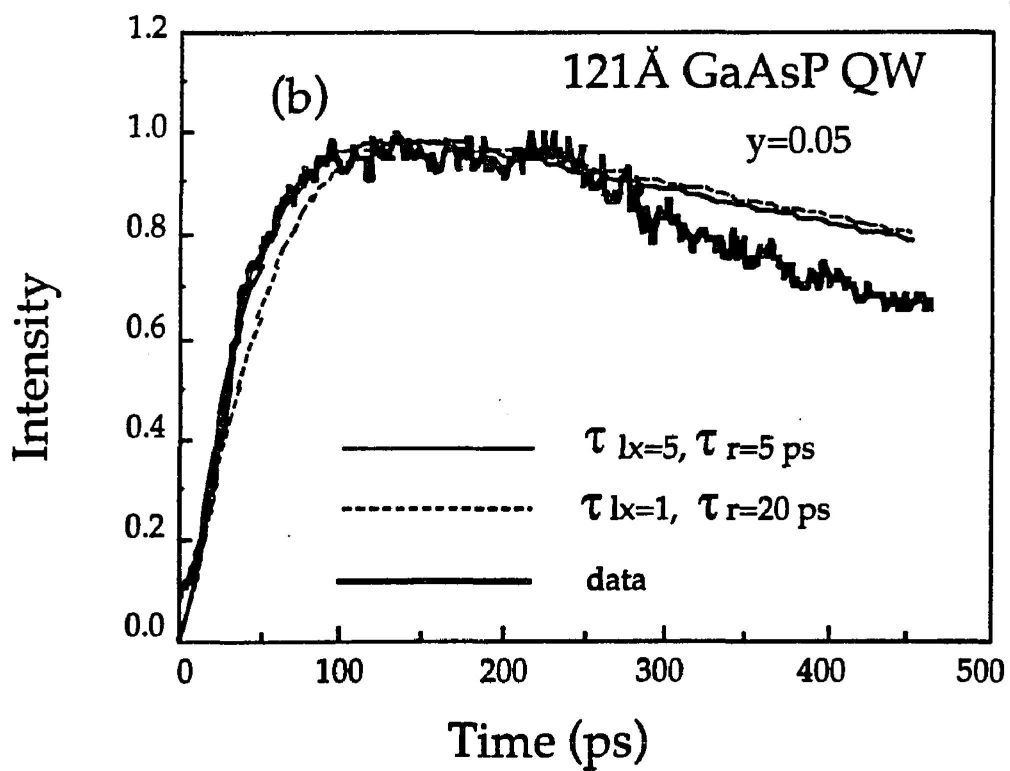
121Å GaAsP QW
(b)
y=0.05
τ lx=5, τ r=5 ps
τ lx=1, τ r=20 ps
data
Intensity
Time (ps)
1.2
1.0
0.8
0.6
0.4
0.2
0.0
0
100
200
300
400
500

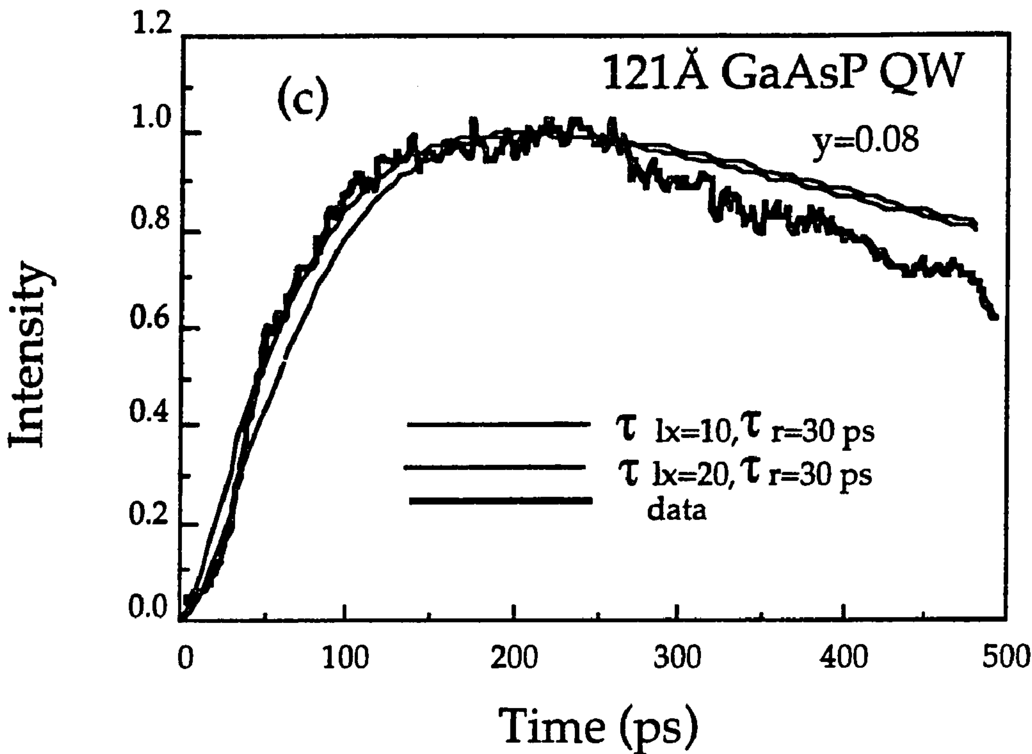

Fig. 8.5.3. Measured PL time profiles (thick solid curves) of (a) the 121Å GaAs QW, (b) the 121Å GaAsP QWs with y=0.05, and (c)the 121Å GaAsP QWs y=0.08 and the fit curves to data (thin solid or dashed curves).

Table 8.5.1. The exciton dynamics parameters obtained by fitting to the lowest localized exciton time profiles for the 121Å AlGaAs/GaAs QW and 121Å AlGaAs/$GaAs_{1-y}P_y$ (y=0.05 and 0.08) QWs.

in ps	GaAs QW	y=0.05	y=0.08
τ lx, τ hx	70	5	10
τ r	60	6	30
τ i	31	36	68
τ d	650	1400	950

60 and 30 ps, respectively. In the fitting procedure for the 121Å GaAsP QW with y=0.05, the exciton inter-subband scattering time from the hmh to lmh exciton within the degenerate state is assumed to be finite value and is found to be 6 ps. From the results, the hmh to lmh exciton inter-subband scattering time is faster than that from the lmh to hmh. Kusano et al.[4] have determined the hmh inter-subband scattering time to lmh exciton to be 190 ps which is much longer than the result obtained in this work. Since the energy separation between the exciton subbands are much smaller than the LO phonon energy, the relaxation processes is most likely due to acoustic phonon interaction.

where E_b^{2D} is the exciton binding energy, $M=m_e+m_h$, $\mu^{-1}=m_e^{-1}+m_h^{-1}$, $\Delta(T)$ is a line width at the lattice temperature T.

8.5.3. Average exciton kinetic energy relaxation

In order to analyze the exciton energy relaxation qualitatively, average exciton kinetic energies as function of delay time were evaluated from the PLs of the individual QWs. The temporal feature of the exciton kinetic energy relaxation was found to be determined by combination of alloy, ADP interaction, and weak LO phonon interaction in general.

Before start discussing the exciton localization, it is important to note that the spectrally integrated PL intensities between the high and low PL edges reach their maximum within 50 to 70 ps and stay at same intensity within 200 to 300 ps time range, as shown in Fig.8.5.4. by a gray curve, except for 48Å QW which decays faster because of higher recombination rate as shown in 3D display in Fig. 8.4.4. (c) . Therefore, the exciton recombination does not affect the exciton relaxation process within 100 ps time range.

The average carrier and exciton kinetic energy $\langle E_k(t) \rangle$ is calculated as function of delay time t from the 3D PL spectrum I(E, t) using, [9]

$$\langle E_k(t) \rangle = \int_{E_1}^{E_2} I(E, t) \bullet E \, dE / \int_{E_1}^{E_2} I(E, t) \, dt - E_0 \qquad (8.5.15)$$

where E_1 and E_2 are low and high energy edges of the PL spectrum because the experiment was carried out within a certain PL energy region, and E_0 is the lowest carrier and exciton state energy determined from the steady state PL peak position at the same lattice temperature.

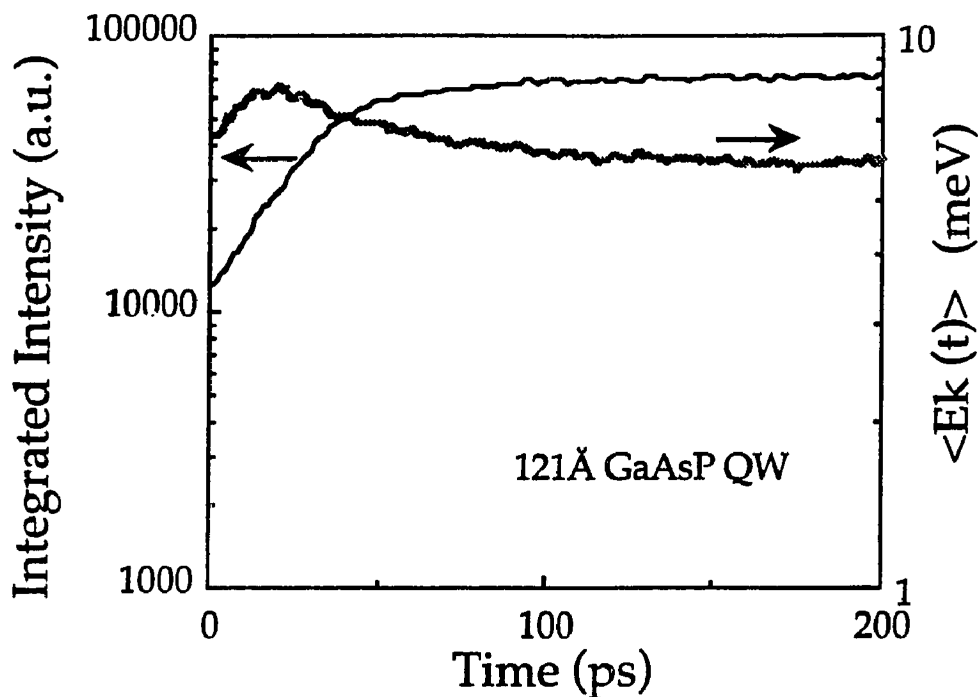

Fig.8.5.4 Average exciton energy relaxation and integrated PL intensity profiles for the 121Å GaAsP QW with y=0.05.

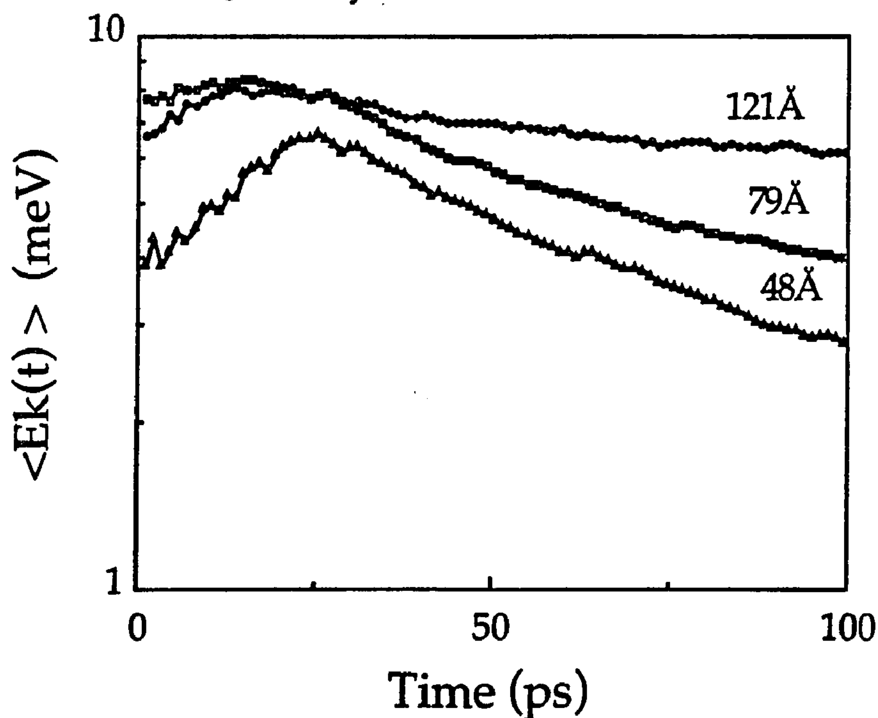

Fig. 8.5.5. The exciton average kinetic energy relaxation of the y=0.05 GaAsP QWs

Using Eq. 8.5.15, the average exciton kinetic energies for the GaAsP QWs with y=0.05 were evaluated and are displayed in Fig. 8.5.5 in semi-logalithmic scale with 100 ps time window after the photoexcitation. The initial exciton energies for three QWs were around 9 meV.

There are two key features on the exciton energy relaxation process.

First, the average exciton kinetic energies reach their maximum within 20 to 30 ps and the maximum position comes later for narrower QWs. The rising and complex profile of exciton kinetic energy within the 30 ps may be attributed to the result of the exciton formation and exciton inter-subband relaxation because the exciton formation time was about 20 to 30 ps according to the result of Damen.[1)] My previous results in the section 8.5.2. show that the inter-subband scattering time is in similar order.

The most important result to be emphasized is that the average exciton kinetic energy profile shows a non-single exponential relaxation process. There are fast and slow components for each profile. The energy relaxation profiles within 30 to 100 ps and 200 to 500 ps for those QWs were fit with single exponential curves. The fast exciton relaxation component are displayed as function of nominal well width in Fig. 8.5.6. The relaxation times increase as the well width increases. Note that the data for 121Å GaAsP QW are slightly off from the linear relationships between L_z and τ_{relax} for both relaxation components.

The fast relaxation process was attributed to inter-island localization due to ADP interaction while the long components to intra-island localization process

as Fujiwara introduced[4]. As an exciton relaxes down to a wider interface island, the exciton binding energy and magnitude of ADP interaction is changed according to the island well width. Therefore, the exciton energy relaxation curve should not be a single exponential. As the exciton is trapped in a widest interface island, the exciton looses a freedom to move around. The exciton is confined in a square well as in a zero dimensional(0D) state. Thus, the long intra-island localization process may be quasi 0D exciton energy relaxation process similar to a quantum dot case. The 0D exciton energy relaxation may be slow process. The time of 1 to 8 ns of
intra-island localization time obtained by Fujiwara[6,7] may also correspond to the exciton relaxation time in the quasi 0D exciton state.

To understand fast exciton energy relaxation process at the interface due to APD interaction, Masumoto[9] introduced an exciton energy relaxation equation as:

$$\langle E_k(t)\rangle = k_B T_L + \Delta E \bullet \exp(-t/\tau_{relax}) \quad (8.5.16a)$$

with

$$\tau_{relax} = \hbar^3 \rho L_z / 2M^{*2} D^{*2} \quad (8.5.16b)$$

and

$$\Delta E = k_B \bullet (T_e(0) - T_L) \quad , \quad (8.5.16c)$$

where T_L is lattice temperature, $T_e(0)$ is initial exciton temperature, ΔE is defined as a relaxation energy, M^* is exciton mass, D^* is exciton ADP, $\hbar$ is Planck constant divided by 2π, ρ is material density, L_z is well width, and τ_{relax} is exciton energy relaxation time. The Eq.8.5.16c predicts that the exciton energy relaxation through ADP interaction is determined by the difference between the $T_e(0)$ and

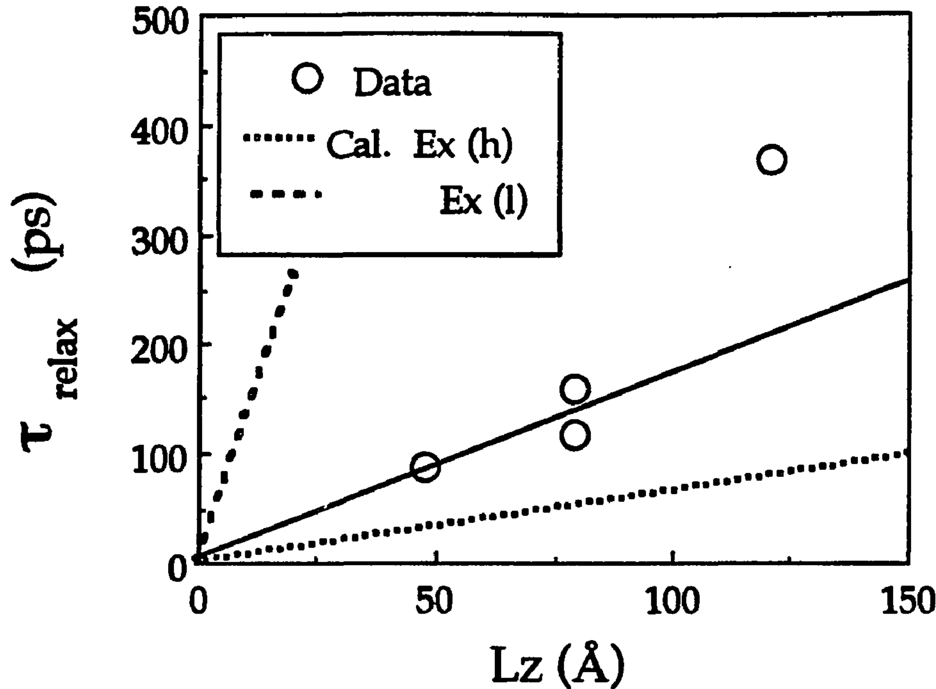

Fig.8.5.6. L_z dependence on the exciton energy relaxation times of the QWs. Open circles are evaluate data for QWs while the lines are theoretical curves using heavy (dotted line) and light exciton mass(dash line). The solid line is just for eye guide.

T_L. Its relaxation time is proportional to L_z and well material density and is inverse proportional to $(M^*D^*)^2$. The wider the well widths, the slower the relaxation process.

The exciton energy relaxation times were calculated using following parameters to compare with the experimental data. Eq.s 8.5.16 contain four parameters such as M, D^*, ρ, and L_z. The ρ and L_z are known parameters determined from the experimental and growth conditions. M^* and D^* are fairly known for regular materials. The ρ, M^* and D^* for GaAsP were determined by

linearly interpolating those values of GaAs and GaP materials and are ρ=5.037-1.177y, M^*_{hh}=0.62+0.17y, M^*_{lh}=0.074+0.066y, and D^*=9.44+0.32y, respectively, where y denotes phosphor composition in the well material. M^*_{hh} and M^*_{lh} denote heavy and light exciton masses. The dotted, and dash lines in Fig. 8.4.7 are calculated curves using relaxation time from Eq. 8.4.16b using heavy exciton mass and light exciton mass, respectively. It is shown that the relaxation times fairly agree with theoretical values. These results indicate that the excitons in the 121Å GaAsP QW are lighter than the heavy mass excitons but heavier than the light exciton mass. The difference from the light mass exciton relaxation time may be originated from a combination effect of degeneracy and the alloy scattering which accelerates the relaxation process. It is true that as the phosphor composition approaches to zero; ie. 121Å GaAs QW, the relaxation process can be determined only by ADP interaction and its relaxation time was about 450 ps which was not far from the relaxation times of 400 ps of 121Å GaAsP QW. Therefore, the contribution of alloy scattering for the exciton relaxation time to y=5% QW is within 10% of the total relaxation times.

To further confirm that the fast exciton relaxation process is dominated by ADP interaction, I have evaluate the fast exciton relaxation energy at a higher lattice temperature. The relaxation energy should decrease linearly as lattice temperature increases as predicted by Eq.s 8.5.16c. In Fig. 8.5.7, the energy relaxation for the 79Å and 121Å GaAsP QWs within 100 ps are depicted as function of k_BT_L in meV. The dashed and dotted lines are linear relationships between the relaxation energies and the k_BT_L for each case. The fast exciton relaxation energy decreases linearly as T_L increases. The difference of 2 meV in initial average exciton kinetic energy between 79Å and 121Å QWs may arise from difference in the quantized subband structures under the stress.

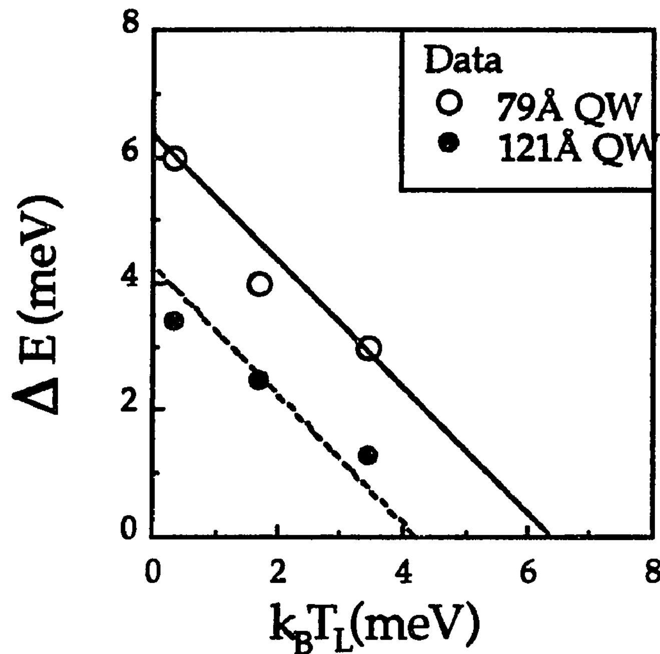

Fig. 8.5.7. The exciton relaxation energy for the 79Å (open circles) and 121Å (dots) QWs at various lattice temperatures. The dashed and dotted lines show linear relationships between the relaxation energies and k_BT_L for each QWs.

By taking a first derivative of the average kinetic energy Eq.8.5.16a with respect to the delay time, the energy relaxation rate as function of delay time is obtained as,

$$d\langle E_k(t)\rangle/dt = -\Delta E(T_L)/\tau_{relax} \bullet \exp(-t/\tau_{relax}) \qquad (8.5.17)$$

where $\Delta E(T_L)/\tau_{relax}$ corresponds to the initial energy relaxation rate and is inverse proportional to L_z (obtained by substituting Eq.8.5.16b into the Eq.8.5.16a). The initial relaxation rates due to ADP interaction in the QWs are evaluated from the experimentally obtained $\Delta E(T_L)$ and τ_{relax}. These values are depicted in Fig. 8.5.8 as the open circles with error bars. The peak energy relaxation rates for the 48, 79, and 121Å GaAsP QW are evaluated to be about 8 x

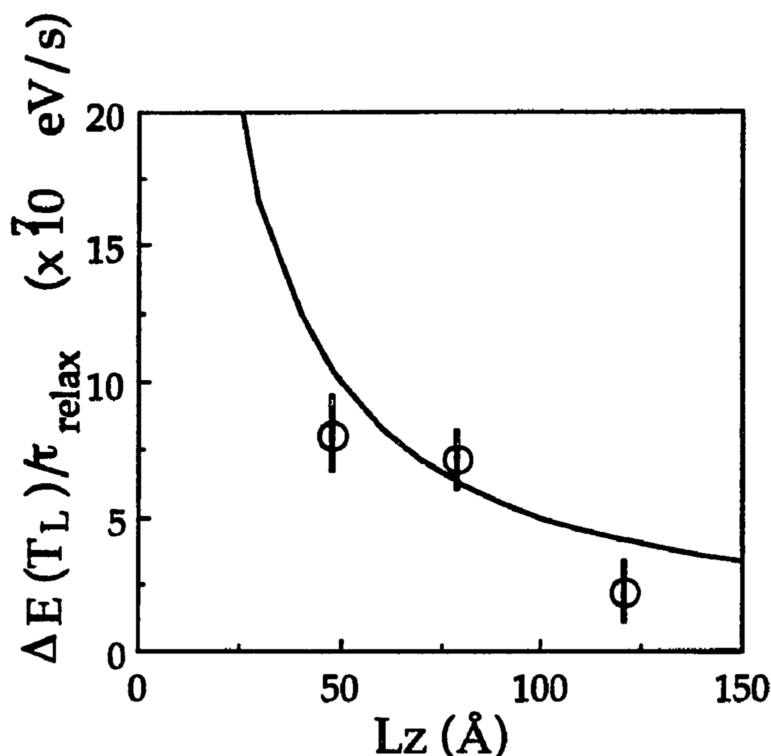

Fig. 8.5.8 Energy relaxation rate determined from the evaluated $\Delta E(T_L)/\tau_{relax}$ (open circles) and the fit curve $\Delta E(T_L)/\tau_{relax}=5\times10^9/L_z$ (eV/s).

10^7, 7.5×10^7, and 3×10^7 eV/s, respectively. The solid curve is a calculated curve using $\Delta E(T_L)/\tau_{relax}=5\times10^9/L_z$ (eV/s) where 5×10^9 (eV•Å/s) is a fit parameter which is about one third of the theoretically calculated value 1.4×10^{10} (eV•Å/s) assuming $\Delta E(T_L)$=9 meV and $M^*=M^*_{hh}$. The evaluated initial energy relaxation rate is found to follow the inverse proportional relationship as the theory for the ADP interaction predicts within twice the error bars which are mainly determined by fluctuation of $\langle E_k(t)\rangle$.

8.6. Conclusion

The hmh and lmh exciton formation from electron-hole pair, hmh(lmh) exciton to lmh(hmh) exciton inter-subband scattering, exciton localization to

interface islands, and exciton annihilation were investigated in same structures consisting of a non-strained 121Å GaAs/$Al_xGa_{1-x}As$ (y=0 with x=0.35) and strained 121Å $GaAs_{1-y}P_y$/$Al_xGa_{1-x}As$ (y=0.05 and 0.08 with x=0.35) single quantum wells using time-resolved PL spectroscopy. From the dynamic Stokes shifts, I have determined the exciton localization times to the interface islands arising from the well width fluctuation. Using the solution of the six level coupled rate equations to fit the measured PL time profiles of the different QW samples at the lowest PL emission edges, the hmh and lmh exciton formation times, the hmh (lmh) to lmh(hmh) exciton inter-subband scattering times, and the exciton annihilation times were evaluated for strained quantum wells.

The 2D localized exciton energy relaxation dynamics in strained AlGaAs/GaAsP (y=5%) QWs was also investigated at various lattice temperatures. Since the valence subbands were altered by the built-in stress, lowest exciton states were found to be either degenerate, light mass, or heavy mass exciton determined by the nominal well width. The 2D exciton kinetic energy relaxation was found to consist from a fast and a slow time relaxation processes at 4 °K. The fast relaxation components within 30 to 100 ps after the photoexcitation were attributed to inter-island localization through acoustic deformation potential interaction. Using exciton-ADP interaction model to understand how exciton looses its energy in interface islands, it was confirmed that the localized exciton relaxes its energy by ADP interaction with a weak alloy scattering which contributes 10% of the total relaxation time. Exciton mass dependence on localization process has been observed as theory predicts. The

relaxation time was confirmed to be determined by the lattice temperature and well width.

The slow relaxation process was attributed to intra-island localization process and is suggested to be quasi zero dimensional exciton behavior.

8.7. Reference in Chapter 8

1). T. C. Damen, J. Shah, D. Y. Oberli, D. S. Chemla, J. E. Cunningham, and J. M. Kuo, J. of Luminesc. 45, 181 (1990) and Phys. Rev. B, 42, 7434 (1990)

2). Y. Takiguchi, Kai Shum, R.R. Alfano, Emil S. Koteles, D. C. Bertolet, and Kei May Lau, SPIE Proc. 1655, (1992)

3). R. Strobel, R. Eccleston, J. Kuhl, and K. Kohler, Phys. Rev. B 43, 12564 (1991)

4). J. Kusano, Y. Segawa, Y. Aoyagi, S. Namba, and H. Okamoto, Phys. Rev. B 40, 1685 (1989)

5). J. Feldmann, G. Peter, E. O. Gobel, P. Dawson, K. Moore, C. Foxon, and R. J. Elliott, Phys. Rev. Lett. 59, 2337 (1987)

6). K. Fujiwara, K. Kanamoto, and N. Tsukada, Phys. Rev. B, 40 , 9698 (1989)

7). K. Fujiwara, H. Katahama, K. Kamamoto, R. Cingolani, and K. Ploog, Phys. Rev. Lett. 43, 13978 (1991)

8). G. Bacher, J. Kovac, K. Streubel, H. Schweizer, and F. Scholz, Phys. Rev. B, 45, 9136(1992)

9). Y. Masumoto, S. Shionoya, and H. Kawaguchi, Phys. Rev. B, 29, 2324 (1984)

10). Karl Hess and C. T. Sah, Phys. Rev. B, 10, 3375 (1974)

11). T. Takagahara, Phys. Rev. B, 31, 6552 (1985)

12). P. K. Basu and Partha Ray, Phys. Rev. B, 45, 1907 (1992)

13).D. C. Bertolet, Jung-Kuei Hsu, Kei May Lau, E. S. Koteles and D. Owens, J. Appl. Phys. 64, 6562 (1988)

14). E. S. Koteles, D. A. Owens, D. C. Bertolet, Jung-Kuei Hsu, and Kei May Lau, Surface Science, 228, 314 (1990)

15). G. Basterd, "Wave mechanics applied to semiconductor

heterostructures" les editions de physique, France (1988)

16). Y. Takiguchi, Kai Shum, R.R.Alfano, Semicond. Sci. Technol. 7, B170, (1992)

CHAPTER 9

CONCLUSION

Carrier and exciton energy relaxation dynamics in semiconductor bulk and quantum well structures under built-in biaxial tension and external uniaxial compressive stress have been investigated using picosecond time-resolved photoluminescence spectroscopy.

I have confirmed that the built-in and external stresses in semiconductor microstructures can tune the band structures and dramatically change the carrier and exciton dynamics. The PL kinetics arising from the carrier and exciton energy relaxation and recombination processes were mainly determined by the lower energy states which were altered by the stress. The transient carrier and exciton dynamics under different stresses were observed by applying an external uniaxial stress onto a semiconductor sample. The photoluminescence kinetics in the strained semiconductor were strongly affected by the strain induced band structure changes. In other words, the carrier and exciton dynamics in semiconductor structures can be tuned by the stress. Using the knowledge obtained on the carrier and exciton dynamics under stresses investigated in this research, new types of strained photonic devices will be developed.

The main results on the carrier and exciton dynamics under various types of stress investigated in this research are summarized as follows.

The n-type GaAs grown on Si substrates, which incorporates about 3 kbar of biaxial tension and removes valence band degeneracy, reveals fundamental knowledge on hmh and lmh thermalization processes, inter-subband hole scattering, and hole cooling (average energy relaxation). The carrier thermalization and cooling process was analyzed with cascade relaxation models using a series of rate equations. The hole cooling process was analyzed by fitting the measured PL spectra with spontaneous emission spectra calculated from Fermi's Golden rule as function of delay time. The average energy relaxation of the hole system was evaluated from the PL kinetics.

Rate equation analysis confirmed that the light mass hole ($mj=\pm 3/2$) thermalizes within 5 to 7 ps which is faster than that of the heavy mass hole ($mj=\pm 1/2$) within 6 to 10 ps due to the mass difference on the carrier-carrier scattering. The inter-subband scattering time is found to be around 130 ps to 300 ps which is one order of magnitude slower than the intra-subband relaxation times. The hmh and the lmh recombines with residual electrons originated from donor within 20 to 30 ps.

The spontaneous emission spectral analysis indicated that the holes take about 100 ps to be cooled down to few meV above the lattice temperature through Fröhlich interaction with emitting LO phonons. During the period, the holes release their energies to the lattice with a rate between 0.1 and 0.2 meV/ps. The hole kinetic energies relax down exponentially with 26 to 28 ps

relaxation time which is still about six times slower than an expected time from the theory of Fröhlich interaction.

The electron dynamics in a Be-modulation doped 188Å (the lowest valence subband is hmh) and 40 Å GaAs/AlGaAs (the lowest valence subband is lmh) multiple quantum wells has been investigated using the time-resolved PL spectroscopy method. The electron interacting with cold light mass hole transfers its kinetic energy to the light mass hole more efficiently than the electron to heavy mass hole because energy transfer through elastic collision depends on mass difference between two colliding particles. In the 188 Å MQW, the electron cooling time due to collision with lmhs was found to be 43 to 50 ps. Since the LO phonons are accumulated in the system, the electrons take six time longer time to cool down to equilibrium temperature than the theoretically expected relaxation time. For the 40Å MQW, the electrons in the system cool down to the lattice temperature with 30 ps cooling time assuming a single exponential relaxation process and showed no phonon accumulation effect. Applying uniaxial stress along [100] direction onto the 188Å MQW/Si at 4K, the electron dynamics was confirmed to be changed according to the valence subband structure altered by the compressive stress. To understand the change in the electron relaxation time under various uniaxial compressions along [100] direction.

The exciton dynamics in a GaAs single QW grown on a Si substrate under uniaxial compression and a series of biaxially tensioned GaAsP QWs have been investigated. Applying uniaxial compressive stress on the biaxially strained GaAs QW/Si, the band structure was tuned so that the lowest

exciton subband would be either heavy or light mass exciton. Since there was found anti-crossing of band edges from the steady state modulation PL spectroscopy, the heavy and light mass exciton may not co-exist at the same energy level. The average exciton energy relaxation process under various subband structures was found to consist of a fast and a slow processes. The fast process is attributed to the energy relaxation due to LO phonon interaction where the exciton mass affects the relaxation time. The exciton relaxation time above the crossover stress becomes half of the relaxation time below the crossover stress when the lowest exciton band was switched to the light mass hole subband (where the exciton mass is heavy) as LO phonon interaction theory predicted. Further, it was confirmed that the lmh or light mass exciton thermalizes faster than the hmh or heavy mass exciton in the same manner as the hole in n-type GaAs/Si. The lowest hole or exciton mass mainly determines the carrier and exciton thermalization process within 10 to 100 ps time scale.

The balance between the stress effect and quantum confinement alters the band structure and was found to affect the PL kinetics. From a six level rate equation model analysis giving the PL time profile at the lowest localization state, the exciton formation time, inter-subband relaxation, and annihilation recombination process were investigated. The exciton formation time was found to be within 5 to 10 ps under biaxial stress. The exciton takes about 6 to 30 ps to scatter down to the lowest exciton subband. The exciton takes about 650 ps to 1.5 ns to recombine and annihilate a photon.

The PL from strained GaAsP having interface roughness is found to show dynamic Stokes shift arising from the two dimensional exciton

localization to the interface roughness and islands. The exciton localization process was found to be a multiple exponential relaxation process and consists of inter- and intra-island localization processes. The fast energy relaxation process was found to release energy to the lattice through acoustic deformation potential interaction whose strength was experimentally confirmed to be determined by well width, well material composition, and lattice temperature. The slow intra-exciton localization process was suggested to be a zero dimensional exciton process, where the exciton is trapped in square potential well as a quantum dot.

CHAPTER 10

FUTURE DIRECTION

There are several important topics left to be investigated using stress effects.

First, it is important to investigate the carrier and exciton energy relaxations under various types of stress at different lattice temperatures. In this thesis, I have investigated the dynamics mainly at low lattice temperature. However, for real device applications, room temperature carrier and exciton dynamics are required to be studied. I have already measured the PL kinetics at various lattice temperatures for several samples but did not discuss the results in this thesis. Further data analysis will give more knowledge on the dynamics at higher lattice temperature.

Secondly, the photoexcitation intensity dependence on the carrier and exciton dynamics are also important because the carrier-carrier interaction and the quasi-Fermi level after photoexcitation, are sensitive to the carrier density in the stress tuned band structure. I have measured some samples under various photoexcitation intensities. The data analysis is required to understand the carrier-carrier interaction and the quasi-Fermi level effects on the PL spectrum and kinetics.

Thirdly, since the 2.0 eV photoexcitation used in this research was too high giving too much excess energies to the carriers and excitons, many kinds

of scattering mechanism were involved which made analysis more complicated. Using a tunable ultrafast laser such as Ti: Sapphire laser and Forsterite laser(giving tunable wavelength region from 700 nm to 1.3 μm), resonant and non-resonant carrier and exciton photoexcitation experiments can be carried out to investigate hot or warm carrier energy relaxation process in various structures. When the phonon energy is tuned below and above a transition energy, the energy relaxation and inter- and intra-subband scattering processes can be better understood more.

Using higher time resolution techniques (such as pump & probe methods with a femtosecond tunable laser, the fast carrier and exciton dynamics such as hole burning, band renormalization, screening effect, exciton formation time, intra-subband thermalization time under various stresses can be investigated. Since the stress alters the band structure to one's needs, particular carrier and exciton dynamics can be studied selectively.

As another key feature of strained QWs is the effect on the non-linear optical properties as function of the stress. This work is interesting because the stress can tune the band structure continuously. When a strained intrinsic QW in which the hmh locates lower energy is excited by a pulses below the absorption, the virtually excited excitons may show different nonlinear behavior because of the mass difference from the excitons in ordinary QW. Switching valence band mass from hmh to lmh may show interesting non-linear effects on self-phase-modulation and four wave mixing.

CHAPTER 11

LIST OF PUBLICATIONS

1). K. Shum, Y. Takiguchi, J. M. Mohaidat, F. Liu, R. R. Alfano and H. Morkoc, Appl. Phys. Lett. 56, 2328 (1990)

2). Y. Takiguchi, Kai Shum, R. R. Alfano, E. S. Koteles, D. C. Bertolet, J. K. Hsu, and K. M. Lau Semicond. Sci. Technol. 7,B170 (1992)

3). Y. Takiguchi, Kai Shum, R. R. Alfano, E. S. Koteles, D. C. Bertolet, J. K. Hsu, and K. M. Lau, Proc. 7th International Conference of Hot Carrier at Nara in Japan (1991)

4). Kai Shum, Y. Takiguchi, J. M. Mohaidat, R. R. Alfano, K. Adomi, and H. Morkoc, Semicond. Sci. Technol, 7 B195 (1992)

5). Y. Takiguchi, Kai Shum, R.R. Alfano, M. Dutta, and P.G. Newman, Proc. SPIE Vol. 1599 (1991)

6). Kai Shum, Y. Takiguchi, J. M. Mohaidat, and R. R. Alfano, Phys. Rev.B.44, 4044 (1991)

7), Kai Shum, Y. Takiguchi, J. M. Mohaidat, and R. R. Alfano, Submitted to Appl. Phys. Lett.

8). Hao Qiang, F. H. Pollak, Kai Shum, Y. Takiguchi, R. R. Alfano, S. F. Fang, H. Morkoc, Appl. Phys. Lett. 60, 2651, (1992)

9).Y. Takiguchi, Kai Shum, R. R. Alfano, E. S. Koteles, D. C. Bertolet, J. K. Hsu, and K. M. Lau, Proceedings of OSA '92, 43 ,Albuquerque, NM (1992)

10). Y. Takiguchi, Kai Shum, P. R. Alfano, H. Qiang, and F. H. Pollak, H. Morkoc, Proc. LEOS '92 , Boston, 137 (1992)

11). Y. Takiguchi, Kai Shum, R. R. Alfano, E. S. Koteles, D. C. Bertolet,

J. K. Hsu, and K. M. Lau, submited to Phys. Rev. B

12). Kai Shum and Y. Takiguchi, SPIE 1677, 249 (1992)

Chapter 12

Physical constants and Material parameters

The following parameters were used for data analysis: mechanical, electrical and optical parameters. It was difficult for me to find parameters for GaAs, AlGaAs, and GaAsP tabulated in a paper. Therefore, it will be convenient if I tabulate the parameters for those semiconductor materials I used.

12.1 Physical constants

Table 12.1 Physical constants

Parameter	symb	unit	value
Avogadro's Number	N_A	molecules/mol	6.02217×10^{23}
Boltzmann's Constant	k_B	eV/K	8.62×10^{-5}
Electron Charge	e	C	1.60219×10^{-19}
Free electron mass	m_0	kg	9.10956×10^{-31}
Permittivity of feee space	ε_0	F/cm	8.854×10^{-14}
Permeability of free space	μ_0	H/cm	1.257×10^{-8}
Planck's Constant	h	J•s	6.62620×10^{-34}
Velocty of light in vacuum	c	m/s	2.997925×10^{8}

Table 12.2 Pressure units

bar	dyn/cm^2	N/m^2	Pa	torr
1	10^6	10^5	10^5	750.0638

12.2. Material parameters

The parameters are mainly for GaAs, AlAs, and GaP and are sited from Adachi's papers and some other books listed in the reference later. In this thesis, I needed the parameters as function of lattice temperature, material composition, and amount of stress. However, there was none regarding the stress dependence on the parameters.

Table 12.3 Band gap energy as function of lattice temperature

	GaAs	AlAs	GaP
Eg(Γ)	$1.519 - \frac{5.405\times10^{-4}T^2}{T+204}$ (eV)	$3.169 - \frac{6.0\times10^{-4}T^2}{T+204}$ (eV)	not found
Eg(X)	$1.981 - \frac{4.60\times10^{-4}T^2}{T+204}$ (eV)	$2.239 - \frac{6.0\times10^{-4}T^2}{T+204}$ (eV)	$2.338 - \frac{5.771\times10^{-4}T^2}{T+372}$ (eV)
Eg(L)	$1.815 - \frac{6.05\times10^{-4}T^2}{T+204}$ (eV)	not found	not found

Table 12.4 Material parameters 1

at 300 K

Materials / parameters	Si	GaAs	AlAs	GaP
Atomic Weight	28.09	144.63		
Break down field (V/cm)	$\sim 3\times10^{5}$	$\sim 4\times10^{5}$		
Crystal structure	Diamond	Zincblende	Zincblende	
Density (g/cm^2)	2.328	5.32 (5.36)	5.6611	4.130
Dielectric Constant ε_s (Ks)	11.9	13.1	10.06	11.1
Effective density of state in conduction	2.8×10^{19}	4.7×10^{17}		
in valence band	1.04×10^{19}	7.0×10^{18}		
Effective mass (unit of m_0) electrons	ml=0.98 mt=0.19	0.067	0.150	0.17
light hole	0.16	0.082	0.150	0.14
heavy hole	0.49	0.45	0.76	0.79
Lowest energy gap (eV)	1.12	1.424	2.168 (X) 3.169 (γ)	2.25 (X) 2.74(γ)
Lattice constant (Å)	5.41953	5.6533	5.6611	5.4512

Table 12.5 Material parameters 2

Materials / Parameters	Si	GaAs	AlAs	GaP
Melting point (°C)	1415	1238	1740	
Thermal expansion (1/°C)	2.6×10^{-6}	6.4×10^{-6}	5.2×10^{-6}	5.91×10^{-6}
Elastic Stiffness Constant				
C11 ($\times 10^{11}$ (dyn/cm^2)		11.88	12.02	14.120
C12		5.38	5.70	6.253
C44		5.94	5.89	7.047
LO phonon Energy (meV)	63	36.25	50.09	
TO phonon Energy (meV)		33.29	44.88	
Valence band deformation potential (eV)				
a		2.7	2.6	3.0
b		-1.7	-1.5	-1.5
d		-4.55	-3.4	-4.6

Table 12.6. Material parameters 3

Materials / Paramenters	Si	GaAs	AlAs	GaP
Intravalley defoemation potential (eV)				
in Γ valley		6.8	6.3	
in X valley		-2.5	-2.3	
in L valley		0.23	0.55	
Intervalley deformation potential (eV/cm) x10^9				
between Γ and X valleys		0.5-1.1		
between Γ and Lvalleys		0.15-1.0		
between L and Xvalleys		0.34-1.1		
between X and Xvalleys		0.27-1.1	1.47	
between L and L valleys		1		
Exciton Rydberg Energy (eV)		4.7	17.0	
Exciton Bohr Radius (Å)		115	42	

Table 12.7. Material parameters 4

Paramenters \ Materials	Si	GaAs	AlAs	GaP
Refractive Index at λ=1 μm		3.655	3.178	3.452
Thermal Conductivety (W/cm/deg.)	1.5	0.44	0.91	0.77
Dielectric permittivity at optical freq. ε_∞, K_∞		11.1	8.16	8.46
Tetrahedral distance (Å)	2.36	2.44		
Intrinsic carrier concentration (cm^{-3})	1.45×10^{10}	8×10^{6}		
Thermal Diffusivity	0.9	0.44	$= \frac{\text{thermal conduction}}{\text{density x specific heat}}$	
Specific heat (J/g °C)	0.7	0.35		

GLOSSARY

In this glossary, I will list technical and physical terms used in this thesis and briefly explain the terms.

Acoustic deformation potential (ADP)
: A crystal potential change induced by an acoustic vibration mode of lattice.

Acoustic phonon
: A phonon having a acoustic vibration mode.

Biaxial stress
: A two dimensional stress applied to a sample from two direction. Its unit is in kbar.

Bloch function
: A periodic electron wave function which reflects the periodic crystal potential.

Bose distribution
: Average number of particles(Spin is equal to 1) with an energy of hω at a given temperature T.

Built-in stress
: A stress generated in a heterostructure having lattice mismatch or mismatch in their thermal expansion coefficients.

Carrier energy relaxation
: Energy loss process of a photoexcited hot carrier to the lattice or other carriers.

Cold electron gas
: Electrons in a n-type doped semiconductor material at a low lattice temperature. The electron

	gas arised from the donors is described by the low temperature distribution function.
Confined energy level	Discrete energy levels in a QW structure arising from the quantum confinement
Crystal orientation	A direction in a crystal which consists of many atoms.
de Broglie wavelength	The wavelength of a particle wave $\lambda = h/mv$ having a momentum mv, where h is the Planck constant.
Density of states	Capacity of aquiring carriers per unit energy per unit volume
Double heterostructure	A structure in which one material is sandwiched by other different material.
Effective mass	Carrier mass determined by the crystal potential in a given direction.
Exciton	Hydrogen-like atomic energy states of an electron bound to a hole.
Exciton dynamics	Exciton temporal behavior determined by the interactions among themselvs and with other particles.
Fröhlich interaction	Same as optical phonon interaction
Hamiltonian	An energy operator.
Heavy hole	An electron vacancy in valence band having heavy effective mass determined by the band structure.
Heterostructure	A structure of a material grown on another different material.

Hot carriers	Carriers described by a distribution with a higher temperature than lattice temperature.
Hydrostatic dilation	A stretching stress applied to a sample from all direction equally. Its unit is given in kbar.
Hydrostatic stress	A stress applied to a sample from all directions equally. The unit is in kbar.
Impurity scattering	Interaction between carriers and impurities or doped atoms exist in a semiconductor material.
Inter-subband scattering	A carrier scattering from one subband to another subband through phonon interaction.
Inter-valley scattering	Carriers scattereing between valleys in a conduction band where there are three band minima called Γ-, X- and L-vallyes.
k vector	A vector representing the momentum of a carrier.
Kronig-Penney model	A crystal potential model modeled as a series of square potential barriers in one dimension by Kronig and Penney .
Lattice constant	A spatial period of a crystal structure in a given direction.
Lattice mismatch	A difference in the lattice constants between the two different materials at the interface of heterostructure.
Light hole	An electron vacancy in valence band having light effective mass arising from the band structure.
LO phonon emission	Emission of longitudinal optical vibration mode from a hot carrier interacting with lattice atoms.

Metal Organic Chemical Vapor Deposition (MOCVD)	
	A thin atomic layer growing method using metal organic gas flew on a heated substrate to grow an epilayer.
Molecular Beam Epitaxy (MBE)	A thin atomic layer growing method using atomic beam in vacuum chamber to grow the epilayer on heated substrate.
Multiple quantum well (MQW)	A QW structure which repeats many single QW along the growth direction
Phonon energy	An energy of quantized lattice vibration mode.
Optical deformation potential	
	A crystal potential induced by optical phonon.
Piezoelectric scattering	Phonon scattering through piezoelectric effect.
Phonon scattering	Interaction of carriers with the lattice which emits various kind of vibrational mode.
Phonon wave vector	A vector representing phonon momentum.
Photoemission	A process when carriers in the semiconductor recombine and emit the excess energy as photons.
Photoexcitation	Excitation of carrier to high energy states by optical stimulation.
Photogenerated carriers	Free carriers generated by light illuminated on a semiconductor sample.
Photoluminescence(PL)	A photons emitted when electrons in the conduction and holes in the valence band recombine.
Photon	Quantized light wave
Polar optical phonon interaction	

Interaction of carrier with lattice in a polar semiconductor material like GaAs inducing a lattice vibration in optical mode.

Quantum confinement Quantum mechanical quantization of energy states as the well width of a double heterostructure becomes narrower.

Quantum well (QW) A double heterostructure of material whose low band gap material thickness becomes thinner than 200Å and the electron energy states become discrete (quantized).

QW laser A QW structure used to achieve high energy and low threshold semiconductor laser.

Radiative transition Transitions of electrons in the conduction to holes in the valence band resulting in photons.

Schrödinger equation An equation describing carrier behavior in a potential structure, assuming a wave nature of carrier.

Spontaneous emission process

A process when carriers recombine and emit photons, spontaneously.

Stokes shift An energy shift of PL from an original position.

Stress induced band shift Band structure change when a stress is applied to a samplearising from the crystal structure change.

Thermalization A process of hot carriers loosing their excess energy to lattice. Their distribution function becomes Fermi-Dirac distribution.

Uniaxial stress	**A stress applied to a sample in one direction. The unit is given in kbar.**
Valence band degeneracy	**A band structure whose heavy and light valence subbands have a same energy level at k=0**

APPENDIX

A. 1. Time spread in optics

A.1.1. introduction

When a femtosecond laser pulse propagates in condensed matter material or even in a gaseous media, the arrival time of the pulse and the laser pulse shape will vary due to group velocity (GV) and group velocity dispersion (GVD) of the material media[1]. These effects are caused by wavelength dependent properties of index of refraction of the media. GV and GVD become more apparent when the length of the materials become long or when the duration of the laser pulse becomes extremely short in the femtosecond time regime. GV and GVD become real problems especially in the field of optical communication because the transmission capacity of the fiber cable is limited by the pulse duration and shape of the signal after propagating the long distance in a fiber.

A.1.2. Index of refraction

The index of refraction of a material as function of wavelength determines how light propagates in that material. The Sellmeier's equation or polynomial fitting using measured index values describes the index of refraction as function of wavelength.

A modified Sellmeier's equation using Drude model of charge driven harmonic oscillator as discussed by Feynman et al.[2] is given by:

$$n_{\Phi} = 1 + A\frac{\lambda^2}{(\lambda^2 - \lambda_0^2)} \quad , \qquad \text{(A.1.1)}$$

Table A.1.1. A and λ_0 values for various kinds of optical materials.

	BK7	Quartz	KDP	Water	Air	LaSFN9
A	0.50531	0.44920	0.49823	0.32494	2.725×10^{-4}	0.81149
λ_0(nm)	87.7397	84.4218	88.3755	92.3268	76.4875	125.896
	KD*P	Urea	$LiNbO_3$	CdSe	CS_2	Acetone
A	0.49569	0.46918	1.20464	1.45176	0.58464	0.34913
λ_0 (nm)	84.7532	110.161	159.123	250.009	158.416	97.0437

where A and λ_0 are the constant and the resonance wavelength for a given material, respectively. The values of A and λ_0 for various materials are calculated using typical refractive indices listed in several optical catalogue and optics handbooks[3)] are tabulated in Table A.3.1. Using these values for materials, the index of refraction at various wavelengths can be calculated.

A1.3. Group velocity and group velocity dispersion

An optical pulse contains many frequency components, and each component travels with its phase velocity determined by the index of refraction. This wave assemble travels together as a group in the form of a wave packet.

The phase velocity v_Φ of wave is determined by its angular frequency ω and propagation constant k as;

$$V_{\Phi} = \frac{\omega}{k} = \frac{c}{n_{\Phi}}. \tag{A.1.2}$$

The group velocity v_g[1] is the velocity of plane of constant amplitude of group of waves and is given by $(\lambda / n_{\Phi} \bullet dn_{\Phi} / d\lambda << 1)$

$$v_g = \frac{d\omega}{dk} = \frac{c}{n_{\Phi} - \lambda \frac{dn_{\Phi}}{d\lambda}}, \tag{A.1.3}$$

where λ is a wavelength in vacuum.

From Eq. A.1.3, the group index n_g at a wavelength λ is defined by;

$$n_g = n_{\Phi} - \lambda \frac{dn_{\Phi}}{d\lambda}. \tag{A.1.4}$$

Differentiating n_{Φ} given by the modified Sellmeier's Eq.(A.1.1) with respect to λ and substituting the result into Eq.(A.1.4), the equation for the group index of refraction is obtained;

$$n_g = 1 + A\frac{\lambda^2}{(\lambda^2 - \lambda_0^2)} + 2A\frac{\lambda_0^2 \lambda^2}{(\lambda^2 - \lambda_0^2)^2}. \tag{A.1.5}$$

which depends on A and λ_0 for the given material.

The calculated index of refraction n_{Φ} and the group index of refraction n_g for BK7 glass are displayed in Fig.A.1.1. The group index of refraction differs significantly from the phase index of refraction in the ultraviolet region.

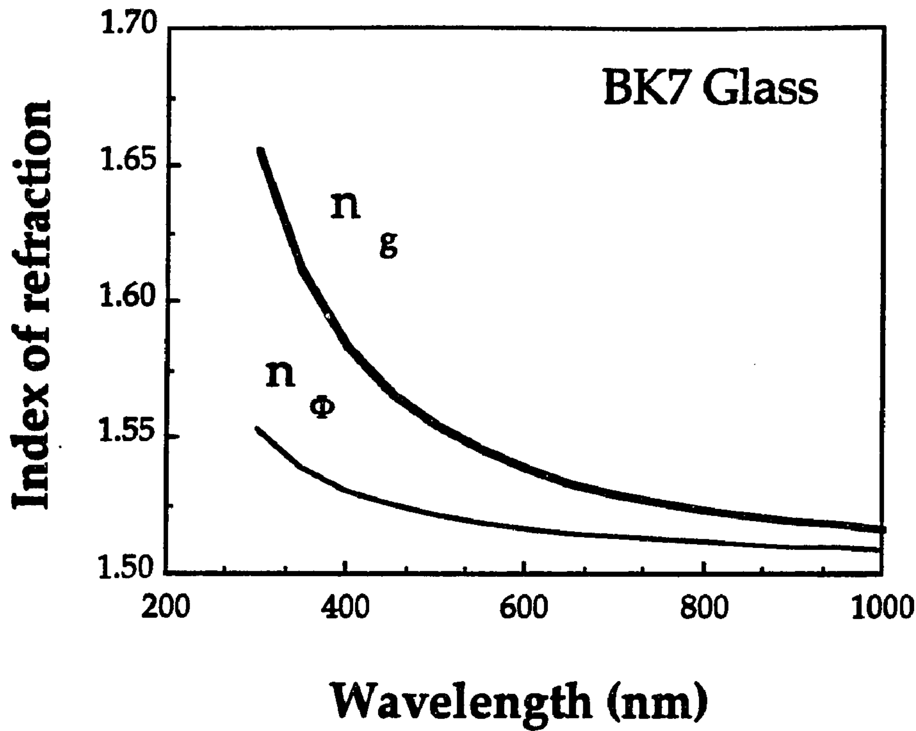

Fig. A.1.1. Phase and group refractive index of BK7 glass.

A.1.4. Pulse propagation in dispersive medium

The propagation time difference between the plane of constant phase and plane of constant amplitude for a pulse traveling in a dispersive material of length L is given by,

$$Td(L) = (n_g - n_\Phi)\, L/c \quad . \tag{A.1.6}$$

Using the modified Sellmeier's equation and the group index from Eq.(A.1.5), the retardation time is obtained as;

$$Td(L) = \frac{L}{c}\,\lambda\,\frac{dn_\Phi}{d\lambda} ,$$

$$= \frac{L}{c} \frac{2 A \lambda_0^2 \lambda^2}{\left(\lambda^2 - \lambda_0^2\right)^2} . \tag{A.1.7}$$

From Eq.(A.1.7), Td(L) is always positive for $\lambda \neq \lambda_0$, which means that the plane of constant amplitude travels slower than the plane of constant phase.

A.1.5. Gaussian pulse propagation

When a Gaussian pulse of electric field

$$E(z, t) = E_0 \exp\left(-\frac{2 \ln 2\, t^2}{t_{in}^2} \right) \exp\left\{ i\left(\omega t - kz\right) \right\} , \tag{A.1.8}$$

with the pulse duration t_{in} in Full Width at Half Maximum propagates in a dispersive material, the pulse field becomes broaden.

Following Yariv[4], the output field shape is still Gaussian upon passing through a media of thickness L with a duration time t_{out} of the form:

$$E(z,t) = \frac{1}{\sqrt{1 + i\frac{8 \ln 2\ aL}{t_{in}^2}}} \exp\left\{ -\frac{\left(t - L/v_g\right)^2}{\frac{t_{in}^2}{2 \ln 2} + \frac{32 \ln 2\, a^2 L^2}{t_{in}^2}} \right\} \exp\left(i\omega t\right) , \tag{A.1.9}$$

where a is the GVD term which is equal to $d^2k/d\omega^2/2 = k''/2$.

The expression for a using the modified Sellmeier's equation is:

$$a = \frac{1}{2}\frac{d}{d\omega}\left(\frac{1}{v_g}\right) = A\frac{\lambda^3(3\lambda_0^2\lambda^2 + \lambda_0^4)}{2\pi c^2(\lambda^2 - \lambda_0^2)^3}, \qquad (A.1.10)$$

where λ is the central wavelength of the pulse spectrum.

The output pulse duration:

$$t_{out}(L) = \sqrt{t_{in}^2 + \frac{(8\ln 2\, a\, L)^2}{t_{in}^2}} = \sqrt{t_{in}^2 + \tau(L)^2}. \qquad (A.1.11)$$

is obtained from FWHM of the intensity profile from Eq.(A.1.9). The intensity profile of the Gaussian laser pulse after traveling in dispersive plate is obtained from Eq.(A.1.9) using $E\,E^* = I(t)$.

The value of $\tau(L)$ is defined using Eq.(A.1.10) as,

$$\tau(L) = \frac{2\ln 2}{\pi c^2}\lambda^3\left\{\frac{6A\lambda_0^2\lambda^2 + 2A\lambda_0^4}{\left(\lambda^2 - \lambda_0^2\right)^3}\right\}\frac{L}{t_{in}}. \qquad (A.1.12)$$

This equation can be simplified as:

$$\tau(L) = B\frac{L}{t_{in}}, \qquad (A.1.13)$$

where B is defined as a constant determined by the material and the central

Table A.1.2. B values for various materials.

	BK7	Quartz	KDP	Water	Air	LaSFN9
300 nm	5.13042	4.12711	5.15520	3.77653	0.00195	23.8764
410	3.26164	2.65289	3.27028	2.36250	0.00129	12.8118
530	2.36833	1.93566	2.37234	1.70341	0.00095	8.65788
620	1.97433	1.61670	1.97693	1.41611	0.00080	7.01974
1060	1.10460	0.90754	1.10534	0.78847	0.00045	3.74253
1300	0.89378	0.73474	0.89427	0.63745	0.00036	2.00340

	KD*P	Urea	$LiNbO_3$	Cd Ce	CS_2	Acetone
300 nm	4.60033	9.00928	88.1385	3843.05	34.7548	4.64847
410	2.95388	5.23815	37.5086	295.221	17.9500	2.85696
530	2.15436	3.66001	23.1523	115.118	11.1045	2.04417
620	1.79895	3.00579	18.1449	77.2961	8.71007	1.69431
1060	1.00951	1.63837	9.13225	30.4555	4.38982	0.93844
1300	0.81726	1.31976	7.25814	23.2755	3.48975	0.75802

$B(\lambda) \times 10^{-25}$ sec^2/m

wavelength λ of the laser pulse. Values of B for different materials are listed in Table A.1.2 at various wavelengths.

The output pulse duration can be simply related:

$$t_{out}(L) = \sqrt{t_{in}^2 + \left(\frac{B\,L}{t_{in}}\right)^2} \quad . \qquad \text{(A.1.14)}$$

Once we know the incident pulse duration t_{in}, thickness of material L, and B of the material at the laser central wavelength, the output pulse duration t_{out} can be determined using Eq.(A.1.14). Fig. A.1.2. and Fig. A.1.3. display the calculated t_{out} as function of the incident pulse duration for various dispersion conditions for BK7 glass and for air, respectively.

The central wavelength of the laser pulse was set to 600 nm. As the pulses travel longer into the material, the peak intensities decrease and the pulse durations become wider. The shorter the incident pulse, the quicker the pulse broadening and reduces its peak intensity as compared to a wider pulse.

The intensity profile at z=L is obtained from Eq.(A.1.9):

$$I(L,t) = \frac{1}{\sqrt{1+\left(\frac{8\ln 2\ aL}{t_{in}^2}\right)^2}} \exp\left\{-\frac{2(t - L/v_g)^2}{\frac{t_{in}^2}{2\ln 2} + \frac{32\ln 2\, a^2 L^2}{t_{in}^2}}\right\} , \qquad \text{(A.1.15)}$$

The intensity profile at z=L reforming in terms of B is given by,

$$I(L, t) = \frac{1}{\sqrt{1 + \left(\frac{B\,L}{t_{in}^2}\right)^2}} \exp\left\{ - \frac{\frac{4\ \ln 2}{t_{in}^2}(t - L/v_g)^2}{1 + \left(\frac{BL}{t_{in}^2}\right)^2} \right\} . \quad (A.1.16)$$

The pulse intensity profile at time t and path L is calculated from Eq. (A.1.16).

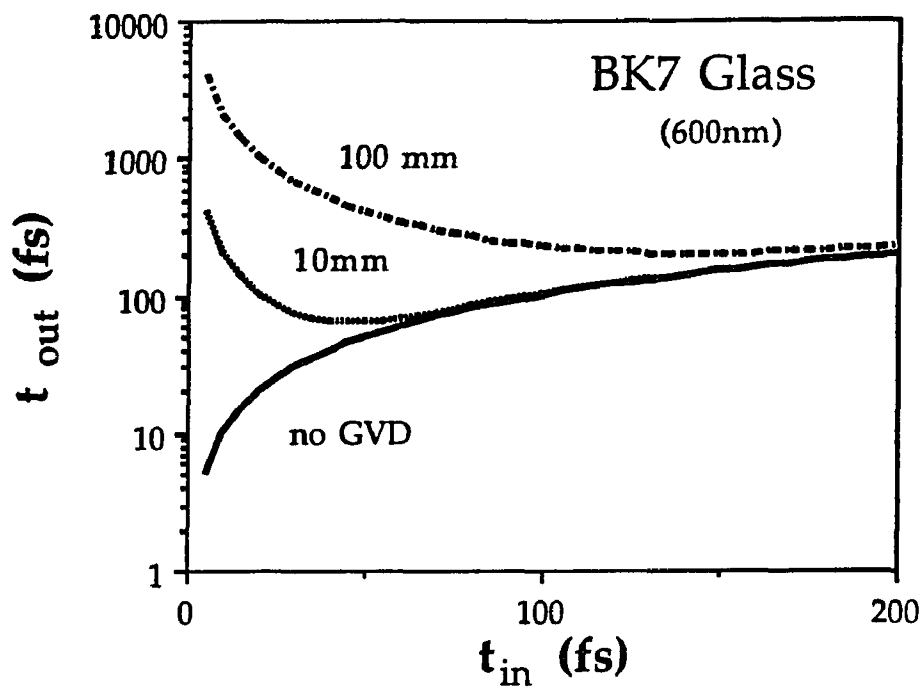

Fig.A.1.2. Pulse broadening due to GVD in BK7 glass.

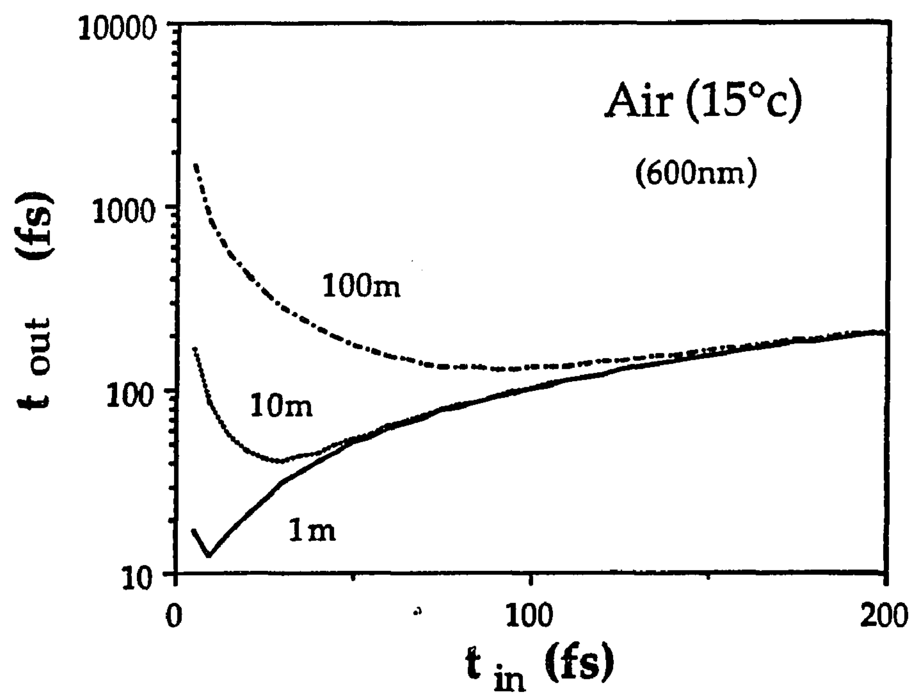

Fig. A.1.3. Pulse broadening due to GVD in air.

A.1.6. GV and GVD effects in different structured optical elements

When the thickness of the material varies across the plane of constant amplitude, the time retardation Td(L), the pulse duration $t_{out}(L)$ and intensity profile I(L,t) after propagating through these regions become a functions of the pathlength L over which the laser pulse travels.

A.1.6.1. Plates

The most common optical elements found in experimental setups are beam splitters and optical filters. The pulse propagation effects through these platelike materials are important to evaluate. The output pulse duration $t_{out}(L)$ for various incident pulse durations of Gaussian femtosecond pulse passing through BK7 glass, KDP and air with various thickness L are calculated at the central wavelength of 600 nm using Eq.(A.1.14). In the calculation for KDP, the index of refraction for ordinary ray is used considering the phase matching condition.

Some of the salient results are: a 10 fs pulse at 600 nm becomes 20 fs wide after traveling about 2 m of air while for only 25 mm of BK7 glass broadens a 10 fs to 500 fs. On the other hand, a 3 mm KDP crystal set at phase matching angle causes a 10 fs pulse broadens to 60 fs while for 100 μm crystal the pulse broadens only to 10.2 fs. A 5 μm BK7 glass plate causes 98.7 atto second (as: 1×10^{-18} sec.) broadening for a 10 fs pulse.

A.1.6.2. Prism

Another common optical element found in a femtosecond laser cavity nowadays is prisms. Four Prisms are used in CPM laser cavity to produce

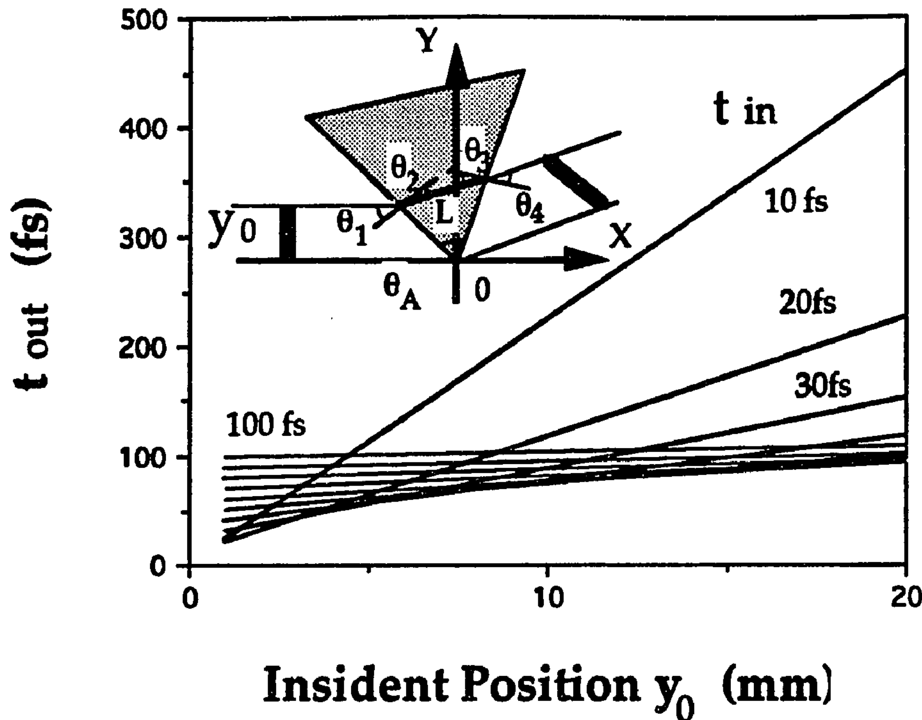

Fig. A.1.4. Retardation time of pulse front due to the GV in prism.

pulses as short as 27 fs duration[5)] by controlling the chirp of pulses and compensating GVD in the laser cavity.

A pulse ray trajectory analysis is useful to determine the pulse propagation pathlength in the prism. The pulse is refracted at the surface determined by Snell's law. The velocities of the pulse in air and the prism are the group velocities of the air and the prism glass material.

Time retardation Td(L) for a short laser pulse at 620 nm incident at y_0 off a prism made of BK7 glass as shown in the inset of Fig. A.1.4 is found to be:

$$T_d(L) = \frac{y_0}{c}\frac{2A\lambda_0^2\lambda^2}{\left(\lambda^2 - \lambda_0^2\right)^2} C(\lambda, \theta_1, \theta_A) \quad . \tag{A.1.17}$$

As shown in Fig.A.1.4, the larger the value of y_0, the longer the pathlength in the prism and larger the retardation time. Therefore, the plane of constant amplitude after the ray emerging from the prism declines from the plane of constant phase with a retardation angles θr which is computed for this case to be 1.4724°. This time retardation as function of incident position along the prism surface causes a time spread when the time profile of the whole plane wave is measured after the prism. Using the retardation angle, the time spread determined by maximum retarded time is calculated to be about 857 fs in the case of the beam diameter of the laser is 10 mm with corresponding longest pathlength of 11.39 mm in the prism.

The longer the pathlength in the prism, the wider the output pulse duration becomes due to GVD. Using the pathlength L into Eq.(A.1.14), the pulse broadening as function of the incident position y_0 is given by:

$$t_{out}(L) = \sqrt{t_{in}^2 + \left(\frac{B y_0 C(\lambda, \theta_1, \theta_A)}{t_{in}}\right)^2} \quad . \qquad (A.1.18)$$

The pulse broadening for 10 fs to 100 fs pulses for 10 fs steps are computed and displayed in Fig. A.1.4. for a BK7 glass prism. A 30 fs pulse duration increases by factor of 5 when the y_0 position changes from 0 to 10 mm. Larger effects arises for shorter pulses.

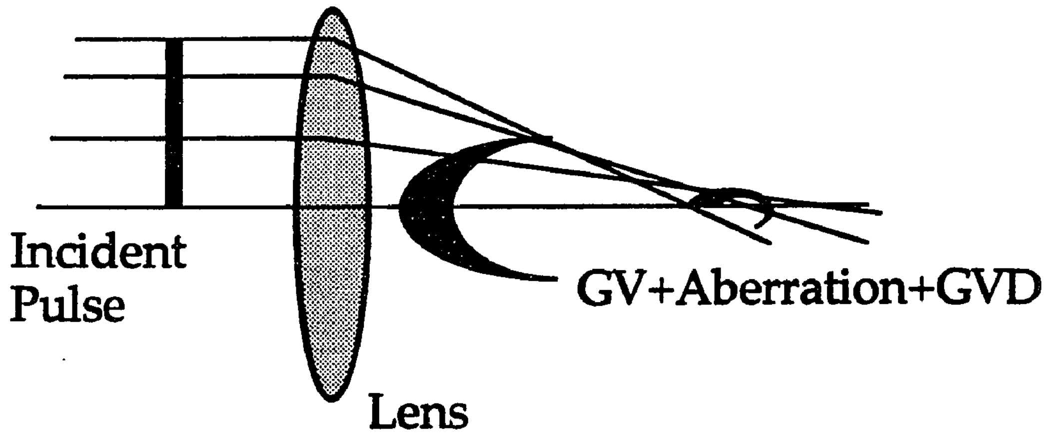

Loop of Time !!

Fig. A.1.5. Complex loop of pulse front after a convex lens.

Therefore, the pulse duration measured at the output of a prism is a combined effect due to both GV and GVD with respect to space across the rear surface of the prism.

$$\Delta t_{out\,y_0} = \frac{1}{t_{out}(y_0)}\left(\frac{B y_0 C}{t_{in}}\right)\frac{\Delta y_0}{y_0}\,. \qquad \text{(A.1.19)}$$

A.1.6.3. Lenses

The most common optical element which can be found in an optical setup is a lens.

As an ultrashort pulse propagates in a lens, the pulse front starts converging into the focal point after emerging from the lens. The pulse profile at the focal point is affected by not only GV and GVD but also spherical aberration of the lens. The pulse traveling through the optical axis is retarded more than that from the edge due to GV. As schematically shown in Fig.A.1.5, the plane of constant amplitude becomes a complex profile near the focal point which causes

the pulse to spread. The spherical aberration which is a characteristics of convex lens arises from the mismatch between the radius of convex and the index of refraction. If the index of refraction of lens is too high, a beam traveling through the edge of the lens has shorter focal length than one near the center. Since both the aberration and the GV retardation are parabolic, the plane of constant amplitude becomes looped around the focal point. When the pulse duration time is measured at the focal point, the loop causes a time spread due to time delay of aberration. For example, a 30 fs laser pulse centered at 600 nm having a 20 mm beam diameter is incident onto the lens. The pulse near the focal point becomes about 100 fs due to GV and aberration. When the laser beam is reduced to 1 mm incident on the lens at 5 mm from the optical axis, the time spread is about 30 fs.

In addition to the pulse spreading due to GV and the spherical aberration, the pulse duration after passing through the lens is broadened by GVD. The duration time of the pulse passing through the center of the lens becomes wider than that through the edge of the lens. According to the numerical calculations, the duration time of a 30 fs pulse passed through the optical axis is broadened to be 100.5 fs and the pulse entered at y_0=10 mm away from the axis is broadened to 64.7 fs.

The propagation time retardation, spherical aberration and the pulse broadening effects are schematically illustrated. The actual pulse profile at the focal point is complex and is determined by combination of GV, aberration, and GVD. Therefore, the pulse duration time measured at the focal point is determined by both the loop and the pulse broadening. Because of these

effects, lenses should not be used to focus femtosecond laser pulse below 30 fs to excite material. In this case, the pulse duration at the focal point can be 140 fs for 30fs incident pulse. Lens causes serious pulse broadening effects and can not keep the original temporal resolution to give information of the materials such as lifetime or relaxation times on a femtosecond time scale.

Focusing of pulses below 30 fs should be accomplished by concave mirrors which has small aberration problem.

Care is really required when a combination lenses is used for any femtosecond experiments. Metallic concave mirrors seem to be best for the femtosecond experiments but we must investigate this further.

A.1.7. Reference in appendix

1). For example, A. Yariv and Pochi Yeh : "Optical waves in crystal" Wiley Interscience Publication (1984)

2). R.P.Feynman, R.B.Leighton, M.L.Sands;"The Feynman Lecture on Physics I " Addison-Wesley Publishing Company, Inc. (1965)

3). For example, KDP data: A. Yariv and Pochi Yeh "Optical waves in crystal" Wiley Interscience Publication (1984), BK7 data: Ed. Tokyo Astronomical Observatory "Rika Nenpyo", Maruzen Co. Ltd. (1985), Optical glass data : Catalogue from Spindler Hoyer(1989), Other nonlinear materials data: Ed. The Laser society of Japan " Laser handbook" , Ohmsha (1982)

4). A.Yariv : "Optical Electronics" CBS College Publishing (1985)

5). J.A. Valdmanis, R.L.Fork, and J.P.Gordon, Optics Letter 10, 131 (1985)

A.2 Computer programs

In this appendix 2, several computer programs for Hamamatsu Temporal Analyzer C2280, IBM, and Macintosh cpersonal computers are attached.

The language I have used to write following programs are several kind of "BASIC" languages. Hamamatsu TA accepts HBASIC, C-language, assembler, and machine language while IBM and Macintosh currently accept C-language, assembler, machine language, GWBASIC, Quick BASIC, and so on. Since the programming with BASIC language is very easy. Therefore, I have adopted "BASIC" language. If one uses to write the program with C-language, the computation speed can be very fast.

A cable connecting TA and IBM through RS232C is regular DB25 connection cable while a cable connecting TA and Macintosh is DB25 to Mini DIN 8 Male cable. To buy them, DB25 cable # GD0250-1 from MISCO company (1-800-US MISCO) and Mini DIN8/DB 25 cable #ACC0593 from MacWarehouse (1-800 -255-6227) are recommended.

The index for the program is listed bellow.

A.2.1 Communication program

A.2.1.1 "IBM.BAS" for Hamamatsu C2280 TA

A.2.1.2 "Mactran.BAS" for Hamamatsu C2280 TA

A.2.1.3."Bitran.BAS" for Hamamatsu C2280 TA

A.2.1.4. "TA Trans" in Macintosh Quick Basic(b)

A.2.1.4 "prlist.BAS" for Hamamatsu C2280 TA

A.2.2. Data Analysis Program

A.2.2.1 "Fit.BAS" for Hamamatsu C2280 TA

A.2.2.2 "Specfit.BAS" for Hamamatsu C2280 TA

A.2.2.3 Average carrier energy analysis program"Avee.BAS" for Hamamatsu C2280 TA

A.2.3 . Theoretical calculation programs

A.2.3.1. Six level rate equation

A.2.3.2 Quantum well Eigenstate Level

A.2.3.3. Superlattice Miniband calculation program

A. 2. 1. Communication programs

Time-resolved images are analyzed either by TA or other computers. When the image data or a part of the image data needed to be transferred to other computers, programs which can read the data file in TA and communicate with other computer are important. Therefore, I have written several programs connecting TA with IBM and Macintosh computers through RS232C interface port. TA runs a program in HBASIC while IBM runs a communication program in GWBASIC and Macintosh runs another communication program in QuickBASIC.

A.2.1.1. Program Name "IBM.BAS" in Hamamatsu C2280 TA

This program is used to transfer streak camera data such as temporal or spectral intensity profiles in ASCII format to IBM computer. On the IBM computer, there is a program named "TA.BAS" in GWBASIC which will work together with this program to communicate each other.

```
10'-------------------------------
20 ' IBM transfer by TAKI
30'-------------------------------
40 PRINT "**********************************************"
50 PRINT " Transfer ASCII data to IBM "
60 PRINT " "
70 PRINT "      Did you convert the data to ASCII ?"
80 PRINT "**********************************************"
90 INPUT "Input your DATA FILE NAME = ",FD$
100 OPEN "I",#1,FD$
110 FOR I=0 TO 511
120  INPUT #1,W
130  IF EOF(1) THEN GOTO 170
140  INPUT #1,IN
150  RSPRINT W,IN
160 NEXT I
170 CLOSE #1
180 END
```

A.2.1.2. Program Name "Mactran.BAS" in Hamamatsu C2280 TA

This program is used to transfer streak camera data such as temporal or spectral intensity profiles in ASCII format to Macintosh computer. On theMacintosh computer, there is a program named "TA trans" in Quick BASIC which will work together with this program to communicate each other.

```
10'----------------------------------------------
20'   Macintosh data transfer
30'    6/23/92   by Taki
40'----------------------------------------------
 50 PRINT "**********************************************"
60 PRINT "  Transfer ASCII data to Mac "
70 PRINT " "
80 PRINT "       Convert the data to ASCII ?"
 90 PRINT "**********************************************"
100 INPUT "Input your DATA FILE NAME =  ", FD$
110 OPEN "I",#1,FD$
120 FOR I=0 TO 2000
130  INPUT #1,W$
140  IF EOF(1) THEN GOTO 200
150  RSPRINT W$
160  FOR II=0 TO 5
170    PRINT " "
180  NEXT II
190 NEXT I
200 CLOSE #1
210 FOR I=0 TO 20
220  PRINT " "
230 NEXT I
240 RSPRINT "END"
250 END
```

A.2. 1.3. Program Name "Bitran.BAS" in Hamamatsu C2280 TA

This program enable to transfer profile data saved through "TA.68K" streak camera image analysis program. The saved data are written in binary format. This program read the binary data saved in a floppy disk, convert the binary data to ASCII format, and transfer the ASCII data to either IBM or Macintosh computer.

```
10'----------------------------------------------------------
20 '  TA data transfer program
30 '              6/25/92 by Taki
40'----------------------------------------------------------
50 PRINT "**********************************************"
60 PRINT "  TA Data transfer Program  "
70 PRINT "      (Binary data to ASCII) "
80 PRINT "**********************************************"
90 DIM PRF(1024)
100 FREE
110 ALLOC &H12000&
120 INPUT "Input your Data File Name ?     ",F$
130 OPEN "DI",#1, F$
140   PNT=FRE(1)
150'-------------------------------------
160 '  Data direct read from floppy disk
170'-------------------------------------
180 FOR J=1 TO 600
190     DIRECT READ #1,PNT
200     PNT=PNT+128
210 IF EOF(1) THEN GOTO 230
220 NEXT J
230 FOR I=1 TO 24
240  PRINT " "
250 NEXT I
260'----------------------------
270 ' Initial values for parameters
280'----------------------------
290 PRFMAX=0
300'-----------------------
310 '  data process
320'-----------------------
330 PN=FRE(1)+28+128+36
340 X=PEEK(PN)
350 PRINT "**********************************************"
360 PRINT " # of window   --- ",X
```

```
370 PRINT "*********************************************"
530  PN=PN+2
540  PRINT "window    left edge   right edge"
550 PRINT "---------------------------------------------"
560 X=X-1
570 FOR J=0 TO X
580   WN=PEEK(PN)
590   PN=PN+4
600  WL=PEEK(PN)
610  PN=PN+2
620  WR=PEEK(PN)
630   PRINT WN,WL,WR
640   PN=PN+2
650 NEXT J
660 '---------------------------
670 '  window select
680 '---------------------------
690 PRINT "------------------------------------------------"
700 PRINT "   Which window do you want to analyze?  "
710 PRINT "------------------------------------------------"
720 INPUT WNS
730 PNT=FRE(1)+28+128+36+2+8*(X+1)+2+512*4*WNS
740 '----------------------
750 '  Data
760 '----------------------
770 PRFMAX=1
780 FOR I=0 TO 511
790   PRF(I)=PEEK(PN,TL)
800    PNT=PNT+4
810 NEXT I
820 CLOSE #1
830 PRINT "**********************"
840 PRINT " Data loaded !!"
850 PRINT "**********************"
860 GCLR
870'-----------------------------------------
880 '   IBM  computer data transfer
890'-----------------------------------------
900 PRINT "====================================="
910  PRINT "    Is your IBM computer in operation (y/n)?  "
920 PRINT "====================================="
930  CD$=INKEY$
940   IF CD$="y" OR CD$="Y" THEN GOTO 960
950 GOTO 930
960  PRINT "--------------------------"
970  PRINT "  Start sending data to IBM "
980  PRINT "--------------------------"
990  FOR ID=0 TO 511
1000     RSPRINT ID,PRF(ID)
```

```
1010        FOR KK=0 TO 4
1020            PRINT " "
1030        NEXT KK
1040 NEXT ID
1050 PRINT "******************************"
1060 PRINT " Finish transfering Data!!"
1070 PRINT "******************************"
1080 RSPRINT "END"
1090 '-----------------------------------
1100 '    another window
1110 '-----------------------------------
1120 PRINT "---------------------------------------------------------"
1130 PRINT "   Do you want to analyze another window(y/n)?   "
1140 PRINT "---------------------------------------------------------"
1150 INPUT V$
1160    IF V$="Y" OR V$="y" THEN GOTO 300
1170 END
```

A.2.1.4. Program Name "TA Trans" in Macintosh Quick Basic(b)

This program works together with either "Bitrans.BAS" or "Mactrans.BAS" program in Hamamatsu C2280 TA.

```
'-------------------------------
' TA Data transfer program
'      7/17/91
'      6/23/92  modified
'            by Taki
'-------------------------------
DIM x$(2000)
INPUT " New Data File Name?  ",f$
   OPEN "COM1:9600,N,8,1,CS,DS,CD" AS #1
  OPEN f$ FOR OUTPUT AS #2
10 PRINT "-------------------"
   PRINT "  Ready to start(y/n)?"
   PRINT "-------------------"
     INPUT st$
     IF st$="y" OR st$="Y" THEN GOTO 20
  GOTO 10
20 '-------------------
    '  Raw Data transfer
    '-------------------
  FOR i=0 TO 2000
     INPUT #1,x$(i)
     IF MID$(x$(i),2,3)="END" THEN GOTO 30
    NEXT i
30   CLOSE #1
      n=i-1
  FOR i=0 TO n
    PRINT #2, x$(i)
  NEXT i
     CLOSE #2
END
```

A.2.1.5. Program Name 'TA.BAS" in IBM PC in GWBASIC

This program works together with either "Bitrans.BAS" or "IBM.BAS" program in Hamamatsu C2280 TA.

```
10'-----------------------------------------------------
20'    Trnafer program between TA and IBM
30'-----------------------------------------------------
40 OPEN "COM1:9600,N,8,1,CD,DS,CD" AS #1
50 INPUT "Inout your file Name = ",F$
60 OPEN F$ FOR OUTPUT AS #2
70 FOR I=0 TO 511
80  INPUT #1, X,Y
90  PRINT #2, X,Y
100 NEXT I
110 CLOSE
120 END
```

A.2.1.5. List out program "Prlist.BAS" in Hamamatsu C2280 TA

This program list-out any ASCII file format through RS232C printer connected to Hamamatsu C2280 TA. The files and Data are required to be converted to ASCII format before they are transferred to the printer.

```
10 '*****************************
20 '   list the program
30 '*****************************
40 PRINT "******************************************"
50 PRINT "    Program listout through RS-232C"
60 PRINT "******************************************"
70 PRINT "   Did you change File Type to Ascii?  "
80 INPUT "       (Y/N)    ",H$
90 IF H$="y" OR H$="Y" THEN GOTO 120
100 PRINT "&&&&&&  Please change the file type to ASCII using  &&&&&&"
110 PRINT "        SAVE 'FILE NAME', A   "
120 INPUT " Input program File name    =  ",F$
130 OPEN "I",#1,F$
140 M=1
150 RSPRINT CHR$(27)+"N"+CHR$(10);
160 RSPRINT "--------------------"
170 RSPRINT F$
180 RSPRINT "--------------------"
190 FOR I=0 TO 1000
200   LINE INPUT#1,X$
210   RSPRINT X$
220     IF EOF(1) THEN GOTO 250
230     GOSUB 270
240 NEXT I
250 CLOSE#1
260 END
270 ' SUBROUTINE
280   FOR J=1 TO 50
290     PRINT "  "
300   NEXT J
310 M=M+1
320 RETURN
```

A.2.2. Data analysis programs

To analyze streak images on TA, following programs enable to investigate various parameter from the streak image directly. For the analysis, rise and fall times with several components are first important parameter to be extracted from the time-resolved PL spectra saved in TA. Spectral fit using Fermi's Golden rule for time-resolved PL spectra for a semiconductor is important to extract carrier and exciton temperatures at a delay time.

A.2.2.1 "Fit.BAS" for Hamamatsu C2280 TA

This program enable to read binary data saved in a floppy disk and analyze spectral and temporal features of the image. Within the program, the data can be smoothed using FFT frequency filtering, the streak speed non-linearity is corrected, spectral sensitivity distribution is corrected, carrier temperature is extracted, and rise and fall times with several components are determined. The fit is done by eye. The procedure will be repeated until the calculated curve fits to the data.

```
10 '****************************************
20 ' TA profile Data Fitting Program
30 '                    900322 by Taki
40 '****************************************
50 FOR I=0 TO 24
60   PRINT " "
70 NEXT I
80 PRINT "**********************************************"
90 PRINT " TA Profile Data Fitting Program"
100 PRINT "            by Taki "
110 PRINT " "
120 PRINT "   You can    1.load  "
130 PRINT "               2.smooth "
140 PRINT "               3.axes calibration"
150 PRINT "               4.intensity normalization"
160 PRINT "               5.intensity calibration"
```

```
170 PRINT "                    6.Curve Fitting"
180 PRINT "                    8.save to floppy disk"
190 PRINT "*********************************************"
200 DIM PRF(600),PRFL(600),Y(600),FC(600),FL(600),XPRF(600)
210 DIM DF(600),R(600),XR(600),GM(600),XGM(600)
220 FREE
230 ALLOC &H12000&
240 GCLR
250 INPUT "Input your Data File Name ?     ",F$
260 OPEN "DI",#1,F$
270     PNT=FRE(1)
280 PRINT "--------------------------------------------"
290 PRINT "   Following Data are: Spectrum(S)"
300 PRINT "                       Time (T)"
310 PRINT "--------------------------------------------"
320 INPUT DS$
330 '--------------------
340 '  Data direct read from floppy disk
350 '--------------------------
360 FOR J=1 TO 600
370     DIRECT READ #1,PNT
380     PNT=PNT+128
390 IF EOF(1) THEN GOTO 410
400 NEXT J
410 FOR I=1 TO 24
420   PRINT " "
430 NEXT I
440 '--------------------
450 ' Initial values for parameters
460 '--------------------
470 KB=8.61735E-05
480 PRFMAX=0
490 T0=1
500 A1=1
510 A2=0
520 A3=0
530 SW=0
540 SL=1
550 AX$="s"
560 IA=1
570 IB=0
580 IC=0
590 G=0
600 '----------------------------
610 '  data process
620 '--------------------------
630 PN=FRE(1)+28+128+36
640 X=PEEK(PN)
650 PRINT "*********************************************"
```

```
660 PRINT " # of window  — ",X
670 PRINT "*********************************************"
680  PN=PN+2
690  PRINT "window    left edge   right edge"
700  PRINT "--------------------------------"
710 X=X-1
720 FOR J=0 TO X
730   WN=PEEK(PN)
740   PN=PN+4
750  WL=PEEK(PN)
760  PN=PN+2
770  WR=PEEK(PN)
780   PRINT WN,WL,WR
790   PN=PN+2
800 NEXT J
810 '---------------------------
820 '  window select
830 '---------------------------
840 PRINT "--------------------------------------------------"
850 PRINT "   Which window do you want to analyze?  "
860 PRINT "--------------------------------------------------"
870 INPUT WNS
880 PNT=FRE(1)+28+128+36+2+8*(X+1)+2+512*4*WNS
890 '-------------------------
900 '  Data
910 '-------------------------
920 FOR I=0 TO 511
930   PRF(I)=PEEK(PNT,L)
940    IF PRF(I)<1 THEN PRF(I)=1
950   IF PRF(I)>PRFMAX THEN PRFMAX=PRF(I)
960    PRFL(I)=LOG(PRF(I))
970    PNT=PNT+4
980 NEXT I
990 CLOSE #1
1000 PRINT "**********************"
1010 PRINT " Data loaded !!"
1020 PRINT "************************"
1030 '-----------------------
1040 '  Monitor profile
1050 '-----------------------
1060  GOSUB 3440
1070 PRINT "--------------------------------------------------"
1080 PRINT "    Do you need to smooth the data(y/n)??"
1090 PRINT "--------------------------------------------------"
1100 INPUT AA$
1110  IF AA$="y" OR AA$="Y" THEN GOTO 1130
1120   GOTO 1210
1130   '---------- FFT noise reduction -----------
1140   CFFT PRF,XPRF
```

```
1150    FOR II=30 TO 482
1160          PRF(II)=0
1170          XPRF(II)=0
1180    NEXT II
1190  IFFT PRF,XPRF
1200 GOSUB 3440
1210 FOR I=1 TO 24
1220  PRINT " "
1230 NEXT I
1240 '------------------
1250 '  Data selection
1260 '------------------
1270  IF DS$="S" OR DS$="s" THEN GOTO 1780
1280 '----------------------
1290 '  data search
1300 '----------------------
1310 PRINT "---------------------------"
1320 PRINT "  Data Search : 6 -- Move right"
1330 PRINT "                4 -- Move left "
1340 PRINT "                7 -- Jump left"
1350 PRINT "                9 -- Jump right"
1360 PRINT "              e/E -- End "
1370 PRINT "---------------------------"
1380  X2=250
1390    B$=INKEY$
1400    LINE X2+64,0,X2+64,399
1410     IF B$="6" THEN GOTO 1470
1420     IF B$="4" THEN GOTO 1540
1430     IF B$="7" THEN GOTO 1610
1440     IF B$="9" THEN GOTO 1680
1450    IF B$="e" OR A$="E" THEN GOTO 1780
1460 GOTO 1390
1470      LINE X2+65,0,X2+65,399
1480      LINE X2+64,0,X2+64,399,0
1490     Y(X2-1)=350-PRF(X2-1)*256/PRFMAX
1500     Y(X2)=350-PRF(X2)*256/PRFMAX
1510       LINE X2+63,Y(X2-1),X2+64,Y(X2)
1520     X2=X2+1
1530 GOTO 1740
1540       LINE X2-1+64,0,X2-1+64,399
1550       LINE X2+64,0,X2+64,399,0
1560      Y(X2+1)=350-PRF(X2+1)*256/PRFMAX
1570     Y(X2)=350-PRF(X2)*256/PRFMAX
1580       LINE X2+65,Y(X2+1),X2+64,Y(X2)
1590    X2=X2-1
1600 GOTO 1740
1610      LINE X2+54,0,X2+54,399
1620      LINE X2+64,0,X2+64,399,0
1630       Y(X2+1)=350-PRF(X2+1)*256/PRFMAX
```

```
1640      Y(X2)=350-PRF(X2)*256/PRFMAX
1650       LINE X2+65,Y(X2+1),X2+64,Y(X2)
1660       X2=X2-10
1670 GOTO 1740
1680      LINE X2+74,0,X2+74,399
1690      LINE X2+64,0,X2+64,399,0
1700      Y(X2-1)=350-PRF(X2-1)*256/PRFMAX
1710     Y(X2)=350-PRF(X2)*256/PRFMAX
1720      LINE X2+63,Y(X2-1),X2+64,Y(X2)
1730      X2=X2+10
1740  PRINT X2,PRF(X2)
1750   LOCATE 15,2
1760   OPRINT "X=",X2
1770 GOTO 1390
1780'-----------------------------
1790 '  Axis linearity calibration
1800'-----------------------------
1810 PRINT "*************************************************"
1820 PRINT "   Axis calibration "
1830 PRINT "*************************************************"
1840 INPUT "Do you need to calibrate the axis(y/n)?  ",AX$
1850   IF AX$="n" OR AX$="N" THEN GOTO 2070
1860  IF DS$="T" OR DS$="t" THEN GOTO 1890
1870  IF DS$="S" OR DS$="s" THEN GOTO 1990
1880 GOTO 1840
1890PRINT "-----------------------------------------"
1900 PRINT "    Input Streak linearity curve "
1910 PRINT "              y(x)=a+bx+cx^2"
1920PRINT "-----------------------------------------"
1930INPUT "(a,b,c)",A1,A2,A3
1940     T0=A1*512+A2/2*(512^2)+A3/3*(512^3)
1950    FOR I=0 TO 511
1960          PRF(I)=PRF(I)*T0/(A1+A2*I+A3*I^2)
1970    NEXT I
1980  GOTO 2070
1990PRINT "-------------------------------"
2000 PRINT "   wavelength = sw + cr*x"
2010 PRINT "  "
2020 PRINT "  Input Sw ( Starting wavelength (nm))"
2030  PRINT "      SL (slope  (nm/ch)  )"
2040PRINT "-------------------------------"
2050 INPUT "Sw  =   ",SW
2060 INPUT "SL  =   ",SL
2070 FOR I=1 TO 24
2080  PRINT " "
2090 NEXT I
2100'-----------------------------
2110 '   Intensity calibration
2120'-----------------------------
```

```
2130 PRINT "--------------------------------------------------------"
2140 PRINT "Do you need to calibrate intensity(y/n) ?  "
2150 PRINT "--------------------------------------------------------"
2160 INPUT c$
2170   IF c$="N" OR c$="n" THEN GOTO 2280
2180 PRINT "----------------------------------------------"
2190 PRINT "   Input intensity Calibration curve"
2200 PRINT "       y=a + bx + cX^2"
2210 PRINT "----------------------------------------------"
2220 INPUT "(a,b,c)",IA,IB,IC
2230 FOR I=0 TO 511
2240 IF IA=0 AND IB=0 THEN GOTO 2280
2250   XX=SW+SL*I
2260     PRF(I)=PRF(I)/(IA+IB*XX+IC*XX^2)
2270  NEXT I
2280    FOR I=1 TO 24
2290      PRINT " "
2300    NEXT I
2310 GOSUB 3440
2320 '------------------------------------
2330 '  Switch to Logarithmic
2340 '------------------------------------
2350 PRINT "----------------------------------------------------------------------"
2360 PRINT "Do you want to monitor the data in log scale(y/n) ?  "
2370 PRINT "----------------------------------------------------------------------"
2380 INPUT G$
2390   IF G$="Y" OR G$="y" THEN G=1
2400       IF G$="Y" OR G$="y" THEN GOSUB 3440
2410  G=0
2420 '------------------------------------------------
2430 '  Curve Fitting
2440 '------------------------------------------------
2450   IF DS$="t" OR DS$="T" THEN GOTO 3020
2460 PRINT "****************************************************"
2470 PRINT "   Spectrum Fitting Curves"
2480 PRINT "****************************************************"
2490 INPUT "Starting wavelength (nm) = ",SW
2500 INPUT "Slope          (nm/ch) = ",SL
2510 INPUT " Electron Temp. (K)    = ",TE
2520 INPUT " Lattice Temp.  (K)    = ",TL
2530 INPUT " Ferm Energy Level (eV) = ",EF
2540 INPUT " Elh - Ehh  (eV)  = ", DE
2550 INPUT " Gamma (Broadening)    =",GA
2560  A=KB*TE
2570  B=KB*TL
2580 PRINT "*********************************"
2590 PRINT "  Calculating the spectrum"
2600 PRINT "*********************************"
2610 FOR J=0 TO 511
```

```
2620  EE=1239.9/(SW+SL*J)
2630 R1=.79659*EE/TE*EXP(-.62*(EE-1.5768)/A)
2640  R2=R1/(1+EXP((.378*(EE-1.5768)-EF)/B))
2650  R3=EE/TE*EXP(-.76*(EE-1.6149)/A)
2660  R4=R3/(1+EXP((.232*(EE-1.6149)-(EF-DE))/B))
2661 IF EE<1.5768 THEN c=0 ELSE c=1
2662 IF EE<1.6149 THEN D=0 ELSE D=1
2670 R(J)=c*R2+D*R4
2680  GM(J)=GA/(EE^2+GA^2)
2690 NEXT J
2700 GOSUB 3440
2710 CURVE R,,X,64,350
2720 LOCATE 20,2
2730 OPRINT "Te =",TE
2740 LOCATE 20,3
2750 OPRINT "Tl =",TL
2760 LOCATE 20,4
2770 OPRINT "Ef =",EF
2780 LOCATE 20,5
2790 OPRINT "gamma=",GA
2791 LOCATE 2,11
2792 OPRINT "SW =",SW
2793 LOCATE 2,12
2794 OPRINT "SL =",SL
2800'---------------------------------
2810 '  Convolusion of broadening
2820'---------------------------------
2830 PRINT "**********************************"
2840 PRINT "  Comvoluting the broadening"
2850 PRINT "**********************************"
2860 CFFT R,XR
2870 CFFT GM,XGM
2880 FOR J=0 TO 511
2890  R(J)=R(J)*GM(J)-XR(J)*XGM(J)
2900  XR(J)=R(J)*XGM(J)+XR(J)*GM(J)
2910 NEXT J
2920 IFFT R,XR
2930 CURVE R,,X,64,350
2940 PRINT "----------------------------------------------"
2950 PRINT "  Do you want to trya gain (Y/n)  "
2960 PRINT "----------------------------------------------"
2970 INPUT H$
2980 IF H$="y" OR H$="Y" THEN GOTO 2460
2990 GOTO 3350
2991'----------------------------------------------
3000'  (1+R-exp(-t/A)-Rexp(-t/B)){Cexp(-t/D)+exp(-t/E)}/(C+1)
3010'---------------------------------
3020  PRINT "*******************************************************"
3030 PRINT "      Fitting the data with "
```

```
3040 PRINT " (1+R-exp(-t/A)-Rexp(-t/B))
                              •{Cexp(-t/D)+exp(-t/E)}/(C+1)/(1+R)"
3050 PRINT "*****************************************************"
3060 INPUT "Rising Components (A,R,B) = ",B0,R0,B1
3070 INPUT "Decay Components (C,D,E) = ",B2,B3,B4
3080      IF B3=0 THEN B2=.000001
3090      IF B4=0 THEN B3=.000001
3100 FOR I=0 TO 511-X2 STEP 3
3110 FCC=(1+R0-EXP(-1*I/B0)-R0*EXP(-1*I/B1))
                        *(B2*EXP(-1/B3*I)+EXP(-1/B4*I))
3111 FC(I)=FCC/(1+R0)/(c+1)
3120 FC(I+1)=FC(I)
3130 FC(I+2)=FC(I)
3140 NEXT I
3150 GOSUB 3440
3160 CURVE FC,,X,64 +X2,350
3170 LOCATE 17,1
3180 OPRINT "A=",B0
3190 LOCATE 17,2
3200 OPRINT "R=",R0
3210 LOCATE 17,3
3220 OPRINT "B=",B1
3230 LOCATE 17,4
3240 OPRINT "C=",B2
3250 LOCATE 17,5
3260 OPRINT "D=",B3
3270 LOCATE 17,6
3280 OPRINT "E=",B4
3290 PRINT "--------------------------------"
3300 PRINT " Do you want to try again (y/n)? "
3310 PRINT "--------------------------------"
3320 INPUT D$
3330 IF D$="n" OR D$="N" THEN GOTO 3380
3340 GOTO 2420
3350 '-----------------------------------
3360 '  another window
3370 '-----------------------------------
3380 PRINT "------------------------------------------"
3390 PRINT " Do you want to analyze another window(y/n)? "
3400 PRINT "------------------------------------------"
3410 INPUT E$
3420   IF E$="Y" OR E$="y" THEN GOTO 600
3430 END
3440 '--------------------------
3450 ' Monitor profile
3460 '--------------------------
3470 GCLR
3480 LINE X2+64,50,X2+64,350
3490 IF G=1 THEN GOTO 3610
```

```
3500 CURVE PRF,,X,64,350
3510  LOCATE 10,15
3520 OPRINT "T i m e / Spectrum"
3530 LOCATE 5,1
3540 OPRINT "Intensity"
3550    LOCATE 12,18
3560    OPRINT F$
3570 GOTO 3680
3580 '-----------------------------
3590 '   LOG plot
3600 '---------------------------
3610  CURVE PRFL,,X,64,350
3620  LOCATE 10,15
3630  OPRINT "T i m e / spectrum"
3640  LOCATE 5,1
3650  OPRINT "L o g (Int.)"
3660    LOCATE 12,18
3670    OPRINT F$
3680  RETURN
```

A.2.2.2. Spectrum Fitting Program "Specfit.BAS" in Hamamatsu C2280 TA

This program operates similar as Fit.BAS program except that the spectrum fitting is for QW structures. The program can be extensively used for externally strained MQW analysis.

```
10 '************************************************************
20 '   Spectrum fitting using Fermi's Golden Rule in QW
30 '
40 '                  900322 by Taki
50 '              modified 920512 by Taki
60 '************************************************************
70 FOR I=0 TO 24
80   PRINT " "
90 NEXT I
100 PRINT "*********************************************"
110 PRINT " Spectrum Fitting Program"
120 PRINT "          by Taki "
130 PRINT " "
140 PRINT "   You can    1.load  "
150 PRINT "              2.smooth "
160 PRINT "              3.Sensitivity calibration"
170 PRINT "              4.intensity normalization"
180 PRINT "              5.intensity calibration"
190 PRINT "              6.Curve Fitting"
200 PRINT "              8.save to floppy disk"
210 PRINT "*********************************************"
220 DIM PRF(600),PRFL(600),Y(600),FC(600),FL(600),XPRF(600)
230 DIM DF(600),R(600),XR(600),GM(600),XGM(600),WWL(600)
240 DIM EE(600),R2(600),R4(600),R6(600),R8(600)
250 DIM RR(600)
260 FREE
270 ALLOC &H12000&
280 GCLR
290'-----------------------------
300 INPUT "Input your Data File Name ?    ",F$
310PRINT"--------------------------"
320 PRINT " Spectral Information"
330PRINT"--------------------------"
340 INPUT " Wavelength at 0 (ch) = ",SW
350 INPUT " Dispersion (nm/ch) = ",SL
360 '--------
370 SW=866.93
380 SL=-.16953
390 '---------
```

```
400  PRINT "**********************************************"
410 PRINT " Sample & Experimental Conditions"
420  PRINT "**********************************************"
430 INPUT "Quantum Well Width (A) = ",LZ
440         LZ=LZ*1E-10
450 INPUT "External Stress   (kbar)= ",EX
460 INPUT "Photoexcitaion Density  = ",DN
470 OPEN "DI",#1,F$
480   PNT=FRE(1)
490'---------------------------------------
500 '  Data direct read from floppy disk
510'---------------------------------------
520 FOR J=1 TO 600
530     DIRECT READ #1,PNT
540     PNT=PNT+128
550 IF EOF(1) THEN GOTO 570
560 NEXT J
570 FOR I=1 TO 24
580   PRINT " "
590 NEXT I
600 '--------------------
610 ' Initial values for parameters
620 '--------------------
630 H=6.64E-34
640 PI=3.14159
650 E=1.6092E-19
660 C=2.9987E+08
670 !=8.85E-12
680 KB=8.61735E-05    : ' kb=kb/e
690 M0=9.11E-31
700 ME=.067*M0
710 '  GOTO 740
720 MLH=.087*M0
730 MHH=.62*M0
740 '  MLH=0.62*M0
750 '  MHH=0.087*M0
760 GX=1.2929
770 FX=.5858
780  PRFMAX=0
790  G=0
800'----------------------------------------------------
810 IA=-1.7769E+07: IB=117790! :  IC=-312.23  :  ID=.41369
820 IE=-2.7399E-04 : IFF=7.2575E-08
830'----------------------------------------------------
840 '  data process
850 '--------------------------
860 PN=FRE(1)+28+128+36
870 X=PEEK(PN)
880 PRINT "**********************************************"
```

```
890 PRINT " # of window   — ",X
900 PRINT "*********************************************"
910  PN=PN+2
920  PRINT "window    left edge   right edge"
930 PRINT "-----------------------------------------"
940 X=X-1
950 FOR J=0 TO X
960   WN=PEEK(PN)
970   PN=PN+4
980  WL=PEEK(PN)
990  PN=PN+2
1000  WR=PEEK(PN)
1010   PRINT WN,WL,WR
1020   PN=PN+2
1030 NEXT J
1040 '----------------------------
1050 '  window select
1060 '----------------------------
1070 PRINT "-----------------------------------------------------"
1080 PRINT "   Which window do you want to analyze?  "
1090 PRINT "-----------------------------------------------------"
1100 INPUT WNS
1110 PNT=FRE(1)+28+128+36+2+8*(X+1)+2+512*4*WNS
1120 '--------------------------
1130 '  Data read & Spectral calibration
1140 '--------------------------
1150 FOR I=0 TO 511
1160    WWL(I)=SW+SL*I
1170       EE(I)=1239.85/WWL(I)
1180    CF=IA+IB*WWL(I)+IC*WWL(I)^2+ID*WWL(I)^3
           +IE*WWL(I)^4+IFF*WWL(I)^5
1190   PRF(I)=PEEK(PNT,L)*CF
1200    IF PRF(I)<1 THEN PRF(I)=1
1210   IF PRF(I)>PRFMAX THEN PRFMAX=PRF(I)
1220   ' PRFL(I)=LOG(PRF(I))
1230   PNT=PNT+4
1240 NEXT I
1250 CLOSE #1
1260 PRINT "**********************"
1270 PRINT " Data loaded !!"
1280 PRINT "************************"
1290 '---------------------
1300 '  Monitor profile
1310 '---------------------
1320  GOSUB 3970
1330 GOTO 2110
1340 PRINT "-----------------------------------------"
1350 PRINT "    Do you need to smooth the data(y/n)??"
1360 PRINT "-----------------------------------------"
```

```
1370 INPUT AA$
1380  IF AA$="y" OR AA$="Y" THEN GOTO 1400
1390   GOTO 1480
1400   '---------- FFT noise reduction -----------
1410   CFFT PRF,XPRF
1420    FOR II=30 TO 482
1430          PRF(II)=0
1440          XPRF(II)=0
1450    NEXT II
1460  IFFT PRF,XPRF
1470 GOSUB 3970
1480 FOR I=1 TO 24
1490  PRINT " "
1500 NEXT I
1510 '------------------------
1520 '  data search
1530 '------------------------
1540 PRINT "-----------------------------------"
1550 PRINT "  Data Search : 6 -- Move right"
1560 PRINT "                4 -- Move left "
1570 PRINT "                7 -- Jump left"
1580 PRINT "                9 -- Jump right"
1590 PRINT "                e/E -- End "
1600 PRINT "----------------------------"
1610  X2=250
1620    B$=INKEY$
1630    LINE X2+64,0,X2+64,399
1640     IF B$="6" THEN GOTO 1700
1650     IF B$="4" THEN GOTO 1770
1660     IF B$="7" THEN GOTO 1840
1670     IF B$="9" THEN GOTO 1910
1680     IF B$="e" OR A$="E" THEN GOTO 2010
1690 GOTO 1620
1700       LINE X2+65,0,X2+65,399
1710       LINE X2+64,0,X2+64,399,0
1720      Y(X2-1)=350-PRF(X2-1)*256/PRFMAX
1730      Y(X2)=350-PRF(X2)*256/PRFMAX
1740        LINE X2+63,Y(X2-1),X2+64,Y(X2)
1750      X2=X2+1
1760 GOTO 1970
1770        LINE X2-1+64,0,X2-1+64,399
1780        LINE X2+64,0,X2+64,399,0
1790       Y(X2+1)=350-PRF(X2+1)*256/PRFMAX
1800      Y(X2)=350-PRF(X2)*256/PRFMAX
1810        LINE X2+65,Y(X2+1),X2+64,Y(X2)
1820     X2=X2-1
1830 GOTO 1970
1840       LINE X2+54,0,X2+54,399
1850       LINE X2+64,0,X2+64,399,0
```

```
1860       Y(X2+1)=350-PRF(X2+1)*256/PRFMAX
1870       Y(X2)=350-PRF(X2)*256/PRFMAX
1880        LINE X2+65,Y(X2+1),X2+64,Y(X2)
1890        X2=X2-10
1900 GOTO 1970
1910       LINE X2+74,0,X2+74,399
1920       LINE X2+64,0,X2+64,399,0
1930       Y(X2-1)=350-PRF(X2-1)*256/PRFMAX
1940      Y(X2)=350-PRF(X2)*256/PRFMAX
1950       LINE X2+63,Y(X2-1),X2+64,Y(X2)
1960      X2=X2+10
1970   PRINT WWL(X2),PRF(X2)
1980    LOCATE 15,2
1990    OPRINT "X=",X2
2000 GOTO 1620
2010'--------------------------
2020 '  Switch to Logarithmic
2030'--------------------------
2040 PRINT "--------------------------------------------------------"
2050  PRINT "Do you want to monitor the data in log scale(y/n) ?  "
2060 PRINT "--------------------------------------------------------"
2070 INPUT G$
2080    IF G$="Y" OR G$="y" THEN G=1
2090   IF G$="Y" OR G$="y" THEN GOSUB 4110
2100  G=0
2110'----------------------------------
2120 '  Curve Fitting
2130'-------------------------------------
2140 PRINT "**************************************************"
2150 PRINT "   Spectrum Fitting Curves"
2160 PRINT "**************************************************"
2170 INPUT " Electron Temp. (K)    = ",TE
2180 INPUT " Lattice Temp.  (K)    = ",TL
2190 INPUT " LH Temp. (K)          = ",TLH
2200 INPUT " HH Temp. (K)          = ",THH
2210 INPUT " Quasi-Fermi E in VB (meV) = ",EFV
2220         EFV=EFV*.001
2230 INPUT " Gamma (Broadening) (meV)   =",GA
2240         GA=GA*.001
2250   ETE=KB*TE
2260   ETL=KB*TL
2270   ETLH=KB*TLH
2280   ETHH=KB*THH
2290   PP=LOG(DN)+2*LOG(H)-LOG(4*PI)
                 +LOG(LZ)-LOG(2)-LOG(ME)-LOG(ETE*E)
2300   PPP=EXP(PP)
2310 EFE=ETE*LOG(EXP(PPP)-1)
2320'---------------------
2330 ' Stress Effects
```

```
2340 '------------------------
2350 ELH1=1.492+.00453*EX    : '11LH transitio
2360 EHH1=1.498+.000267*EX   : '11HH
2370 EHH2=1.521+.000267*EX   : '13HH
2380 EHH3=1.541+.000267*EX   : '22HH
2390 ESO=1.78+.00453*EX
2400 IF ELH1<EHH1 THEN MV=MLH ELSE MV=MHH
2410 IF ELH1<EHH1 THEN EG=ELH1 ELSE EG=EHH1
2420    DD1=.0351
2430#=ELH1-EG
24400#=EHH1-EG
245000#=EHH2-EG
2460000#=EHH3-EG
2470 MR=ME*MV/(ME+MV)
2480 RI=SQR(15.32+.46*(GX-4*EG/(ESO-EG)*(FX-(EG/ESO^1.5))*EX))
2490 MB=EG*ESO/(EG+2/3*(ESO-EG))
2500 W0=4*PI^2*RI*E^2*MB/(3*ME*E0*H^4*C^3*LZ)
2510 PRINT "*********************************"
2520 PRINT " Calculating the spectrum"
2530 PRINT "*********************************"
2540 MR=ME*MLH/(ME+MLH)
2550 FOR J=0 TO 511
2560    IF EE(J)<ELH1 THEN GOTO 2620
2570   EC=MR/ME*(EE(J)-ELH1)
2580   EV=MR/MLH*(EE(J)-ELH1)
2590  R1=W0*MR*EE(J)/(1+EXP((EC-EFE)/ETE))
2600  R2(J)=R1/(1+EXP((EV-EFV+D0)/ETLH))
2610 GOTO 2630
2620   R2(J)=0
2630 NEXT J
2640 MR=ME*MHH/(ME+MHH)
2650 FOR J=0 TO 511
2660    IF EE(J)<EHH1 THEN GOTO 2720
2670   EC=MR/ME*(EE(J)-EHH1)
2680   EV=MR/MHH*(EE(J)-EHH1)
2690  R3=W0*MR*EE(J)/(1+EXP((EC-EFE)/ETE))
2700  R4(J)=R3/(1+EXP((EV-EFV+D1)/ETHH))
2710 GOTO 2730
2720   R4(J)=0
2730 NEXT J
2740  FOR J=0 TO 511
2750   IF EE(J)<EHH2 THEN GOTO 2810
2760      EC=MR/ME*(EE(J)-EHH2)
2770      EV=MR/MHH*(EE(J)-EHH2)
2780  R5=W0*MR*EE(J)/(1+EXP((EC-EFE)/ETE))
2790  R6(J)=R5/(1+EXP((EV-EFV+D2)/ETHH))
2800 GOTO 2820
2810 R6(J)=0
2820 NEXT J
```

```
2830 MR=ME*MHH/(ME+MHH)
2840 FOR J=0 TO 511
2850  IF EE(J)<EHH3 THEN GOTO 2910
2860   EC=MR/ME*(EE(J)-EHH3)
2870   EV=MR/MLH*(EE(J)-EHH3)
2880  R7=W0*MR*EE(J)/(1+EXP((EC-EFE+DD1)/ETE))
2890  R8(J)=R7/(1+EXP((EV-EFV+D3)/ETHH))
2900 GOTO 2920
2910  R8(J)=0
2920 NEXT J
2930 FOR J=0 TO 511
2940   R(J)=R2(J)+R4(J)+R6(J)+R8(J)
2950   XR(J)=0
2960  GM(J)=GA/((EE(J)-EE(255))^2+GA^2)/PI
2970   XGM(J)=0
2980  NEXT J
2990 GOSUB 3970
3000 ' CURVE R,,X,64,350
3010 'CURVE GM,,X,64,350
3020 LOCATE 5,2
3030 OPRINT "Te ="
3040 LOCATE 10,2
3050 OPRINT TE
3060 LOCATE 20,2
3070 OPRINT "Tl ="
3080 LOCATE 25,2
3090 OPRINT TL
3100 LOCATE 5,3
3110 OPRINT "Thh ="
3120 LOCATE 10,3
3130 OPRINT THH
3140 LOCATE 20,3
3150 OPRINT "Tlh ="
3160 LOCATE 25,3
3170 OPRINT TLH
3180 LOCATE 5,4
3190 OPRINT "Efc ="
3200 LOCATE 10,4
3210 OPRINT EFE
3220 LOCATE 20,4
3230 OPRINT "Efv ="
3240 LOCATE 25,4
3250 OPRINT EFV
3260 LOCATE 20,5
3270 OPRINT "gamma="
3280 LOCATE 26,5
3290 OPRINT GA
3300 GOTO 3350
3310 LOCATE 2,11
```

```
3320 OPRINT "SW =",SW
3330 LOCATE 2,12
3340 OPRINT "SL =",SL
3350 '-----------------------------------
3360 '  Convolusion of broadening
3370 '-----------------------------------
3380 PRINT "**********************************"
3390 PRINT "  Comvoluting the broadening"
3400 PRINT "**********************************"
3410 CFFT R,XR
3420 CFFT GM,XGM
3430 FOR J=0 TO 511
3440   RR(J)=R(J)*GM(J)-XR(J)*XGM(J)
3450   XR(J)=R(J)*XGM(J)+XR(J)*GM(J)
3460 NEXT J
3470 IFFT RR,XR
3480 FOR J=0 TO 511
3490   IF J<256 THEN R(J)=RR(J+256)
3500   IF J>255 THEN R(J)=RR(J-255)
3510 NEXT J
3520 CURVE R,,X,64,350
3530 PRINT "-----------------------------------"
3540 PRINT "   Do you want to shift the curve(y/n)?"
3550 PRINT "-----------------------------------"
3560 INPUT SHH$
3570   IF SHH$="n" OR SHH$="N" THEN GOTO 3710
3580 INPUT " Amount of shift (Neg. -- Left, Pos. -- Right) = ",SH
3590 IF SH<0 THEN GOTO 3640
3600 FOR J=0 TO 511
3610   IF J<SH THEN RR(J)=0 ELSE RR(J)=R(J-SH)
3620 NEXT J
3630 GOTO 3710
3640 FOR J=0 TO 511
3650   IF J>511+SH THEN RR(J)=0 ELSE RR(J)=R(J-SH)
3660 NEXT J
3670 INPUT "Curve Normalize Factor (the larger the NF, smaller the peak) = ",G
3680 CURVE RR,G,X,64,350
3690 INPUT"Chabge the NF, again(Y/n)PRINT ",GA$
3700   IF GA$="y" OR GA$="Y" THEN GOTO 3670
3710 PRINT "-----------------------------------"
3720 PRINT "  Do you want to try, again (Y/n)PRINT  "
3730 PRINT "-----------------------------------"
3740 INPUT H$
3750 IF H$="y" OR H$="Y" THEN GOTO 2140
3760 '----------------------------
3770 '  save data to floppy disk
3780 '----------------------------
3790 INPUT "Do you want to save the analyzed data into FD (y/n) ?",SV$
3800 IF SV$="N" OR SV$="n" THEN GOTO 3880
```

```
3810 '----------------
3820 INPUT "New File Name (*.dat) =    ",FF$
3830 OPEN "O",#2,FF$
3840 FOR I=0 TO 511
3850   PRINT #2,EE(I),PRF(I),R(I)
3860 NEXT I
3870 CLOSE #2
3880 '------------------------------------
3890 '    another window
3900 '------------------------------------
3910 PRINT "------------------------------------------------------------"
3920 PRINT "   Do you want to analyze another window(y/n)?   "
3930 PRINT "------------------------------------------------------------"
3940 INPUT E$
3950    IF E$="Y" OR E$="y" THEN GOTO 830
3960 END
3970 '----------------------------
3980 '   Monitor profile
3990 '----------------------------
4000 GCLR
4010 LINE X2+64,50,X2+64,350
4020 IF G=1 THEN GOTO 4140
4030 CURVE PRF,,X,64,350
4040  LOCATE 14,15
4050  OPRINT "Wavelength "
4060 LOCATE 5,1
4070 OPRINT "Intensity"
4080    LOCATE 12,18
4090    OPRINT F$
4100 GOTO 4210
4110 '----------------------------
4120 '   LOG plot
4130 '--------------------------
4140  CURVE PRFL,,X,64,350
4150  LOCATE 10,15
4160 OPRINT "Wavelength"
4170  LOCATE 5,1
4180  OPRINT "L o g (Int.)"
4190    LOCATE 12,18
4200    OPRINT F$
4210 END
```

A.2.2.3. Average carrier energy analysis program "Avee.BAS" in Hamamatsu C2280 TA

This program enables to analyze an average carrier or exciton energy and an integrated PL profile as function of delay time.

```
10'-----------------------------------------------
20 '   Average energy analysing program
30 '
40 '                    3/16/92
50 '              Taki
60'-----------------------------------------------
70 DIM AE(600)P,PD(600)
80 IOPEN 0
90 GCLR
100 X0=65
110 PRINT "-----------------------------------------"
120 PRINT "  Input left and right cursols"
130 PRINT "------------------------------------"
140 INPUT "(Left, Right) =  ", LC, RC
150 LC=LC+X0
160 RC=RC+X0
170 LINE LC,0,LC,511
180 LINE RC,0,RC,511
190 PRINT "-------------------------------------------"
200 PRINT  " Do you need to adjust the cursols(y/n)?"
210 PRINT "-------------------------------------------"
220 INPUT B$
230  IF B$="n" OR B$="N" THEN GOTO 490
240 PRINT "****************************************"
250 PRINT "  Left Cursol "
260 PRINT "     4  (left)      6 (right) "
270 PRINT "             e  (end)"
280 PRINT "****************************************"
290    LINE LC,0,LC,511,0
300 A$=INKEY$
310    IF A$="4" THEN LC=LC-1
320    IF A$="6" THEN LC=LC+1
330  LINE LC,0,LC,511
340    IF A$="e" OR A$="E" THEN GOTO 360
350 GOTO 290
360 PRINT "****************************************"
370 PRINT "  Right Cursol"
380 PRINT "    4  (Left)       6(Right) "
390 PRINT "             e (end)"
400 PRINT "****************************************"
410 A$="b"
```

```
420  LINE RC,0,RC,511,0
430 A$=INKEY$
440   IF A$="4" THEN RC=RC-1
450   IF A$="6" THEN RC=RC+1
460  LINE RC,0,RC,511
470  IF A$="e" OR A$="E" THEN GOTO 490
480 GOTO 420
490 '--------------------------------------
500 '   Energy Averaging
510 '-------------------------
520 NN=479
530 PRINT "****************************************"
540 PRINT "   Analysis Time Window "
550 PRINT "       from mm (ch) to nn (ch)<479 ?"
560 PRINT "****************************************"
570 INPUT " (mm ,NN ) =  ",MM,NN
580 PRINT "--------------------------"
590 PRINT " Input Calibration Curve"
600 PRINT "   W = W0 - dw*x(ch)"
610 PRINT "--------------------------"
620 INPUT "(W0, dw )",W0,dw
630 PRINT "**************************************************"
640 PRINT "  Do you want to: "
650 PRINT "          print-out the data (P)? "
660 PRINT "       or  save the data to FD(F)? "
670 PRINT "**************************************************"
680 INPUT S$
690 IF S$="F" OR S$="f" THEN GOTO 810
700 INPUT "Are you ready for print(y/n) ?  ",PR$
710 IF PR$="n" OR PR$="N" THEN GOTO 700
720 RSPRINT "**********************************************************"
730 RSPRINT "   Average Energy Relaxation Process "
740 RSPRINT "**********************************************************"
750 RSPRINT " "
760 RSPRINT " Window Position (Left, Right) =  ",LC-X0, RC-X0
770 RSPRINT "  "
780 RSPRINT "Channel  Average Energy (eV) Intensity "
790 RSPRINT "----------------------------------------------"
800 GOTO 850
810 PRINT "-----------------------"
820 PRINT "  New File Name "
830 PRINT "-----------------------"
840 INPUT FD$
850 FOR J=MM TO NN
860  P=0
870 PW=0
880 LINE X0, 0,X0+511,0
890 FOR I=LC TO RC
900    W=W0-dw*(I-X0)
```

```
910  E=1239.85/W
920  IN=IGET(I-X0,J,0 )
930   IF IN>65000& THEN IN=0
940  EN=E*IN
950  P=P+IN
960  PW=PW+EN
970 ' PSET I,0
980 NEXT I
990 IF P=0 THEN GOTO 1040
1000  AE(J)=PW/P
1010 PD(J)=P
1020 IF S$="p" OR S$="P" THEN RSPRINT J,AE(J),P
1030 PSET X0,J
1040 NEXT J
1041 IF S$="p" OR S$="P" THEN GOTO 1210
1050 OPEN "O",#1,FD$
1060 PRINT #1,"The Average Carrier Kinetic Energy"
1070 PRINT #1,"Window "
1080 PRINT #1,LC-X0
1090 PRINT #1,RC-X0
1100 PRINT #1,"Start Channel"
1110 PRINT #1,MM
1120 PRINT #1," "
1130 FOR K=MM TO NN
1140  PRINT #1,AE(K)
1150 NEXT K
1160 PRINT #1," "
1170 FOR K=MM TO NN
1180  PRINT #1,PD(K)
1190 NEXT K
1200 CLOSE #1
1210 '--------------------
1220 '  try another window
1230 '--------------------
1240 INPUT "Do you want to try another window (y/n)?",W$
1250  IF W$="n" OR W$="N" THEN END
1260 GOTO 90
1270 END
```

A.2.3. Theoretical calculation programs

Following theoretical calculation are done in Macintosh Quick Basic.

A.2.3.1. Six level rate equation

This program enables to calculate populations in six different energy levels and fit the calculated result to the data transferred from TA. This program was used for exciton relaxation model in Chapter 4.3.

```
'---------------------------------------
' Six level model/ Fitting
'   Modified
'            2/13/92
'              Taki
'---------------------------------------
DIM d(600),f(3,600)
h=0
  dmax=0
  dmin=0

 x0=80
 wx=300
 y0=50
 wy=200
 g=30
 xg=.6
 g1=.95

  nlb0=1 : nhb0=3
  nlx0=0 : nhx0=0
  nhi0=0

INPUT "Input your Data File Name = ",dfn$
INPUT "Streak Time (ps/ch) = ",sp
INPUT " Log (G) or linear (L) plotting ?  ",pl$
INPUT "Which is lower, Heavy(h) or Light(l) exciton energy level? ",ex$
 IF ex$="h" OR ex$="H" THEN h=1

 OPEN dfn$ FOR INPUT AS #1
 FOR i=1 TO 500
    INPUT #1,d(i)
    IF d(i)>dmax THEN dmax=d(i)
    IF EOF(1) THEN GOTO 10
 NEXT i
```

```
10 CLOSE #1
   n=i-1
   FOR i=1 TO n
      d(i)=d(i)/dmax
   NEXT i

 FOR i=1 TO n
      IF d(i)=0 THEN d(i)=.000001
      IF d(i)<0 THEN d(i)=.000001
      IF pl$="L" OR pl$="l" THEN GOTO 5
      d(i)=LOG(d(i))+5
      IF d(i)<0 THEN d(i)=0
5 NEXT i
'------------------------------------------------
200 CLS
PRINT "          Nlhb  --------"
PRINT "                      Tlhx             Nhhb --------"
PRINT "          Nlhx ---------                       Thhx"
PRINT "                                  Tlh   "
PRINT"                                         Nhhx --------"
PRINT "                                                  Thhi"
PRINT "                                         Nhhi---------"
PRINT "                                                  Td"
PRINT "                                          Ng  ----------"
PRINT "*******************************************************"
PRINT "**   Exciton Formation  **"
  'INPUT "Nlhb(0),  Nhhb(0)  = ",nlb0,nhb0
  IF h=0 THEN nlb0=3 AND nhb0=1
  IF h=1 THEN INPUT " Tlhx, Thhx =",tlx1,thx1
  IF h=0 THEN INPUT " Thhx, Tlhx =",tlx1,thx1
   tlx=tlx1/sp
   thx2=thx1/sp

PRINT "** Exciton Scattering **"
  'INPUT "Nlhx(0), Nhhx(0) = ",nlx0,nhx0
  IF h=1 THEN INPUT "Tlh = ",tlh1
  IF h=0 THEN INPUT "Thl = ",tlh1
  tlh=tlh1/sp

PRINT "** Exciton Localization **"
  'INPUT "Nhhi(0) = ",nhi0
  IF h=1 THEN INPUT "Thhi = ",thi1
  IF h=0 THEN INPUT "Tlhi = ",thi1
  thi=thi1/sp

PRINT "**  Exciton Recombination   **"
  INPUT "Td = ",td1
  td=td1/sp
```

```
'------------------------------------
' Solutions for six level rate equations
'------------------------------------
INPUT "Calculation step (ch) =",s
CLS
FOR k=1 TO 3

 dt=5*(k-2)/sp
 thx=thx2+dt

      fmax=0
      fmin=0

a1=1/(-1/tlh+1/tlx)
c=nhb0/thx
a=nlb0/tlx*a1+nlx0
b=nlb0/tlx*a1
c1=c/thi/(1/td-1/thx)
a2=a/thi/(1/td-1/tlh)
b1=b/thi/(1/td-1/tlx)


FOR j=1 TO n STEP s
    i=-1*j

nlb=nlb0*EXP(i/tlx)
nhb=nhb0*EXP(i/thx)

GOTO 20
'-------------------------
' Special Initial Condition
'-------------------------
nlx=(nlb0/tlx*a1+nlx0)*EXP(i/tlh)
nlx=nlx-nlb0/tlx*a1*EXP(i/tlx)

nhx=nhx0*EXP(i/thi)+c/(1/thx-1/thi)*(EXP(i/thi)-EXP(i/thx))
  nhx=nhx+a/(1/tlh-1/thi)*(EXP(i/thi)-EXP(i/tlh))
nhx=nhx-b/(1/tlx-1/thi)*(EXP(i/thi)-EXP(i/tlx))

nhi=nhi0*EXP(i/td)+1/thi*nhx0/(1/thi-1/td)*(EXP(i/td)-EXP(i/thi))
  nhi=nhi+c1/(1/thx-1/thi)*(EXP(i/thi)-EXP(i/thx))
  nhi=nhi-c1/(1/thi-1/td)*(EXP(i/td)-EXP(i/thi))
  nhi=nhi+a2/(1/tlh-1/thi)*(EXP(i/thi)-EXP(i/tlh))
  nhi=nhi-a2/(1/thi-1/td)*(EXP(i/td)-EXP(i/thi))
  nhi=nhi-b1/(1/tlx-1/thi)*(EXP(i/thi)-EXP(i/tlx))
nhi=nhi+b1/(1/thi-1/td)*(EXP(i/td)-EXP(i/thi))

20'-------------------------
  ' Relaxation
```

```
'----------
nlx=nlb0/tlx*a1*EXP(i/tlh)
nlx=nlx-nlb0/tlx*a1*EXP(i/tlx)

nhx=c/(1/thx-1/thi)*(EXP(i/thi)-EXP(i/thx))
  nhx=nhx+a/(1/tlh-1/thi)*(EXP(i/thi)-EXP(i/tlh))
nhx=nhx-b/(1/tlx-1/thi)*(EXP(i/thi)-EXP(i/tlx))

nhi=0
  nhi=nhi+c1/(1/thx-1/thi)*(EXP(i/thi)-EXP(i/thx))
  nhi=nhi-c1/(1/thi-1/td)*(EXP(i/td)-EXP(i/thi))
  nhi=nhi+a2/(1/tlh-1/thi)*(EXP(i/thi)-EXP(i/tlh))
  nhi=nhi-a2/(1/thi-1/td)*(EXP(i/td)-EXP(i/thi))
  nhi=nhi-b1/(1/tlx-1/thi)*(EXP(i/thi)-EXP(i/tlx))
nhi=nhi+b1/(1/thi-1/td)*(EXP(i/td)-EXP(i/thi))

f(k,j)=nhi/td
      IF f(k,j)<0 OR f(k,j)=0 THEN f(k,j)=.0000001
      IF f(k,j)>fmax THEN fmax=f(k,j)

NEXT j

FOR i=1 TO n STEP s
     f(k,i)=f(k,i)/fmax
 NEXT i

'--------------------
' Data plot
'--------------------
IF pl$="L" OR pl$="l" THEN GOTO 50
 FOR i=1 TO n STEP s
      f(k,i)=LOG(f(k,i))+5
      IF f(k,i)<0 THEN f(k,i)=0
 NEXT i
50
     IF pl$="l" OR pl$="L" THEN g=150

100 ' CLS-------------

   IF k=1 OR k=3 THEN GOTO 102

IF pl$="L" OR pl$="l" THEN PRINT "DATA File(linear) =",dfn$
IF pl$="G" OR pl$="g" THEN PRINT "DATA File(log) =",dfn$
'PRINT "Nlhb(0), Nhhb(0) = ",nlb0,nhb0
IF h=1 THEN PRINT " Tlhx, Thhx =",tlx1,thx1
IF h=0 THEN PRINT " Thhx, Tlhx =",tlx1,thx1
'PRINT "Nlhx(0), Nhhx(0) = ",nlx0,nhx0
IF h=1 THEN PRINT "Tlh, Thhi, Td = ",tlh1, thi1,td1
IF h=0 THEN PRINT "Thl, Tlhi, Td = ",tlh1, thi1,td1
```

```
'PRINT "Nhhi(0) = ",nhi0

      LINE (x0,y0)-(x0+wx,y0)
      LINE (x0+wx,y0)-(x0+wx,y0+wy)
      LINE (x0+wx,y0+wy)-(x0,y0+wy)
      LINE (x0,y0+wy)-(x0,y0)

102 '-----------
 FOR i=1 TO n-s STEP s
        ' CIRCLE (i*10+x0,y0+wy-d(i)*g),3
   IF k=1 THEN  LINE (i*xg+x0,y0+wy-d(i)*g)-(i*xg+x0+s*xg,y0+wy-d(i+s)*g)
   IF k=1 THEN  LINE (i*xg+x0,y0+wy-d(i)*g+1)-(i*xg+x0+s*xg,y0+wy-
d(i+s)*g+1)
     LINE (i*xg+x0,y0+wy-f(k,i)*g*g1)-(i*xg+x0+s*xg,y0+wy-f(k,i+s)*g*g1)
  NEXT i
 NEXT k
STOP
 GOTO 300
      INPUT "Change scale (y/n)?",g$
      IF g$="n" OR g$="N" THEN GOTO 300
      PRINT " Present Scale =",g
      INPUT "Scale =",g
      GOTO 100

300 INPUT "Try again(y/n)?  ",tr$
    IF tr$="N" OR tr$="n" THEN END
    GOTO 200

END
```

A.2.3.2. Quantum well eigen state energy

The quantum eigen states in confined ideal structure can be calculated using following two programs. A.2.3.2.1 is for GaAs/AlGaAs QW having different fraction of Al in the barrier while A.2.3.2.2 is for superlattice structure where tunnel phenomena constructs miniband structure along the confinement direction.

A.2.3.2.1

```
'********************************
' Quantum well energy level
'********************************
DIM s(100), m(5,3),e(3),eg(5)

PI=3.141592
'---------------------------
' mass of electrons and holes
' m(i,j)    i=1 : GaAs
'           i=2 : AlGaAs (x=?)
'           i=3 : AlAs
'           j=1 : Conduction Band
'           j=2 : Valence Band (lh)
'           j=3 :        (hh)
'---------------------------
PRINT "****************************************"
PRINT "  Al(x)Ga(1-x)As material Composition: x"
PRINT "****************************************"
INPUT x
   m(1,1)=.067
   m(1,2)=.1059
   m(1,3)=.62
   m(2,1)=m(1,1)+(m(3,1)-m(1,1))*x
   m(2,2)=m(1,2)+(m(3,2)-m(1,2))*x
   m(2,3)=m(1,3)+(m(3,3)-m(1,3))*x
   m(3,1)=.15
   m(3,2)=.15
   m(3,3)=.76
'---------------------------
' Energy levels
'---------------
INPUT "Temperature (K) = ",t
   eg(1)=1.519-.0005405*t^2/(t+204)
   eg(3)=2.239-.0006*t^2/(t+408)
   eg(2)=eg(1)+(eg(3)-eg(1))*x
```

```
e(1)=(eg(2)-eg(1))*2/3
e(2)=e(1)/2
e(3)=e(2)
'--------------------
'  Calculation
'--------------------
INPUT "  Lz (Å) = ",lz
  PRINT "**************************************"
 PRINT "   QW Eigenenergy state"
  PRINT "**************************************"
 PRINT "   Temperature (K) = ",t
 PRINT "   Well Width (A) = ",lz
 PRINT " "
1 FOR k=1 TO 3
 IF k=1 THEN PRINT " <  In Conduction Band > "
 IF k=2 THEN PRINT " < In Valence Band >"
 IF k=2 THEN PRINT " --- Light Hole --- "
 IF k=3 THEN PRINT " --- Heavy Hole --- "
 r=m(2,k)/m(1,k)
 ii=0
10 FOR i=ii TO .999 STEP .001
 x1=TAN(.081537*lz*SQR(e(k)*m(1,k))*2*PI*i)-2*i*SQR((1-i^2)*r)/((r+1)*i^2-1)
 i=i+.001
 x2=TAN(.081537*lz*SQR(e(k)*m(1,k))*2*PI*i)-2*i*SQR((1-i^2)*r)/((r+1)*i^2-1)
 IF x1<0 AND x2>0 THEN GOTO 100
 IF x1>0 AND x2<0 THEN GOTO 100
 NEXT i
100 '--------------------
 FOR j=i-.001 TO i STEP .0001
  x1=TAN(.081537*lz*SQR(e(k)*m(1,k))*2*PI*j)-2*j*SQR((1-j^2)*r)/((r+1)*j^2-1)
  j=j+.0001
  IF j>1 THEN GOTO 300
  x2=TAN(.081537*lz*SQR(e(k)*m(1,k))*2*PI*j)-2*j*SQR((1-j^2)*r)/((r+1)*j^2-1)
  IF x1<0 AND x2>0 THEN GOTO 200
  IF x1>0 AND x2<0 THEN GOTO 200
  j=j-.0001
 NEXT j
200 '--------------------
   en=j^2*e(k)
   PRINT j,en
   ii=i
   IF ii>.9999 THEN GOTO 300
   GOTO 10
300 NEXT k
400 FOR l=1 TO 5
     PRINT " "
   NEXT l
END
```

A.2.3.2.2. Miniband structure calculation program

```
'------------------------------------------------
'  Miniband Width Calculation
'    10/3/91
'    Taki
'------------------------------------------------
      CLS
INPUT "Well Width (Å) =",a1
         a=a1*1E-10
INPUT "Barrier Width (Å) = ",b1
         b=b1*1E-10
INPUT "Effective Mass = ",me
         m=me*9.11E-31
INPUT "Potential Height(V) =",V1
         v=V1*1.602E-19
         h=6.626E-34/2/3.14159
         j=m^.5/h

FOR k=1 TO V1*1000
          e=k*1.602E-22
         co=COS(a*(2*e)^.5*j)
         d=EXP(b*(2*(v-e))^.5*j)
         ch=(1/d+d)/2
         i= (v/e-1)
         g=(1-co^2)*(ch^2-2)
              IF i<0 OR i=0 THEN GOTO 10
              IF g<0 OR g=0 THEN GOTO 10
         x=co*ch+(v/2/e-1)*(g/i)^.5
         IF x>-1 AND x<1 THEN PRINT k

10 NEXT k

LPRINT DATE$,"/",TIME$
LPRINT " "
LPRINT "***************************************"
LPRINT "  Miniband in a superlattice"
LPRINT "***************************************"

LPRINT " "
LPRINT "Well Width (Å) =",a1
LPRINT "Barrier Width (Å) = ",b1
LPRINT "Effective Mass = ",me
LPRINT  "Potential Height(V) =",V1
LPRINT " "

p=0
INPUT "Lower Energy Edge=",l
LPRINT  "Lower Energy Edge(meV) = "
```

```
    GOTO 30

20 IF p=1 THEN END
   p=1
   INPUT "High Engery Edge =",l
LPRINT  "High Engery Edge = "
   l=l+1

30  FOR k=l-1 TO l STEP .1
         e=k*1.602E-22
         co=COS(a*(2*e)^.5*j)
         d=EXP(b*(2*(v-e))^.5*j)
        ch=(1/d+d)/2
        i= (v/e-1)
        g=(1-co^2)*(ch^2-2)
           IF i<0 OR i=0 THEN GOTO 40
           IF g<0 OR g=0 THEN GOTO 40
        x=co*ch+(v/2/e-1)*(g/i)^.5
           LPRINT  k,x
40     NEXT k
    LPRINT " "
    LPRINT " "
    IF p=0 THEN GOTO 20
END
```

BIBLIOGRAPHY

Agrawal , G. P. and Dutta, N. K. "Long wavelength semiconductor lasers" Van Nostrand Reinhold, New York (1986)

Alfano, R. R. "Semiconductor Probed by Ultrafast Laser Spectroscopy", Academic Press, New York (1984)

Asono, H. at al., IEEE Photonics Tech. Lett. 3, 415 (1991)

Bacher, G., Kovac, J. ,Streubel, K., H. Schweizer, and F. Scholz, Phys.Rev. B, 45, 9136(1992)

Basterd, G. "Wave mechanics applied to semiconductor heterostructures" les editions de physique, France (1988)

Basu, P. K. and Partha Ray, Phys. Rev. B, 45, 1907 (1992)

Bernier, G., J. Beerens, J. De Boeck, K. Deneffe, C. van Hoof, and G. Borghs, Solid State Comm. 69, 727 (1989)

Bertolet, D. C., Jung-Kuei Hsu, Kei May Lau, E. S. Koteles and D. Owens, J. Appl. Phys. 64, 6562 (1988)

Blakemore, J., "Gallium Arsenide", Ameriacn Institute of Physics, New York (1987)

Bradley, D. J., and W. Sibbett: Appl. Phys. Lett. 25, 382 (1975)

Casey et.al " Heterostructure lasers" Part A and B, Academic Press, Inc. California(1978)

Cesar, C.L., M. N. Islam, C. E. Soccolish, R. D. Feldmann, R. F. Austin, and K. R. German, in ": Ultrafast Phenomena VII", Springer-Verlag, New York (1990)

Chandrasekhar, M., and F.H. Pollak, Phys. Rev. B, 15, 2127 (1977)

Chen, Y., A. Freundlich, H. Kamada and G. Neu, Appl. Phys. Lett. 54 (1989)

Conwell, E. M., "High field transport in semiconductor", Academic Press, New York (1967)

Damen, T. C., J. Shah, D. Y. Oberli, D. S. Chemla, J. E. Cunningham, and J. M. Kuo, J. of Luminesc. **45**, 181 (1990)

Damen, T. C., J. Shah, D. Y. Oberli, D. S. Chemla, J. E. Cummingham, and J. M. Kuo ,Phys. Rev. B, **42**, 7434 (1990)

Esaki, L., and R. Tsu, IBM Research Note, RC-**2418** (1969) and IBM J. Res. Develop.**61**, Jan. (1970)

Feldmann, J., G. Peter, E. O. Gobel, P. Dawson, K. Moore, C. Foxon, and R. J. Elliott, Phys. Rev. Lett. **59**, 2337 (1987)

Feldmann, J., R. Sattmann, E. O. Gobel, J. Kuhl, J. Hebling, K. Ploog, R. Muralidharan, P. Dawson, and C. T. Foxon, Phys. Rev. Lett. **62**, 1892 (1989)

Feldmann, J., J. Nunnenkamp, G. Peter, E. Gobel, J. Kuhl, K. Ploog, P. Dawson, and C. T. Foxon, Phys. Rev. B, **42**, 5809 (1990)

Fischer, R., W. Kopp, H. Morkoc, M. Pion, et al., Appl. Phys. Lett. **48**, 1360 (1986)

Fork, R.L., B. I. Breene, and C. V. Shank, Appl. Phys. Lett., **38**, 671 (1981)

Freundlich, A., H. Kamada, and G. Neu, Phys. Rev. B. **40**, 1652 (1989)

Fujiwara, K., K. Kanamoto, and N. Tsukada, Phys. Rev. B, 40 , 9698 (1989)

Fujiwara, K., H. Katahama, K. Kamamoto, R. Cingolani, and K. Ploog, Phys. Rev. Lett. **43**, 13978 (1991)

Gandhi, S. K., "VLSI Fabrication Principle", Wiley-International, New York (1967)

Hall, R. N. , G. E. Fenner, J. D. Kingsley, T. J. Soltys, and R. O. Carlson, Phys. Rev. Letter 9, 366 (1962)

Harris , "Ultrafast Phenoimena VII", Springer Verlag, New York (1990)

Hess , Karl and C. T. Sah, Phys. Rev. B, 10, 3375 (1974)

Hess, K. Appl. Phys. Lett. 35, 484 (1979)

Hiyamizu, S., T. Mimura, T. Fujii, and K. Nambu, Appl. Phys. Lett. 37, 805 (1980)

Hochtrasser,R. M. , W. Kaiser, and C. V. Shank, "Picosecond Phenonena II", Springer-Verlag, Berlin and New York (180)

Huang, C. P. , M. Asaki, S. Backus, H. Natherl, M. M. Murnane, and H. C. Kapteyn, Conf. Proc. "Ultrafast Phenomena", Th. E2 (1992)

Iwamura, H. , T. Saku, H. Kobayashi, and Y. Horikoshi , J. Appl. Phys. 54, 2692 (1983)

Joma, M., et al., Appl. Phys. Lett. 58, 2220 (1990)

Kane, E.O., J. Phys. Cham. Solid, 1, 249 (1957)

Kash, K., and J. Shah ,Appl. Phys. Lett. 45, 401 (1984)

Keller, U., W. H. Knox, and H. Roskos, in "Ultrafast Phenomena VII", Springer-Verlag, New York (1990)

Kinoshita, K., Y. Takiguchi, I. Hayashi, Y. Tsuchiya, K. Oba, M. Yamanaka, H. Niki, K. Miyanaga, T. Yamanaka, Y. Izawa, C. Yamanaka, SPIE Proc. 693, 111 (1986)

Koteles, E. S., D.A.Owens, D. C. Bertolet, J-K. Hsu, and K.M.Lau Surface Science, 228, 314 (1990)

Kronig, R. de, and W. J. Penney, Proc. Royal, Sco. London, A130, 499 (1930)

Kusano, Jun-ichi, Y. Segawa, Y. Aoyagi, S. Namba, and H. Okamoto, Phys. Rev. B , 40, 1685 (1989)

Lawaetz, P. , Phys. Rev. B, 4, 3460 (1971)

Leburton, J. P. , J. Appl. Phys. 56, 2850 (1984)

Lee, Johnson , M. O. Vassell, E. Koteles, C. Jagannth, K.T. Hsu, G. J. Jan, C. P. Liu, and I. F. Change, Phys. Rev. B, 40, 1703 (1989)

Lee, Johnson, and M. O. Vassell, Phys. Rev. B. 37, 8855 (1988)

Lee, Johnson, and M. O. Vassell, Phys. Rev. B. 37, 8861 (1988)

Lee, Shun, Ph.D thesis at the City College of CUNY (1992)

Lester, L. F., et al. , IEEE Photonics Tech. Lett. 3, 403 (1991)

Luttinger, J. M. , and W. Kohn, Phys. Rev. 97, 869 (1955)

Luttinger, J. M. , Phys. Rev. 102, 1030 (1956)

Masumoto, Y. , S. Shionoya, and H. Kawaguchi, Phys. Rev. B, 29, 2324 (1984)

Nakano, N. , H. Kuroda, E. Inuzuka, Y. Takiguchi, M. Sujiyama, Y. Tsuchiya, and Y.Suzuki, SPIE Prooc. 491, 962 (1984)

Nye. J. F. , "Physical Properties of crystal", Oxford at the Clarendon Press, (1984)

Pollak, F. H. , and M. Cardona, Phys. Rev. 172, 816 (1968)

Pollak, F.H. , C.W. Higginbothan, and M. Cardona, J. Phys. Soc, Jpn, Suppl. 21, 20 (1966)

Qiang, H., and F.H. Pollak, Kai Shum, Y. Takiguchi, R. R. Alfano, Appl. Phys. Lett. (1992)

Qiang, H., F. H. Pollak, and G. Hackman, Solid State Comm. 76, 1087 (1990)

Ridley, B. K., "Quantum phenomena in semiconductors" Oxford University Press, Oxford (1988)

Sakai, S., T. Soga, M. Takeyasu, X. W. Hu, et al. Proc. IEEE Int. Semiconductor Laser Conf. D-3 (1986)

Schiller, N. H., Y. Tuchiya, E. Inuzuka, Y. Suzuki, K. Kinoshita, K. Kamiya, H. Iida, and R.R.Alfano, Optical Spectra 14, 55 (1980)

Schokley, W., and W. T. Read, Jr., Phys. Rev. 87, 835 (1952)

Serreze, H. B., and Y. C. Chen, IEEE Photonics Tech. Lett. 3, 397 (1991)

Shah, J., and R.C.C. Leite, Phy. Rev. Lett. 22, 1304 (1969)

Shah, J., Phy. Rev. B. 10, 3697 (1978)

Shah, J., and R.F. Leheny, in "Semiconductor Probed by Ultrafast Laser Spectroscopy" edited by R.R.Alfano, Academic Press, 1984

Shank, C.V., R. L. Fork, B. I. Greene, C. Weisbuch, and A. C. Gossard, Surf. Sci., 113, 108 (1982)

Shank, C.V., R. L. Fork, R. Yen, J. Shah, B. I. Greene, A.C. Gossard, and C. Weisbuch, Solid State Comm., 47, 981 (1983)

Shum, K., Y.Takiguchi, J.M. Mohaidat, F. Liu, R.R.Alfano and H. Morkoc, Appl. Phys. Lett. 56, 2328 (1990)

Soga, T., T. jimbo, and M. Umeno, Appl. Phys. Lett., 56, 1433 (1990)

Spector, H. N. , Johnson Lee, and Paul Melman, Phys. Rev. B, 34, 2554 (1986)

Streubel, K., Bacher, G. , Kovac, J. , H. Schweizer, and F. Scholz, Phys. Rev. B, 45, 9136(1992)

Strobel, R., R. Eccleston, J. Kuhl, and K. Kohler, Phys. Rev. B, 43, 12564, (1991)

Takagahara, T. , Phys. Rev. B 31, 6552 (1985)

Takiguchi, Y. , Kai Shum, R.R.Alfano, Proc. of Hot Carrier Conference at Nara, Japan (1991)

Takiguchi, Y. , Kai Shum, R.R. Alfano, Emil S. Koteles, D. C. Bertolet, and Kei May Lau, SPIE Proc. 1655, (1992)

Takiguchi, Y. , Kai Shum, R. R. Alfano, Emil S. Koteles, D. C. Bertolet, and K. M. Lau, Semicond. Sci. Technol. 7,B170 (1992)

Takiguchi, Y., K. Kinoshita, M. Suyama, Y. Inagaki, and Y. Tsuchiya, Proc. SPIE 693, 105 (1986)

Takiguchi, Y. , S. Aoshima, and Y. Tsuchiya, Proc. SPIE 693, 118 (1986)

Takiguchi, Y. , Kai Shum, R. R. Alfano, M. Dutta, and P.G. Newman to be published in Proc. SPIE Vol. 1599

Takiguchi, Y. , Kai Shum, R. R. Alfano, E. S. Koteles, D. C. Bertolet, J. K. Hsu, and K. M. Lau, to be published in "7th International Conference of Hot Carrier as Nara in Japan ,1991" Proceedings

Tang, W. T. Appl. Phys. Lett. 39, 786 (1981)

Tsuchiya, Y. , E. Inuzuka, and Y. Suzuki, Proc. 13 the International Conference on High Speed Photography and photonics

(Tokyo) (1978)

Unlu, H., and H. Morkoc, Solid State Tech. Mar., 83 (1988)

Valdmanis, J. A., and R. L. Fork, IEEE J. Quant. Electronics, QE-22, 112 (1986)

van der Ziel, J. P., R. Dingle, R. C. Millar, W. Wieg, and W. A. Nordland, Appl. Phys. Lett. 26, 463 (1975)

Voisin, P., C. Delalande, M. Voos, L. L. Chang, A. Segmuller, C. A. Chang, and L. Esaki, Phys. Rev. B, 30, 2276 (1984)

Weisbuch, C., R. Dingle, A. C. Gossard, and W. Wiegmann, Solid State Comm. 38, 709 (1981)

Windhorn, T. H., and G.M. Metze, Appl. Phys. Lett. 47, 1031 (1985)

Yang, L., at al., IEEE Photonics Tech. Lett. 3, 430 (1991)

Yao, S. S., Ph. D thesis at the City College of CUNY (1982)

Zemon, S., S. K. Shastry, P. Norris, C. Jagannath, and G. Lambert, Solid State Comm. 58, 457 (186)